CONF-820131--

CHARGE STATES AND DYNAMIC SCREENING OF SWIFT IONS IN SOLIDS

Proceedings of the U.S.-Japan Seminar on
Charged-Particle Penetration Phenomena

January 25-29, 1982

East-West Center
Honolulu, Hawaii

Date Published - January 1983

Sponsored by

U.S. National Science Foundation
and
Japan Society for the Promotion of Science

with assistance from

New York University
and
Oak Ridge National Laboratory

Prepared by the
OAK RIDGE NATIONAL LABORATORY
Oak Ridge, Tennessee 37830
Operated by
UNION CARBIDE CORPORATION
for the
U.S. Department of Energy
Under Contract No. W-7405-eng-26

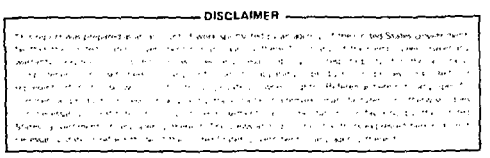

PREFACE

This report is the proceedings of the U.S.-Japan Seminar on Charge States and Dynamic Screening of Swift Ions in Solids that was held January 25-29, 1982, at the East-West Center in Honolulu. The Seminar was modeled on a series of informal workshops held at New York University over a period of several years.

Past workshops have included as main topics:

- Wake Phenomena - 1977
- Current Stopping Power Problems - 1978
- The Penetration of Low-Energy Particles - 1979
- The Penetration of Charged Particles Under Extreme Conditions - 1980
- The Penetration of Exotic Particles in Matter - 1981.

The U.S.-Japan Seminar and its precursors at NYU were designed to encourage informality and spontaneity in the exchange of information and in highlighting of key problems in areas of current importance.

This conference was sponsored by the U.S. National Science Foundation and by the Japan Society for the Promotion of Science. Additional support was provided by New York University and the U.S. Department of Energy. The organizational effort on the Japanese side was led by Prof. R. Ishiwari, whom we thank for his tireless efforts in behalf of the meeting. Finally, we want to thank all the participants for their many formal and informal contributions toward a very successful conference.

U.S. Organizers

J. C. Ashley
R. H. Ritchie
W. Brandt

TABLE OF CONTENTS

TABLE OF CONTENTS (CONT.)

TABLE OF CONTENTS (CONT.)

Stopping Powers of Zr, Pd, Cd, In and Pb for 6.5 MeV Protons and Mean Excitation Energies

R. Ishiwari, N. Shiomi and N. Sakamoto
Department of Physics, Nara Women's University, Nara 630, Japan

Stopping powers of Zr, Pd, Cd, In and Pb have been measured for 6.5 MeV protons. Mean excitation energies have been extracted from the stopping power data by taking into account Bloch correction and Z_1^3 correction. For the shell correction the Bonderup shell correction has been used. The results agree fairly well with those of other authors.

I Introduction

In the previous experiment[1,2], the stopping powers of 16 kinds metallic elements from Be to Au have been measured for 6.5 MeV protons and mean excitation energies have been obtained from the stopping power data by taking into account Bloch correction[3,4] and Z_1^3 correction[4,5,6] and by using the Bonderup shell correction[7]. The results agreed fairly well with those obtained by other authors[8,9,10].

In the present experiment, stopping powers of Zr, Pd, Cd, In and Pb have been measured for 6.5 MeV protons. Mean excitation energies have been extracted from the stopping power data also using Bloch correction, Z_1^3 correction and the Bonderup shell correction.

II Experimental Procedure

Fig. 1 shows the experimental set up. Protons of 6.75 MeV from the cyclotron of Kyoto University were analyzed by the analyzing magnet with momentum resolution of 0.1%. The magnetic field was kept constant within 0.01% during the measurement. Then, protons entered the scattering chamber through a double slit system S_2 and S_3, the diameter of which was 1.5mm each and 35 cm apart.

Protons were scattered by a thin gold foil of 180μg/cm^2 at the center of the scattering chamber. Protons scattered at an angle of 15 degrees were used for the present measurements. The scattered protons were collimated by a double slit system S_4 and S_5, the diameter of which was 1.5mm each and 7.8cm apart. Then protons passed through the target and all protons that passed through the target were detected by a surface barrier silicon detector.

To determine the energy loss of protons in the target, the pulse height of protons that passed through the target and the pulse height of protons that did not pass through the target were recorded. In order to measure the above two pulse heights simultaneously in one exposure, special device was used for target mounting. This device is shown also in Fig. 1. The part indicated as A is essentially an ammeter. When A.C. power is supplied, the hand indicated as B makes a pendulum motion. A double frames indicated as C are fixed to the hand B. To one of the frames the target is fixed and the other frame is left empty. When A.C. power is supplied and the hand B makes a pendulum motion, the incident beam traverses the two frames. Therefore, protons that pass through the target and protons that do not pass the target hit the detector alternatively. Thus, the pulse heights of protons with and without the target were recorded simultaneously in one exposure. In principle this method is the same as what we call absorber wheel technique that was used in the previous experiment[1,2], but is much more efficient in saving the time of data collection than the absorber wheel technique.

The pulses from the silicon detector were amplified by a low noise amplifier and fed into a 4096 channel pulse height analyzer. By taking the average values for both peaks with and without the target, the difference of the pulse heights has been determined with an uncertainty of ±0.15% irrespective of the averaging range. The energy calibration of the pulse height spectrum was made with a very high precision pulse generator(ORTEC 448). The ionization defect of the silicon detector has been investigated in the previous experiment[2] and has turned out to be substantially zero for 6.5 MeV protons.

All target foils used in the present experiment were manufactured by

Goodfellow Metals Ltd. The thickness of the target has been determined by the weight per area method. Square samples of 2cm by 2cm were cut out with a razor blade. Each foil was weighed five times on a Metler ME 30/36 electro-michro balance which has an absolute accuracy of 1 μg. The area of each foil was measured also five times with a Tiyoda LTG bi-AII microscope which can read to 1μm. The repeticion of the whole set of weight per area measurement for the same sample on different days showed a standard deviation of 0.1∼0.15%. Therefore, the uncertainty of the foil thickness was assigned to be ±0.15% for all samples. The purities of the foils are 99.8% for Zr, 99.95% for Pd, 99.7% for Cd, 99.8% for In and 99.99% for Pb. No correction was made for impurities. The thickness of the samples are 16.410 mg/cm^2 for Zr, 14.443 mg/cm^2 for Pd, 16.180 mg/cm^2 for Cd, 17.016 mg/cm^2 for In and 21.847 mg/cm^2 for Pb.

In the present method, the proton beam traverses the target during the measurement. So the possible nonuniformity of the target thickness is automatically averaged and the observed energy loss corresponds to the average thickness of the target, that is the thickness obtained by the weight per area method.

In general, the observed energy loss divided by the average path length of protons in the target, $\Delta E/\Delta X$, corresponds, to a good approximation, to the stopping power, $-dE/dX$, at the "average energy" defined by $\bar{E} = E_0 - \Delta E/2$, where E_0 is the incident energy. The thicknesses of the sample targets were chosen such that the energy loss of protons in the target was about 500 keV. Therefore, the average energies were very close to 6.5 MeV. For convenience when comparing the present results with other experiments, the present results have been reduced to 6.500 MeV by assuming that the stopping power is proportional to $(\ln v^2)/v^2$ in a narrow velocity range.

From the above mentioned uncertaintes of the energy loss and target thickness, the uncertainty of the stopping power is calculated to be 0.25%.

Making allowances for unexpected errors, the final uncertainty of the present results was assigned to be ±0.3%.

III Results

In table 1 the present results are shown and compared with the data of H.H Andersen et al.[11,12] (below refered to as the Risø data) and the compilation of H.H. Andersen and J.F. Ziegler[9]. The Risø value for Zr is higher than the present value by 1.96% and the difference is statistically significant. The Risø value for Pb is 0.7% higher than our value but the difference is not statistically significant. The trend that the Risø data are higher than our data agrees with the previous experiment. The value for Zr of Andersen and Ziegler[9] is also higher than the present value by 2.2% and the difference is also significant. Values of Andersen and Ziegler[9] for other elements agree with our values within the statistical errors.

IV Analysis

The mean excitation energies were extracted from the present data by taking into account Bloch correction and Z_1^3 correction. The Bethe-Bloch formula[13,14] of the stopping power is written as

$$-\frac{dE}{dX} = \frac{4\pi e^4 z_1^2}{mv_1^2} N_2 Z_2 \left(\ln \frac{2mv_1^2}{I} + \ln \frac{1}{1-\beta^2} - \beta^2 - \frac{C}{Z_2} + \Phi + Z_1 L_1 \right) \quad ---(1)$$

where e is the elementary charge, m is the mass of electron, z_1 and v_1 are the atomic number and the velocity of the incident particle, N_2 is the number of the target atoms per cm^3, Z_2 is the atomic number of the target atom, I is the mean excitation energy and β is v_1/c (c is the speed of light) and C/Z_2 is the shell correction. The symbol Φ denotes the Bloch correction[3,4] term which is given by

$$\Phi = \psi(1) + \mathrm{Re}\ \psi(1+i\xi), \quad \xi = z_1 v_0 / v_1, \quad ---(2)$$

v_0 is the Bohr velocity ($v_0 = e^2/\hbar$) and ψ denotes the logarithmic derivative of the Γ Function. The term $L_1 Z_1$ is the Z_1^3 correction term[4,5,6]. In the theory of Ashley, Ritchie and Brandt, L_1 is given as a function of reduced energy $x = v_1^2/v_0^2 Z_2$, an adjustable parameter b that is a scaled lower impact parameter cutoff in the collision of protons with

target atom electrons and a constant, χ, that appears in the statistical model of the atom. In the present analysis, we used the values of b and χ which were determined in the previous work[2], that is b ≈ 1.3 and χ = 1.358. For the shell correction we used the Bonderup shell correction[7]. The Bonderup shell correction is also a function of χ. We have calculated C/Z_2 with χ = 1.358.

From eq.(1), putting the experimentally determined stopping power into -dE/dX, we have extracted the mean excitation energy.

Table 2 shows the results of the present analysis. For the estimation of the uncertainty of the I values, we took b = 1.3±0.2 and the uncertainty of the Bonderup shell correction to be ±10%, although the shell corrections have been calculated to within 0.5% numerically.

V Discussion

In table 3, the present results of mean excitation energy are compared with other authors[8,9,10]. For Pb, the present result is slightly lower than the value of other authors. But the differences are well within the statistical uncertainty. For Zr the present result is higher than the results of other authors. The difference might be statistically significant, although the uncertainties of the values given by Andersen and Ziegler[9] and Ziegler[10] are not known. However, if we assume the uncertainty of the values of Andersen and Ziegler[9] and Ziegler[10] to be 10 eV, the differences are not statistically significant. This difference is certainly due to the difference of the absolute value of the stopping power. The present stopping power value is significantly lower than the values of Andersen and Ziegler and also the Risø data. Careful remeasurement of Zr is desired.

Recently, Berger[15] has calculated mean excitation energy by using Bichsel's method[16] of calculating shell correction. In Bichsel's method, the higher corrections than M shell are assumed to have the same shape as Walske's[17,18] L shell correction. And each correction term is scaled by two free parameters multiplied to energy and shell correction value.

Bichsel's shell correction gives almost the same I values as the Bonderup shell correction for the atomic number up to ~50, but gives systematically higher I values for heavier elements.

For example, Berger's I value for Pb is 823±30. The difference between our value and Berger's value is 77 ±42 eV. So the difference is not statistically significant with 5% significant level. As noted in the present experiment as well as the previous experiment[1,2], the Risø data are systematically too high and are not very suited for extracting I values from them. More accurate stopping power measurements of Au and Pb for protons from 3 to 9 MeV are now being planned. Detailed discussion of Berger's estimation of I values will be given elsewhere[19].

In table 4, the present I values and I values of 16 kinds metallic elements obtained in the previous work[2] are tabulated and compared with the Risø data and compilations of Turner[8], Andersen and Ziegler[9] and Ziegler[10]. Overall agreements of our data with the values of other authors are very good.

VI Acknowledgments

The authors would like to thank Prof. T. Yanabu and Prof. H. Takekoshi for the use of the cyclotron. Thanks are also due to kind cooperation of the members of the cyclotron Laboratory.

References

1) R. Ishiwari, N. Shiomi and N. Sakamoto, Phys. Lett., 75A (1979) 112. "Stopping Powers of Be, Al, Ti, V, Fe, Co, Ni, Cu, Zn, Mo, Rh, Ag, Sn, Ta, Pt and Au for 6.75 MeV Protons".

2) R. Ishiwari, N. Shiomi and N. Sakamoto, Nucl. Instrum. Methods, 184 (1982) 61. "Stopping Powers of Metallic Elements for 6.75 MeV Proton".

3) J. Lindhard, Nucl. Instrum. Methods, 132 (1976) 1. "The Barkas Effect-or Z_1^3, Z_1^4- Corrections to Stopping of Swift Charged Particles".

4) R.H. Ritchie and W. Brandt, Phys. Rev., A17 (1978) 2102. "Projectile-Charge Dependence of Stopping Powers".

5) J.C. Ashley, R.H. Ritchie and W. Brandt, Phys. Rev., B5 (1972) 2393. "Z_1^3 Effect in the Stopping Power of Matter for Charged Particles".

6) J.C. Ashley, R.H. Ritchie and W. Brandt, Phys. Rev., A8 (1973) 2402. "Z_1^3- Dependent Stopping Power and Range Contributions".

7) E. Bonderup, K. Dan. Vidensk. Selsk. Mat. Fys. Medd., 35 (1967) No.17. "Stopping of Swift Protons Evaluated from Statistical Atomic Model".

8) J.E. Turner, P.J. Roecklein and R.B. Vora, Health Physics 18 (1970) 159. "Mean Excitation Energies for Chemical Elements".

9) H.H. Andersen-J.F. Jiegler,"Hydrogen Stopping Powers and Ranges in All Elements". (Pergamon, New York, 1977).

10) J.F. Jiegler, Nucl. Instrum. Methods, 168 (1980) 17. "The Stopping of Energetic Ions in Solids".

11) H.H. Andersen, H. Simonsen, H. Sørensen and P. Vajda, Phys. Rev.,186 (1969) 372. "Stopping Power of Zr, Gd and Ta for 5-12 MeV Protons and Deuterons. Further Evidence of an Oscillatory Behavior of the Excitation Potential".

12) H. Sørensen and H.H. Andersen, Phys. Rev., B8 (1973) 1854. "Stopping Power of Al, Cu, Ag, Au, Pb and U for 5-18 MeV Protons and Deuterons".

13) H.A. Bethe, Ann. Physik,5 (1930) 325. "Zur Theorie des Durchganges Schneller Korpuskularstrahlen durch Materie".

14) F. Bloch, Ann. Physik, 16 (1933) 285. "Zur Bremsung rasch bewegter

Teilchen beim Durchgang durch Materie".

15) M.J. Berger and S.M. Seltzer, "Mean Excitation Energies for Use in Bethe's Stopping-Power Formula", Proceedings of the United States-Japan Seminar "Charge state and Dynamic Screening of Swift Ions in Solids". January 1982 Honolulu, This ORNL-Report.

16) H. Bichsel, "A Fortran Program for The Calculation of The Energy Loss of Heavy Charged Particles". UCRL-17538 (University of California, 1967)

17) M.C. Walske, Phys. Rev., 88 (1952) 1283. "The Stopping Power of K-Electrons".

18) M.C, Walske, Phys. Rev., 101 (1956) 940. "Stopping Power of L-Electrons".

19) R. Ishiwari, N. Shiomi and N. Sakamoto, to be Published.

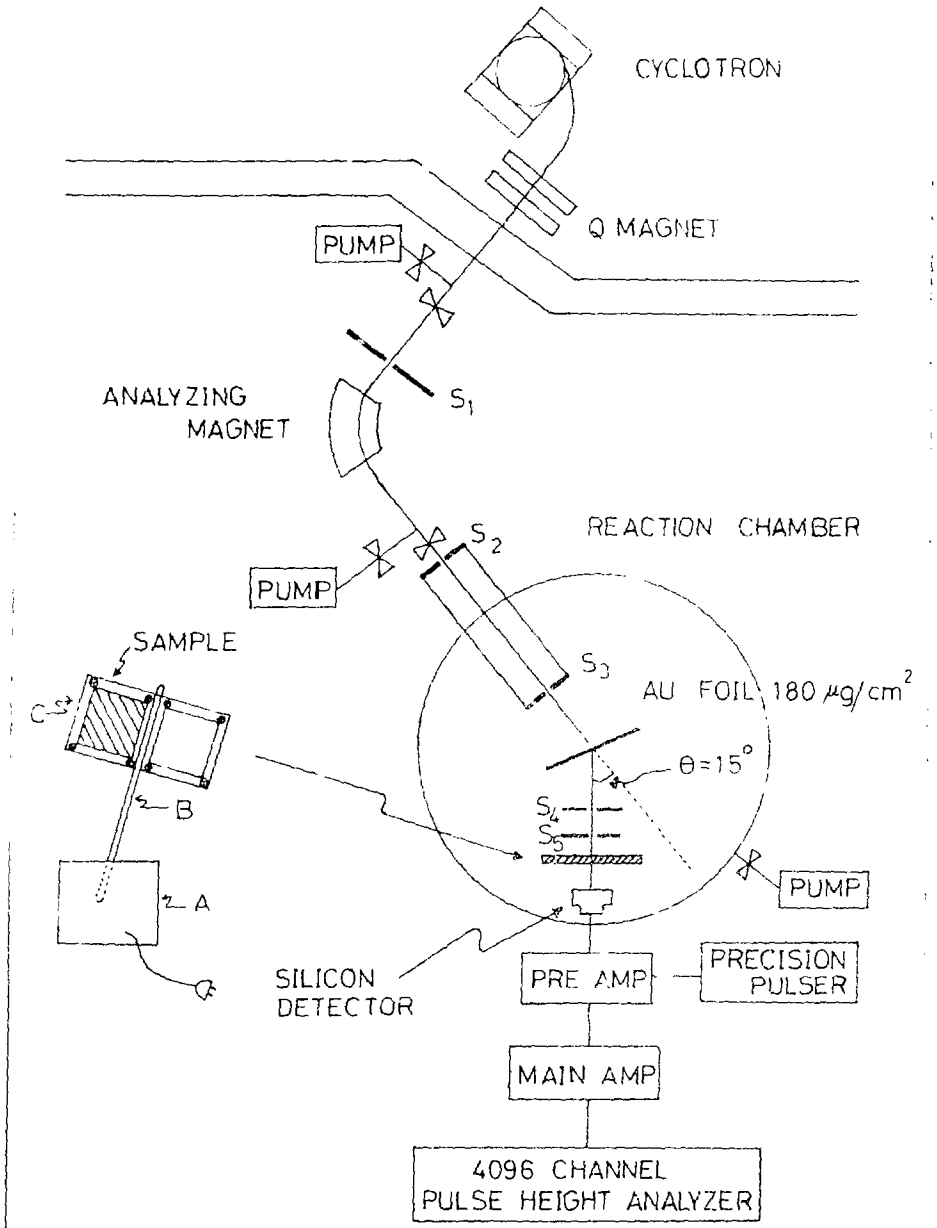

Fig. 1. Experimental Set up.

Table 1. Present results are compared with the Risø data and compilation of Andersen and Ziegler.

Z_2	Elements	-dE/dX (keV/mg cm^{-2}) Present data	Risø data[1]	Andersen[2] -Ziegler
40	Zr	32.71±0.10	33.35±0.10	33.44
46	Pd	30.74±0.09		30.78
48	Cd	30.37±0.09		30.13
49	In	29.73±0.09		29.88
82	Pb	23.18±0.07	23.35±0.14	23.37

1) H.H. Andersen et al., Phys. Rev., 186 (1969) 372, Phys. Rev., B8 (1973) 1854.

2) H.H. Andersen and J.F. Ziegler, Stopping powers and ranges in all elements, Hydrogen, Pergamon (1977).

Table 2. Analysis of the present data. The symbol K denotes the Bloch constant.

Z_2	Elements	S(keV/mg cm^{-2})	$\Phi(v_1,z_1)$	C/Z_2	L_1	I(eV)	K
40	Zr	32.71±0.10	-0.00465	0.262	0.0450±0.0074	401±11	10.0±0.3
46	Pd	30.74±0.09	-0.00465	0.287	0.0479±0.0083	459±14	9.8±0.3
48	Cd	30.37±0.09	-0.00465	0.293	0.0488±0.0086	457±14	9.5±0.3
49	In	29.73±0.09	-0.00465	0.297	0.0493±0.0087	485±15	9.9±0.3
82	Pb	23.18±0.07	-0.00465	0.372	0.0598±0.0128	746±30	9.1±0.4

Table 3 Comparison of the present I values with those of other authors.

		Mean Excitation Energy I(eV)				
Z_2	Elements	Present	Risø[1]	Turner[2]	Andersen-Ziegler[3]	Ziegler[4]
40	Zr	401±11			378	382
46	Pd	459±14		436	458	456
48	Cd	457±14		462	471	466
49	In	485±15		481	480	479
82	Pb	746±30	773±20	767	759	761

1) H.H. Andersen et al., Phys. Rev., 180 (1969)372, Phys. Rev., B8 (1973) 1854.

2) J.E. Turner dt al., Health Physics 18 (1970) 159.

3) H.H. Andersen and J.F. Ziegler, Hydrogen, Pergamon (1977).

4) J.F. Ziegler, Nucl. Inst. Meth., 168 (1980) 17.

Table 4 Comparison of Nara data of I values for 21 kinds of metallic elements with I values of other authors.

		Mean excitation Energy (eV)				
Z_2	Elements	Nara	Andersen[1] (Risø)	Turner[2]	Andersen[3]	Ziegler[4]
4	Be	64.0±1.0		61.7	62.7	63
13	Al	167.6±2.8		163	162	162
22	Ti	232.3±4.9	229.8±2.6	224	230	228
23	V	241.8±5.2	239.2±2.8	250	239	237
26	Fe	282.5±6.5	280.6±3.1	277	280	284
27	Co	295.9±6.9	298.8±3.7	290	296	304
28	Ni	312.7±7.5	303.2±3.7	312	310	314
29	Cu	323.5±7.9	319.8±3.2	316	322	330
30	Zn	331.3±8.2	323.1±3.8	319	320	323
40	Zr	401.2±11			378	382
42	Mo	413 ±12		422	406	393
45	Rh	445 ±14		440	443	436
46	Pd	459 ±14		456	458	456
47	Ag	464 ±15	469 ±8	466	466	470
48	Cd	457 ±14		462	471	466
49	In	485 ±15		481	480	479
50	Sn	471 ±15		486	487	512
73	Ta	676 ±26		692	684	682
78	Pt	730 ±29		711	759	760
79	Au	746 ±30	771 ±20	760	755	742
82	Pb	746 ±30	773 ±20	767	759	761

1) H.H. Andersen et al., Phys. Rev., 180 (1969) 372, Phys. Rev., B8 (1973) 1854.

2) J.E. Turner et al., Health Physics 18 (1970) 159.

3) H.H. Andersen and J.F. Ziegler, Hydrogen, Pergamon (1977).

4) J.F. Ziegler, Nucl. Inst. Meth., 168 (1980) 17.

Geometrical Effect on Stopping Power Measurement (Angle dependent Energy Loss) of 7 MeV Protons

R. Ishiwari, N. Shiomi, and N. Sakamoto
Department of Physics, Nara Women's University, Nara 630, Japan

It was found in our previous experiment, that when extremely sharply collimated protons pass through a thin target of random matter, the energy loss of protons measured with extremely high angular resolution increases by several percent as the emergence angle increases from zero to 1.78°. In the present experiment, this effect has been investigated systematically by changing the target thickness for Be, Al, Cu, Ag, and Ta.

1. Introduction

When well collimated protons pass through a thin target of random matter, protons will lose their energy according to the thickness of the target and the direction of protons will diverge due to multiple scattering with atomic nuclei in the target.

In the previous experiment[1], it was confirmed that if we collimate the proton beam extremely sharply and make the angular resolution of the detector extremely high, the energy loss of protons increases by several percent as the emergence angle increases. It has been discussed that the essence of this phenomenon is very likely the dependence of the energy loss on the average impact parameter of protons with atomic nuclei.

In the present experiment, in order to investigate the nature of this effect more systematically, the increase of the energy loss with increasing emergence angle has been measured with an improved experimental arrangement and by changing the target thickness for Be, Al, Cu, Ag, and Ta.

II. Experimental Procedure

The shematic diagram of the experimental arrangement is shown in Fig. 1. The proton beam of 7 MeV from the cyclotron of Kyoto University was collimated by a double diaphragm system S_1 and S_2, the diameter of which was 0.7mm each and 166cm apart. The divergence of the incident beam was less than 0.05° before hitting the thin target. In order to prevent the slit scattered protons originated at the diaphragm S_2 from affecting the energy loss measurement, a baffle S_3 of 1.5mm in diameter was placed 15cm behind the diaphragm S_2. The target was placed 11mm behind the baffle. The detector system consisted of the diaphragm S_4 of 0.7mm in diameter and a surface barrier silicon detector, which was placed 161cm behind the target. The detector subtended a solid angle of 1.5×10^{-7} sr as seen from the target. The detector system was movable perpendicurarly to the direction of the incident beam in a range of 5cm. At the displacement of 5cm, the emergence angle was 1.78°. In this arrangement, the energy loss measurement was quite free from the slit scattered protons at 1cm displacement.

The pulses from the detector were amplified with a low noise amplifier and fed into a 4096 channel pulse height analyzer. Another silicon detector was used to monitor the angular distribution due to multiple scattering. The energy of the incident proton was measured by the analyzing magnet with an accuracy of 0.01%.

In order to monitor the gain of the detector-amplifier system, the pulses of protons which was scattered by a thin Au foil of 180μg/cm^2 were measured. Fig. 2 shows the device for mounting the target and thin Au foil. The part indicated as A is essentially an ammeter. When an A.C. power is supplied, the hand indicated as B makes a pendulum motion. A double frames indicated as C are fixed to the hand B. To the left side frame the sample target is fixed and to the right side frame the thin Au foil is fixed. When an A.C. power is supplied and the hand B makes a pendulum motion, the incident beam traverses the target and the thin Au foil alternatively. The pulses of protons which pass through the target and pulses of protons which are scattered by the thin Au foil hit the detector alter-

natively. Thus, the two pulse heights are recorded on the 4096 channel pulse height analyzer simultaneously in one exposure. Because the energy of the incident protons was very well stabilized, the energy of the scattered protons by the thin Au foil was also very stable. Thus, we could monitor the gain of the detector-amplifier system. The stability of the detector-amplifier system was also crosschecked by a very high precision pulse generator(ORTEC 448).

The above mentioned pendulum method could not be applied in the case of zero emergence angle, because the counting rate of protons that passed through the thin Au foil was too high. So when the measurement at zero emergence angle was made the sample target was stopped. Because there would be a nonuniformity of the target thickness, the measurement was made at the same stopped position for 1cm displacement. Then, the pendulum measurements were performed from 1cm through 5cm. The value of the pulse height for zero emergence angle was normalized by the measurement made at 1cm displacement.

In principle, in our method the energy loss should be determined by measuring the difference between the pulse height of protons that passed through the target and the pulse height of the incident protons. Actually, however, in order to avoid the extremely high counting rate of the incident protons, protons scattered at 0.33° have been measured.

The pulse height of the incident protons has been determined from the pulse height of these scattered protons by the Au foil. The energy loss of 7 MeV protons in the Au foil was estimated to be 4 keV by using our previous stopping power data[2]. The decrease of the energy loss due to elastic scattering was negligible. The energy calibration of the pulse height spectrum was performed with the high precision pulse generator. The ionization defect of the surface barrier silicon detector has been investigated in the previous experiment[2] and has turned out to be substantially zero.

All targets were commercially obtained. The thicknesses of the targets were; 2.198mg/cm^2, 4.244mg/cm^2,and 6.441mg/cm^2 for Be, 2.502mg/cm^2, 4.143mg/cm^2, and 5.427mg/cm^2 for Al, 3.743mg/cm^2, 7.576mg/cm^2, and 11.311mg/cm^2 for Cu, 4.333mg/cm^2, 8.712mg/cm^2, and

13.027mg/cm^2 for Ag, 7.291mg/cm^2 and 10.444mg/cm^2 for Ta.

The measurements of energy losses and the angular distribution due to multiple scattering of 7 MeV protons have been repeated four times for one target at seven energence angles between 0° and 1.78°(5cm perpendicular displacement of the detector).

III. Results

The energy loss as a function of emergence angle and the angular distribution due to multiple scattering are shown in Fig. 3. The theoretical prediction of the angular distribution is calculated using Molière's theory[3] and is also shown in Fig. 3.

As seen in the previous experiment[1], the agreement of the observed angular distribution and Molière's theory is fairly good. The energy loss is found to increase for all targets with increasing emergence angles also in the present experiment.

As clearly seen from the figure, the increase of the energy loss shows a strong dependence on the target thickness. The increase is larger for thinner target.

It appears that there is a trend that energy loss increases first gradually and finally saturates.

IV. Discussion

The increase of the energy loss with increasing emergence angle has been confirmed again in the present experiment.

As already discussed in detail in the previous paper[1], the increase of the energy loss can not be explained by the following three effects; (1) The increase of the target thickness with the increase of the emergence angle, i.e. $1/\cos\alpha$ where α is the emergence angle. (2) The increase of the actual path length of protons due to multiple scattering. (3) The increase of the energy loss due to the energy transfer to the recoil atom. Also, in the previous paper, it was confirmed that this effect is not due to target texture.

The essence of this effect is very likely the depencence of the energy loss on the average impact parameter of protons with atomic nucleus. Our computor simulation[4] shows that this is the case.

It appears that this effect may have the depencence on the target atomic number. However, because this effect have strong dependence on the target thickness, at present stage it is difficult to compare the strength of the effect for different target quantitatively.

If we tentatively compare the saturation value of the increase of the energy loss when the energy loss is about 120±19 keV, it appears that the effect becomes large as the target atomic number increases from Al through Ta. In the case of Ta, the energy loss is 172 keV and the increase does not reach the saturation. However, in the case of Be, the effect is much larger than the case of Al. So another effect might be working for the case of Be.

More systematic experimental study and theoretical explanation are needed for the proper understanding of this phenomenon.

Achnowledgments

The authors would like to thank prof. T. Yanabu and Prof. H. Takekoshi for their support throughout the work. Thanks are also due to Mr. H. Fujita and members of the Cyclotron Laboratory of Kyoto University for their kind ccoperation. Finally, this work was spported by the Grant-in-Aid for Scientific Research.

References

1. R. Ishiwari, N. Shiomi, and N. Sakamoto, "Geometrical effect on the measurement of stopping power: Angle dependent energy loss of 7 MeV protons in metallic and organic thin foils", to appear in Phys. Rev., A 25 No.5 (1982).
2. R. Ishiwari, N. Shiomi, and N. Sakamoto "Stopping powers of Be, Al, Ti, V, Fe, Co, Ni, Cu, Zn, Mo, Rh, Ag, Sn, Ta, Pt, and Au for 6.75 MeV protons", Phys. Lett. 75A 112 (1979).
3. G. Molière, Z. Naturforsch 3a 78 (1948).
   H.A. Bethe, "Molière theory of multiple scattering", Phys. Rev., 89 1256 (1953).
4. N. Sakamoto, N. Shiomi, and R. Ishiwari, "Computer simulation of geometrical effect on the stopping power for 7 MeV protons". Proceedings of the U.S.-Japan Seminar "Charge States and Dynamic Screening of Swift Ions in Solid", this ORNL report(1982).

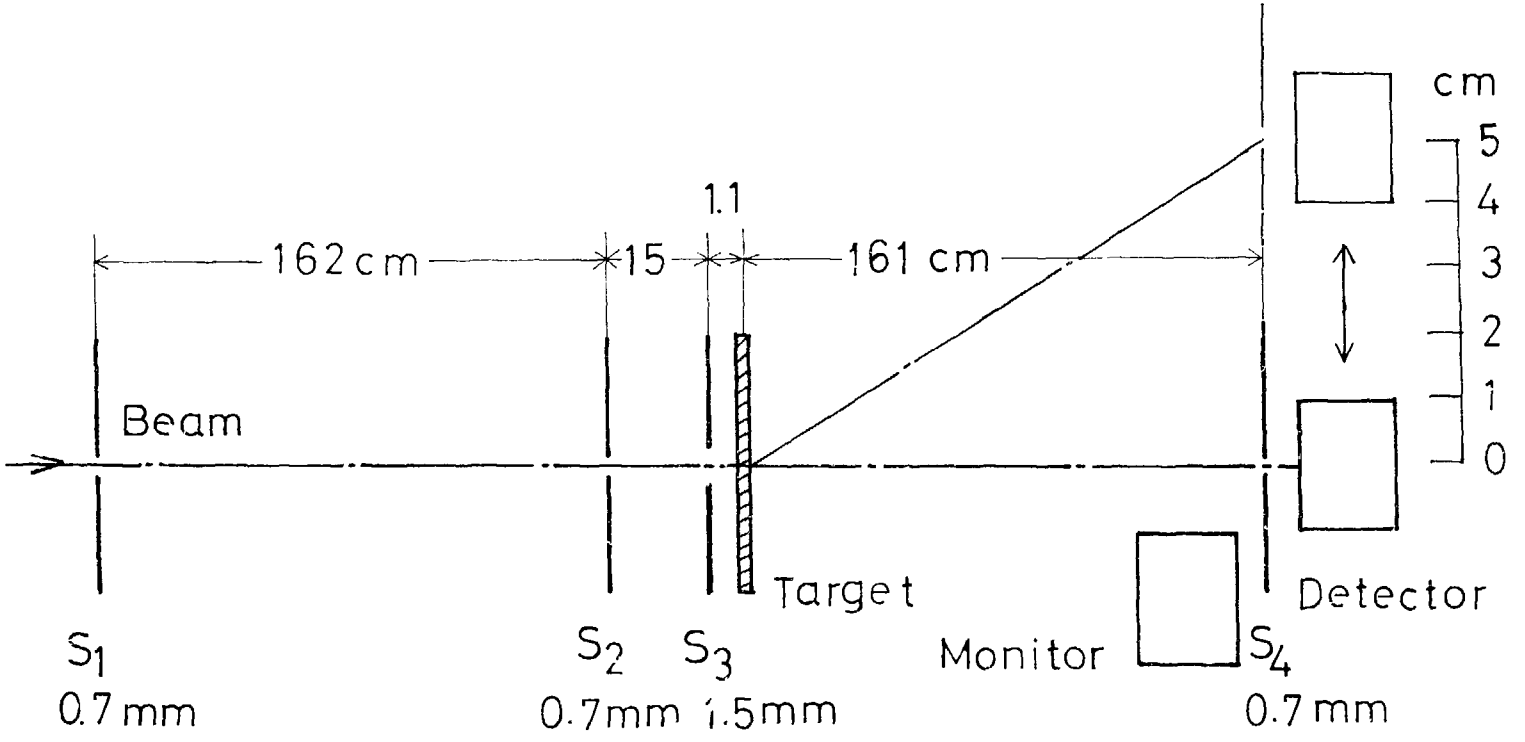

Fig. 1. Schematic diagram of experimental arrangement.

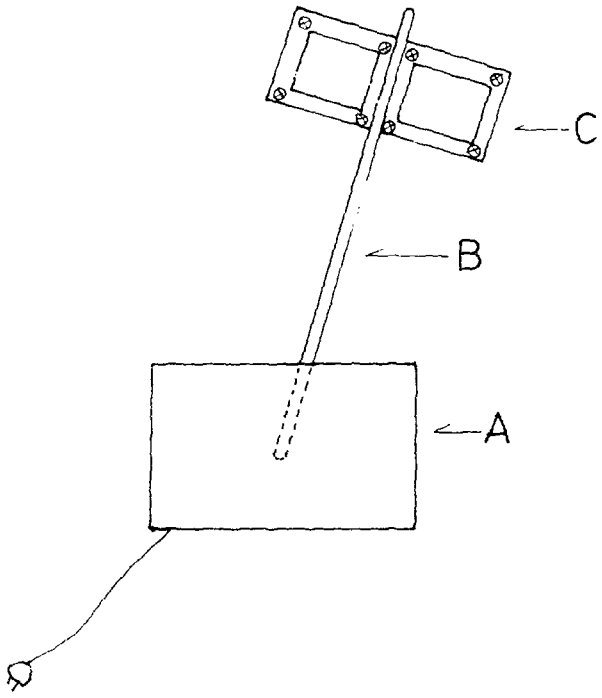

Fig. 2. Schematic diagram of the device for mounting the target and the thin Au foil.

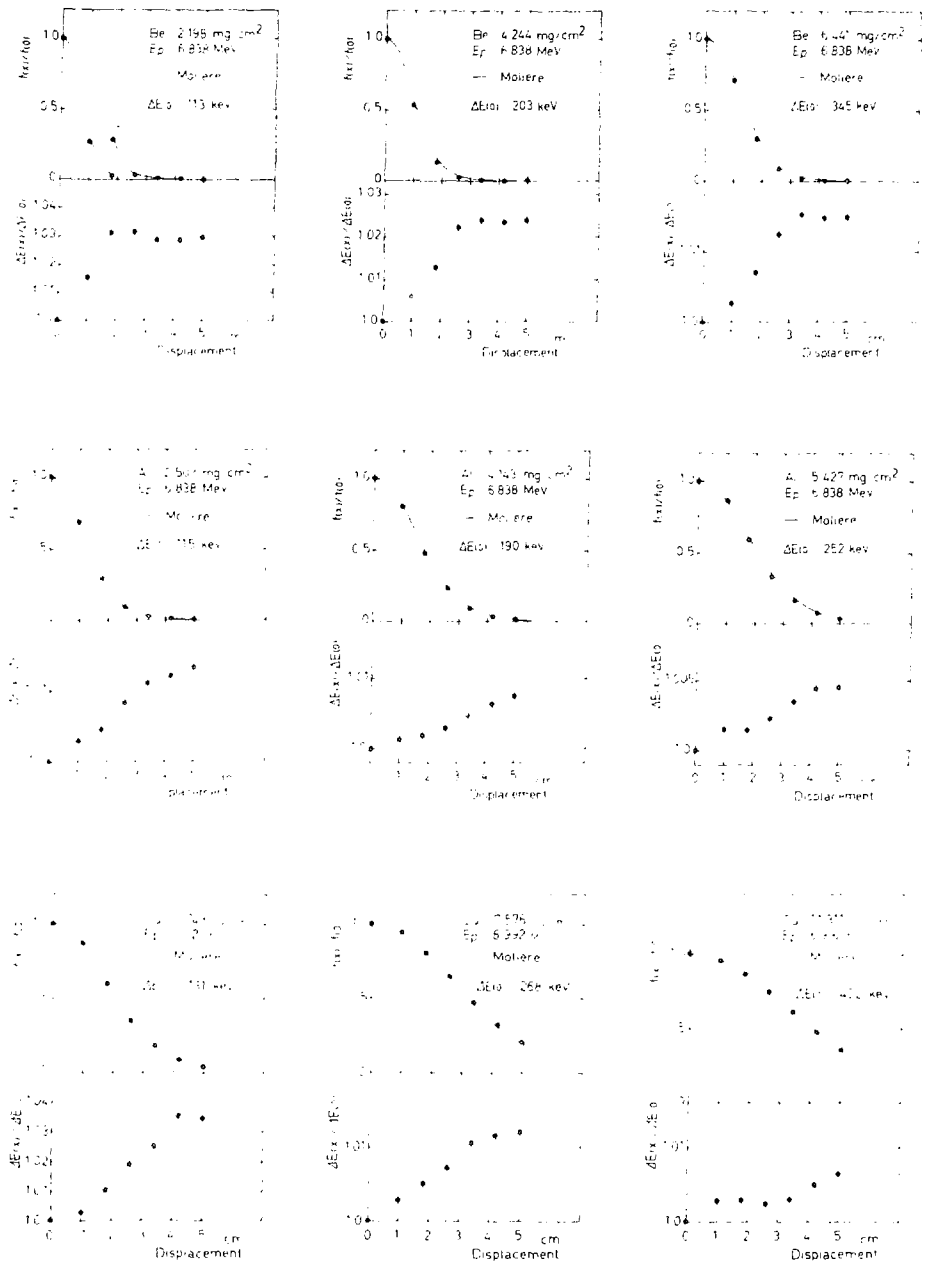

Fig. 3. Angular distribution due to multiple scattering and energy loss as a function of emergence angle. Solid curves are the predictions of Molière's theory.

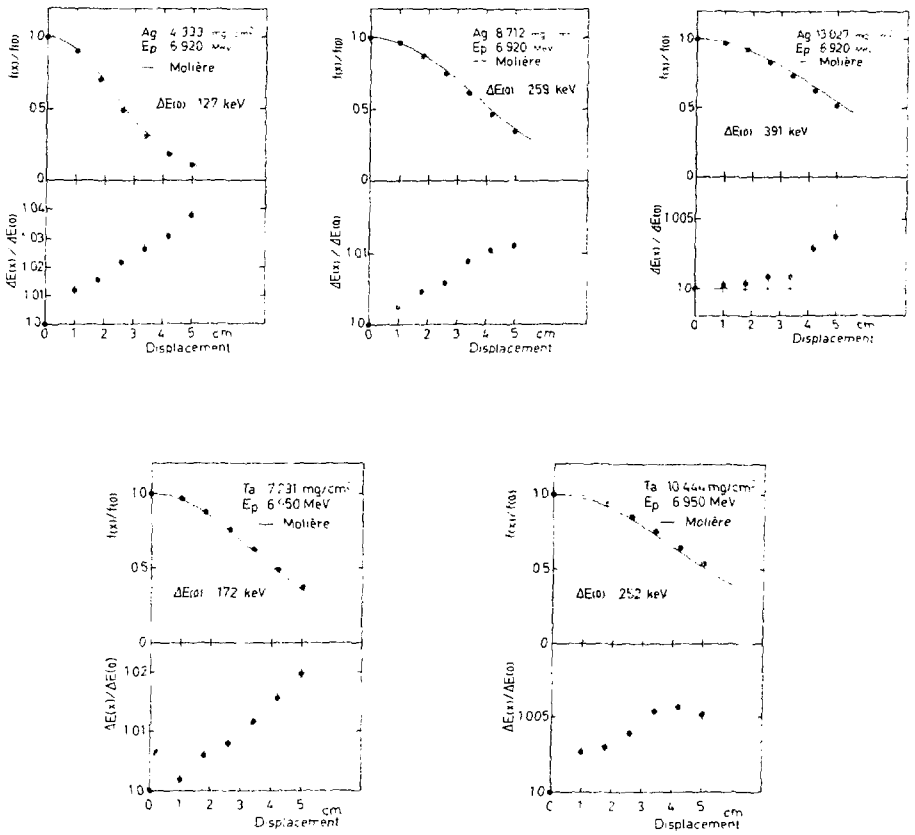

Fig. 3.(continued)

Computer Simulation of Geometrical Effects on the Stopping Power for 7 MeV Protons

N. Sakamoto, N. Shiomi and R. Ishiwari
Department of Physics, Nara Women's University, Nara 630, Japan

I. Introduction

We have recently studied the angle-dependent energy loss of 7 MeV protons in metallic and organic thin foils.[1] In this study it has been found that the energy loss of protons becomes large with increasing emergence angle in all targets. Since this increase of energy loss of protons has been observed in organic targets which have turned out to be perfectly amorphous, it is proved that the increase of energy loss is not due to target texture effect. The increase of energy loss could not be explained also by following three effects; (i) the increase of the target thickness caused by the deflection of protons, (ii) the increase of the path length due to multiple scattering and (iii) the energy transfer to recoil nuclei during multiple scattering process. Therefore the observed increase of energy loss with increasing emergence angle is concluded to be due to hitherto unknown new effect. And this effect is very likely the dependence of energy loss on the impact parameter with the atomic nucleus. At this stage, however, no theoretical work which deals with multiple scattering and the impact parameter dependence of energy loss at the same time is known. Hence we decided to investigate the origin of this effect by a computer simulation.

II. Principle of the Calculation

In this calculation we use a very simple model. Target atoms are described as spheres of radius R and treated by a statistical model such as the Thomas-Fermi model. Hence if protons enter the inside of these spheres, they are scattered by the target nuclei and lose a part of their energy. If protons traverse the outside of these spheres, no scattering and no energy loss take place.

Let us consider the case of emergence at angle α (Fig.1). As protons undergo a number of small angle scattering within the target,

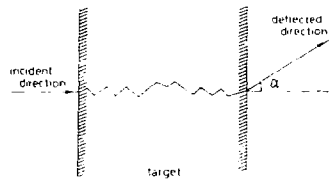

Fig.1 Schematic representation of collisions through the target for emergence at angle α.

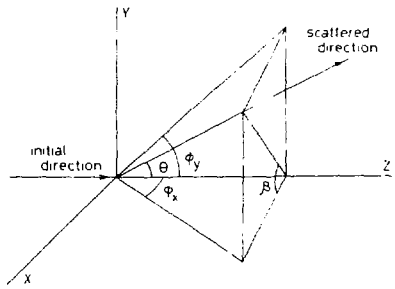

Fig.2 Illustrating the spatial angles θ and β and the projected angles ϕ_x and ϕ_y.

it is convenient to use two projected angles ϕ_x and ϕ_y instead of using the polar angle θ and the azimuth angle β of the track of a scattered protons (Fig.2). The relation between the projected angles and the actual scattering angles is given by[2]

$$\tan\phi_x = \tan\theta\cos\beta, \tag{1}$$

$$\tan\phi_y = \tan\theta\sin\beta. \tag{2}$$

Under the small angle approximation $\tan\theta$ can be replaced by θ, and then $\tan\phi_x$ and $\tan\phi_y$ can be also replaced by ϕ_x and ϕ_y, respectively.

$$\phi_x = \theta\cos\beta, \tag{3}$$

$$\phi_y = \theta\sin\beta. \tag{4}$$

After the n-times collisions the direction of a proton can be given as

$$\sum_{i=1}^{n} \phi_{x,i} = \sum_{i=1}^{n} \theta_i\cos\beta_i, \tag{5}$$

$$\sum_{i=1}^{n} \phi_{y,i} = \sum_{i=1}^{n} \theta_i\sin\beta_i. \tag{6}$$

If protons are detected at deflection angles of α and ϕ, where α denotes the polar angle and ϕ denotes the azimuth angle, after their passage through the target, the relation between these angles and the projected angles is expressed by

$$\tan\alpha\cos\phi = \sum_{i=1}^{n} \phi_{x,i}, \tag{7}$$

$$\tan\alpha\sin\phi = \sum_{i=1}^{n} \phi_{y,i}. \tag{8}$$

As seen in Eqs.(5)-(8), to decide a pair of detection angles means to attach a certain boundary condition to the collisions which protons undergo within the target. From these relations it is easily understood that this boundary condition has a strong effect on the individual collision if the number of collisions is small, in other words if the target is thin.

Next we consider the relation between a scattering angle and an impact parameter. Coulomb potential of a nucleus which is partially screened by atomic electrons is described by

$$V(r) = -\frac{Z_1 Z_2 e^2}{r} u(r), \tag{9}$$

where Z_1 and Z_2 are atomic numbers of an incident proton and a target atom, respectively. A good analytical approximation of the Thomas-Fermi screening function is given by Molière[3] and expressed as

$$u(r) = 0.1e^{-6r/a_{TF}} + 0.55e^{-1.2r/a_{TF}} + 0.35e^{-0.3r/a_{TF}}. \tag{10}$$

The Thomas-Fermi screening radius a_{TF} is given by

$$a_{TF} = 0.8853a_0 Z_2^{-1/3}, \tag{11}$$

where a_0 is the Bohr radius. Supposing a scattering angle is sufficiently small, the scattering angle can be described by

$$\theta = \frac{p_\perp}{p_{//}}, \tag{12}$$

where $p_{//}$ denotes a proton momentum parallel to its initial direction and $p_\perp$ denotes a momentum transfer perpendicular to this direction. Using Eqs.(9) and (10), we can calculate $p_\perp$ and finally find the relation between θ and the impact parameter b.[4]

$$\theta = \frac{2Z_1 Z_2 e^2}{M_1 v_1^2 b} g\left(\frac{b}{a_{TF}}\right), \tag{13}$$

$$g(\zeta) = \int_0^{2\pi} \cos\xi d\xi \left\{ u\left(\frac{\zeta}{\cos\xi}\right) - \frac{\zeta}{\cos\xi} u'\left(\frac{\zeta}{\cos\xi}\right) \right\}, \tag{14}$$

where M_1 and v_1 are mass and velocity of an incident proton.

Considering the ionization energy loss, Kitagawa and Ohtsuki have derived the energy loss formula of ions with the impact parameter b by one atom.[5] This formula is shown to give the correct Bethe-Bloch formula. In present calculation we use their expression

$$\Delta F(b) = -\frac{2Z_1^2 e^4}{mv_1^2} \int_{-\infty}^{\infty} dz \int_0^{2\pi} d\xi \int_{x_{min}}^{\infty} x dx q^2 \left(K_0^2(qx) + K_1^2(qx)\right) \rho(r), \tag{15}$$

where

$$r = \sqrt{z^2 + x^2 + b^2 - 2bx\cos\xi}\ , \tag{16}$$

$$q = \frac{I}{\hbar v_1}\ . \tag{17}$$

Functions $K_0(qx)$ and $K_1(qx)$ are the modified Bessel functions, and m is electron rest mass and I is the mean ionization energy of stopping material. The density of the atomic electrons $\rho(r)$ is given by Molière formula[3]

$$\rho(r) = \frac{Z_2}{4\pi r}\left(\frac{0.3}{a_{TF}}\right)^2 \left\{0.35e^{-0.3r/a_{TF}} + 8.8e^{-1.2r/a_{TF}} + 40e^{-6r/a_{TF}}\right\}. \tag{18}$$

Once the impact parameter is given, we can calculate the scattering angle and the energy loss from Eqs.(13)-(18). Since the target material is assumed to be random medium, the impact parameter is considered to be uniform and determined by psudo-random numbers from a computer. Protons undergo a number of collisions within the target and then leave the target with a certain deflection angle and energy loss. In present calculation we can also compute the average values of the scattering angle θ, the mean square angle of scattering θ^2, the azimuth angle β, the impact parameter b, the number of collisions N and the actual path length T.

III. Results and Discussion

In Fig.3 we show the results of calculation for a copper target of

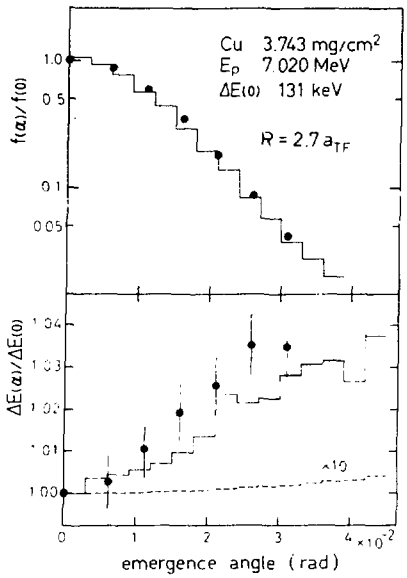

Fig.3 Calculated and measured angular distribution due to multiple scattering and energy loss as a function of emergence angle α. Solid circles indicate experimental results.

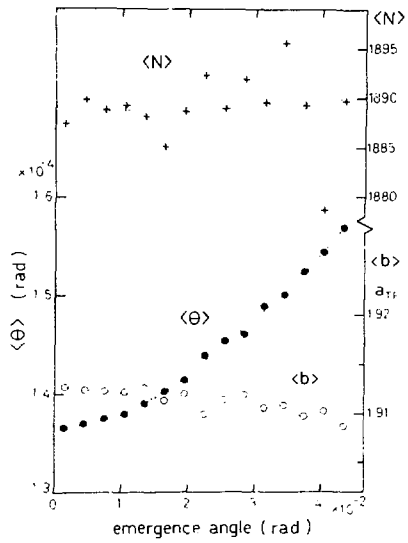

Fig.4 Average values of the number of collisions <N>, the scattering angle <θ> and the impact parameter <b> as a function of emergence angle.

3.743 mg/cm^2 and the incident proton energy of 7.020 MeV together with our experimental data. The angular distribution due to multiple scattering is shown on the upper half, where solid circles denote experimental results. The radius R, which is the radius of the target atom, is used to determine the mean free path and is treated as a free parameter in present calculation. In order to obtain a good fit to the experimental angular distribution we used the value of $R = 2.7a_{TF}$. On the lower half relative values of energy loss are shown as a function of emergence angle. Solid line shows the results of calculation, which give a fairly good agreement with experimental results. At this point we will examine the contribution of elastic energy transfer to recoil atoms. Under the small angle approximation the energy transfer to a recoil atom due to a single collision is described by

$$\frac{M_1}{M_2} E_0 \theta^2, \tag{19}$$

where M_2 is mass of target atoms and E_0 is an incident energy of protons. Then the total energy E_t transfered to recoil atoms in multiple scattering process is given by

$$E_t \approx \frac{M_1}{M_2} \bar{E} \sum_{i=1}^{n} \theta_i^2 , \qquad (20)$$

where $\bar{E}$ is the average energy of protons within the target. Including the contribution of this effect in our calculation of energy loss, we obtain slightly larger energy loss, which is shown by a dotted line in Fig.3. At small emergence angles this line is not shown in the figure, because this line coincides with a solid line. As seen in Fig.3 the contribution of this effect is very small. A dashed line in Fig.3 shows the increase of the actual path length with increasing emergence angle. This effect is also too small to explain the experimental results. Therefore, we can conclude that the observed increase of the energy loss with increasing emergence angle is not due to the effects of the increase of the actual path length and the elastic energy transfer to the recoil atoms but due to the impact parameter dependence of energy loss in an individual collision.

Fig.4 shows the variation of the average values of the collision number, the scattering angles and the impact parameters as a function of emergence angle. The emergence angle becoming large, the number of collisions shows a slight increase, the scattering angle becomes somewhat quadratically large and the impact parameter shows a slight decrease. From these results it can be seen that deciding the detection angle does have an effect on the individual collision which protons undergo within the target. This is the reason why the energy loss of protons increases with increasing emergence angle.

Another result of computation is shown in Fig.5. This calculation is performed in order to examine whether the computer simulation can predict the target thickness dependence of the geometrical effect with the same parameter R or not. The thickness of a copper target is 7.576 mg/cm^2, which is about twice as thick as the former target. The agreement between calculation and experiment is very good in spite of a poor statistics of calculation.

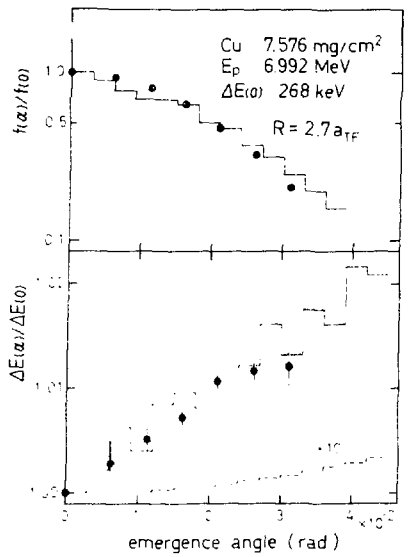

Fig.5 Calculated and measured angular distribution due to multiple scattering and energy loss as a function of emergence angle α for 6.992 MeV protons transmitted through a 7.576 mg/cm^2 Cu target. Solid circles indicate experimental results. A dotted line shows the variation of energy loss which includes the contribution from the elastic energy transfer to recoil atoms, and a dashed line represents the relative length of actual path.

As seen above, computer simulation is found to give fairly good results and reproduce the target thickness dependence of the geometrical effect well. More systematic study of this phenomenon will bring us more precise information about an individual collision which ions undergo within a target material.

IV. Conclusion

Computer simulation has been performed to investigate the origin of geometrical effects on the stopping power for 7 MeV protons. An individual collision which protons undergo within the target foil is found to be somewhat restricted by the determination of detecting angles. Therefore, if the energy loss of protons depends on the impact parameter, this restriction causes the emergence angle dependence of the energy loss. Using the energy loss formula of Kitagawa and Ohtsuki, which describes the impact parameter dependence of stopping power, and the screened Coulomb potential, we can reproduce both the angular distributions due to multiple scattering and the relative energy losses very well. The effects of the increase of the actual path length and the elastic energy transfer to recoil atoms are proved to be too small to explain experimental results.

Finally we will mention the relation between usual stopping power value and the energy loss measured at zero emergence angle. In usual stopping power measurement, all protons that pass through the target are measured. Hence, if we measure only protons that emerge at zero angle, the resultant stopping power will be smaller than that of usual definition. For example, the deviation is about 1.5% in the case of the thinner target (3.743 mg/cm^2). This kind of deviation is expected to be larger when the target is thinner. Therefore, it is worthy to note that the measured stopping power will be systematically small if one detects only ions that emerge at zero angle and uses a very thin target.

References

1 R. Ishiwari, N. Shiomi and N. Sakamoto, to be published in Phys. Rev. A.

2 W. T. Scott, Rev. Mod. Phys. 35, 231(1963).

3 G. Molière, Z. Naturforsch. 2a, 133(1947).

4 J. Lindhard, V. Nielsen and M. Scharff, Mat. Fys. Medd. Dan. Vid. Selsk. 36, no.10(1968).

5 M. Kitagawa and Y. H. Ohtsuki, Phys. Rev. B5, 3418(1972)

Current Stopping Power Analyses

by

L. E. PORTER

Department of Physics and Astronomy

University of Montana

Missoula, Montana 59812 USA

I. Mean Excitation Energies

A. Overview

Modified Bethe-Bloch stopping power theory permits fairly accurate calculation of energy losses over a broad interval of projectile velocity $v=\beta c$ insofar as several parameters appearing in the revised Bethe-Bloch formula have been correctly evaluated. Since the parameters cannot in general be ascertained by calculation from first principles, fits of theory to measurement remain the best method of evaluation. The parameters alluded to are, in the notation of reference 1. (or 2.) and 3.: The target mean excitation energy, I; the shell correction scaling parameters, V_L and W_L, V_M and W_M, V_N and W_N; the composite single free parameter of the Barkas (projectile-z^3) effect correction formalism[4-6], b, and the strength of the correction term, ξ; the high velocity density effect correction parameter[7], δ; and the low velocity charge state parameter[3], λ. Of these parameters, all are presumably independent of the nature of the projectile, and with the exception of δ, of projectile velocity. The shell correction scaling parameters, used in conjunction with the calculated shell corrections of Walske[8], increase substantially the multiplicity of parameters to

be established for all target materials save those of low atomic number, Z. Moreover, both the shell correction scaling parameters and the Barkas effect parameters characterize terms which generally make small contributions to the total stopping number. Unfortunately, the extent, consistency, and accuracy of existing measurements rarely will support the simultaneous determination of more than two given parameters.

Several stratagems are consequently adopted in order to reduce the number of parameters required in fitting a given set of measurements. The density effect correction is needed only for relativistic projectile velocities, where a projectile-z^3 correction[9] also becomes necessary. By contrast, shell corrections, the (low velocity) Barkas effect correction, and the charge state correction all increase monotonically with decreasing projectile velocity. Thus by judicious selection of the energy interval covered by a set of stopping power measurements the number of needed parameters can conceivably be reduced to a tractable few.

Experience in analyzing various sets of stopping power data indicates that even the most accurate data now available enables the extraction of at most two parameters of Bethe-Bloch theory[1]. The pair selected in the majority of analyses conducted so far comprises the mean excitation energy, I, and one of the two projectile-z^3 effect parameters, b or ξ. However, the number of parameters required to describe the measurements generally consists of this pair plus several shell correction scaling parameters, despite the selection of projectile energies high enough to justify neglect of a charge state parameter and sufficiently low to warrant suppression of any density effect correction.

Hence the approach used has been to specify the shell correction scaling parameters, accepting the concomitant uncertainty in this procedure, and then to search for a minimum error function between theory and measurements in the remaining two-parameter space. Results of some of the more recent such analyses are reported herein.

The existence of two parameters, b and ξ, associated with the Barkas effect correction reflects a minor controversy over the proper method of effecting this correction. Whereas the original projectile-z^3 effect formalism[4-6] featured a single, composite, model-dependent parameter, initially evaluated through fits to data as b=1.8±0.2, subsequent resurrection of the Bloch term[10] for inclusion in the stopping power formula was accompanied by a suggestion that the projectile-z^3 term be multiplied by a factor somewhat less than two[11]. An alternative approach to inclusion of the Bloch term[10] was simply to re-evaluate the original composite parameters, resulting in a recommendation[12] that b=1.4±0.1. Thus a subsidiary objective of some recent studies has been to ascertain which of the two approaches might prove more effective in fitting data, where effectiveness was judged on the basis of quality of fit and of plausibility of resulting values of the particular parameter employed. The primary purpose of all recent studies has been to establish as accurately as feasible the mean excitation energy for each target material considered.

B. Physical State Effects

Whenever the individual atoms of a target material are joined to others, the effects of aggregation on stopping power and on the parameters of modified Bethe-Bloch theory must be considered. One aspect

of this complicated subject is the characterization of different physical states of a substance by means of different values of the mean excitation energy. Such an analysis of the recently reported stopping power data for 0.3-5.5 MeV alpha particles traversing liquid water and water vapor[13] has just been completed[14]. However, the measurements for projectile energies below 2.0 MeV were omitted in order to eliminate a charge state parameter from the formulation. Thus each of the two-parameter searches, for I and b or for I and ξ, could be carried out.

Results of these searches were surprising in the sense that the less accurate liquid water data proved amenable to both approaches, yielding plausible values of both b and ξ, whereas the water vapor data provided unacceptable values of these Barkas effect parameters. The extracted values of I, b, and ξ, accompanied by the respective values of σ (the root-mean-square relative deviation of calculated from measured stopping powers), appear in Table 1. The fixed value of b at 1.90 corresponds to that obtained in the aforementioned polystyrene study[1], and the fixed values of ξ at 1.0 and 2.0 correspond (at least approximately) to the two approaches to inclusion of the projectile-z^3 effect term[11,12]. Another gambit was employed, chiefly because of the obvious difficulties in fitting the water vapor data, in that the value of b became fixed at 1.90 while a best-fit value of I was sought for each of four selected values of ξ in the interval from 0.5 to 2.0. Results of this phase of the study appear in Table 2. Here σ achieves a minimum at $\xi = 0.58$ for the liquid water data but no minimum for the water vapor data. The difference between I-values with ξ fixed averages about 8 eV, and increases monotonically with increasing ξ. A compro-

mise value of $\xi = 1.0$ was selected, partly because the value of σ for water vapor decreased steadily with decreasing ξ in the interval studied and for liquid water achieved a minimum between $\xi = 0.5$ and $\xi = 1.0$, and partly because this selected value conformed to one[12] of the two approaches to inclusion of the z^3-effect term[11,12]. Moreover, if the Lindhard approach[11] were literally adopted by fixing ξ at (about) 2.9, resulting values of b would become implausibly high. Thus the mean excitation energy of water was taken as 68 eV for liquid water and 60 eV for water vapor. A Bragg's rule[15] prediction, based on the constituent I-values of Fano[16] is 67.5 eV. The water vapor value lies far below a recently published theoretical value[17] of 71.6 eV. A comparison of the measurements[13] analyzed herein with two other sets of data indicated that a similar analysis of either of the other sets would yield values of mean excitation energy even lower than those now reported[14].

II. z^n-Effects

Evaluation of the various parameters of modified Bethe-Bloch theory is complicated by the question of inclusion of higher-order z^n-terms than the previously discussed z^3-term. Yet application of even the projectile-z^3 correction to the Bethe-Bloch formula has been approached in at least two ways[11,12]. Clearly it would be advantageous to know at least one parameter very accurately so as to reduce the number to be extracted from measurements. Attention is often focussed on the mean excitation energy in this connection, since it presumably depends on neither the identity nor velocity of the

projectile.

A. Inert Gases

The mean excitation energy of an inert gas should be easily extracted from stopping power data collected with gas targets, since no aggregation effects could exist for such cases. Furthermore, the use of known shell corrections should permit a closer scrutiny of the projectile-z^3 correction term[4-6] in order to discover the proper form of its inclusion[11,12]. Hence the Walske shell corrections were utilized in conjunction with the best available values of scaling parameters[18] while analyzing all reliable extant stopping power data for protons and alpha particles traversing Ne, Ar, Kr, and Xe gas targets[19]. Results of the I and b, and of the I and ξ, searches are shown in Tables 3. and 4., respectively. Chiefly because of considerable dispersion in extant measurements at low projectile velocities, where the projectile-z^3 effect is most important, the question as to the proper method of including that correction could not be clearly resolved. However, although some revision of the form of the projectile-z^3 correction[4-6] may be in order, there appeared to be little reason for the literal adoption of the Lindhard suggestion[11].

Recommended values of I and b, with ξ fixed at 1.0, for the inert gases studied are displayed in Table 5.

B. Metals

Target elements which have been extensively studied for the purpose of determining mean excitation energies include Al, Cu, Ag, and Au. The existence of one set of very accurate measurements[20], corroborated by the Nara group[21], suggested the possibility of

ascertaining three or more parameters of modified Bethe-Bloch theory[22]. This belief proved fatuous, however, so that instead an attempt was made to evaluate I and b, or I and ξ, with shell corrections specified[2,8,18]. When formerly used shell corrections[2,8] were employed, the resulting values of I and b, and of I and ξ, are shown respectively in Tables 6 and 7. (The charge state parameter, λ, was set at 0.95 for analysis of the Li-projectile data.) Both b- and ξ-values evinced remarkable dependences on z and Z. This situation was considerably improved by shifting to a more recent set of shell corrections[8,19] for Al, Cu, and Ag in the I and b searches with ξ fixed at 1.0, as shown in Table 8. The resulting values of b were essentially the same as those previously found[2] for Al, Ni, and Ag, and the I-values for different projectiles manifested sufficient consistency to warrant recommendations that for b = 1.35 the mean excitation energies of Al, Cu, and Ag are 165 eV, 329 eV, and 480 eV, respectively.

C. Gases of Low Atomic Number

A recent study of low-Z target gases provided a state-of-the-art analysis of extant stopping power data for proton and alpha particle projectiles[23]. In this case reliable calculated values of I were used, with ξ fixed at 1.0, and a value of b was recommended on the basis of visual best fits to the data. However, although some of the measurements analyzed were at projectile energies requiring a charge state correction, none was employed. The suggested values of b were 0.6 for H_2 and He and 1.8 for N_2, O_2 and CH_4.

References

1. L. E. Porter, "Mean excitation energy of polystyrene extracted from proton stopping power measurements," Phys. Rev. B22, 2221-2225 (1980).

2. L. E. Porter and S. R. Bryan, "Projectile-z^3 and -z^4 corrections to Bethe-Bloch stopping power theory and mean excitation energies of Al, Si, Ni, Ge, Se, Y, Ag, and Au," Nucl. Instrum. Methods 178, 227-231 (1980).

3. L. E. Porter, "Heavy ion stopping powers and the low velocity projectile-z^3 effect," Phys. Rev. B16, 1812-1821 (1977).

4. J. C. Ashley, R. H. Ritchie, and W. Brandt, "Z_1^3-effect in the stopping power of matter for charged particles," Phys. Rev. B5, 2393-2397 (1972).

5. J. C. Ashley, R. H. Ritchie, and W. Brandt, "Z_1^3-dependent stopping power and range contributions," Phys. Rev. A8, 2402-2408 (1973).

6. J. C. Ashley, "Influence of the Z_1^3 contribution to stopping power on the evaluation of mean excitation energies and shell corrections," Phys. Rev. B9, 334-336 (1974).

7. R. M. Sternheimer and R. F. Peierls, "General expression for the density effect for the ionization loss of charged particles," Phys. Rev. B3, 3681-3692 (1971).

8. M. C. Walske, "The stopping power of K-electrons," Phys. Rev. 88, 1283-1289 (1952) and "The stopping power of L-electrons," Phys. Rev. 101, 940-944 (1956).

9. J. D. Jackson and R. L. McCarthy, "z^3 corrections to energy loss and range," Phys. Rev. B6, 4131-4141 (1972).

10. F. Bloch, "Zur Bremsung Rasch bewegter Teilchen beim Durchgang durch Materie," Ann. Phys. 16, 285-320 (1933).

11. J. Lindhard, "The Barkas effect--or z_1^3, z_1^4-corrections to stopping of swift charged particles," Nucl. Instrum. Methods 132, 1-5 (1976).

12. R. H. Ritchie and W. Brandt, "Projectile-charge dependence of stopping powers," Phys. Rev. A17, 2102-2105 (1978).

13. D. I. Thwaites, "Stopping cross sections of liquid water and water vapour for alpha particles within the energy region 0.3 to 5.5 MeV," Phys. Med. Biol. 26, 71- (1981).

14. L. E. Porter and D. I. Thwaites, "Physical state effects on the mean excitation energy of water as determined from alpha particle stopping power measurements," Phys. Rev. A (to be published).

15. W. H. Bragg and R. Kleeman, "On the α particles of radium, and their loss of range in passing through various atoms and molecules," Phil. Mag. 10, 318-340 (1905).

16. U. Fano, "Penetration of protons, alpha particles, and mesons," Ann. Rev. Nucl. Sci. 13, 1-66 (1963).

17. G. D. Zeiss, W. J. Meath, J. C. F. McDonald, and D. J. Dawson, "Accurate evaluation of stopping and straggling mean excitation energies for N, O, N_2, O_2, NO, NH_3, H_2O, and N_2O using dipole oscillator strength distributions," Radiat. Res. 70, 284-305 (1977).

18. H. Bichsel, private communication, 1980.

19. L. E. Porter and R. G. Jeppesen, "Mean excitation energies and Barkas-effect parameters for Ne, Ar, Kr, and Xe as extracted from proton and alpha particle stopping power measurements," (in preparation).

20. H. H. Andersen, J. F. Bak, H. Knudsen, and B. R. Nielsen, "Stopping power of Al, Cu, Ag, and Au for MeV hydrogen, helium, and lithium ions. Z_1^3 and Z_1^4 proportional deviations from the Bethe formula," Phys. Rev. A16, 1929-1940 (1977).

21. R. Ishiwari, private communication, 1981.

22. S. R. Bryan, "Bethe-Bloch stopping power parameters extracted from recent accurate measurements," M. A. Thesis, University of Montana 1981 (unpublished); L. E. Porter and S. R. Bryan, "Bethe-Bloch stopping power parameters for Al, Cu, Ag, and Au extracted from recent accurate measurements," (in preparation).

23. Hans Bichsel and L. E. Porter, "Stopping power of protons and alpha particles in H_2, He, N_2, O_2, CH_4, and Air," Phys. Rev. A (to be published).

Target	Phase	I(eV)	b	ξ	σ
H_2O	Liquid	63.4	1.90	0.58	0.27
		64.7	2.32	1.00	0.27
H_2O	Vapor	49.8	1.90	-0.29	0.60
		52.0	19.4	1.00	0.62
		52.6	8.36	2.00	0.62

Table 1. Results of two-parameter searches, I and b or I and ξ, for both phases of the water target. I represents the mean excitation energy, b the free parameter of the z^3-correction formalism, ξ the amplitude of the z^3-correction term, and σ the root-mean-square relative deviation of calculated from measured stopping powers. (The underlined quantity is that one fixed for a particular search.)

Target	Phase	ξ	I(eV)	σ
H_2O	Liquid	0.5	63	0.28
		1.0	68	0.29
		1.5	74	0.38
		2.0	80	0.49
H_2O	Vapor	0.5	56	0.92
		1.0	60	1.38
		1.5	65	1.85
		2.0	70	2.35

Table 2. Results of one-parameter searches, with b (the free parameter of the z^3-correction formalism) fixed at 1.90. I represents the mean excitation energy, ξ the amplitude of the z^3-correction term, and σ the root-mean-square relative deviation of calculations from measurements.

Target	Projectile	I±ΔI(eV)	b±Δb	σ_{min}
Ne	proton	141.9±5.2	1.45±0.19	0.78
	α-particle	129.4±0.5	1.65±0.01	0.86
	both	129.9±0.7	1.64±0.03	1.02
Ar	proton	190.1±2.1	5.30±0.32	1.25
	α-particle	182.4±0.8	2.15±0.04	1.48
	both	184.4±1.4	2.10±0.05	1.88
Kr	proton	347.1±2.7	4.11±0.29	1.31
	α-particle	309.7±1.9	2.49±0.08	0.72
	both	327.7±1.5	2.02±0.03	2.41
Xe	α-particle	500.3±2.1	1.38±0.01	0.86
	both (+ protons)	505.0±1.9	1.36±0.01	2.34

Table 3. Results of two-parameter searches with ξ fixed at 1.0. I represents the mean excitation energy, b and ξ the free parameter and amplitude, respectively, of the z^3-correction term, and σ the rms relative deviation of calculations from measurements.

Target	Projectile	I±ΔI(eV)	ξ±Δξ	σ
Ne	proton	142.1±6.6	1.47±0.41	0.80
	α-particle	131.2±0.7	1.24±0.03	0.84
Ar	proton	160.1±5.2	-1.60±0.35	1.13
	α-particle	176.4±1.0	0.49±0.04	1.42
Kr	proton	281.9±17.1	-2.26±0.72	1.20
	α-particle	296.5±2.3	0.16±0.05	0.80
Xe	α-particle	647	3.8	1.98

Table 4. Results of searches for I and ξ, including the rms relative deviation of calculations from measurements, σ.

Target	I(eV)	b
Ne	130	1.64
Ar	184	2.10
Kr	328	2.02
Xe	505	1.56

Table 5. Recommended values of the two parameters established, where I represents the mean excitation energy and b the free parameter of the z^3-correction term.

Target	Projectile	I(eV)	ΔI(eV)	b	Δb	σ
Al	proton	170.2	0.8	2.26	0.21	0.27
	alpha	166.3	1.1	1.10	0.06	0.11
	Li	163.8	1.5	0.77	0.04	0.36
Cu	proton	329.6	2.5	3.29	1.02	0.22
	alpha	325.8	3.9	1.49	0.17	0.41
	Li	339.2	7.4	1.06	0.07	0.18
Ag	proton	525.7	1.2	5.22	0.21	3.14
	alpha	488.2	0.7	5.52	0.47	1.60
	Li	525.6	1.5	1.37	0.02	0.94
Au	proton	839.2	1.6	4.10	0.05	3.44
	alpha	809.0	10.0	2.20	0.25	0.73
	Li	845.8	11.5	1.39	0.05	0.49

Table 6. Results of the searches for I (mean excitation energy) and b (free parameter of the z^3-correction term) for metals, with σ rms relative deviation of calculations from measurements).

Target	Projectile	I	ΔI	ξ	Δξ	σ
Al	proton	169.2	0.9	0.58	0.08	0.22
	alpha	170.5	1.4	1.67	0.05	0.27
	Li	180.3	2.4	2.58	0.08	0.06
Cu	proton	327.2	2.2	0.14	0.20	0.19
	alpha	330.0	5.5	1.30	0.12	0.42
	Li	385.1	5.6	2.50	0.10	0.06
Ag	proton	462.8	1.7	-2.20	0.08	1.15
	alpha	472.8	4.9	1.95	0.06	1.15
	Li	475.0	5.1	0.30	0.08	1.53
Au	proton	712.4	2.2	-3.02	0.06	0.82
	alpha	793.5	7.0	0.62	0.07	0.69
	Li	898.4	3.6	1.90	0.00	0.88

Table 7. Results of the searches for I (mean excitation energy) and ξ (amplitude of z^3-correction term) for metals, with σ (rms relative deviation of calculations from measurements).

Target	Projectile	I(eV)	ΔI(eV)	b	Δb	σ
Al	proton	166.5	1.0	1.37	0.00	0.20
	alpha	165.2	0.9	1.36	0.03	0.25
	Li	162.7	2.2	0.98	0.04	0.41
	Li*	161.2	-	1.37	-	0.29*
Cu	proton	329.0	1.4	1.30	0.04	0.23
	alpha	329.0	2.7	1.40	0.01	0.42
	Li	329.0	5.9	1.26	0.05	0.76
Ag	proton	485.2	2.2	1.24	0.02	0.89
	alpha	480.0	1.7	1.40	0.01	1.07
	Li	467.1	10.4	1.35	0.04	1.51

(* => λ=1.24 rather than 0.95)

Table 8. Results of searches for I (mean excitation energy) and b (free parameter of the z^3-correction term) for metals, with σ(rms relative deviation of calculations from measurements).

Stopping Power of Ni, Ag, Au and Pb for ~7 MeV/n α-particles and Carbon Ions (Z_1^3 proportional deviation from the Bethe formula)

Tadayoshi Doke* and Tan Takahashi**

* Science and Engineering Research Laboratory, Waseda University, Kikuicho-17, Shinjuku-ku, Tokyo, Japan

** Institute of Physical and Chemical Research, Hirosawa, Wako-shi, Saitama, Japan

1. Introduction

In the end of the 1960's, Andersen, Simonsen and Sørensen[1] carried out the measurements of stopping powers of a number of elements for protons, deuterons, and α-particles using the calorimetric-compensation technique and showed some Z_1^3 proportional deviations from the Bethe formula. Recently, Andersen and his co-workers[2] again made the measurements of stopping power of several elements for protons, α-particles and lithium ions in order to perform a more detailed investigation on the deviation from the Bethe formula.

To ascertain the Z_1^3 deviation of stopping power for heavier ions, it is desirable to make precise experiments using projectiles more massive than lithium ions, which are almost completely ionized. Until now, however, no experiment using such projectiles was made, except the experiment by Kelley, Sellers and Hanser.[3] They measured the energies deposited in a silicon detector of 94.6 μm in thickness but could not directly show the Z_1^3 deviation from the Bethe formula because the thickness of silicon detector was too thick, although their data were compared with theoretical estimations of the deposited energies.

Recently, we attempted to measure the stopping powers of several metals for ~7 MeV/n α-particles and carbon ions, although thus obtained data need a small correction for effective charge. In this paper, our

results obtained until now are presented and shown the analytical results.

2. Experimental Procedure

The experimental arrangement for measuring stopping powers of metals is shown in Fig. 1. The ion beams of α-particles and $^{12}C^{+6}$-particles were obtained from variable energy heavy ion cyclotron at the Institute of Physical and Chemical Research(IPCR). The energies of ion beams used in the present experiment are ~7 MeV/n and the extracted beam was passed through a beam analysing magnet, by which the beam energy defined, and after passing through a clearing magnet and a quadrupole-pair magnet, focused on the target foil put at the center of 75 cm target chamber without a beam collimation. The size of target foils was about 20 mm x 20 mm. The foil was removed when the spectrum of the beam was measured. The magnetic field in the beam analysing magnet was measured by the proton NMR frequency of the beam ana[illegible]. The relation between the magnetic field and the particle energy was calibrated by using α-particles of 8.766 MeV emitted from ThC' and by using the resonance elastic scattering of protons on ^{12}C at proton energy of 14.255 MeV. The accuracy of the energy determination is estimated to be within ±0.3 %. After passing through the foil, the beam was collimated by a collimator with three apertures as shown in Fig. 1. The silicon surface barrier detector with an active area of 130 mm^2 and a depletion layer of 0.8 mm was placed to analyse the energy of beam from the collimator about 1 cm from the third aperture in the collimator.

The energy resolution of 27 keV(fwhm) was achieved for 5.486 MeV ^{241}Am α-particles. The relation of pulse height versus ion energy is calibrated by aid of the analysing magnet without target foil. The counting rate was kept to be about 200 cps to prevent piling up of pulses from detector. In Fig. 2 and 3, the energy spectra for α-particles and carbon ions with and without target foil are shown for Ni and Pb, respectively. The beam spectra with target foil are shifted to low energy side and broadened and showed nearly Gaussian distributions.

Under the condition that the energy loss at target to the incident energy of ion, $\Delta E/E_i$, is equal to or less than one tenth of E_i, the metal

foils were selected as targets from the metal foils supplied from Goodfellow Co. Ltd.. The thickness of the target foil was determined by measuring the weight and area. The results are as follows: Ni(12.04 ± 0.05 mg/cm^2), Ag(13.41 ± 0.06), Au(19.29 ± 0.07) and Pb(25.11 ± 0.21) for α-particle experiments and Ni(5.158 ± 0.023 mg/cm^2), Ag(5.196 ± 0.045), Au(12.03 ± 0.05) and Pb(5.334 ± 0.022) for carbon ion experiments.

The energy loss at target foil, ΔE, was obtained by subtracting the ion energy E_0 after passing through the target, which was given as a mean energy of the spectrum measured by the silicon detector, from E_i and the stopping power of the target material was obtained by dividing ΔE by the thickness of the target. Here, we can consider that the ion energy corresponding to thus obtained stopping power is given by $E_i - \Delta E/2$ without introducing a large error. The energies of α-particles and carbon ions shown in Fig. 2 and Fig. 3 are given as $E_i - \Delta E/2$. The experimental error in our stopping power measurement consisted of peak fitting error(±0.5%), energy calibration error(±0.3%) and the error in determination of target thickness(±0.4 ~ 0.8%) and the over-all error was ranged from ±0.7% to ±1.2%.

3. Results and Discussion

In order to analyse our results, we use a semiempirical expression for the stopping power of a projectile at velocity v and charge Z_1e in a target with atomic number Z_2 and mass number A_2 as

$$-\frac{dE}{dx} = \frac{4\pi N_0 e^4 Z_2}{m v^2 A_2} Z_1^2 (L_0 + Z_1 L_1 + Z_1^2 L_2), \qquad (1)$$

where N_0 is Avogadro's number, m and e are the electronic mass and charge, respectively, L_0 is the Bethe stopping number per target electron, L_1 is the Z_1^3 term which expresses the Z_1^3 deviation from the Bethe formula and L_2 is the Bloch term which is given by[4)]

$$L_2 = \psi(1) - \mathrm{Re}\psi(1 + i\xi) \qquad (2)$$

where ξ is $(Z_1e^2)/(\hbar v)$ and ψ is the logarithmic derivative of the gamma-function. When the projectile has a possibility of electron capture, in the expression (1), Z_1 should be replaced by the so-called effective

charge Z_1^* .

From the expression (1), $L_0 + Z_1 L_1$ is given by

$$L_0 + Z_1 L_1 = L = \left(-\frac{dE}{dx}\right) \frac{m v^2 A_2}{4\pi N_0 e^4 Z_2 Z_1^2} - Z_1^2 L_2. \qquad (3)$$

For both cases of α-particles and carbon ions, L_0 is common if the same target is used for each case and the velocity of the projectile is equal. Accordingly, L_1 is given by the following formula,

$$L_1 = (L_c - L_\alpha)/(Z_c^* - Z_\alpha), \qquad (4)$$

where L_c and L_α are L for carbon ion and α-particle, respectively, and Z_c^* is the effective charge of carbon ion and Z_α is the net nuclear charge of α-particle. Since L can be determined from the experimental stopping power, we can obtain L_1 from formula (4), if the stopping powers of the same material for carbon ions and α-particles of the same velocity are measured.

In our experiment, the average energies per nucleon of α-particles corresponding to the measured stopping powers slightly differed from those of carbon ions, as seen from Fig. 2 and 3. To estimate the stopping power for α-particles with the same velocity as that of carbon ions, we corrected the value of stopping power measured for α-particles to that at the same velocity as that of carbon ion, assuming the energy dependence of Bloch's stopping power formula.[6] For effective charge correction for carbon ions, the formula used by Pitts and Bennett for Z_1^3 deviation from the Bethe formula($Z_1^* \sim Z_1[1 - \exp(-0.95v/Z_1^{2/3} v_0)]$) [7] and the formula used by Bichsel for calculation of stopping powers [8] were used. Table 1 shows the stopping powers of Ni, Ag, Au and Pb (without effective charge correction) for carbon ions and α-particles with the same velocity, that is, the same MeV/n, as well as the value of L_1 for both projectiles obtained by using two charge correction formulas. The stopping powers in the table are shown in Fig. 4 as well as 9 times of the stopping powers for α-particles obtained by Ishiwari et al.[3] and 36 times of those for protons by Andersen et al.[2] The solid lines in the figure are obtained from Bloch's stopping power formula. Our values for α-particles are in good

agreement with those of Ishiwari et al. rather than those of Andersen et al. or the lines obtained from Ziegler's formula.

Recently, Ishiwari's group[10] tried to plot the values of $L_1 Z_2^{1/2}$ for $x = (v/v_0)^2/Z_2$ and compare with the function $F(b/x^{1/2})/x^{3/2}$ obtained by Ashley, Ritchie and Brandt by adjusting the parameter b.[11] χ-value was chosen to be 1.29. The results are shown in Fig. 5 as well as our results. The effective charge correction of the data in the figure was made by using Pierce and Blann's formula. It seems that the points plotted in the figure except for Ni are on the line of b = 1.4 although Ishiwari's data are in favor of the line of b = 1.1. If we use Ziegler's formula for effective charge correction, however, our data will show the same tendency as that of Ishiwari's data. The best fit values of b for our data is ranging from 1.3 to 1.4 for effective charge correction due to Pierce and Blann's formula and from 1.2 to 1.3 for Ziegler's effective charge correction, except for the data of Ni, which gives 0.8 to 0.9.

4. *Conclusion*

The stopping powers of Ni, Ag, Au and Pb for 7 MeV/n α-particles and carbon ions have been measured and the Z_1^3 term, showing Z_1^3 deviation from the Bethe formula, L_1 was derived. These results are in fairly good agreement with the function of Ashley, Ritchi and Brandt when b was chosen to be about 1.3, except for the data of Ni, which is in favor of b ~ 0.9, although the experimental error is considerably large.

References

1) H.H.Andersen, H.Simonsen and H.Sφrensen, Nucl. Phys. A125, 171 (1969).
2) H.H.Andersen, J.F.Bak, H.Knudsen and B.R.Nielsen, Phys.Rev. A16, 1929 (1977).
3) J.G.Kelly, B.Sellers and F.A.Hanser, Phys. Rev. B8, 103 (1973).
4) F.Bloch, Ann. Phys. (Leipz.) 16, 285 (1933).
5) J.F.Ziegler, "The stopping powers and ranges of ions in matter" Vol.4, Pergamon Press, New York (1977).
6) R.H.Ritchie and W.Brandt, Phys. Rev. 17, 2102 (1978); T.E.Pierce and M.Blann, Phys. Rev. 173, 390 (1968).

7) J.F.Ziegler, "Handbook of Stopping Cross-Sections for Energetic Ions in All Elements" Vol.5 of The Stopping and Ranges of Ions in Matter, Pergamon Press, New York (1980).

8) R.Ishiwari, N.Shiomi and S.Shirai, Bull. Inst. Chem. Res., Kyoto Univ. 55, No.1, 60 (1977).

9) H.H.Andersen, C.C.Hanke, H.Sørensen and P.Vajda, Phys. Rev. 153, 338 (1967); H.H.Andersen, C.C.Hanke, H.Simonsen, H. Sørensen and P.Vajda, Phys. Rev. 175, 389 (1968).

10) R.Ishiwari et al., Private communication.

11) J.C.Ashley, R.H.Ritchie and W.Brandt, Phys. Rev. A8, 2402 (1973).

Table 1 Stopping power values for ~ 7 MeV/n α-particles and C-ions, and their Z_1^3 deviation term L_1.

Stopping Material	Energy (MeV/n)	Stopping power for C-ion ($MeV/mg.cm^2$)	Stopping power for α-particle ($MeV/mg.cm^2$)	L_1 (1)*	L_1 (2)**	L_1 (3)
Ni	7.039	1.347±0.016	0.1502±0.0011	0.0270	0.0427±0.014	0.0464
Ag	7.097	1.069±0.010	0.1190±0.0008	0.0286	0.0424±0.012	0.0458
Au	6.908	0.839±0.006	0.0928±0.0007	0.0339	0.0453±0.010	0.0479
Pb	7.148	0.814±0.006	0.0895±0.0008	0.0374	0.0491±0.011	0.0517

* No effective charge correction.
** corrected by using Pierce and Blann's effective charge formula.
*** corrected by Ziegler's effective charge formula.

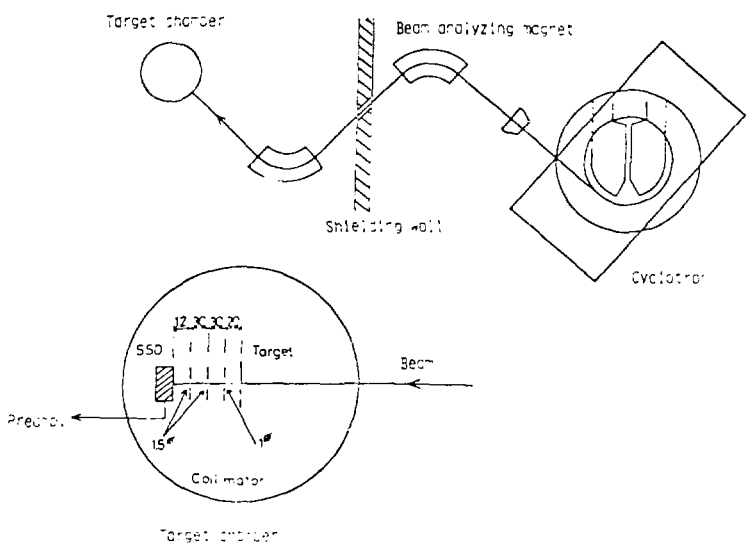

Fig. 1 Experimental arrangement for measuring stopping powers

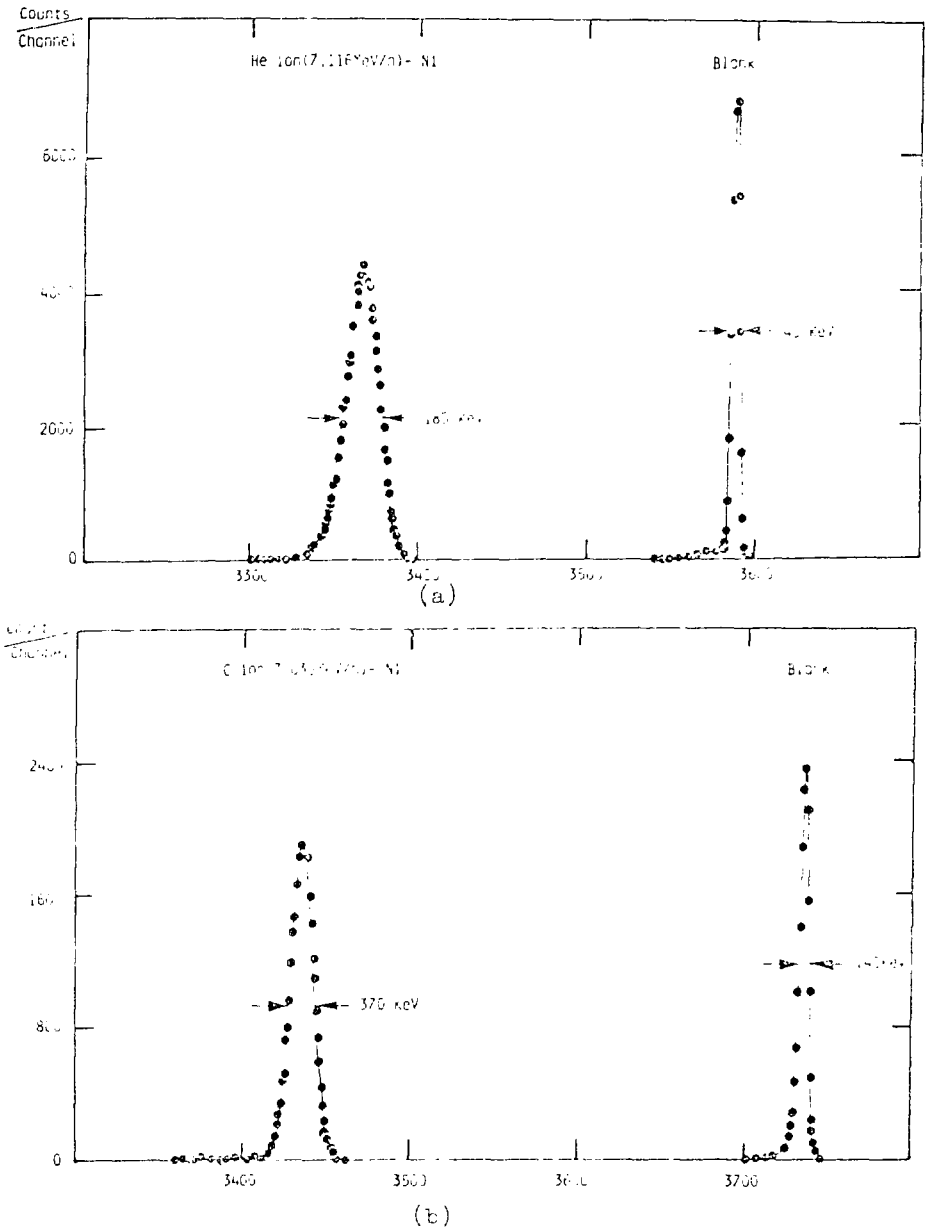

Fig. 3 Energy spectra of α-particles(a) and C-ions(b) obtained with the apparatus shown in Fig. 1. The lower energy peak, in each case, resulted from those ions which lost energy in traversing Ni-target and the higher energy peak from incident beam which was measured without Ni-target.

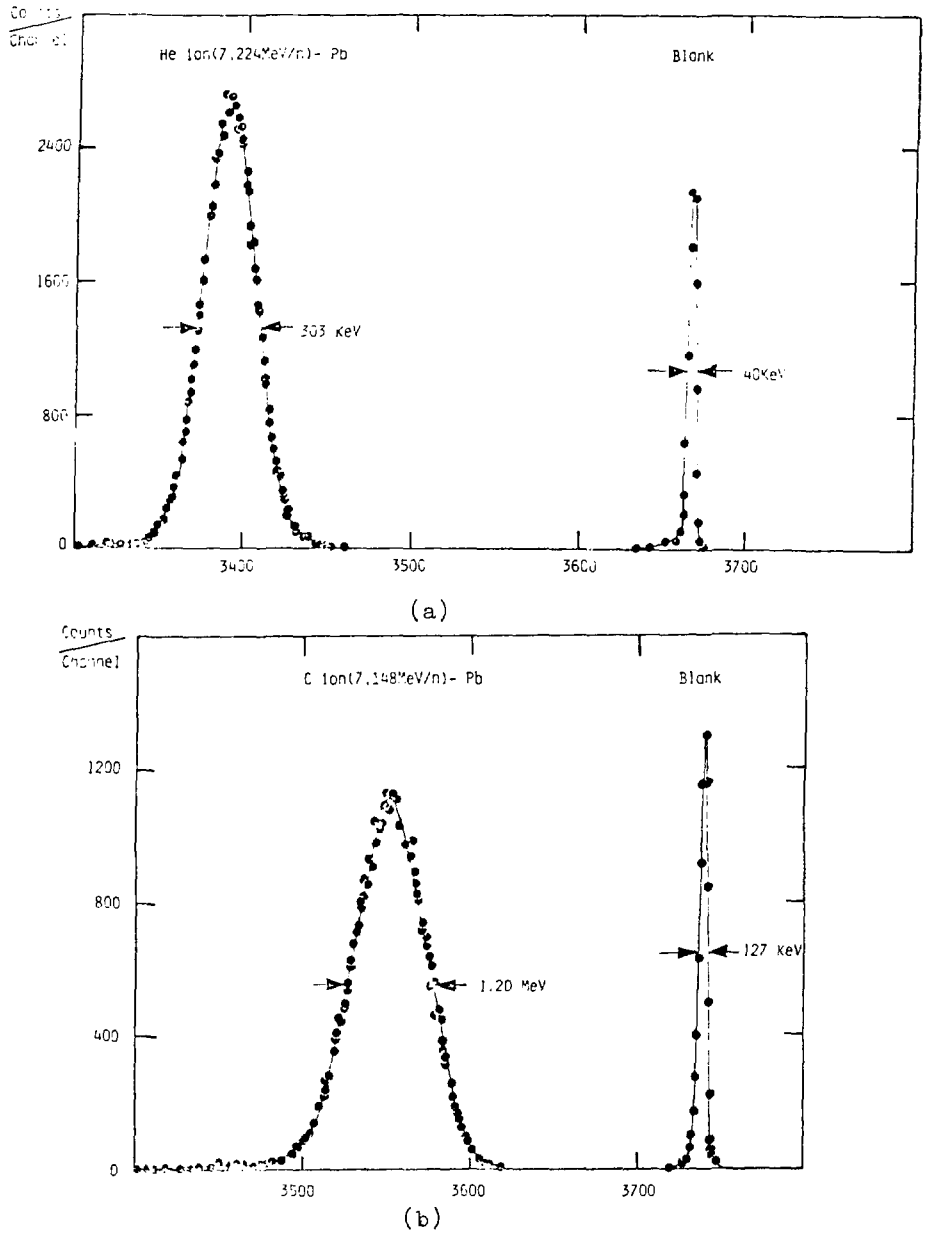

Fig. 3 Energy spectra of α-particles(a) and C-ions(b) obtained with the apparatus shown in Fig. 1. The lower energy peak, in each case, resulted from those ions which lost energy in traversing Pb-target and the higher energy peak from incident beam which was measured without Pb-target.

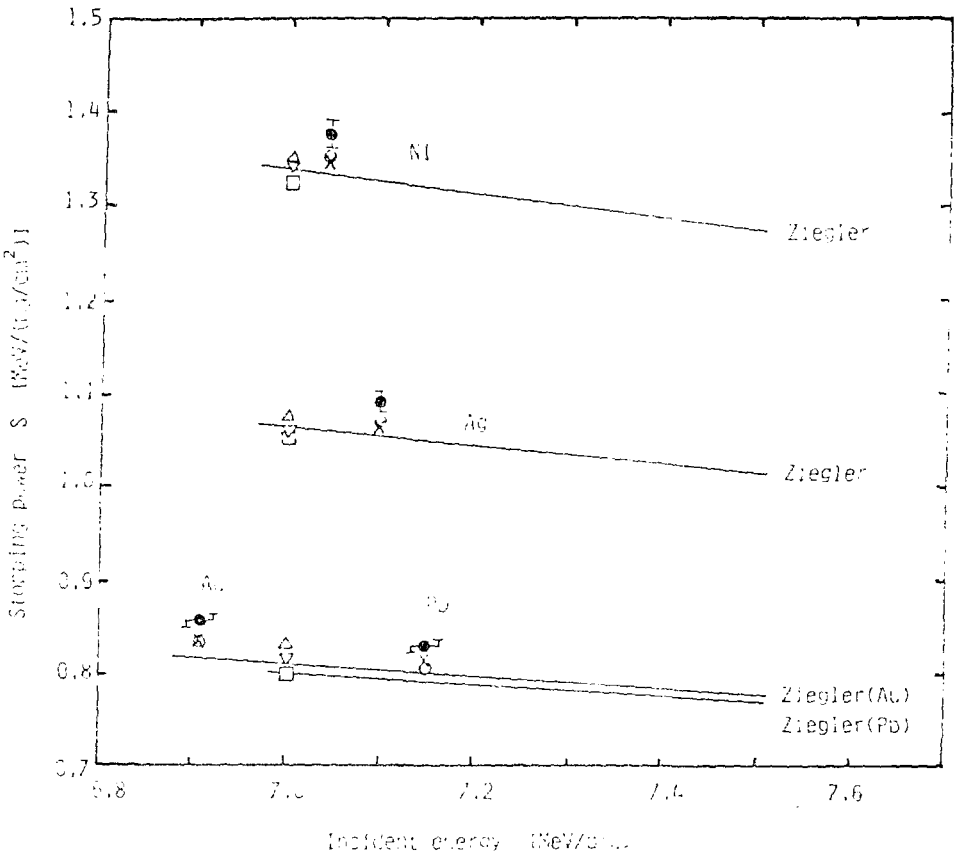

Fig. 4 Stopping powers of Ni, Ag, Au and Pb for α-particles and C-ions. In this figure, the values of the stopping power for α-particles and the values of the stopping power for carbon ions are shown. × : the present data for C-ions, ● : corrected by Brice, Pierce and Blann's effective charge formula, ○ : the present data for α-particles, Δ : Ishiwari's data for α-particles, ▽ : Andersen's data for protons, —— : calculated from Ziegler's formula for α-particles and □ : taken from Northcliffe and Schilling's table for α-particles.

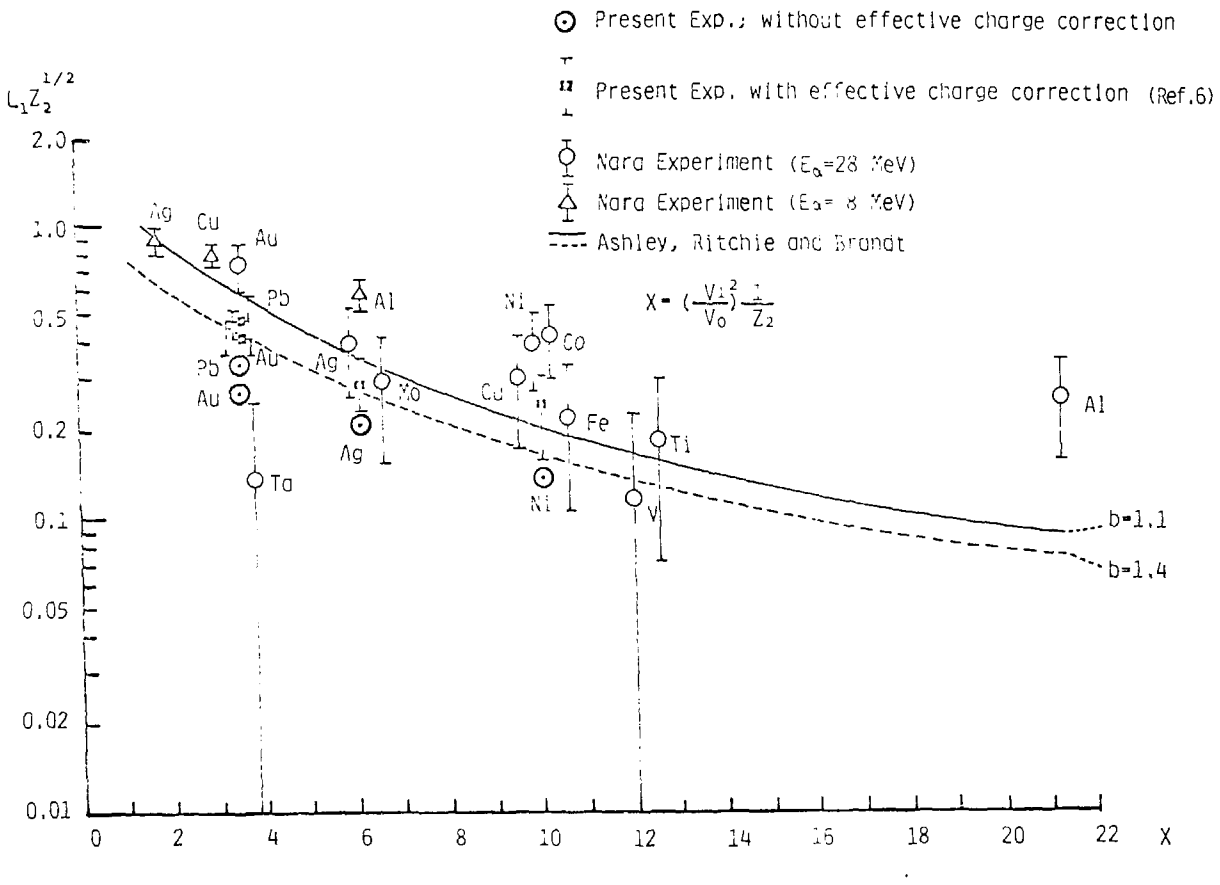

Fig. 5 Experimental values of $Z_2^{1/2} L_1$ as a function of $(v/v_0)^2/Z_2$.

MEAN EXCITATION ENERGIES FOR USE IN BETHE'S STOPPING-POWER FORMULA*†

M. J. Berger and S. M. Seltzer
Center for Radiation Research
National Bureau of Standards
Washington, D.C. 20234

A review has been made of the mean excitation energies that can be derived from the analysis of stopping-power and range measurements, and from semi-empirical dipole oscillator-strength distributions for gases and dielectric-response functions for solids. On the basis of this review, mean excitation energies have been selected for 43 elemental substances and 54 compounds. Additivity rules have also been considered which allow one to estimate the mean excitation energies for compounds for which no direct data are available. These additivity rules are based on the use of mean excitation energies for atomic constituents which, to a certain extent, take into account the effects of chemical binding and physical aggregation.

1. Introduction

In the course of preparing new stopping-power tables, we have reviewed the information on the mean excitation energies (I-values) required as input for the Bethe stopping-power formula. We have attempted to select the best I-values for elements and compounds, on the basis of the guidance provided by earlier critical data analyses,[1-11] by analyzing old and recent stopping-power and range data, and by taking into account I-values derived from dipole oscillator-strength distributions and dielectric-response functions.

2. Mean Excitation Energies for Elements

For the gases H_2, He, N_2, O_2, Ne, and Ar reliable mean excitation energies are now available which have been derived from experimental dipole oscillator-strength distributions.[12-17] For aluminum, a particularly accurate I-value has been obtained by Shiles *et al.*[18] from a dielectric-response function constructed from optical data. We have

---

*To be published in the Proceedings of the Seminar on Charge States and Dynamic Screening of Swift Ions in Solids, East-West Center, Honolulu, Hawaii, January 25-29, 1982.

†This work was supported by the Department of Energy (Office of Health and Environmental Research) and by the Office of Naval Research.

given great weight to these results when selecting I-values. For other elements we have relied on the customary analysis of stopping-power and range measurements.

In order to be able to extract accurate I-values from stopping-power measurements with use of the Bethe stopping-power formula, one must have adequate knowledge of several corrections: (a) the shell correction, important when the velocity of some of the electrons in the target atoms is comparable to the velocity of the incident projectile; (b) the z^3 and z^4 correction, which represent departures from Born approximation; and (c) the density-effect correction which becomes non-negligible for protons at energies greater than a few hundred MeV.

We have followed the method developed by H. Bichsel for the analysis of stopping-power data, and have adopted his recommended I-values for many elements. Bichsel evaluates the z^4 correction from the stopping-power theory of Bloch,[19] and the z^3 correction from the theory of Ashley, Ritchie, and Brandt.[20,21] The shell correction is evaluated according to Walske[22,23] for the K and L shells. The corrections for the higher shells are treated as scaled L-shell corrections, with two free scaling parameters for each shell. For a few key elements (including Aℓ, Cu, Ag, and Au) the shell-correction scaling parameters, a dimensionless impact parameter in the Ashley-Ritchie-Brandt expression for the z^3 correction, and the mean excitation energy I are all chosen so as to give the best possible agreement between measured and calculated stopping-powers or ranges. The scaling parameters for the key elements are fitted by semi-empirical functions of the atomic number Z. The set of semi-empirical shell corrections thus obtained, anchored for low Z-values by the Walske theory, is then available for the extraction of I-values from stopping-power or range data for any element.

As an alternative to the semi-empirical shell corrections of Bichsel, one has available the theoretical shell corrections of Bonderup,[24] derived on the basis of Lindhard's[25] statistical stopping-power theory. It turns out that the Bonderup shell corrections are rather close to those of Bichsel for atomic numbers up to ~ 47, but are larger for very high Z. This is illustrated in Table 1 with data for copper, silver, and lead.

Table 2 gives the results of an analysis employing the two types of shell corrections applied to two high-quality experiments: (a) medium energy (3 to 18 MeV) stopping-power measurements by Sørensen and Andersen;[26] and (b) high-energy (750 MeV) proton range measurements by Barkas and von Friesen.[27] It can be seen from Table 2 that for copper the same I-value is obtained regardless of the type of shell correction. For lead and uranium, however, the use of the Bonderup shell corrections leads to estimated I-values that are significantly lower for the medium-energy experiment than for the high-energy experiment, whereas with Bichsel's shell corrections more or less the same I-value is obtained regardless of the energy. Inasmuch as one expects the mean excitation energy to be an energy-independent material constant, this indicates that the Bonderup theory, while applicable for moderately large atomic numbers, needs modification for high atomic numbers; as suggested by Andersen and Nielson,[28] this may be due to the non-relativistic treatment of inner-shell electrons in Bonderup's theory.

With the use of Bichsel's empirical shell corrections we have extracted I-values from most of the proton stopping-power measurements in the 1 to 20-MeV region previously analyzed by Andersen and Ziegler.[8] We have also re-analyzed the older high-energy data of Bakker and Segre,[29] Thompson[30] and Barkas and von Friesen,[27] including in the analysis also a small density-effect correction evaluated according to Sternheimer.[31] We have also derived I-values from the more recent stopping-power experiments of Ishiwari *et al.*,[32] Nordin and Henkelman,[33] Andersen *et al.*,[34] Besenbacher *et al.*,[35] and Andersen and Nielson.[28] Taking into account the results thus obtained, and the I-values from oscillator-strength and dielectric data, we have arrived at the choice of I-values for elements listed in Table 3. Values are given only for those elements for which there are experimental data. The indicated uncertainties are intended to include not only the experimental uncertainties but also the uncertainties inherent in the data analysis. Our adopted set of I-values is only the latest in a long series of recommendations. To put them in context, we show in Table 4 a comparison with mean excitation energies recommended in the past.

3. Mean Excitation Energies for Compounds

For a considerable number of compounds, experimental data are now available from which reliable I-values can be extracted. In Table 5 such I-values are listed for 13 gases, 27 liquids, and 14 solids. The indicated uncertainties of the I-values again include not only the experimental errors but also the uncertainties inherent in the data analysis.

The I-values for gases in Table 5A are (with one exception) results derived by Zeiss *et al.*,[14] by Thomas and Meath,[36] and by Jhanwar *et al.*[37] from experimental dipole oscillator-strength distributions. The data for liquids in Table 5B are based on an accurate experiment by Thompson[30] who measured partial ranges, relative to those in copper, for protons slowing down from 340 MeV to 200 MeV in many organic liquids, in water, and in a few solids. These data can be interpreted as stopping-power ratios at an intermediate energy of 267.5 MeV. We have re-analyzed Thompson's data, using small multiple-scattering and shell corrections as suggested by Bichsel.[38] This analysis was done relative to copper (assuming I_{cu} = 322 eV) and relative to water (assuming I_{H_2O} = 75 eV); the two sets of I-values thus obtained differed by only 0.6 percent, and an average value has been taken. The I-values for solids in Table 5C include several derived from dielectric-response functions by Painter *et al.*[39] and by Ashley[40] (also private communication).

Even though the number of compounds for which I-values are directly available is large and growing, one would like to be able to estimate I-values for many other compounds. The usual approach to this problem is to assume the validity of a Bragg additivity rule,[41] i.e., to assume that the stopping power of a compounds is the weighted sum of the stopping powers of the atomic constituents. This in turn implies that logI for the compound is a weighted sum of the logI-values for the constituents. Of course such an additivity rule is not strictly correct, because the binding of the electrons, and therefore the I-value for the compounds, depends on the chemical structure, the types of bond involved, etc. Furthermore the mean excitation energy also depends on the phase of the medium. The accuracy of the additivity rule can be improved by

assigning I-values to the atomic constituents which can take one of several values depending on the chemical environment and the phase.

A simple assignment rule, specifying I-values for the constituents H, C, N, and O in gaseous compounds is given in Table 6 (Assignment Rule 1). This rule was obtained by trial and error. As shown in Table 5, the experimental I-values can be represented rather accurately in this way. The departures from additivity are in almost all cases smaller than the uncertainties of the experimental I-values. Another assignment rule specifying I-values for atomic constituents in liquids and solids is also given in Table 6 (Assignment Rule 2). This rule, also obtained by trial and error, represents the experimental I-values well in most cases, with two exceptions (dichloroethane and paraffin wax).

Rules 1 and 2 are successful on a strictly empirical basis, without providing an understanding of the underlying chemical physics. A somewhat deeper analysis of his data was performed by Thompson[30] who compared the relative stopping powers of groups of compounds to obtain the relative stopping powers for atomic constituents in different chemical environments. Thompson's results were interpreted by Westermark[42] in terms of molecular polarizabilities, and this approach was further developed by Brandt[43] into a theory for predicting I-values for compounds from molar refractivity data and the low-energy density effect. We have repeated and up-dated Thompson's analysis to obtain Assignment Rule 3 given in Table 6. This rule is applicable to the liquids in Table 5B and the solids in Group 1 in Table 5C. For liquids, Assigment Rule 3 works somewhat better than Rule 2, but still fails in the case of dichloroethane. For the solids in Group 1, Rule 3 is not quite as good as Rule 2, and also fails to work for paraffin wax.

The phase dependence of the I-values for several elements and compounds is indicated in Table 7. The quoted I-values for "atomic gases" are theoretical results of Dehmer *et al.*[44] and of Inokuti *et al.*[45] obtained from Hartree-Slater oscillator-strength distributions. The I-values for molecular gases are from Zeiss *et al.*,[14] Thomas and Meath,[36] and Jhanwar *et al.*,[37] and are based on experimental dipole oscillator-strength distributions. The I-values for liquids are from the experiment

of Thompson[30] (and for hydrogen also from the stopping-power measurements of Garbincius and Hyman[46]). The I-values for solids are from Table 3. The phase effects, as indicated by the I-value ratios in Table 7, are plausible, but a quantitative explanation is lacking.

4. Concluding Remarks

The available information on mean excitation energies is on the whole, satisfactory. There is of course room for improvement, e.g., in regard to materials commonly used in radiation detectors. For example, the experimental data base is rather limited for graphite and for A-150 tissue-equivalent plastic, and even more inadequate for thermoluminscence detectors such as LiF and CaF_2. In the absence of improvements in the theory of shell corrections, it appears that the most reliable new information on mean excitation energies is likely to come either from stopping-power or range experiments at energies of several hundred MeV (which have been rare in recent years) and from the use of the steadily growing body of semi-empirical oscillator-strength and dielectric-response function data. In regard to Bragg additivity rules to obtain I-values for compounds, the situation seems to be satisfactory for compounds containing only the constituents H, C, N, and O, but in need of improvement for compounds containing other constituents of higher atomic number.

5. Acknowledgements

We have benefitted from the advice and help received from many colleagues, especially H. H. Andersen, J. Ashley, H. Bichsel, M. Inokuti, R. M. Sternheimer, and J. E. Turner. We are particularly indebted to H. Bichsel for making available to us his method, and his computer program, for the analysis of stopping-power data, and for advising us on the choice of I-values. However, the specific choices that we have made are entirely our own responsibility.

6. References

1. National Committee on Radiation Protection and Measurements, Handbook 79 (1961).

2. Fano, U., Ann. Rev. Nucl. Sci. 13, 1 (1963).

3. Berger, M. J. and Seltzer, S. M., Nat. Acad. of Sciences-Nat. Res. Council Publ. 1133, p. 205 (1964); also National Aeronautics and Space Administration Publications SP-3012 (1964) and SP-3036 (1966).

4. Janni, J. F., Air Force Weapons Laboratory Technical Report No. AFWL-TR-65-150 (1966).

5. Bichsel, H., Radiation Dosimetry, 2nd Edition, Vol 1, F. H. Attix and W. C. Roesch, eds. (Academic Press, New York, 1968) p. 157.

6. Turner, J. E., Roecklein, P. D., and Vora, R. B., Health Phys. 18, 159 (1970); see also Dalton, P. and Turner, J. E., Health Phys. 15, 257 (1968).

7. Bichsel, H., American Institute of Physics Handbook, 3rd Edition, D. E. Gray, ed. (McGraw-Hill, New York, 1972), Chap. VIII D.

8. Andersen, H. H. and Ziegler, J. F., Hydrogen: Stopping Powers and Ranges in All Elements (Pergamon Press, New York, 1977).

9. Ahlen, S. P., Rev. Mod. Phys. 52, 121 (1980).

10. Ziegler, J. F., Handbook of Stopping Cross-Sections of Energetic Ions in All Elements, Vol. 5 (Pergamon Press, New York, 1980).

11. Janni, J. F., Trans. American Nucl. Society 34, 653 (1980).

12. Gerhart, D. E., J. Chem. Phys. 62, 821 (1975).

13. Miller, W. F., Ph.D. dissertation, Purdue University, Lafayette, Ind. (1956).

14. Zeiss, G. D., Meath, W. J., MacDonald, J. C. F., and Dawson, D. J., Can. J. Phys. 55, 2080 (1977); Radiat. Res. 70, 284 (1977).

15. Bell, R. J. and Dalgarno, A., Proc. Phys. Soc. 86, 375 (1965); and Proc. Phys. Soc. 89, 55 (1966).

16. Saxon, R. P., Phys. Rev. A8, 839 (1973).

17. Eggarter, E., J. Chem. Phys. 62, 833 (1975).

18. Shiles, E., Sasaki, T., Inokuti, M., and Smith, D. Y., Phys. Rev. B22, 1612 (1980).

19. Bloch, F., Ann. Phys. 16, 285 (1933).

20. Ashley, J. C., Ritchie, R. H. and Brandt, W., Phys. Rev. B5, 2393 (1972).

21. Ashley, J. C., Ritchie, R. H. and Brandt, W., Phys. Rev. A8, 2402 (1973).

22. Walske, M. C., Phys. Rev. 88, 1283 (1952).

23. Walske, M. C., Phys. Rev. 101, 940 (1956).

24. Bonderup, E., Mat. Fys. Medd. Dan. Vid. Selsk. 35, No. 17 (1967).

25. Lindhard, J. and Winther, A., Mat. Fys. Medd. Dan Vid. Selsk. 34, No. 4 (1964).

26. Sørensen, H. and Andersen, H. H., Phys. Rev. B8, 1854 (1973).

27. Barkas, W. H. and von Friesen, S., Nuovo Cimento (Suppl) 19, 41 (1961).

28. Andersen, H. H. and Nielson, B. R., Nucl. Instr. Meth. (1981) in press.

29. Bakker, C. J. and Segre, E., Phys. Rev. 81 489 (1951).

30. Thompson, T. J., University of California, Radiation Laboratory Report UCRL-1910 (1952).

31. Sternheimer, R. M., Phys. Rev. 88, 851 (1952).

32. Ishiwari, R., Shiomi, N., and Sakamoto, N., Phys. Lett. 75A, 112 (1979).

33. Nordin, J. A. and Henkelman, R. M., Phys. Med. Biol. 24, 781 (1979).

34. Andersen, H. H., Bak, J. F., Knudsen, H. and Nielsen, B. R., Phys. Rev. A16, 1929 (1977).

35. Besenbacher, F., Andersen, H. H., Hvelplund, P. and Knudsen, H., Kgl. Danske Vidensk. Selskab, Mat. Fys. Medd. 40 No. 3 (1979).

36. Thomas, G. F. and Meath, W. J., Mol. Phys. 34, 113 (1977).

37. Jhanwar, B. L., Meath, W. J., and MacDonald, J. C. F., Can. J. Phys. 59, 185 (1981).

38. Bichsel, H., AAPM Charged Particle Beam Task Group Workshop, Los Alamos Scientific Laboratory (March, 1978).

39. Painter, L. R., Arakawa, E. T., Williams, W. and Ashley, J. C., Radiat. Res. 83, 1 (1980).

40. Ashley, J. C., Phys. Rev. B19, 5429 (1979).

41. Bragg, W. H. and Kleeman, R., Philos. Mag. 10, 318 (1905).

42. Westermark, T., Phys. Rev. 93, 835 (1954).

43. Brandt, W., Research Report, Radiation Physics Laboratory, E. I. du Pont and Co., Wilmington, Del. (1960); see also Phys. Rev. 104, 691 (1956); Health Phys. 1, 11 (1958).

44. Dehmer, J. L., Inokuti, M., and Saxon, R. P., Phys. Rev. A12, 102 (1975).

45. Inokuti, M., Dehmer, J. L., Baer, T., and Hansen, J. D., Phys. Rev. A23, 95 (1981).

46. Garbincius, P. H. and Hyman, L. G., Phys. Rev. A2, 1834 (1970).

47. Bader, M., Pixley, R. E., Moser, F. J., and Whaling. W., Phys. Rev. 103, 32 (1956).

48. Ritchie, R. H., Hamm, R. N., Turner, J. E., and Wright, H. A., Proc. Sixth Symposium on Microdosimetry, Vol. I. Harwood Academic Publishers, Ltd. 345 (1978).

49. Porter, L. E., Naylor, H., and Duder. J. C., Nucl. Instr. Meth. 155, 25 (1978).

50. Tschalär, C. and Bichsel, H., Phys. Rev. 175, 476 (1968).

51. Barkas, W. H., Barrett, P. H., Cuer, P., Heckman, H., Smith, F. M. and Ticho, H. K., Nuovo Cimento 8, 186 (1958).

TABLE 1. Shell corrections for protons.

T	Copper		Silver		Lead	
(MeV)	Bichsel[a]	Bonderup[b]	Bichsel[a]	Bonderup[b]	Bichsel[a]	Bonderup[b]
3	0.255	0.273	0.320	0.325	0.243	0.336
6	0.206	0.215	0.286	0.292	0.267	0.368
9	0.172	0.176	0.251	0.252	0.254	0.347
12	0.149	0.148	0.223	0.222	0.238	0.321
15	0.132	0.129	0.200	0.198	0.223	0.296
18	0.119	0.114	0.182	0.176	0.208	0.275
50	0.060	0.054	0.098	0.092	0.131	0.160
100	0.035	0.032	0.062	0.056	0.090	0.103
200	0.021	0.019	0.039	0.035	0.061	0.066
500	0.012	0.011	0.023	0.021	0.039	0.040

[a]Calculated with a computer program of Bichsel.

[b]Calculated with a computer program of Bonderup.

TABLE 2. Comparison on mean excitation energies extracted from proton stopping-power and range measurements with the use of Bichsel's and Bonderup's shell corrections.

		I^* (eV), derived with use of					
		Bichsel's Shell Corrections			Bonderup's Shell Corrections		
		Cu	Pb	U	Cu	Pb	U
Stopping-power Measurements	3 MeV	316	813	910	310	745	805
	6	317	814	898	314	736	790
Sørensen and	9	319	810	886	318	738	789
Andersen, Ref. 26	12	319	806	881	319	742	794
	15	319	803	878	320	746	799
	18	318	800	877	320	747	806
Range Measurements	749 → 0 MeV	314	821	889	315	818	885
Barkas and von Friesen, Ref. 27							

*The uncertainties of the I-values resulting from experimental uncertainties are estimated to be 2-3 percent.

TABLE 3. Mean excitation energies for elemental substances. The indicated uncertainies attempt to take into account the uncertainties of the underlying measurements, the errors in the analysis of the measurements, and the dispersion of the I-values derived from various sources.

Z	I (eV)	I/Z (eV)	Z	I (eV)	I/Z (eV)
1 gas	19.2 ± 0.4	19.2	30	330 ± 10	11.0
2 gas	41.8 ± 0.8	20.9	32	350 ± 11	10.4
3	40.0 ± 4.0	13.3	36 gas	352 ± 25	9.8
4	63.7 ± 3.0	15.9	40	380 ± 15	9.5
5	76 ± 8	15.2	41	417 ± 15	10.2
6	78 ± 7	13.0	42	424 ± 15	10.1
7 gas	82 ± 2	11.7	45	449 ± 20	10.0
8 gas	95 ± 2	11.9	46	470 ± 20	10.2
10 gas	137 ± 4	13.7	47	470 ± 10	10.0
13	166 ± 2	12.8	48	469 ± 20	9.8
14	173 ± 3	12.4	49	488 ± 20	10.0
18 gas	188 ± 10	10.4	50	488 ± 15	9.8
20	191 ± 8	9.6	54 gas	497 ± 30	9.2
21	216 ± 8	10.3	64	591 ± 20	9.2
22	233 ± 5	10.6	73	718 ± 30	9.8
23	245 ± 7	10.7	74	727 ± 30	9.8
24	257 ± 10	10.7	77	757 ± 35	9.8
25	272 ± 10	10.9	78	790 ± 35	10.1
26	286 ± 9	11.0	79	790 ± 35	10.0
27	297 ± 9	11.0	82	823 ± 30	10.0
28	311 ± 10	11.1	92	890 ± 30	9.7
29	322 ± 10	11.1			

TABLE 4. Comparison of mean excitation energies for elements recommended in various publications. Values are given in units of eV.

	H_2 (gas)	C (graphite)	N_2 (gas)	O_2 (gas)	Aℓ	Cu	Ag	Pb
NCRP (1961)[1/]	-	78.4	-	-	164	306	462	812
Fano (1964)[2/]	18.3	81	88	101	163	315	478	820
NAS-NRC (1964)[3/]	18.7	78	85	89	163	312	480	795
Janni (1966)[4/]	18.3	77.3	87.5	88.9	163	318	459	779
Bichsel (1968)[5/]	18	78	78	100	164	322	475	820
Turner *et al.* (1970)[6/]	18.2	81.2	89.6	101	163	316	466	767
Bichsel (1972)[7/]	19.2	78	78	93	166	319	475	813
Andersen & Ziegler (1977)[8/]	18.8	77.3	86.7	97.7	162	322	466	759
Ahlen (1980)[9/]	18.5	79.0	82	98.5	164	317	469	793
Ziegler (1980)[10/]	19	79	86	99	162	330	470	761
Janni (1980)[11/]	20.4	73.8	97.8	116	160	321	462	788
Average (References 1-11)	18.7±0.7	78.3±2	85.6±6	98.1±8	163±1.4	318± 6	470± 7	792±22
Values adopted here	19.2±0.4	78 ± 7	82 ± 2	95 ± 2	166±2	322±10	470±10	823±30

TABLE 5. Mean excitation energies for compounds

I_{expt} : value deduced from experiment

ΔI_{expt} : percent uncertainty, estimated from the uncertainty of the measurements and from the errors inherent in the data analysis

ΔI_{fit} : percentage amount by which calculated I-values deviate from I_{expt}. The headings BRAGG(1), BRAGG(2), and BRAGG(3) indicate results obtained with assignment rules 1, 2, or 3 for I-values of atomic constituents.

A. Gas Compounds

Compound	Footnote	I_{expt}* (eV)	ΔI_{expt}	ΔI_{fit} BRAGG(1)
ammonia, NH_3	*a*	53.7	± 2%	- 1.3%
butane, C_4H_{10}	*b*	48.3	± 2	- 1.0
carbon dioxide, CO_2	*c*	88.7	± 8	0.0
ethane, C_2H_6	*b*	45.4	± 2	0.2
heptane, C_7H_{16}	*b*	49.2	± 2	- 0.4
hexane, C_6H_{14}	*b*	49.1	± 2	- 0.8
methane, CH_4	*d*	41.7	± 2	0.0
nitric oxide, NO	*a*	87.8	± 2	2.2
nitrous oxide, N_2O	*a*	84.9	± 2	2.7
octane, C_8H_{18}	*b*	49.5	± 2	- 0.6
pentane, C_5H_{12}	*b*	48.2	± 2	0.4
propane, C_3H_8	*b*	47.1	± 2	- 0.2
water, H_2O	*a*	71.6	± 2	- 2.0

*I_{expt} was derived from semi-empirical dipole oscillator-strength distributions, except for CO_2.

[a] From Zeiss *et al.*[14]

[b] From Jhanwar *et al.*[37]

[c] From stopping-power results of Bader *et al.*,[47] for protons with energies between 300 and 400 keV.

[d] From Thomas and Meath.[36]

TABLE 5. Continued

B. Liquid Compounds*

Compound	I_{expt} (eV)	ΔI_{expt}	ΔI_{fit} BRAGG(2)	BRAGG(3)
acetone, C_3H_6O	64.2	± 2.9 %	3.0 %	- 0.4
aniline, $C_6H_5NH_2$	66.2	± 3.0	- 0.5	0.1
benzene, C_6H_6	63.4	± 2.8	4.0	0.1
n-butyl alcohol, C_4H_9OH	59.9	± 3.2	1.0	0.6
carbon tetrachloride, $CC\ell_4$	166.3	± 2.5	1.5	0.1
chlorobenzene, $C_6H_5C\ell$	89.1	± 2.7	1.5	- 1.0
chloroform, $CHC\ell_3$	156.0	± 2.5	2.2	0.5
cyclohexane, C_6H_{12}	56.4	± 2.9	0.2	0.0
1,2-dichlorobenzene, $C_6H_4C\ell_2$	106.5	± 2.8	1.6	- 0.2
dichlorodiethyl ether, $C_4C\ell_2H_8O$	103.3	± 4.1	- 0.3	- 0.5
1,2-dichloroethane, $C_2C\ell_2H_4$	111.9	± 4.1	11.0	6.8
diethyl ether, $(C_2H_5)_2O$	60.0	± 2.9	0.9	0.4
ethyl alcohol, C_2H_5OH	62.9	± 2.7	0.4	- 0.3
glycerol, $C_3H_5(OH)_3$	72.6	± 2.9	0.8	0.1
n-heptane, C_7H_{16}	54.4	± 2.9	0.1	- 0.1
n-hexane, C_6H_{14}	54.0	± 3.1	0.2	0.0
methanol, CH_3OH	67.6	± 3.2	- 1.9	- 2.7
nitrobenzene, $C_6H_5NO_2$	75.8	± 2.7	1.7	4.8
n-pentane, C_5H_{12}	53.6	± 3.0	0.2	- 0.1
n-propyl alcohol, C_3H_7OH	61.1	± 3.0	0.7	0.2
pyridine, C_5H_5N	66.2	± 2.9	2.4	0.0
styrene, C_8H_8	64.0	± 3.0	3.0	- 0.9
tetrachloroethylene, $C_2C\ell_4$	159.2	± 2.5	0.3	- 2.1
toluene, C_7H_8	62.5	± 3.2	2.9	- 0.1
trichloroethylene, $C_2C\ell_3H$	148.1	± 2.6	1.0	- 0.9
water, H_2O	75.0[a]	± 3.2	0.4	- 0.9
xylene, C_8H_{10}	61.8	± 2.7	2.3	0.6

TABLE 5. Continued

Footnotes for Table 5B

*Experimental I-value was obtained in our analysis of Thompson's[30] measurement of partial proton ranges.

[a]A compromise among the following experimental results: 75.4 ± 1.9 eV from our analysis of Thompson's[30] measurements relative to Cu, assuming I_{Cu} = 322 eV; 74.6 ± 2.7 eV from an analysis of the 61-MeV pion stopping-power measurements of Nordin and Henkelman;[33] 75 eV from Ritchie *et al.*[48] and 75.4 eV from J. Ashley (private communication); both values derived from empirically-based models of the dielectric-response function for liquid water.

TABLE 5. Continued

C. Solid Compounds

Compound	Footnote	I_{expt}	ΔI_{expt}	ΔI_{fit} BRAGG(2)	ΔI_{fit} BRAGG(3)
Group 1					
adenine, $C_5H_5N_5$		71.4	± 5 %	0.4 %	4.1 %
guanine, $C_5H_5N_5O$		75.0	± 5	- 0.4	2.8
Nylon, type 6, $(C_6H_{11}NO)_n$		63.9	± 6	1.3	2.9
paraffin wax, $C_{25}H_{52}$		48.3	± 7	15.7	15.6
polyethylene, $(C_2H_4)_n$		57.4	± 8	- 1.6	- 1.7
polymethyl methacrylate, $(C_5H_8O_2)_n$		74.0	± 4	- 4.2	- 6.3
polystyrene, $(C_8H_8)_n$		68.7	± 4	4.1	- 6.5
Group 2					
A-150 tissue-equivalent plastic		65.1	± 16 %	- 1.7 %	
aluminum oxide, Al_2O_3		145.2	± 3	- 1.8	
calcium fluoride, CaF_2		166	± 8	- 4.7	
lithium fluoride, LiF		94	± 8	- 4.2	
photographic emulsion		331	± 3	- 1.5	
polytetrafluoroethylene, "Teflon," $(C_2F_4)_n$		99.1	± 6	4.2	
silicon dioxide, SiO_2		139.2	± 3	1.3	

TABLE 5. Continued

Footnotes for Table 5C

[a] From dielectric-response function, J. Ashley (private communication).

[b] From 61-MeV pion stopping-power measurements relative to H_2O of Nordin and Henkelman,[33] assuming $I_{H_2O} = 75.0$ eV.

[c] Painter *et al.*[39] give a value 62.2 eV from their dielectric-response function measurements. Thompson's[30] 267.5-MeV proton stopping-power measurements lead to a value of 52.5 ± 1.5 eV. The adopted value 57.4 eV is an average.

[d] Bichsel (private communication) has revised the Tschalär-Bichsel[50] value for PMMA (see footnote *f*) from 74.2 to 73.5 eV by applying z^3 and z^4 corrections. Our analysis of the Nordin-Henkelman data (see footnote *b*) gives a value 74.4 ± 4.7 eV. The adopted value, 74.0 eV, is an average.

[e] The value 68.7 eV is from Ashley's[40] measurement of the dielectric-response function. This value is close to the average of 71 ± 2 eV derived by Porter *et al.*[49] from proton stopping-power measurements at 2.2 - 5.9 MeV, and of 65.2 ± 1.9 eV derived from Thompson's measurements at 267.5 MeV.

[f] From range measurements of Tschalär and Bichsel[50] with 3- to 30-MeV protons.

[g] From stopping-power results of Bader *et al.*[47] for protons with energies between 300 and 400 keV.

[h] From range measurements of Barkas *et al.*[51] using various charged particles with equivalent proton energies up to 700 MeV.

TABLE 6. Mean excitation energies for atomic constituents of compounds.

ASSIGNMENT RULE 1 (gas)

Constituent	I (eV)
H	19.2
C	70
N	82
O	97

ASSIGNMENT RULE 2 (Condensed phase)

Constituent	I (eV)
H	19.2
C	81
N	78
O	106
F	112
Cl	180
Others	1.13 x I_{con}, where I_{con} is the I-value for the element in the condensed phase given in Table 3.

ASSIGNMENT RULE 3 (condensed phase)

(From the analysis of Thompson's data)

Constituent	Type of Bonding	I (eV)
H	saturated	19.0 ± 0.8
	unsaturated	16.0 ± 0.8
C	saturated	81.1 ± 2.5
	unsaturated	79.8 ± 2.3
	highly chlorinated	69.0 ± 3.7
N	amines, nitrates, etc.	105.7 ±10.6
	in ring	81.9 ± 7.0
O	-O-	104.6 ± 9.2
	O=	94.4 ± 4.9
Cl	all	179.7 ±11.9

TABLE 7. Dependence of the mean excitation energy on the phase of the medium.

Substance	Mean Excitation Energy I (eV)						
	Atomic gas (a)	Molecular gas (b)	Liquid (c)	Solid (d)	Ratios (b)/(a)	(c)/(b)	(d)/(a)
^{1}H	15.0	19.2	21.8		1.28	1.14	
^{6}C	62.0			78			1.26
^{7}N	76.9	82.0	90.5		1.07	1.10	
^{8}O	93.5	95.0	104.3		1.02	1.10	
^{13}Al	124			166			1.34
^{14}Si	132			173			1.32
^{22}Ti	182			233			1.28
^{26}Fe	226			286			1.26
^{29}Cu	274			322			1.18
^{32}Ge	292			350			1.20
H_2O		71.6	75.0			1.05	
C_3H_8, propane		47.1	52.0			1.10	
C_5H_{12}, pentane		48.2	53.6			1.11	
C_6H_{14}, hexane		49.1	54.0			1.10	
C_7H_{16}, heptane		49.2	54.4			1.11	

Inner-Shell Ionization and Stopping Power

K. Komaki
College of General Education, University of Tokyo
3-8-1 Komaba, Meguro-ku, Tokyo 153, Japan

For better understanding of various aspects in stopping phenomena such as Z_1^3-dependence, shell correction, geometrical effect, direction dependence etc., it seems to be helpful to examine theoretically and experimentally the elementary processes which include plasmon excitation, single electron excitation and inner-shell excitation/ionization. In the present, impact-parameter dependent stopping power will be discussed in connection with inner-shell ionization.

As long as the motion of the projectile can be treated by the classical theory, that is, the de Broglie wavelength is much smaller than the collision diameter, the notion of impact-parameter dependent stopping power is valid. In the field of the inner-shell ionization, many theories have been developed which give the impact-parameter dependent probability, P(b), of the inner-shell ionization. Among them, perturbed-stationary-state (PSS) treatment is a comprehensive theory which includes the effects of projectile deflection due to Coulomb field of the target atom, the polarization of the target atom and change in the binding energy due to the projectile ion and the formation of molecular orbitals during the collision. According to the PSS theory[1], the probability with which the projectile moving along the trajectory, $\vec{R}(t)$, with impact parameter, b, excite the target atom from i- to f-state is given by,

$$|a_{fi}|^2 = \frac{2Z_1^2 e^4}{\hbar^2 v_1^2(0)} |\langle f|M|i\rangle|^2 \tag{1}$$

and

$$M = \sum_{j=1}^{N} \exp[-iq_{fi}(b)z_j] K_0(q_{fi}(b)|\vec{r}_{\perp j} - \vec{R}_{\perp}(0)|) \tag{2}$$

where $v_1(0)$ is the projectile velocity at the closest approach and $K_\nu(x)$ is the modified Bessel function of the second kind. $|i\rangle$ and $|f\rangle$ are the eigenstates of the electrons in the target atom at the time of the closest approach, t=0, and are described by a fixed-time Schrödinger equation,

$$(H_a+V(t))u_m(t) = W_m(t)u_m(t) \tag{3}$$

where H_a is N-electron Hamiltonian of the target atom and V(t) is the interaction between the projectile and electrons. $\hbar q_{fi}(b)$ is the minimum momentum transfer,

$$q_{fi}(b) = (W_f(0)-W_i(0))/\hbar v_1(0). \tag{4}$$

The energy loss suffered by the projectile is given by,

$$\Delta E(b) = \sum_n (W_n(\infty)-W_0(-\infty))|a_{n0}|^2. \tag{5}$$

If we assume a scaling low,

$$W_n(\infty)-W_0(-\infty) = f(Z_1,Z_2,b)(W_n(0)-W_0(0)), \tag{6}$$

and replace the minimum momentum transfer, $\hbar q_{n0}(b)$, by an average one,

$$\hbar q(b) = I(b)/v_1 , \tag{7}$$

introducing an impact-parameter dependent mean ionization potential, I(b), then we have

$$\Delta E(b) = \frac{2Z_1^2e^4}{mv_1^2(0)} f^2(Z_1,Z_2,b) \int d\vec{r} q^2(b)\rho_0(\vec{r})$$

$$\times [K_0^2(q(b)|\vec{r}_\perp-\vec{R}_\perp(0)|)+K_1^2(q(b)|\vec{r}_\perp-\vec{R}_\perp(0)|)] , \tag{8}$$

using a similar derivation by Kitagawa and Ohtsuki[2]. Here, $\rho_0(\vec{r})$ is the ground-state electron density of the target atom in the presence of the projectile at the closest approach. This result is formally very close to that obtained by Kitagawa and Ohtsuki for a channeled ion moving along

a straight line, $R_{\perp}(t) = b$.

Values of $\Delta E(b)$ and $P(b)$ have been experimentally determined by measuring channeling stopping powers and by coincidence measurement of inner-shell X-rays and deflected projectiles. Comparison of these values with the theory will give detailed informations of stopping as well as inner-shell ionization mechanism.

1. G. Basbas, W. Brandt and R.H. Ritchie, "Perturbed-Stationary-State Theory of Atomic Inner-Shell Ionization by Heavy Charged Particles", Phys. Rev. A7 1971-1976 (1973).
2. M. Kitagawa and Y.H. Ohtsuki, "Quantum-Mechanical Treatment of the Abnormal Stopping Power for Channeling", Phys. Rev. B5 3418-3421 (1972).

PERTURBED STATIONARY-STATE DESCRIPTION OF THE POLARIZATION EFFECT IN INNERSHELL IONIZATION

George Basbas
Physical Review Letters
Post Office Box 1000
Ridge, N.Y. 11961

and

David J. Land
Naval Surface Weapons Center
White Oak, Silver Spring, Maryland 20910

Abstract

A one-parameter trial initial-state wavefunction correlated to a projectile (polarized) is described and used to calculate innershell ionization cross sections for collisions with heavy charged particles. The variational principle is used to determine the parameter. The minimized energy gives the binding effect as a function of projectile position. Existing codes can be readily adapted to incorporate the trial wavefunction. Comparison with the previous theory of the polarization effect is made. Results for K-shell ionization of titanium by protons in the 0.3 - 2.4 Mev energy range agree with measured values.

I. INTRODUCTION.

Over the past three decades the description of innershell ionization by heavy charged particles has advanced from the plane wave Born approximation [1], valid at projectile velocities greater than the mean orbital velocity of the target electron, to theoretical descriptions [2-6], valid at lower projectile velocities, which include the mutual perturbations between target and projectile which the

Born approximation omits.

We report a development in the treatment of the perturbation of the projectile upon the target state from which the ionizing transition takes place. Previous discussions of this influence have organized it into two effects [3]. One is the increase of the binding energy of the target electron which occurs when a slowly moving projectile is in the region of the innershell, and which reduces the cross section for ionization. The other effect is the distortion, or polarization, of the target-electron wavefunction by the field of the slowly moving projectile. This effect increases the cross section.

The effect of Coulomb repulsion [3,4], and the question of the importance of the description of the target atomic states (relativistic [4,7] or many-body wavefunctions [8] in place of the screened hydrogenic states used here), will not be treated here. Neither will the failure of the semiclassical description (or "energy loss" effect) [9] be considered.

The previous development of the polarization effect in innershell ionization [3] arose from the derivation of the Z_1-cubed or Barkas effect in the stopping of heavy charged particles in matter [10]. We apply perturbed stationary-state theory to innershell ionization to obtain cross sec-

tions influenced by the perturbation of the projectile on the wavefunction of the target electron [11]. The description of K-shell ionization by protons and alpha particles in this theoretical framework has already been reported by Land et al. [5]. The effect of binding and of Coulomb repulsion are included. The ''energy loss'' and relativistic effects are also taken into account.

This paper introduces a polarized wavefunction to describe the initial target state, and discusses its properties. We calculate K-shell ionization cross sections to compare with those obtained from the original theory of the polarization effect [3], and to compare with experiment [12].

II. PERTURBED STATIONARY-STATE THEORY.

In the theory of perturbed stationary states [11] the expression for the probability for a transition from state i to state f, when the the atom is initially in unperturbed state $u_i[R(-\infty)]$, is

$$P_{fi} = \left| \int_{-\infty}^{\infty} dt\, e^{i/\hbar \int_{-\infty}^{t} dt' W_{fi}(t')} \frac{\langle u_f[R(t)] \left| \left(\frac{\partial V(t)}{\partial t} \right) \right| u_i[R(t)] \rangle}{W_{fi}(t)} \right|^2 \qquad (1)$$

where $W_{fi}(t) = E_f[R(t)] - E_i[R(t)]$ is the energy separation

between the two states. The interaction between the projectile, with atomic number Z_1, and the target electron is

$$V(t) = \frac{-Z_1 e^2}{|\underline{R}(t) - \underline{r}|}. \tag{2}$$

The states $u_i[R(t)]$ and $u_f[R(t)]$, with eigenvalues $E_i[R(t)]$ and $E_f[R(t)]$, are eigenfunctions of the total Hamiltonian

$$H(t) = H_a + V(t). \tag{3}$$

The Hamiltonian for the unperturbed atom is denoted H_a and has eigenfunctions $u_i[R(\pm\infty)]$ and $u_f[R(\pm\infty)]$.

In this basis the projectile is a static charge fixed at position $\underline{R} = \underline{R}(t)$ for the purpose of defining adiabatically perturbed atomic states. The electron coordinate is $\underline{r}$. The dynamics of the transition induced by the collision are contained in the expression for the transition probability, Eq. (1). In the calculation the projectile coordinate $\underline{R}(t)$ varies with time according to a prescribed trajectory, and the atomic basis states are changed adiabatically to adjust to each new projectile position.

For the sake of illustration we consider K-shell ionization and represent the unperturbed atomic states by screened-hydrogenic wavefunctions for convenience. The form of the polarized wavefunction introduced below makes it easy to adapt existing codes to include polarization regardless

of the choice of unperturbed atomic wavefunctions. As in all past approaches, the final atomic state is represented by an unperturbed wavefunction.

III. POLARIZATION.

A trial polarized wavefunction is introduced for the ground state $u_i[R] \longrightarrow$ trial $\Psi \equiv \Psi_{POL}(\underline{r};\underline{R})$, where

$$\Psi_{POL}(\underline{r};\underline{R}) = N(R)\left[e^{-Z_1|\underline{R}-\underline{r}|} + f(R)\right]\Psi_{2K}(Z_2) \tag{4}$$

and

$$\Psi_{2K}(Z_2) = 2 Z_2^{3/2} e^{-Z_2 r}/\sqrt{4\pi}\,. \tag{5}$$

The target atomic number is Z_2, the unit of length is the Bohr radius (1 a.u.) and $u_i[R(t\to\infty)] = \Psi_{2K}(Z_2)$. The variational parameter f(R) is determined by minimizing the expectation value of the total Hamiltonian for each value of R. The normalizing factor N(R) is chosen to give the usual unit normalization. The following properties of this trial wavefunction are noteworthy:

1). $\Psi_{POL}(\underline{r};0) = \Psi_{2K}(Z_1+Z_2)$.

The form of the trial wavefunction guarantees it to be an exact eigenfunction of the total Hamiltonian in

the united-atom limit. This feature is not contained in the description obtained from a two-center linear combination of atomic orbitals.

2). $\Psi_{POL}(\underline{r};\infty) = \Psi_{2K}(Z_2)$.

The trial wavefunction is guaranteed to be an exact eigenfunction of the total Hamiltonian in the separated-atom limit. In this limit the probability of finding the electron in the vicinity of the projectile is zero. The chosen form describes a perturbed adiabatic ground state which relaxes to the initially unperturbed state when the projectile is removed.

3). Explicit correlation with the projectile is made via the polarization term $e^{-\bar{z}_1|\underline{R}-\underline{r}|}$ which is in the form of a hydrogenic wavefunction for the electron centered on the projectile.

4). If the perturbation is removed ($Z_1 = 0$) the unperturbed atomic state, $\Psi_{2K}(Z_2)$, is recovered.

The variational principle guarantees the proper behavior of the parameter f(R) in the limiting cases given in 1), 2) and 4) above.

IV. EFFECT OF POLARIZATION ON WAVEFUNCTION AND ENERGY.

We discuss the influence of the projectile on the K-shell wavefunction. Its presence causes a slight asymmetry of the exponential hydrogenic wavefunction along the reference line joining projectile and target nucleus. Values of the wavefunction are increased along the reference line, and decreased along the line 180 degrees from it. A peaking relative to the exponential decline occurs and is centered on the position of the projectile.

The influence of the projectile on the binding energy of the target electron (binding effect) is contained in the variation of the expectation value of the total Hamiltonian with projectile position R. A smooth transition from the united-atom value to the separated-atom value occurs in a way reminiscent of molecular-orbital energy diagrams. Identical values of the binding energy shift are obtained for a trial wavefunction in the form of the hydrogenic wavefunction by varying the charge (Z_2 in $\psi_{2K}(Z_2)$, Eq. (5)). This trial wavefunction also has correct united- and separated-atom forms, but not the asymmetry of the polarized wavefunction. The asymmetry does not affect the binding energy, apparently because both the united- and separated-atom limits are correct. The minimization principle varies the parameter in each wavefunction to give essentially the same energy. In this sense the influence of polarization

(the asymmetry) on the ionization process, to be described below, is separate from the binding effect.

V. IONIZATION CROSS SECTION.

The previous theory of the polarization effect [3] has been evaluated for K-shell ionization of titanium by protons in order to make a comparison with the present theory. Our evaluation uses a computer code [5] adapted to include the polarization phenomena. Both theories include Coulomb deflection and binding effects. The influence of the relativistic and ''energy loss'' effects on the cross sections are negligible for this system at the energies over which comparison is made. The agreement between the theories confirms the approach used previously [3] which was derived outside of a formal scattering theoretic framework. The details of how and why polarization diminishes at low velocities in our approach has yet to be studied.

VI. POLARIZATION IN MEASUREMENTS OF K-SHELL IONIZATION.

Comparison of calculations of the polarization effect on K-shell ionization can be made with the data of Brown et al. [12] for 0.3 to 2.4 MeV protons bombarding titanium. Calculations with and without polarization show that where the results differ, the measurements are consistent with the existence of a polarization effect. When the polarization

effect diminishes, the data depart from theoretical predictions in ways which are not now understood. Both calculations include binding, Coulomb deflection, relativistic, and ''energy loss'' effects.

VII. SUMMARY AND CONCLUSION.

The polarization effect in the excitation of inner-shells by heavy charged particles can be described by a trial wavefunction for the initial state. The asymmetry induced in the wavefunction by the correlation with the projectile increases the ionization cross section. The magnitude of this effect on the cross section is identical to the prediction of the previous treatment of the polarization effect. Incorporation of this polarization effect into recent calculations for K-shell ionization of titanium by protons correct the cross sections to produce agreement with recent measurements in the incident velocity regime where the effect of polarization is significant. We conclude that the description of the perturbing influence of the projectile of the target state is accurately and conveniently described by a trial polarized wavefunction.

ACKNOWLEDGEMENTS

One of us (GB) thanks the Naval Surface Weapons Center for hospitality and for making possible this collaboration. This work was supported by the Independent Research Program of the Naval Surface Weapons Center.

REFERENCES.

[1] E. Merzbacher and H. W. Lewis, in Encyclopedia of Physics (ed. S. Flugge, Springer-Verlag, Berlin, 1958) Vol. 34, pp. 166.

[2] A. L. Ford, E. Fitchard and J. F. Reading, Phys. Rev. A 16, 133 (1977); G. L. Swafford, J. F. Reading, A. L. Ford and E. Fitchard, Phys. Rev. A 16, 1329 (1977).

[3] G. Basbas, W. Brandt, R. Laubert, Phys. Rev. A 17 1655 (1978).

[4] W. Brandt and G. Lapicki, Phys. Rev. A 20, 465 (1979).

[5] D. J. Land, M. D. Brown, D.G. Simons and J. G. Brennan, Nucl. Instr. and Meth. 192, 53 (1982).

[6] J. U. Andersen, E. Laegsgaard, and M. Lund, Nucl. Instr. and Meth. 192, 79 (1982).

[7] P. A. Amundsen and L. Kocbach, J. Phys. B 8, L122 (1975); M. Pauli, F. Rosel and D. Trautmann, J. Phys. B 11, 2711 (1978).

[8] G. Basbas, W. Brandt, R. Laubert, Phys. Rev. A 7 983 (1973); J. F. Reading, A. L. Ford, M. Martir and R. L. Becker, Nucl. Instr. and Meth. 192, 1 (1982).

[9] G. Basbas, Summary Report of the Informal Workshop on the Penetration of Low-Energy Particles, p.319, New York University, 1979; W. Brandt and G. Lapicki, Phys. Rev. A 23, 1717 (1981); R. K. Rice, F. D. McDaniel, G. Basbas and J. L. Duggan, Phys. Rev. A 24, 758 (1981).

[10] J. C. Ashley, R. H. Ritchie and W. Brandt, Phys. Rev B 5, 2393 (1972).

[11] G. Basbas, W. Brandt, R. H. Ritchie, Phys. Rev. A 7 1971 (1973).

[12] M. D. Brown, D. G. Simons, D. J. Land and J. G. Brennan, Phys. Rev. A 25, (June) (1982).

Empirical Stopping Powers for Ions in Solids

J. F. Ziegler, J. P. Biersack, and U. Littmark
IBM - Research
Yorktown, New York
10598 U.S.A.

ABSTRACT

The work of Brandt and collaborators on low energy ion stopping powers has been extended to create an empirical formulation for the stopping of ions in solids. The result is a simple computer program (about 60 lines of code) which calculates stopping powers from zero to 100 MeV/amu for all ions in all elemental solids. This code has been compared to the data in about 2000 papers, and has a standard error of 9% for energies above 1 keV/amu.

This approach includes high energy relativistic effects and shell-corrections. In the medium energy range it uses stopping theory based on the local-density approximation and Lindhard stopping in a free electron gas. This is applied to realistic Hartree-Fock charge distributions for crystalline solids. In the low energy range it uses the Brandt concepts of ion stripping relative to the Fermi velocity of solids, and also his formalism for the relation of projectile ionization to its effective charge.

The details of the calculation will be presented, and a broad comparison will be shown with experiment. Special comparative examples will be shown of both the low energy stopping power oscillations which depend on the atomic number of the ion, and also of the target.

This paper will review the three primary subjects which have led to a simple accurate code for the stopping of ions in solids at all energies. First there will be a review of the development of a universal nuclear stopping calculation based on the work of Wedepohl[67a] and the enhancements introduced by Wilson,Haggmark and Biersack[77a]. Then a review will be made of a universal low energy electronic stopping calculation based on the ideas of Lindhard[54a], and Brandt and collaborators[75a,81a-d]. Finally these two stopping powers are combined and compared with the experimental results of 900 papers, including those showing the pronounced Z_1 (ion) and Z_2 (target) oscillations in stopping power at constant ion velocity.

Nuclear Stopping Powers

About 1960 there was extensive theoretical work on the energy loss of an energetic ion to target atoms based on the work of Firsov[57a-b,58a-b,59a] and Lindhard et al.[63a]. These works laid the ground work for most later nuclear stopping calculations. These original studies were based on the Thomas-Fermi model of the atom, which led to erroneous results for collisions in solids between widely separated atoms since the Thomas-Fermi model has an unrealistic long tail of charge. This leads to the calculation too great of stopping powers, and too shallow of ion ranges in solids. A more realistic diatomic potential in a solid would drop to zero rather sharply for atomic separations much greater than about one Angstrom, thus reducing atomic scattering at larger impact parameters.

Extensive work has been done in the last ten years on realistic Hartree-Fock atomic distributions and we have used those calculated by Moruzzi et al.[78a]. In this book the authors treat only 26 solids and we have used their approach to create charge-distributions for all 92 elements in their normal crystallographic form. For normal gases, we have used their most thermodynamically stable solid structure, for these shapes will be useful as a first approximation in calculating the stopping power of compounds, such as Al_2O_3. This procedure has been described in Ref. 80a.

For the charge distribution of the ions, it was decided to use the same charge distribution as for its elemental solid. This was done because (a) target polarization by the ion reduces the effective spatial charge distribution of the ion, and this is better accounted for by solid state distributions than isolated atom distributions, and (b) this makes the calculation reversible and , for example, the interatomic potential of Ni on Ag is the same as Ag on Ni.

The interaction between atoms can be evaluated reasonably well by introducing corrections based on physical data such as phonon distribution curves, elastic constants, compressibility, etc. as reviewed by Johnson[73a]. This approach is not universally applicable, in part because of lack of data, and further it is not very accurate for rather hard collisions. On the other hand, there is the quite complex approach which is known as the multiconfigurational self-consistent-field method which is quite accurate, but which consumes so much computer power that it is prohibitively expensive. However, Wilson et al. showed[77a] that an accurate approximation to this elaborate calculation is the method of Wedepohl[67a] which is called the free-electron method of interatomic potentials. This consists of first calculating the Coulomb interaction energy, V^k, of the collision for any impact parameter (allowing no change in the electron spatial distribution during the collision). Then, in the volume of space in which the two atom's electron distributions overlap, the electrons are allowed to absorb energy, V_k, in excitation. This is done by considering this volume to be a free electron gas, and calculating the difference in energy between the two isolated overlap distributions, and the same number of electrons compressed together into the overlap

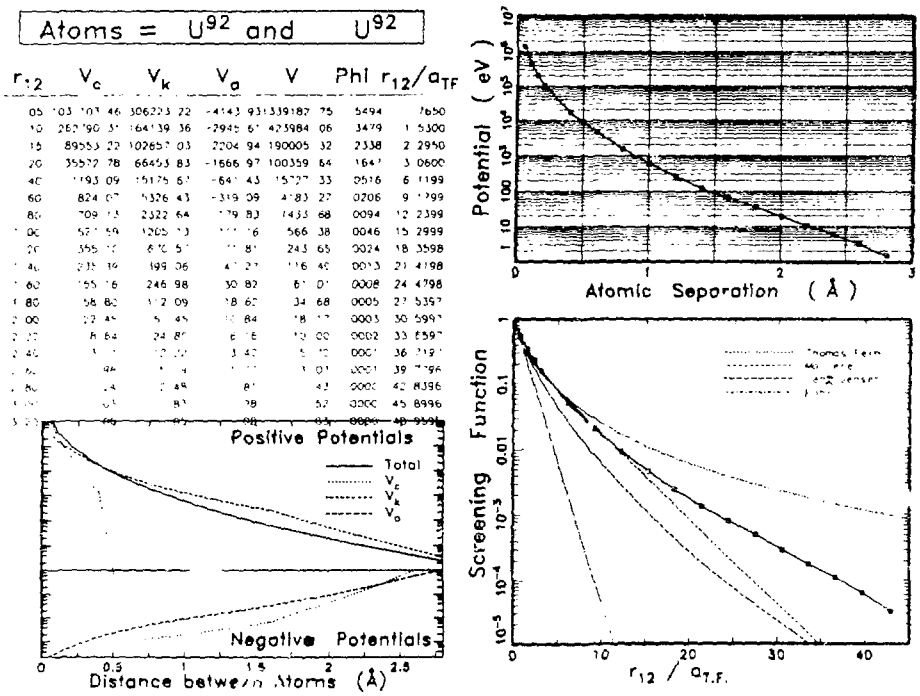

Figure 1

volume. For this overlap region, the free electron gas energy must be decreased because of exchange energy, V_a, because the electrons are not randomly distributed, since their density is affected by the exclusion principle regarding spin.

The results of this type of calculation of interatomic potentials are shown in Figure 1, for the case of U^{92} and U^{92}. In the upper left are shown the values of the various potentials for increasing nuclear separation distances, r_{12}, in units of Angstroms. The various potentials are described in the text and are known as V_c, the Coulomb interaction; V_k, the electron excitation energy; V_a, the exchange energy between electrons; and V, the total interaction, $V_c+V_k+V_a$, in units of eV. The next column labeled "Phi" is called the screening function, and is the summed potential divided by the potential of the two bare nuclei at the same separation without any electron screening. This screening function goes from unity (at zero separation) to zero at the point where both atoms are totally separate and completely screened from each other. The final column of tabulated numbers is labeled r_{12}/a_{TF}, which is the atom separation, r_{12}, reduced after the manner of LSS theory by the Thomas-Fermi screening distance of the two atoms. This final unit is useful in comparing these results with traditional potentials based upon statistical models of the atoms such as the Thomas-Fermi atom.

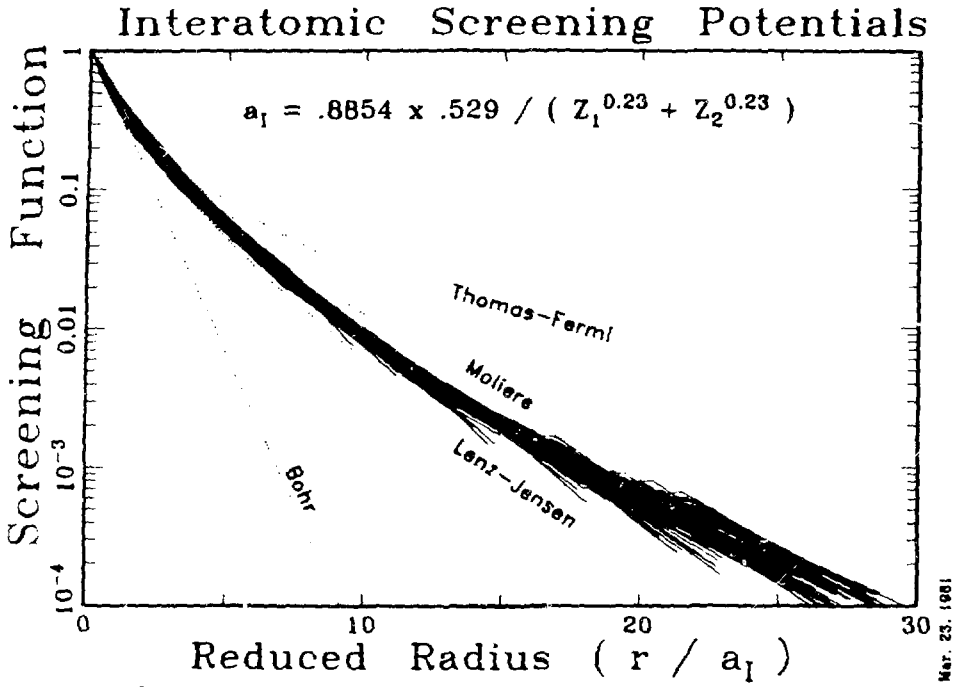

Figure 2

The lower left plot shows the four potentials tabulated above. Of particular interest is how the Coulomb energy goes from repulsive to attractive as a function of interatomic separation. Note further that the total potential, V, shown as a solid curve, is greater than any of its components for small separations, but once the Coulomb potential goes negative is becomes less than V_c. This plot also shows the relative magnitudes of the various contributions, and how they all are significant. The upper right figure shows the final interatomic potential in the physical units of eV versus Angstroms. The lower right figure compares this calculation with those using traditional models such as the Thomas-Fermi, the Moliere, the Lenz-Jensen and the Bohr. The radial separation units are the reduced units based on LSS theory as described above, and it can be seen that the U-U atom potential lies about half-way between the Thomas-Fermi and the Moliere potentials. Other potentials are usually less than this, and they range all the way down to lying between the Bohr and Lenzl/Pb/en potentials for He on He.

The calculation of interatomic potentials was completed for about 500 of the possible 8100 ion-target combinations, chosen at random. The purpose of our interatomic potential calculations was to try to attempt to find a new, more accurate way, to calculate interatomic potentials in a simple algorithm, since each of these individual calculations consumed significant computer time, and it would be prohibitively expensive to repeat the calculation every time it was needed. Merely doing them once for all ion-target combinations, and fitting the resultant potentials, would yield an unwieldily database of about 50,000 numbers. Attempts were made tc fit the individual interatomic potential components as suggested by Biersack, but since we were using Hartree-Fock atoms the potentials did not fit any systematic description which we could find. Finally, we hit

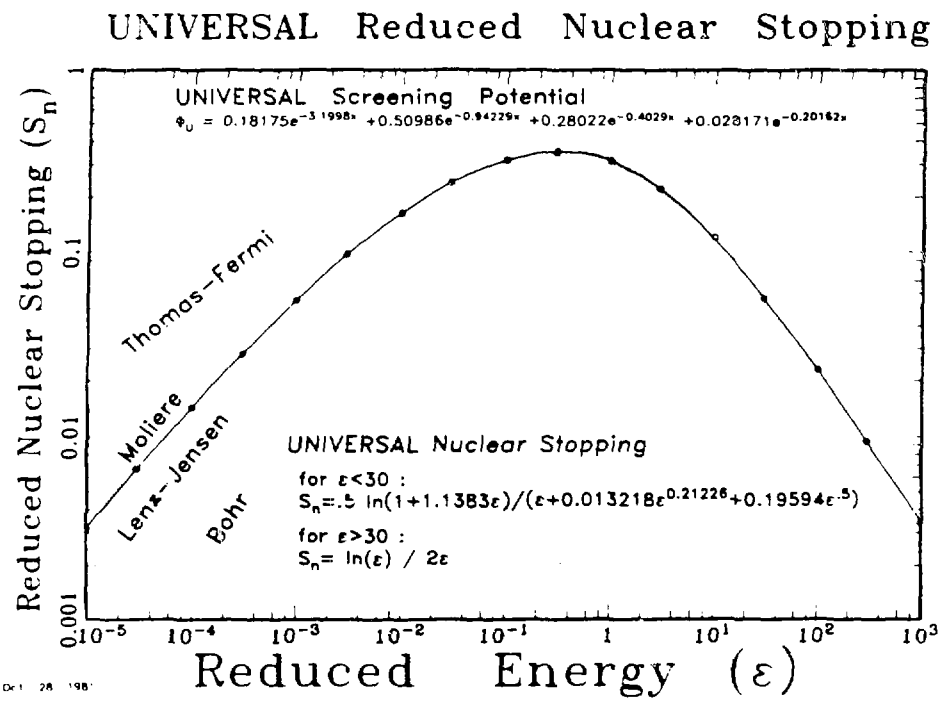

Figure 3

upon a surprisingly accurate method based on the Bohr concept of introducing a reduced radius. This is shown in Figure 2, where all 500 interatomic screening functions are plotted in the reduced radial coordinates shown. The rms average of these potentials can be fitted by the equation:

$$\Phi_u = 0.1818e^{-3.2x} + .5099e^{-.9423x} + .2802e^{-.4029x} + .02817e^{-.2016x}$$

Where the reduced radial coordinate, x, is defined as :

$$x = .8854\ a_o / (Z_1^{0.23} + Z_2^{0.23}),$$

where a_o is the Bohr radius, .529 Angstroms. This algorithm has an rms accuracy of about 16% for all potentials above 2 eV.

This universal interatomic potential can now be used to evaluate the nuclear stopping power of an ion in a solid. The potential is integrated over all impact parameters, and the result is shown in Figure 3 using LSS reduced coordinates of energy loss versus ion energy. The result is somewhat similar to that of Wilson et al.[77a] which they identified as the result of the collision of the carbon-krypton system. In the upper part of the figure is shown the form of the screening potential used in the calculation. The nuclear stopping results are shown as small dots on the figure. Through these values a curve was fitted, and it is shown as the

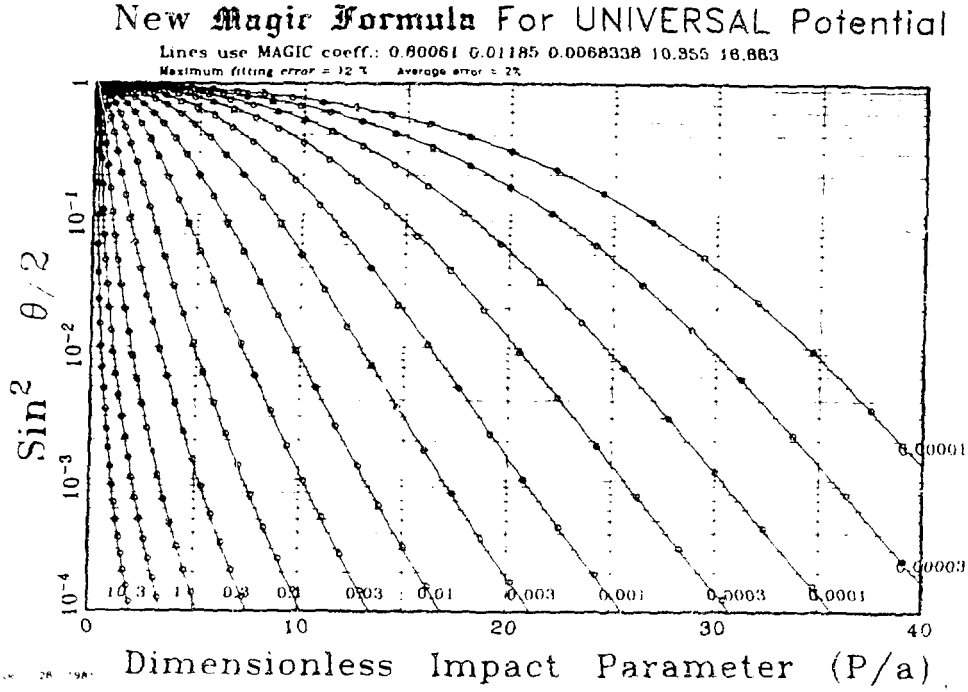

Figure 4

solid line. The accuracy of the fit was better than 1%. The formula used is shown in the lower part of the figure. Also shown are the nuclear stopping curves based on various statistical models of the atom.

The universal interatomic potential can also be used in the Magic Formula as constructed by Biersack and Haggmark[80a]. This formula allows the quick calculation of the angle of deflection of an energetic screened atom colliding with another, based on the incident energy and the impact parameter. This Magic Formula is invaluable in Monte-Carlo calculations in that it speeds up this calculation by a factor of 1000x. We have used the universal screening potential to calculate by complete numerical integration of the orbit equations the final angle of scatter, and these are shown in Figure 5 as dots for the values of reduced energy indicated, ranging from .00001 to 10. These have been fitted with the Magic Formula and the coefficients are shown at the top of the figure. The values of the scattering angle vs. impact parameter has been then calculated using the Magic Formula and the results are shown as solid lines. The accuracy of the Magic Formula to the detailed scattering calculations is about 2%.

The Electronic Stopping of Ions in Solids

Our approach for the electronic stopping of ions in solids is based fundamentally on the Lindhard formalism of the stopping of a particle by free electron gas[54a]. This approach then must be modified by the screening of the ion by its electrons and by its ionization into large charge states by the interaction of the solid on the ions's electrons. Bohr suggested that this stripping of the projectile's electrons could be approximated by assuming that all electrons with classical velocities below the ion's velocity would be stripped. Lindhard suggested that the shielding of the ion by its electrons could be resolved in the Thomas-Fermi model using the TF screening distance.

Recently, Brandt has suggested that the Bohr concept should be revised to include the fact that the electron gas of the solid has itself an intrinsic velocity, and that the electrons which are stripped should be relative to the Fermi velocity of the solid. He has detailed this concept is a series of papers[81a-d]. Ferrell and Ritchie have recently considered the screened potential of an ion and its effect on the ion-solid interaction. They have developed a formalism which is more general than the previous Lindhard approach in that it is not as specific to a given atomic model, such as the Thomas-Fermi in the Lindhard case. This new approach allows for the screening to be used on more general electron distributions, especially that of the shape of e^{-r}/r.

Brandt has also proposed the new concept that the charge-fraction of an ion is dependent only on the ion's reduced velocity, and not on its atomic number. That is, the fraction of the charge left on a Ne ion is the same as that on a Pb ion at the same reduced velocity in the same target. Although this is hard to swallow as a prime condition, it then allows the development of a new formalism which is very powerful in predicting the electronic stopping powers. For Brandt has pointed out that this "charge-fraction" of an ion is not physically important, what is important is the screening of the ion. And each ion will be screened differently by its electrons even at the same velocity. And so it is the screened ion which gives the concept of "effective charge", not the charge fraction.

To clarify these points, consider a large ion penetrating through a target. It has been stripped of some of its ions, and those remaining are distributed in space, screening the nuclear charge. However, the theorist is most comfortable with a point charge, penetrating through a free-electron gas medium. To go from the pure point charge to the lumbering broad partially stripped ion we need a formalism of an effective charge. This effective charge concept is developed so that we may use this charge as an equivalent point charge in the well developed point-charge approach to get stopping powers. So the effective charge includes in it both the ionization level of the ion and the screening of the nucleus by the electrons.

The effective charge as developed by Brandt first assumes that all ions are ionized to the same fraction at the same reduced velocity. Then approximating the ion by an exponential screening function, he can extract a screening length. From this, the effective charge is determined by considering the effect of the screening on the energy loss to the electron-sea of the solid.

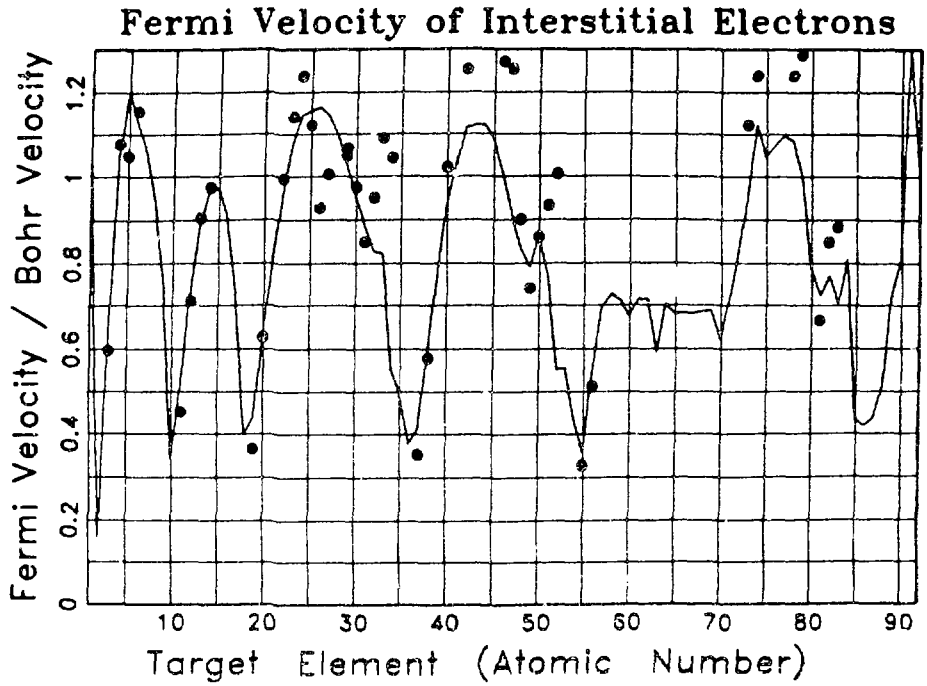

Figure 5

In practice, a factor must be adjusted for the ionization level of the projectile ion. This factor is small, and does not change much in nearby atomic numbers, and ranges from about 1 to 1.5. Since this is the only free parameter in the calculation of electronic stopping powers, it heroically must swallow all the other approximations also.

Empirical Ion Stopping Powers

The nuclear stopping power of ions in solids is taken directly from the preceding discussion of universal interatomic potentials. There are no free parameters in these values.

The electronic stopping powers are developed using the framework of Bohr, Lindhard, Brandt and Kitchie as discussed before. The main steps are shown in Figures 5 - 7. First, it was necessary to develop a method of calculating the Fermi velocities of all solids. This is not rigorously possible, since either real or Hartree-Fock solids do not have a single well defined Fermi-velocity, and this concept is most useful only in statistical models of the atom. But one may redefine the Fermi velocity both theoretically and experimentally. If one looks at the transmission of electrons through a thin foil, the energy loss of the beam will have a large peak at certain electron energies. One may define the Fermi velocity of the solid as that corresponding to a free electron gas which has its maximum interaction at that energy. This approach was used by Isaacson and Brandt[29a] to deduce Fermi velocities of many solids from photon and electron absorption experiments. From a theoretical view, one may take a Hartree-Fock solid and isolate the interstitial electrons, i.e. those

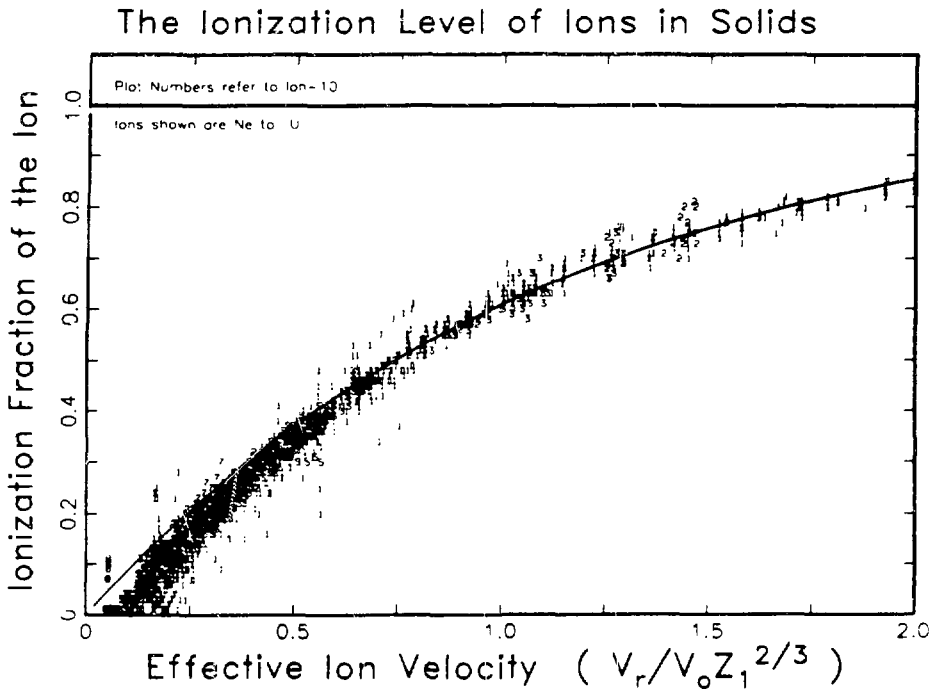

Figure 6

outside the muffin-tin spherically symmetric distributions. Then it can be hypothesized that these electrons constitute the free electrons of the solid, and by considering their local density, the Fermi-velocity of the solid can be determined. Both of these approaches are shown in Figure 5.

The Fermi velocities of all elemental solids are shown in Figure 5 in units of the Bohr velocity. The solid dots are the values derived by Isaacson and Brandt[79a] from photon and electron transmission experiments (see text). The solid line indicates the values we have calculated from Hartree-Fock solids considering only the interstitial electrons. The two results are remarkable consistent, with a mean deviation of 9%. In our work we have used the experimental numbers where they are available, and the theoretical numbers elsewhere.

Figure 6 shows the ionization fraction of ions in solids as suggested by Brandt et al. vs. the reduced ion velocity. Using the Brandt approach it is possible to go from experimental stopping powers to the ionization fraction of the ions, which he states is independent of ion. He has published similar curves, but this figure contains many more data points. The solid line is Brandt's suggested curve.

For ions lighter than Ne (excluded from this plot) the tight bunching of the data points disappears. For ions of atomic number of 10-92, there is a tight bunching which reasonably follows Brandt's curve above about 0.7. Below this there is a small divergence. The divergence can be accounted for by adjustments of the ion screening length, which is called

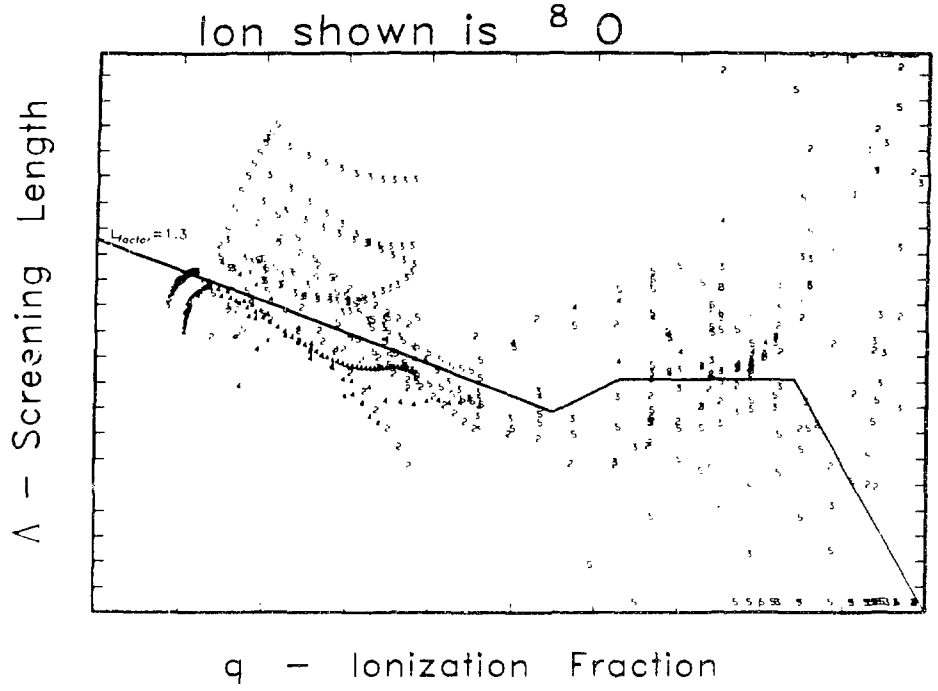

Figure 7

Lambda in Brandt's papers. In order to adjust this screening length, it is first necessary to obtain a new ionization fraction curve which goes through the data points. Once this is done it is possible to adjust the ion screening length.

In Figure 7 is shown the screening length, Lambda, versus the ionization fraction for ions of oxygen in all solids. The data show various solids by plotting their atomic number divided by ten for the data point. The solid line is the Brandt screening factor, multiplied by the factor of 1.3 as noted on the figure's left margin. The bump in the solid line is the additional screening due to inner shell electrons.

A comment is necessary on Figures 6 and 7. The parameter which is found is the screening length of the ion, which is independent of the target. However, this length comes from an assumption of the ionization fraction vs. velocity as shown in Figure 6. These two things circle each other, and either can be varied and accounted for by the other. Thus, the data can be brought up to the original Brandt curve by suitable adjustment of the correction factor on the screening length. Or the reverse can be adjusted: the ionization versus velocity curve could be adjusted to reduce the magnitude of the screening correction factor.

The final empirical stopping powers of ions in solids are now possible to assemble from the various components. First one starts with a data-base of proton stopping powers in all elements. These have been assembled over

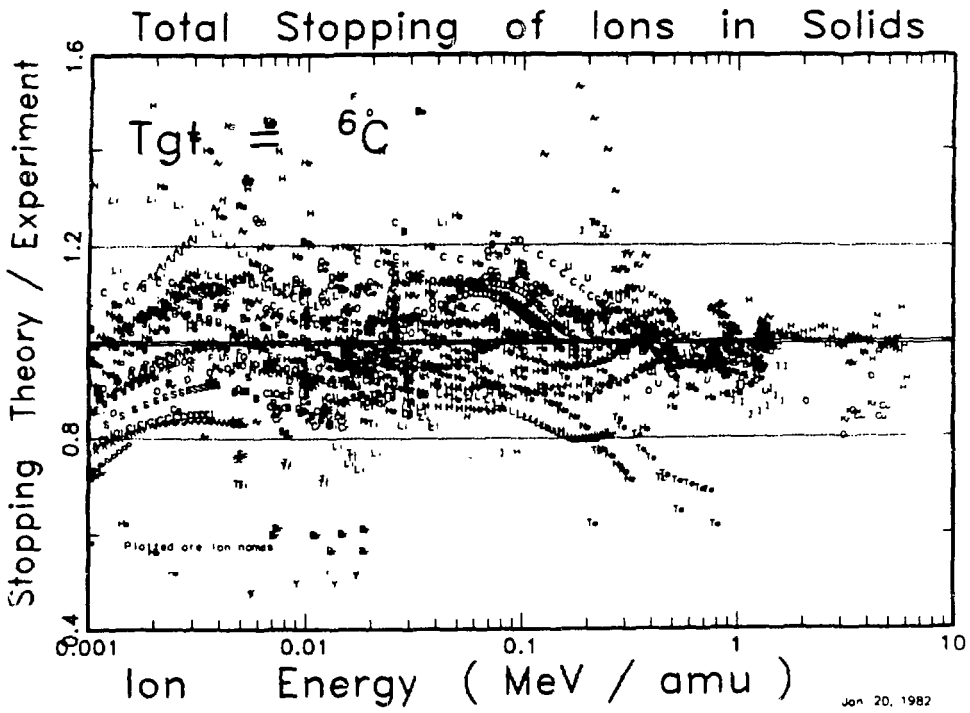

Figure 8

severalyears by techniques outlined in Ref. 77c, where the data-base of hydrogen and helium experimental stopping powers has been combined with calculations based on the Lindhard stopping in a free-electron gas to get stopping powers accurate to about 10% above the energy of 80 keV/amu. These were then extended to 20 keV/amu by using values predicted by the ENR theory[81e] and any experimental data. Below 20 keV/amu the stopping powers were assumed to go as $E^{.45}$ as suggested by an analysis of a great number of stopping measurements[77b,c].

The second item which is calculated is the effective charge of the ion, which is calculated using the Brandt approach, modified as shown in Figures 6 and 7. Finally, the nuclear stopping power is calculated.

Typical results are shown in Figure 8, which shows the ratio of the predicted stopping power to the experimental stopping power for all ions in carbon. A carbon target is shown because there is more data for ion stopping in carbon than in any other material because thin target foils of carbon are readily obtainable in accelerator laboratories. Plotted are the ion names. The accuracy of the predicted stopping powers is about 10%, which is remarkable since this is about the variation of stopping in carbon just due to its method of fabrication. And this source of error is combined with the fact that carbon greatly absorbs gases, especially water vapor, which can cause erroneous stopping power measurements.

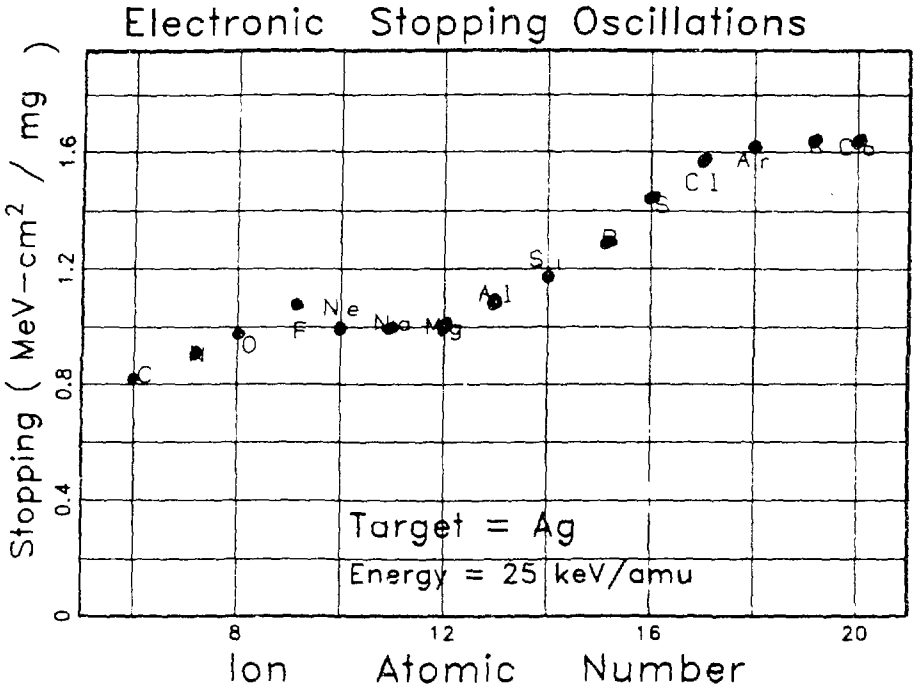

Figure 9

Finally, in Figure 9, is shown the stopping of various ions in Ag at the Bohr velocity[77e]. The predicted values are shown as letters identifying the ions. The values of Ward et al. are shown as dots. The agreement is good. The work on stopping power oscillations of ions in solids appears to be a measurement of the screening function of the ion. Similarly, the change of the degree of oscillation from target to target is a measure of how much interaction there is between the conduction electrons of the solid on the degree of ionization of the ions.

In conclusion, a simple accurate algorithm has been developed to calculate the stopping powers of ions in solids. It is mostly derived from theory, with the following major exceptions: (a) the proton stopping powers are a mix of theoretical values with about 12,000 experimental data points; (b) the Fermi-velocity of a solid is assumed to be that of the interstitial electrons; (c) the screening function of the ion by the solid is adjusted by a single constant which depends only on the ion and not on the solid. This constant ranges from 1 to 1.5, and enters into the calculation only as the argument of a logarithm, so it is not very important.

The final accuracy of the stopping powers have a standard error of 2% for energies above 1 MeV/amu, 4% for energies above 80 keV/amu, and 9% for energies below 80 keV/amu.

A copy of the stopping power program may be obtained from the author.

REFERENCES

54a : J. Lindhard, K. Dan. Vidensk. Selsk. Mat. Fys. Medd., Vol.28, (1954).
57a : O. B. Firsov, Zh. Eksp. Teor. Fiz., Vol. 32, 1464 (1957).
57b : ibid, Vol. 33, 696 (1957)
58a : ibid, Vol. 34, 447 (1958).
58b : ibid, JETP, Vol. 7, 308 (1958).
59a : ibid, JETP, Vol. 9, 1076 (1959).
63a : J. Lindhard, M. Scharff and H. E. Schiott, Mat. Phys. Medd. Dan. Vid. Selsk., Vol. 33, 1 (1963).
67a : P. T. Wedepohl, Proc. Phys, Soc., Vol. 92, 79 (1967).
73a : R. A. Johnson, J. Phys. F, Vol. 3, 295 (1973).
75a : W. Brandt, Atomic Collisions in Solids, Plenum Press, Vol. 1, 261 (1975).
77a : W. D. Wilson, L. G. Haggmark and J. P. Biersack, Phys. Rev., 15B, 2458 (1977).
77b : H. H. Andersen and J. F. Ziegler, "Hydrogen Stopping Powers and Ranges in All Elements", Pergamon Press (1977).
77c : J. F. Ziegler, "Helium Stopping Powers and Ranges in All Elemental Matter", Pergamon Press (1977).
77d : T. L. Ferrell and R. H. Ritchie, Phys. Rev., 16B, 115 (1977).
77e : D. Ward, H. R. Andrews, I. V. Mitchell, W. N. Lennard and R. B. Walker, Can. J. Phys., Vol.57, 645 (1979).
78a : V. L. Moruzzi, J. F. Janak and A. R. Williams, "Calculated Electronic Properties of Metals", Pergamon Press (1978).
80a : J. F. Ziegler, "Handbook of Stopping Cross-sections for Energetic Ions in All Elements", Pergamon Press (1980).
80b : J. P. Biersack and L. G. Haggmark, Nucl. Inst. and Meth., Vol. 174, 257 (1980).
81a : S. Kreussler, C. Varelas and W. Brandt, Phys. Rev. 23B, 82 (1981).
81b : A. Mann and W. Brandt, Phys. Rev. 24B, 4999 (1981).
81c : M. Kitagawa and W. Brandt (unpublished).
81d : W. Brandt, to be published in Nucl. Inst. and Meth., Vol. 191 (1982).
81e : P. M. Echenique, R. M. Nieminen and R. H. Ritchie, Sol. St. Comm., Vol. 37, 779 (1981).

Stopping Power of Rare Gases in Amorphous Silicon for MeV Helium Ions

F. Fujimoto, K. Komaki and A. Ootuka
College of General Education, University of Tokyo
K. Kawatsura and K. Ozawa
Japan Atomic Energy Research Institute
T. Shimada and Y. Katayama
Hitachi Central Research Laboratory

The stopping cross sections of argon, krypton and xenon inside amorphous silicon for α-particle, in which the concentrations of argon, krypton and xenon were 8,7, and 4 at %, respectively, were measured by the RBS method in the incident energy range from 1.0 to 2.6 MeV for argon and 1.0 to 1.6 MeV for krypton and xenon. If we use the stopping cross section of silicon given by Ziegler and assume Bragg's rule, the obtained values of each rare gas were about 30% lower than those for gaseous state given by Ziegler in the energy region near to 1 MeV.

§1. Introduction

The stopping powers of matters for energetic ions play important roles in the ion beam analysis, and were measured by many workers. Ziegler and Andersen collected these observed values of the stopping cross sections and predicted the most probable ones of all elements in solid and gas states for proton[1] and helium ion.[2] According to their results, the stopping cross sections vary with the physical state and are independent of the chemical state.

The stopping cross sections of compounds and mixtures can be calculated by the Bragg's rule by using those of constituent elements. However the validity of the rule are not always consistent and the chemical effect could contributes to the stopping cross section in some cases.[3-5]

Atoms of rare gases have no valence electrons. Therefore it is considered that there are no chemical effects on the stopping power, even if the atoms are located inside a solid. The stopping powers of argon gas

and solid for helium ions have been measured by Chu and Powers[6], Chu et al.[7], and recently by Besenbacher et al.[8] and Besenbacher et al.[9]. The values of gaseous and solid states observed by Besenbacher[8,9] agreed well with those for gaseous state predicted by Ziegler[2].

In the present paper, we study the stopping cross section of rare gas atoms inside amorphous silicon for helium ions with the energy from 1.0 to 2.6 MeV, using the RBS method similar to that done by Feng et al.[3]

§2. Experiment and data treatment

To avoid the channeling effect, an amorphous silicon layer was, at first, deposited on a slice of silicon crystal by electron bombardment. The base and operating pressures of the chamber were 3×10^{-11} and 2×10^{-9} Torr, respectively. The rate of deposition was about 1 Å/sec and a high purity silicon crystal made by the FZ method was used as the deposition material. The thickness of the layer was about 2000 Å. On the amorphous silicon layer the amorphous silicon layer including argon, krypton or xenon was deposited by the sputtering in argon, krypton or xenon gas which was purified from 5 nines one by using porous titanium heated up to about 1000°C. The base pressure of chamber was 2×10^{-7} Torr and the operating one was 7.5×10^{-3} Torr. The rate of the deposition was about 3 Å/sec and substrates were kept without heating. Three samples with argon were made and their thickness was about 1600, 2900 and 4700 Å. The thickness of samples with krypton and xenon was approximately 3800 and 2700 Å, respectively.

A helium ion beam from 2 MV or 5 MV VdG accelerator of JAERI was incident on samples perpendicular to their surfaces and its diameter was 0.8 mm. A silicon surface barrier detector with the acceptance angle 2.8° at lower energy than 1.8 MeV and 1.4° at higher one than 2 MeV was set up at the scattering angle of 150°. The vacuum of the scattering chamber was 1×10^{-7} Torr and the sample was covered by a liquid nitrogen trap. An example of the backscattering spectrum for 1.8 MeV helium ions on a sample including about 8 at % argon. This spectrum shows that the argon concentration in the sample is quite uniform.

When the scattering yields from argon and silicon at the surface are Y_r and Y_s, respectively, as shown in Fig.1, the ratio of the concentrations

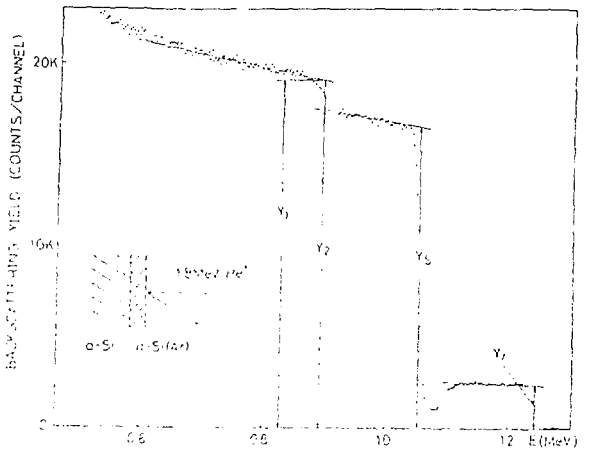

Fig.1. Rutherford backscattering spectrum for 1.8 MeV He^+ ions incident on an amorphous silicon layer including argon deposited on a pure amorphous silicon substrate.

of argon and silicon in the sample, c_r/c_s, is given by

$$\frac{c_r}{c_s} = \frac{k_r s(E_0) + \alpha s(k_r E_0)}{k_s s(E_0) + \alpha s(k_s E_0)} \frac{\sigma_s Y_r}{\sigma_r Y_s} \qquad (1)$$

where k and σ are the kinematic factor for the scattering and the Rutherford scattering cross section, respectively, which are indexed by r and s for argon and silicon, respectively, s(E) is the stopping cross section of the sample at the energy E and α is the ratio of outgoing and incoming path lengths. E_0 is the incident energy. The ratio c_r/c_s was obtained using the stopping cross sections of silicon given by Ziegler for $s(kE_0)/s(E_0)$. The error of c_r/c_s caused by such a treatment for the stopping power is estimated smaller than 1%.

The ratio of stopping cross sections of the sample and the base was deduced from the ratio of the scattering yields from silicon atoms at the interface using the relation,

$$\frac{Y_2}{Y_1} = c_s \frac{k_s s_0(E_i) + \alpha s_0(k_s E_i)}{k_s s(E_i) + \alpha s(k_s E_i)} \qquad (2)$$

where Y_1 and Y_2 are the yield from the base and the sample, respectively, s_0 the stopping cross section of the base and E_i is the energy of the incident ion at the interface. Obtained value of $k_s s(E_i) + \alpha s(k_2 E_i)$ is consist of stopping cross sections at different energies. Using a similar procedure used by Besenbacher et al.[9] we get

$$k_s s(F_i) + \alpha s(k_s E_i) = (k_s + \alpha) s(\bar{E}) \qquad (3)$$

and

$$\bar{E} = k_s E_i (1+\alpha)/(k_s+\alpha). \tag{4}$$

The ion energy at the interface was calculated from the higher and lower edges, $k_r E_0$ and E_r, of the argon spectrum. Letting $\langle s\rangle_{in}$ and $\langle s\rangle_{out}$ the mean stopping cross sections on incoming and outgoing paths, we get

$$E_i = \frac{\langle s\rangle_{in} E_r + \alpha\langle s\rangle_{out} E_0}{k_r\langle s\rangle_{in} + \alpha\langle s\rangle_{out}} . \tag{5}$$

Assuming that $s(E)/s_0(E)$ is independent of energy, $\langle s\rangle_{in}$ and $\langle s\rangle_{out}$ were replaced by $\langle s_0\rangle_{in}$ and $\langle s_0\rangle_{out}$, respectively, and were evaluated by

$$\begin{aligned} \langle s_0\rangle_{in} &= (s_0(E_0) + s_0(E_i))/2 \\ \langle s_0\rangle_{out} &= (s_0(k_r E_i) + s_0(E_r))/2 \end{aligned} \tag{6}$$

which were solved together with eq.(5) by iteration.

Using (2)∿(6) and values given by Ziegler for $s_0(E)$, we obtained $s(\bar{E})$. If we assume Bragg's rule and the stopping cross section of silicon inside the sample is same as that in the base, the stopping cross section of rare gas is given

$$s(\bar{E}) = c_s s_0(\bar{E}) + c_r s_r(\bar{E}) \tag{7}$$

The results are represented by $s_r(\bar{E})/s_0(\bar{E})$

$$\frac{s_r(\bar{E})}{s_0(\bar{E})} = \frac{c_s}{c_r}\left(\frac{Y_1}{Y_2} - 1\right)\frac{k_s s_0(E_i) + \alpha s_0(k_s E_i)}{(k_s+\alpha)s_0(\bar{E})} \tag{8}$$

in the following section.

§3. Results and Discussions

The concentrations of rare gases in samples obtained from (1), with the screening correction for the Rutherford cross section[10] which is only 1.7% in the xenon case and is almost 0 in the argon one, are tabulated in

Table I

		Ar		Kr	Xe
Thickness(Å)	1600	2900	4700	3800	2700
Concentration(at %)	7.9	8.1	7.6	7.2	4.4

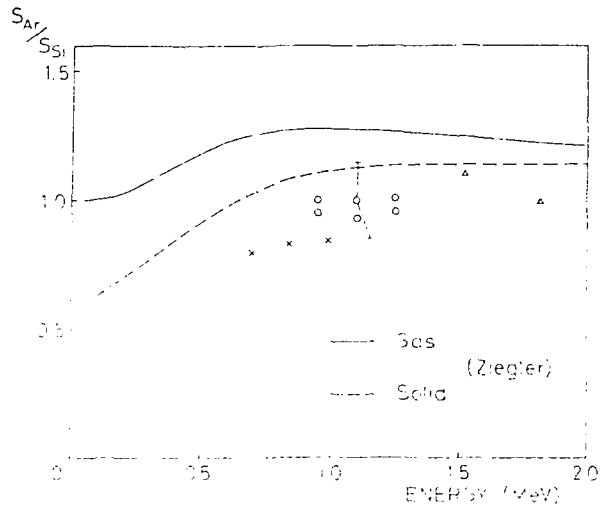

Fig.2. Ratio of stopping cross sections of argon and silicon for He^+ ions obtained from 1600 (o), 2900 (x) and 4700 Å (') thick samples. Solid and broken lines are values for gaseous and solid states given by Ziegler, respectively.

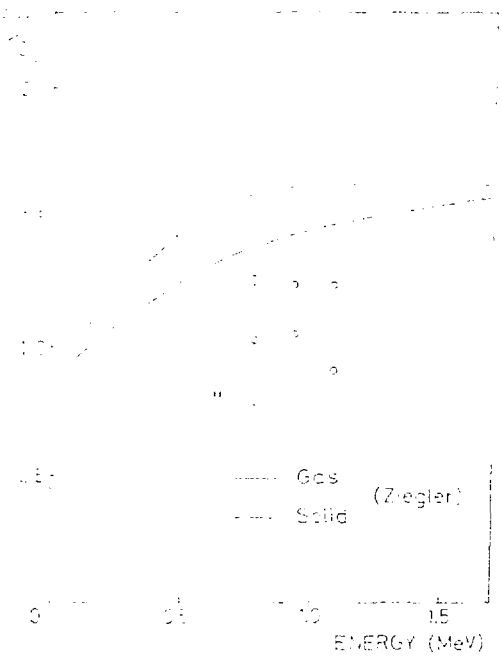

Fig.3. Ratio of stopping cross sections of krypton and silicon for He^+ ions. Solid and broken lines are values for gaseous and solid states given by Ziegler, respectively.

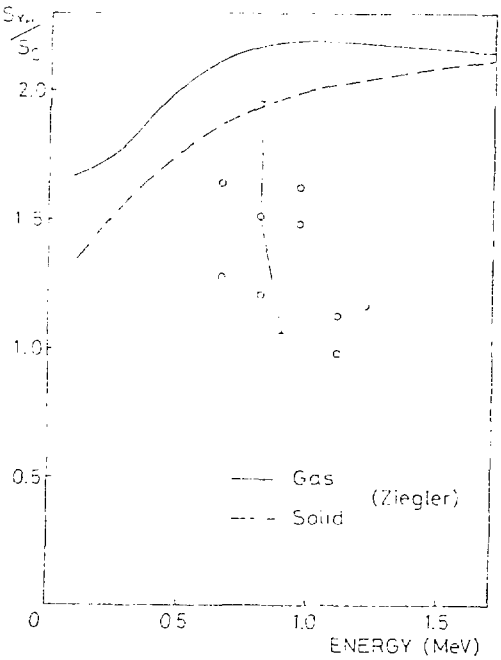

Fig.4. Ratio of stopping cross sections of xenon and silicon for He^+ ions. Solid and broken lines are values for gaseous and solid states given by Ziegler, respectively.

Table I, where the error of the concentration is 5%. The ratios of the stopping cross sections s_r/s_{Si} are shown in Figs.2,3 and 4 for argon, krypton and xenon, respectively. The error arises mainly from $Y_1/Y_2 - 1$ in (8). Procedure, with which $s(\bar{E})$ is adopted instead of $s(E_i)$ and $s(kE_i)$ is valid, when s(E) in the energy region from kE_i to E_i is linear with E. In the case of low energy for argon, the value obtained from (8) must be shifted upward by 3%.

Results shown in Figs.2,3 and 4 indicate that experimental values are about 30% lower than those for gaseous state given by Ziegler[2] and, in argon case, seem to tend to those with increasing of energy.

Besenbacher et al.[9] pointed out that the difference of stopping cross sections for gaseous and solid states can be explained by those of the mean excitation energies. In the present case, however, the mean excitation energies for rare gases do not likely change, even if rare gas atoms are inside silicon.

In order to check whether the stopping cross section of silicon atoms in amorphous silicon is the same as that given by Ziegler, we measured the RBS spectra from pure amorphous silicon layer on polycrystalline aluminum. The result is shown in Fig.5. The observed values of s_{Al}/s_{Si} is about 6%

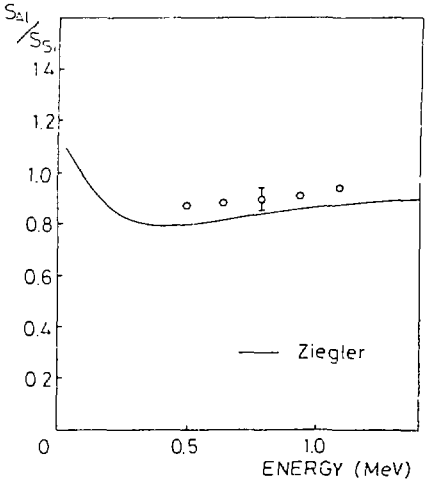

Fig.5. Ratio of the stopping cross sections of aluminum and silicon for He^+ ions. Solid line is the value given by Ziegler.

larger than those given by Ziegler and error is nearly the same.

Possible explanation of above results is that, in the present method, stopping cross section of heavier elements or of the surface layer is somehow underestimated or that stopping cross section of silicon atoms in

amorphous silicon including rare gas atoms is larger than that for pure silicon. The further investigations on this problem seem to be necessary.

References

1. H.H. Andersen and J.F. Ziegler, "Hydrogen stopping powers and ranges in all elements", (Pergamon, New York, 1977).
2. J.F. Ziegler, "Helium stopping powers and ranges in all elements", (Pergamon, New York, 1978).
3. J.S.-Y. Feng, W.K. Chu and M-A. Nicolet, "Stopping-cross-section additivity for 1-2 MeV $^{4}He^{+}$ in solid oxides", Phys. Rev. B10 3781-3788 (1974).
4. R.A. Langley and R.S. Blewer, "Measurement of the stopping cross sections for protons and ^{4}He ions in erbium and erbium oxide: A test of Bragg's rule", Nucl. Instr. and Meth. 132 109-117 (1976).
5. G. Blondiaux, M. Valladon, K. Ishii and J.L. Bebrum, "Search for the influence of chemical effect on the stopping power: The case of oxides", Nucl. Instr. and Meth. 168 29-31 (1980).
6. W.K. Chu and D. Powers, "Energy loss of α particles in noble gases from 0.3 to 2.0 MeV", Phys. Rev. B4 10-15 (1971).
7. W.K. Chu, M. Braun, J.A. Davies, N. Matsunami and D.A. Thompson, "Energy loss of He ions in solidified gases", Nucl. Instr. and Meth. 149 115-120 (1978).
8. F. Besenbacher, H.H. Andersen, P. Hvelplund and H. Kundsen, "Stopping power of swift hydrogen and helium ions in gases", K. Dan. Vidensk. Selsk, Mat. Fys. Medd. 40 No.3 (1979).
9. F. Besenbacher, J. Bøttiger, O. Graversen and J.L. Hansen, "Stopping power of solid argon for helium ions", Nucl. Instr. and Meth. 188 657-667 (1981).
10. H.H. Andersen, F. Besenbacher, P. Loftager and W. Möller, "Large-angle scattering of light ions in the weakly screened Rutherford region", Phys. Rev. A21 1891-1901 (1980).

THE STOPPING POWER OF AN ELECTRON GAS FOR SLOW IONS*

R. H. Ritchie
Health and Safety Research Division
Oak Ridge National Laboratory
Oak Ridge, Tennessee 37830, USA

The electron gas model has been exploited extensively in solid-state physics and in radiation physics. Recent activity in inertial confinement fusion research and in studies of inner-wall damage in the controlled thermonuclear reactor has lent importance to theoretical questions about the penetration of ions in media at velocities below that corresponding to the Bragg maximum in the energy-loss function. Semi-empirical formulas that involve the effective-charge concept have been used widely in recent years to describe the stopping power of matter for swift ions with atomic number appreciably greater than unity. The complexity of energy loss processes in this regime makes it important to study limiting cases in which accurate results may be obtained.

The stopping power of an electron gas for an ion moving at speed v, much less than the Fermi speed v_F, has been of interest for many decades. Fermi and Teller[1] were apparently the first to give a specific theory for the slowing-down of a low-velocity meson in matter. Arguing that the degeneracy of the electron gas restricts participation of struck electrons to those within a range v of v_F, they found that the stopping power of the medium for the meson may be written

$$\frac{dW}{dx} = \frac{\hbar v}{a_0^2} \ln\left(\frac{1}{\alpha r_s}\right) \qquad (1)$$

*Research sponsored by the Office of Health and Environmental Research, U.S. Department of Energy, under contract W-7405-eng-26 with Union Carbide Corporation.

where r_s, the one-electron radius in an electron gas with density n_0, is defined by $r_0 = (1/a_0)(3/4\pi n_0)^{1/3}$ and is expressed in units of the Bohr radius $a_0 = \hbar^2/me^2$. The constant $\alpha = (4/9\pi)^{1/3}$. For the case of an ion with charge Ze, Eq. (1) should be multiplied by Z^2. Although containing the essential physics of the interaction process, Eq. (1) goes to zero, unrealistically, when $r_s = 1/\alpha$.

A more reasonable result from linear dielectric theory is[2]

$$\frac{dW}{dx} = \frac{Z^2 \hbar v}{a_0^2}\left[\ln\left(1+\frac{\pi}{\alpha r_s}\right) - \frac{1}{1+\alpha r_s/\pi}\right] \tag{2}$$

This equation has an acceptable form for all possible r_s.

It is well appreciated that linear response theory is suspect at real metallic densities ($r_s \gtrsim 2$ to 6), particularly if $Z \gg 1$. An improvement may be effected by expressing dW/dx in terms of the transport cross section for scattering of an electron at the Fermi surface on the screened ion at rest in the electron gas.[3] One finds

$$\frac{dW}{dx} = m v v_F n_e \sigma_{tr} \tag{3}$$

and

$$\sigma_{tr} = \int d\sigma (1-\cos\theta) = \frac{4\pi}{k_F^2}\sum_{\ell=0}^{\infty}(\ell+1)\sin^2(\delta_\ell - \delta_{\ell+1}) \tag{4}$$

where θ is the scattering angle of an electron relative to its original direction and δ_ℓ is the phase shift in the ℓ^{th} partial wave. The δ_ℓ may be determined numerically, given the screened potential of the ion. The latter may be determined conveniently using linear dielectric theory. Figure 1 shows 1/v times the stopping power of the medium for a proton in electron gases of various densities as computed[4] from Eqs. (1)-(3). Atomic units ($e = \hbar = m = 1$) are used in specifying all quantities here.

Although the phase shift method codified in Eq. (3) is expected to represent an improvement over linear-response theory [Eq. (2)], it is not self-consistent. The calculation of -dE/dx through determination of the phase shifts δ_ℓ should be quite accurate if the potential is determined self-consistently with the scattering of all the electrons in the electron gas on the ion and with any electrons that may be bound to the ion. The density-functional approach does just this.

Recent years have seen many applications of this method.[5] Echenique, Nieminen, and Ritchie[6] have recently used the density-functional formulation of Hohenberg and Kohn and Kohn and Sham[7] to calculate the self-consistent potential due to a static proton and a He nucleus submerged in electron gases corresponding to metallic densities. The local density approximation for exchange and correlation was used with the parametrization given by Gunnarsson and Lundquist.[8] The scattering phase shifts at the Fermi level were found to satisfy the Friedel sum rule to good approximation. Some of the results found are shown in Fig. 2, where the quantity $(1/v)dW/dx$ is plotted as a function of r_s.

Curve A was calculated from linear response theory [Eq. (2] for Z = 1, while Curve B was computed from the same equation for Z = 2. The stopping power for a slow, singly ionized He atom calculated from linear-response theory using a wave function for the bound electron that was determined self-consistently in the electron gas (ref. 4) is shown as Curve C. Curves D and E were computed from the density-functional approach for a proton and a He nucleus, respectively. As $r_s \to 0$ the density-functional results tend toward agreement with linear theory, as they should. For increasing r_s the energy loss for both projectiles

decreases more rapidly than predicted by linear theory, because bound states of atomic character tend to develop, thereby screening out interactions with the electron gas.

More recently, experimental data[9] on the energy loss of protons in various solids have been found to agree well with the density-functional calculations of reference 5 for protons (Curve D in Fig. 2). The latter appear to agree better with experiment than the phase shift results which are, in turn, better than the results of linear-response theory.

Extension of the density-functional approach to treat low-velocity ions having a wide range of nuclear charge has also been made by Echenique, Nieminen, and Ritchie.[10] Pronounced, periodic fluctuation in the energy loss is found, which is in general agreement with experiment.[11] A fuller account of this calculation will be published elsewhere.

In conclusion, it appears that the density-functional method, which has proved to be very important in solid-state theory, is capable of giving useful results in the theory of charged-particle energy losses in solids.

References

1. E. Fermi and E. Teller, *Phys. Rev.* 72, 399 (1947).
2. R. H. Ritchie, *Phys. Rev.* 114, 644 (1959).
3. J. Finneman, Dissertation (The Institute of Physics, Aarhus Univ., 1968) (unpublished).
4. T. L. Ferrell and R. H. Ritchie, *Phys. Rev.* B16, 115 (1977).
5. See, e.g., N. D. Lang in *Theory of the Inhomogeneous Electron Gas*, Eds., S. Lundquist and N. H. March (Plenum, New York, 1981).
6. P. M. Echenique, R. M. Nieminen, and R. H. Ritchie, *Solid State Commun.* 37, 779 (1981).

7. P. Hohenberg and W. Kohn, *Phys. Rev.* B136. 964 (1964); W. Kohn and L. J. Sham, *Phys. Rev.* A140, 1133 (1965).

8. O. Gunnarsson and B. Lundquist, *Phys. Rev.* B13, 4274 (1976).

9. W. Brandt and M. Kitigawa, *Phys. Rev.* B25, 5631 (1982).

10. P. M. Echenique, R. M. Nieminen, and R. H. Ritchie, to be published.

11. F. H. Eisen, *Can. J. Phys.* 46, 570 (1968); J. Bottiger and F. Bason, *Radiat. Eff.* 2, 105 (1969).

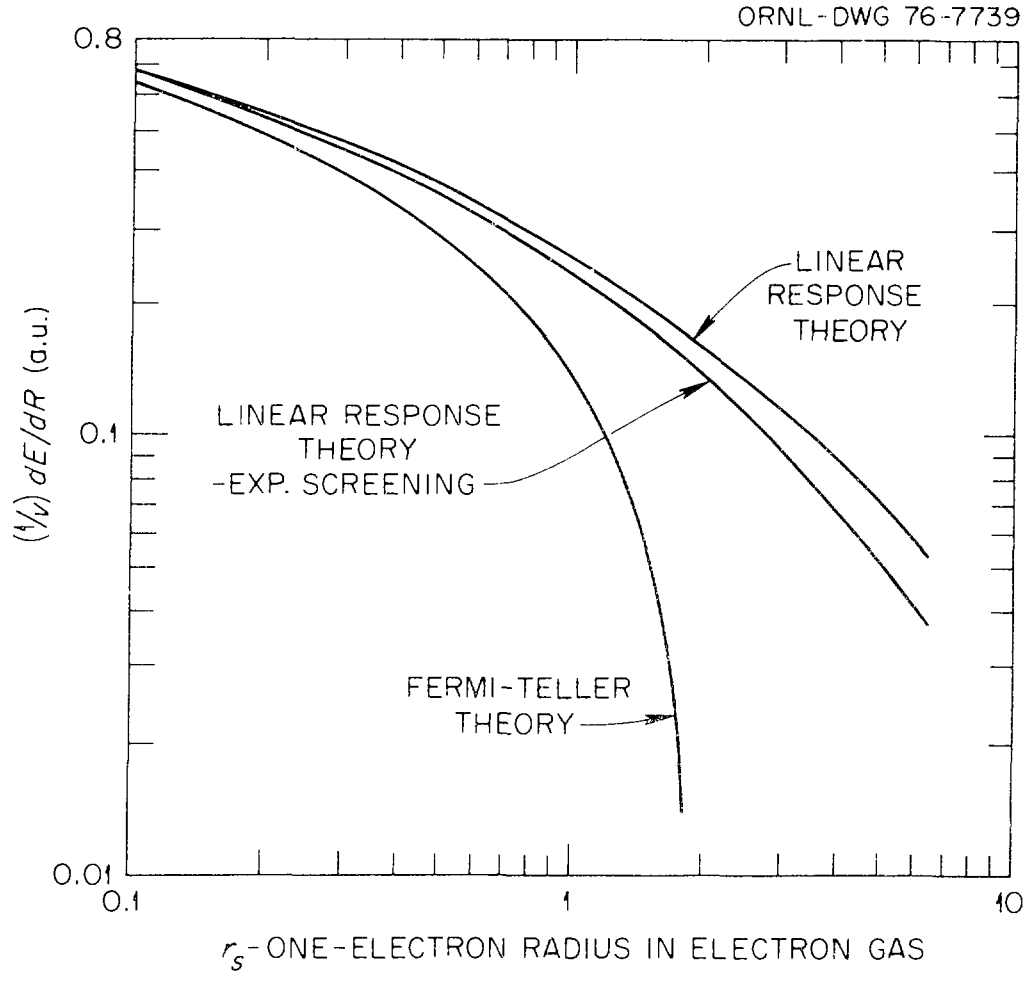

Fig. 1. The stopping power of an electron gas for a low-velocity proton versus the one-electron radius r_s. These values were computed from linear response theory.

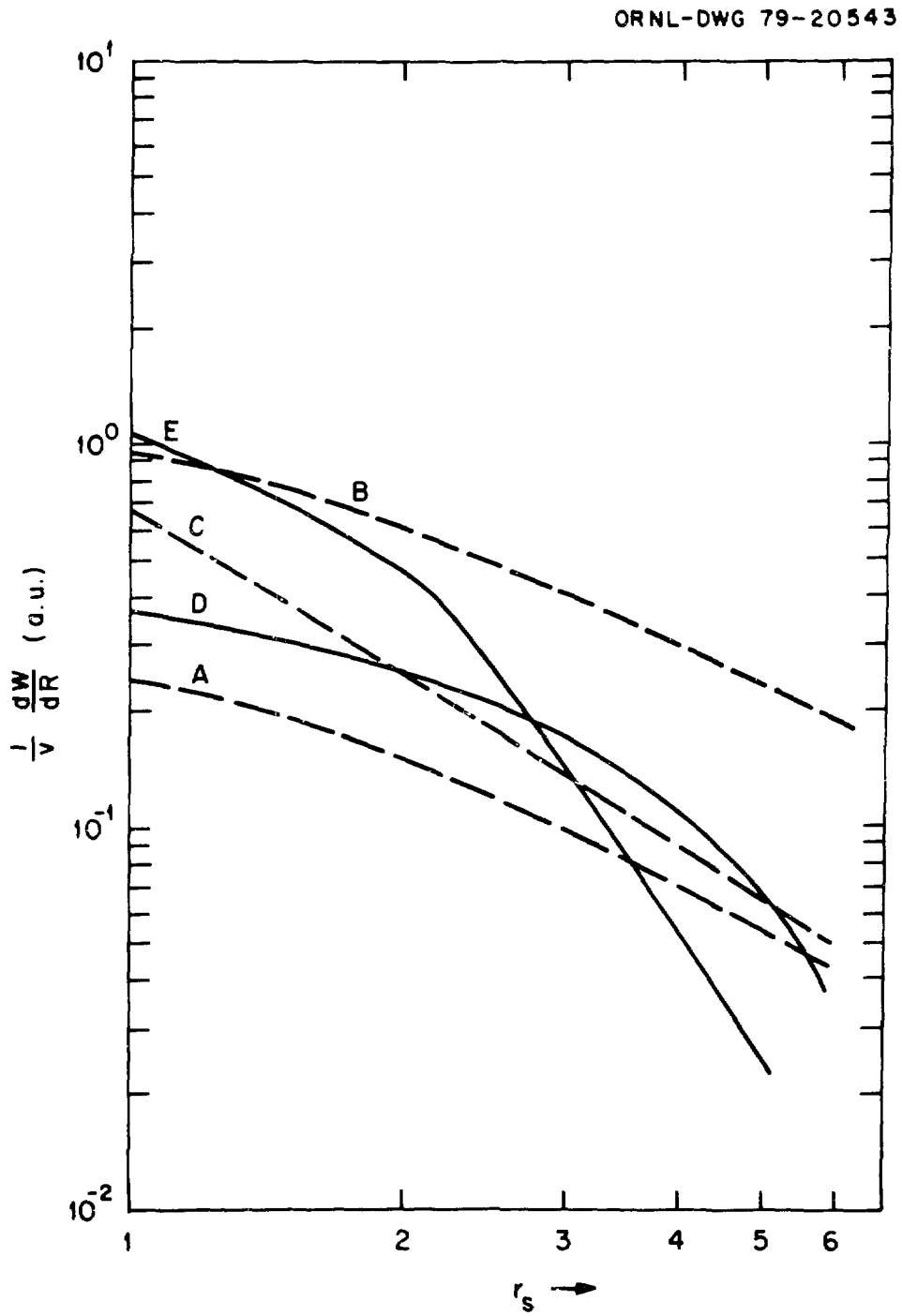

Fig. 2. The stopping power of an electron gas for a proton and for a He^+ ion at low velocities versus the one-electron radius r_s.

Ion-Channelling Fffects in Scanning Ion Microscopy with a Ga^+ Probe

R. Levi-Setti
The Enrico Fermi Institute and Department of Physics
The University of Chicago
Chicago, Illinois 60637, U.S.A.

I. INTRODUCTION

The scanning ion microscope (SIM) can be applied to the study of several aspects of the ion-solid interaction in conditions which are seldom accessible to conventional accelerator experiments. Its ability to image the target material and the practicality of directing the ion beam to intercept preselected microscopic areas of the target make it possible to probe local interaction properties in a comparative manner. The recent development of liquid metal ion sources has made it feasible to follow this approach using intense, finely focused beams of heavy ions. Such beams can be used as scanning probes for imaging purposes, as milling devices (direct ion beam writing) in electronic microfabrication, and for microanalysis by secondary ion mass spectrometry. Imaging of bulk specimens in the SIM takes advantage of the contrast arising from several ion-solid interaction processes such as secondary electron (SE) and secondary ion (SI) emission, the latter related to sputtering of the target material. These processes are strongly affected by ion-channelling penetration phenomena in crystalline materials. This report describes preliminary observation of such phenomena carried out with a 60 keV Ga^+ SIM, which provides a focused probe $\sim$100 nm wide.

II. THE SCANNING ION MICROSCOPE

The instrument used in these experiments was originally developed as a scanning transmission ion microscope[1] (STIM) and used a field ionization source of hydrogen ions. This ion source was recently replaced by a Gallium liquid metal ion source,[2] consisting of a Ga-wetted W tip. This preserves the point-like configuration of the field ion source, thus providing the source brightness needed for high resolution scanning ion microscopy using heavy metal ions. The optical column (see Fig. 1) which contains a two-electrode accelerating and focusing lens, deflection and stigmator

electrodes, forms a probe ~100 nm wide. The probe semi-angle is 1.5 x 10^{-4} r at the target and the probe current is 80 pA for a typical source current of 4 μA. This operating source current represents an optimum to minimize chromatic aberration while maximizing the collected probe current.[3]

A channel multiplier detector collects the SE signal with a bias of +45 V or the SI signal with a bias of -3000 V with respect to the grounded target. The SE signal is usually displayed on the CRT through an analog amplifier. For lower detected currents (<2 MHz count rate), such as those collected in SI emission, the individual counts are displayed as pulses on the CRT screen. A record of the signal intensities observed, e.g., in a line scan with either signal, can be obtained with a multichannel pulse-height analyzer.

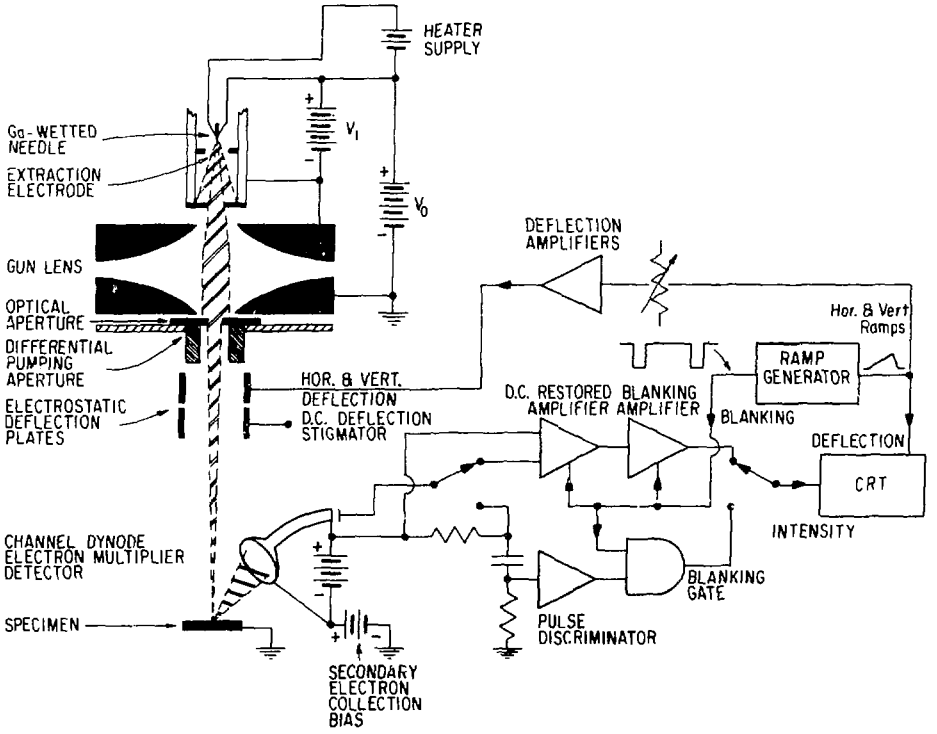

Fig. 1. Schematics of the University of Chicago 60 kV Ga^+ scanning ion microscope.

The entire SIM is designed as an ultra-high vacuum system (10^{-9} Torr) and is free of hydrocarbon contaminants. In these conditions, the ion beam effectively cleans the specimen surfaces by sputtering away absorbed or oxydation layers in a few minutes scans.

III. IMAGE CONTRAST IN THE SIM

Several physical processes may contribute to originate image contrast in the SIM. Much as in the SEM, the SE signal is modulated by the surface topography of three dimensional objects, yielding topographic contrast. Although this aspect is not dealt with here in any detail, two micrographs of a biological specimen are shown in Fig. 2a), b).

Another source of contrast is the Z-dependence of the SE emission yields. This differs considerably for primary electrons vs. primary ions, as summarily shown in Fig. 3).

Of particular interest in the SIM are the contrast phenomena originating in the interaction of the incident ion beam with the bulk structure of the target material. While in the SEM it is only the backscattered electrons which may carry information about subsurface structure, in the SIM, as will be shown, also the copious SE signal carries such information. Such a property must be attributed to the mechanism of energy transfer to the solid, which differs for 10-20 keV primary electrons in a typical SEM as compared with, e.g., that of 60 keV Ga^+ in our SIM. In fact, while the deposition of electron excitation by primary electrons near the surface is primarily determined by electronic stopping, for heavy ions in our velocity range, nuclear stopping also contributes significantly. The latter initiates an atomic collisional cascade which is responsible for sputtering, SI emission and also recoil-induced SE emission.[4] As a result, the SE signal in the SIM is modulated not only by the surface topography, but also by processes taking place beneath the shallow SE escape depth. Both the SE and SI yields under ion bombardment depend strongly on the physical and chemical bulk properties of the target, in addition to surface effects. Such dependence originates contrast even in smooth samples, as long as they are structurally or chemically differentiated. Further insight into the ion-solid interaction can be gained in the SIM by the direct correlation

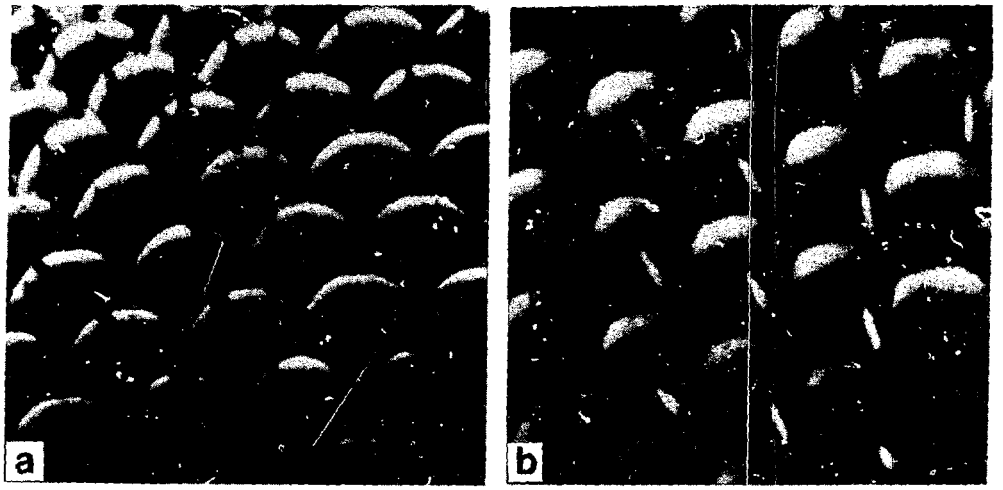

Fig. 2. a), b): Two views of the eye of Drosophila melanogaster, obtained in the SIM with the SE signal. Uncoated, 72 μm f.s.

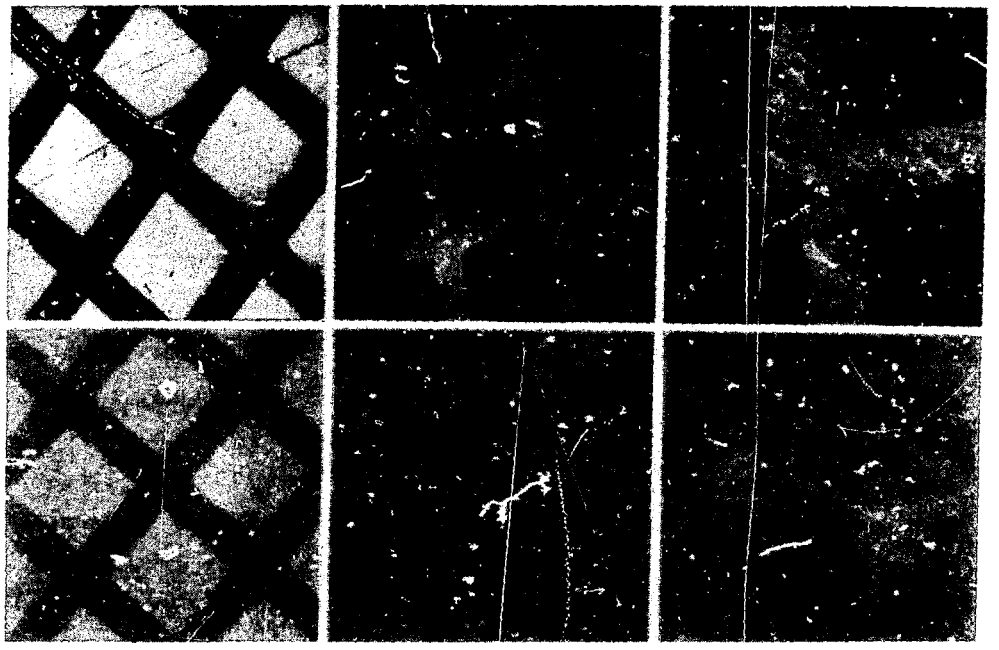

Fig. 3. Z-contrast in the SIM (top) vs. SEM (bottom). Pattern obtained by evaporation of Ag (left), Au (center), Pt (right) on Fe substrate through 200 mesh mask. SEM micrographs obtained with 10 kV Coates and Welter.

of local image contrast from SE and SI emission, as well as by sputtering tests (ion-beam writing) performed on the particular structures being imaged.

IV. ION CHANNELLING AND CRYSTALLOGRAPHIC CONTRAST: PHYSICAL CONSIDERATIONS

Ion-channelling in crystalline materials strongly affects the secondary yields. Here both the sputtering yields[5,6] (and consequently also the SI yields) and the SE yields[7,8] depend critically on lattice orientation with respect to the incident beam direction. The anisotropy of the SE yields under noble gas ion bombardment of crystals has been previously exploited[9] to obtain crystallographic contrast in the emission electron microscope (EEM). In this instrument, the secondary electrons are accelerated and focused by an optical column which projects an image of the emitting surface on a photographic plate.

We have chosen to examine in the SIM samples of recrystallized α-brass. This alloy, containing 70% Cu, 30% Zn, is a solid solution, with lattice structure isomorph with f.c.c. Cu. It should be noted that for Ga^+ ions of energy E on either Cu or Zn, elements which are contiguous in the periodic table, the efficiency γ for energy transfer T_m in a head-on collision

$$\gamma = \frac{T_m}{E} = \frac{4M_1M_2}{(M_1 + M_2)^2} \qquad (1)$$

is very close to unity. This maximizes the secondary effects resulting from nuclear stopping. For 60 keV Ga^+ ions on Cu, the Thomas-Fermi energy parameter

$$\varepsilon = E \frac{a_{TF}M_2}{Z_1Z_2e^2(M_1 + M_2)} \qquad (2)$$

equals 0.21, and the nuclear stopping cross section is near its maximum.[10] To obtain an estimate of the contrast effects to be expected, it is relevant to consider a calculation[11] of the rates of energy loss for channelled and unchannelled Cu atoms in a Cu lattice. This is reproduced in Fig. 4a), c). For Cu atoms channelled along the <110> direction in Cu, dE/dx is primarily due to electronic stopping. Extrapolating the $E^{1/2}$ dependence from ∿25 to 60 keV, one obtains a loss rate (∿75 eV/Å) for channelled ions which is

1/4 of the overall dE/dx for unchannelled ions. For the latter case ∿2/5 of the energy loss is due to nuclear stopping.

Such a difference in the rate of energy deposition is reflected, although not necessarily in a proportional manner, in the yields of SE emission and sputtering. Data on such yields in the literature, approaching the case of Cu^+ on Cu at 60 keV as relevant here, exist for Kr^+ on Cu. These are reproduced in Fig. 4b), d). For SE emission,[8] the yield for <110> Cu relative to random Cu is ∿1/3.2. A similar ratio is found for the sputtering yields.[5]

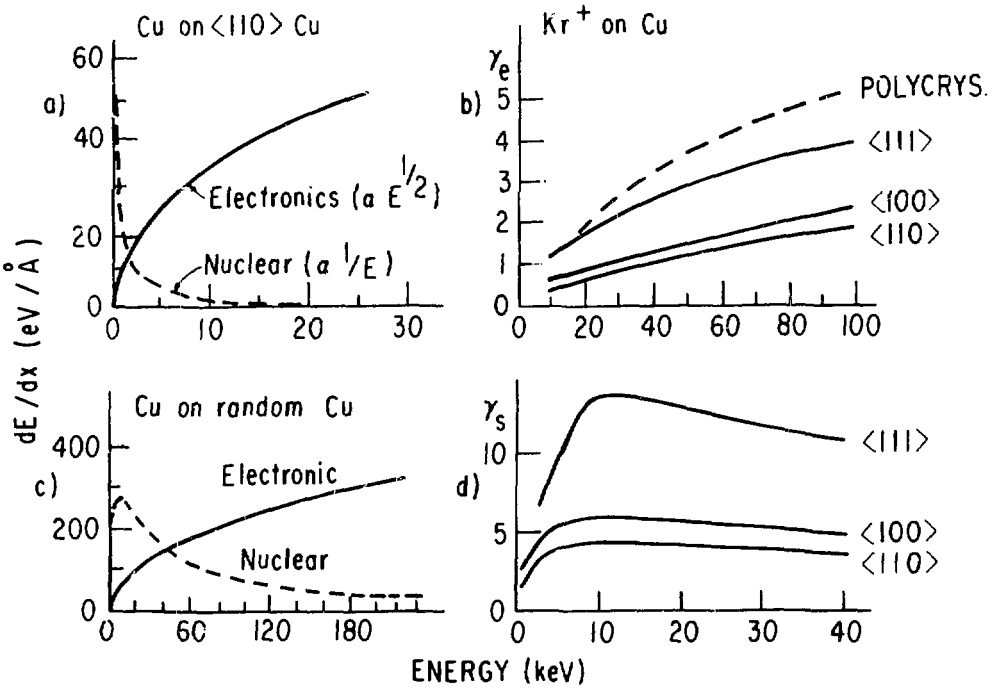

Fig. 4. a), c). Comparison of the rates of energy loss for <110>-channelled Cu atoms in Cu, with those for unchannelled atoms. Adapted from Ref. 11.

b). Secondary electron emission coefficient γ_e for Kr^+ ions incident on a Cu lattice, as a function of primary energy. Adapted from Ref. 8.

d). Sputtering yields γ_s for Kr^+ ions incident on a Cu lattice, as a function of primary energy. Adapted from Ref. 5.

Also relevant to the experimental observation of channelling effects in the SIM are the critical channelling angles. For 60 keV Ga^+ ions incident on a Cu lattice, the axial channelling condition is expressed, in the notation of Lindhard,[12] in terms of the critical angle

$$\psi_2 = \left(\frac{3a_{TF}^2 \, Z_1 Z_2 e^2}{E \, d^3} \right)^{1/4} \qquad (3)$$

where E is the ion energy, d the atom spacing along the string direction, $a_{TF} = a_0 \cdot 0.8853 \, (Z_1^{2/3} + Z_z^{2/3})^{-1/2}$ is the Thomas-Fermi screening radius and a_0 is the Bohr radius.

For planar channelling, the corresponding critical angle as formulated by Francken and Onderdelinden[13] is

$$\psi_{2p} = \sqrt{N d_p} \left(\frac{a_{TF}^2 \, Z_1 Z_2 e^2}{E} \right)^{1/3} \qquad (4)$$

where N is the atomic number density and d_p the relevant interplanar distance.

For the lowest indices, such critical angles are in our case

ψ_2	<110>	<100>	<111>
	8.3°	6.4°	4.2°
ψ_{2p}	(110)	(100)	(111)
	5.4°	6.4°	6.9°

These values for ψ_2 give an approximate measure of the half-width of the channelling dips which one should expect to observe in, e.g., SE emission, as a result of primary ion channelling in our experiment on brass.

V. OBSERVATION OF CRYSTALLOGRAPHIC CONTRAST IN THE SIM

We have obtained[14] extensive evidence of crystallographic contrast in the SIM on samples of metals and alloys. Samples of recrystallized α-brass were polished and lightly etched with HNO_3 to expose the crystalline structure smeared by the polishing process. Fig. 5a), c) shows two views of a brass specimen thus prepared, as observed at normal incidence in the SIM, with the SE signal. The contrast between pairs of crystallites, which are

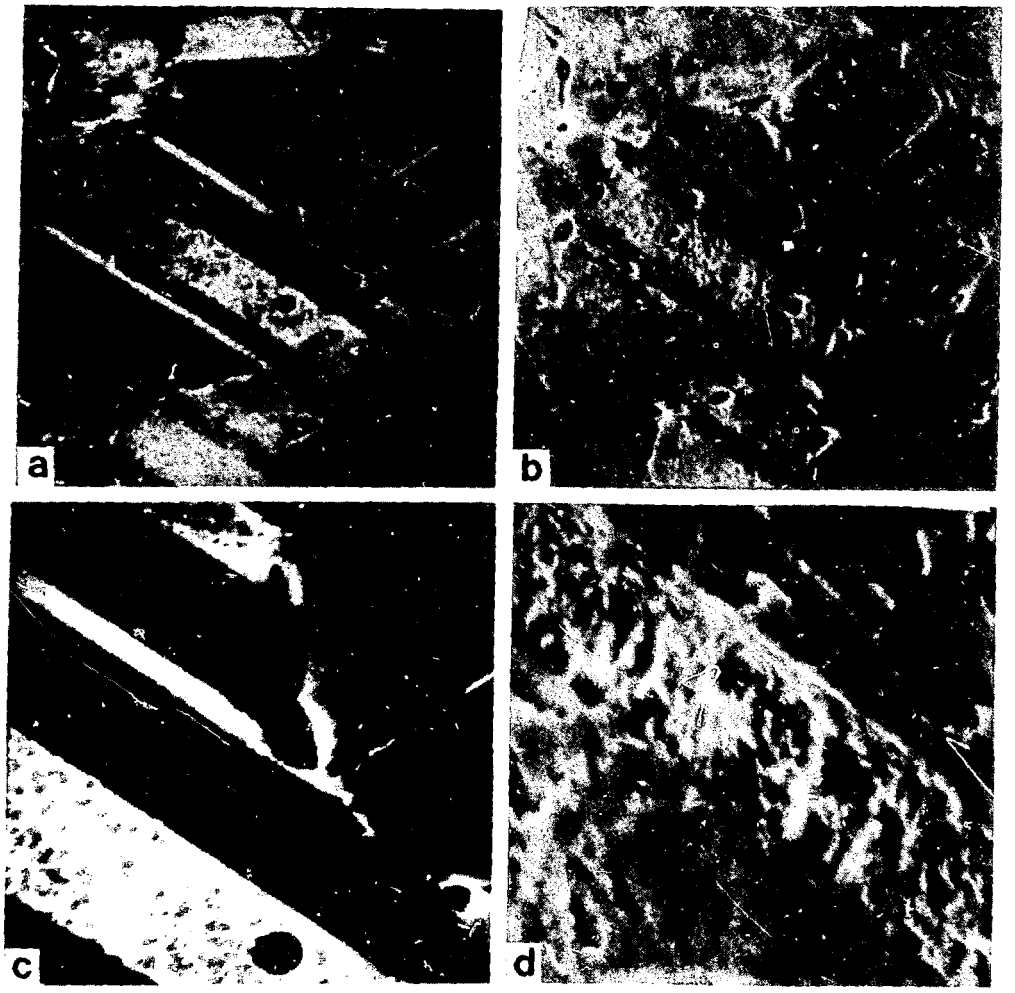

Fig. 5. Comparison of crystallographic contrast due to SE emission in the SIM, a),c), and in the SEM, b),d).
a) SIM micrograph of a sample of recrystallized, polished, HNO_3-etched brass. 60 kV Ga^+ UC-SIM, 160 µm f.s.
b) Same view as in a), obtained with a 10 kV Coates and Welter SEM.
c) Detail of a) in the SIM, 64 µm f.s.
d) Magnified detail of b) in the SEM, 13 µm f.s.

randomly oriented, and twin structures is very pronounced. For comparison, Fig. 5b), d) shows the same area and a magnified detail as seen in a 10 kV SEM, also collecting the SE signal. Although the crystallite structure is clearly visible also in the SEM images, the contrast in these is due to the variations in the surface topography of the sample. Evidence that the high contrast in the SIM micrographs is due to primary ion channelling is obtained by comparing images of the same sample area for different primary beam incidence angles. This is shown in Fig. 6. The image in Fig. 6a) is taken at normal incidence, that in Fig. 6b) after a rotation by 10° around a horizontal axis. Such tilt angle is larger than the critical channelling angles discussed in Part IV for this experiment and is sufficient to close particular channelling directions in the sample and to open new ones. This results in contrast reversals, dramatically evident in the above comparison for the two orientations. The actual crystallographic orientation of individual crystallites could be obtained, as done in the EEM,[9] by mapping the SE emission signal in ϕ and θ.

The magnitude of the maximum contrast observed between channelled (dark areas) and unchannelled (bright areas) conditions is obtained by measuring the intensity of the SE signal when the probe is directed sequentially on a pair of such preselected areas. The yield ratio observed is 1:3.2, indeed the same value as obtained by the Toulouse group[8] for <110> Cu relative to random Cu under 60 keV Kr^+ ion bombardment. By ramping a retarding potential applied to the SE detector, we have also obtained integral energy spectra of the SE emitted in channelled and unchannelled conditions respectively. These spectra are shown in Fig. 7.

Although these spectra originate from a rather primitive method of analysis, inadequate to reveal possible discrete features, the spectrum from channelled ions does fall off somewhat more rapidly than that from unchannelled ions. This difference could be related to the lattice orientation of the depth distribution of primary energy dep ition, in turn affecting the energy lost by the emitted electrons.[15]

Imaging with the overall SI signal also reveals crystallographic contrast. Figs. 6c) and d) compare the same sample as imaged by the SE and SI

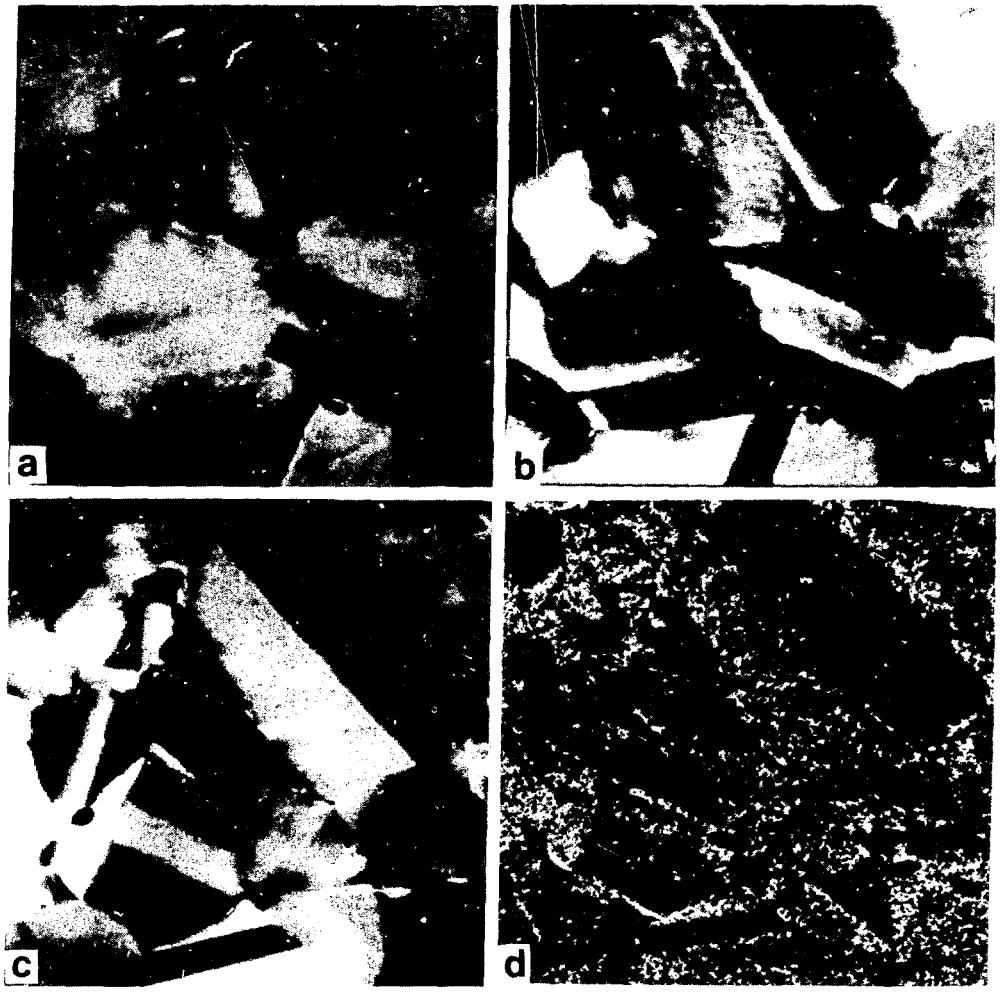

Fig. 6. a) SEM image of recrystallized, polished, HNO_3-etched brass, obtained at normal incidence in the SIM. 64 μm f.s.
b) Same specimen region as in a), after rotation of the sample by 10° around a horizontal axis. Contrast reversals when compared to a) are attributed to primary ion channelling.
c) Another region of the same brass specimen, seen at normal incidence in the SE mode. 72 μm f.s.
d) Secondary ion image of the same specimen area as in c), 200,000 counts displayed.

signals respectively at normal incidence. For the latter, due to the much lower SI yield, the micrograph is obtained by the pulse-mode type of display. For most crystallites, a direct correlation is observed for SE and SI emission. This is anticipated from the correlation in the lattice orientation dependence of the SE and sputtering yields, illustrated in Fig. 4b), d). There are, however, some exceptions. Already the crystallites in the lower right hand corner of Fig. 6c) exhibit anticorrelation between the two emission processes. This is further demonstrated in the comparison of Fig. 8a) and b), also obtained at normal incidence. The existence of occasional anticorrelation between SE and SI emission suggests that SI emission is not always proportional to the rates of neutral atom sputtering. Clearly other effects intervene which affect the ionization probabilities of the sputtered atoms in some as yet undetermined relationship with primary ion channelling. A more detailed study of the dependence of SI emission on primary ion channelling and its relationship to SE emission will probably be best carried out by the approach presented here.

The SIM yields an accurate measurement of the surface amorphization dose. Mixing due to the collisional cascade in fact destroys the crystalline structure over the first few surface layers beyond a certain radiation dose. The onset of amorphization is first detected by the disappearance of crystallographic contrast in SI images. For 60 keV Ga^+ ions on brass, this occurs for an overall dose in ex-

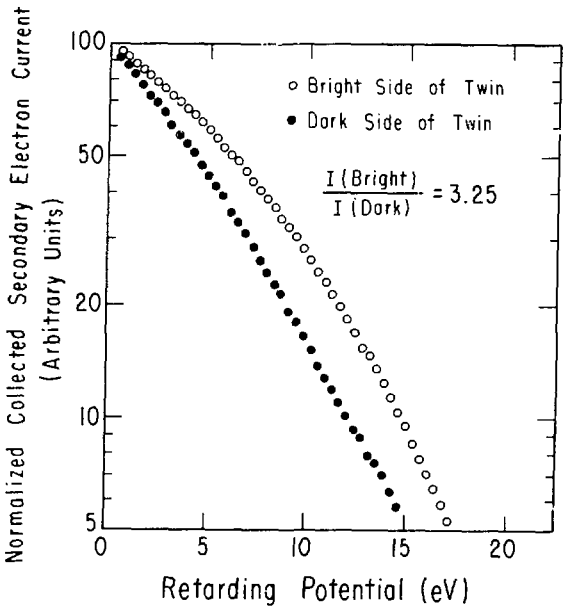

Fig. 7. Integral SE spectra obtained with a variable retarding potential. 60 keV Ga^+ ions incident on brass in channelled (full points) and unchannelled (open points) conditions.

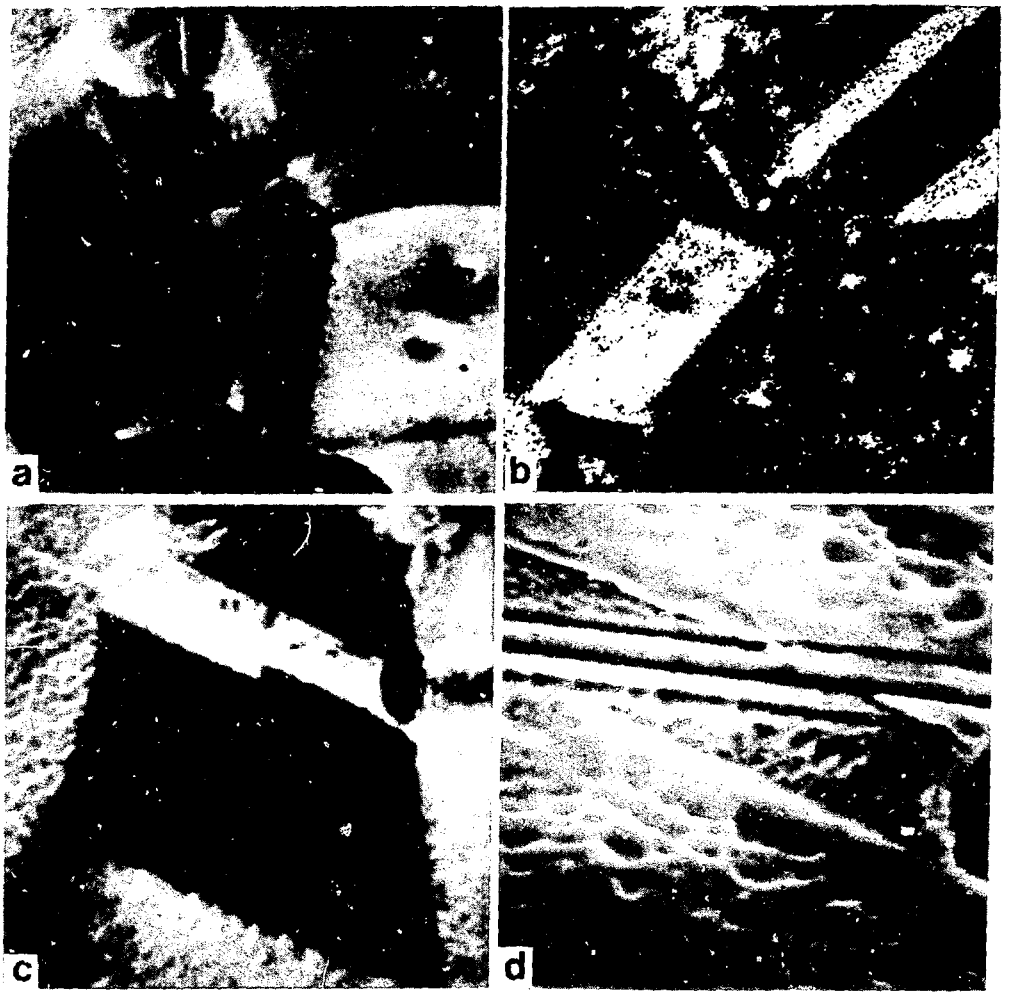

Fig. 8. a),b) Another comparison of SE,a), and SI,b), emission from the same brass specimen area. 64 μm f.s.
c) SE image of crystallites in brass specimen. 32 μm f.s.
d) Magnified detail of c), after Ga^+ ion-beam writing in line scans, observed with 10 kV Coates and Welter SEM. Beam doses are, for top line : 7.1×10^{17} ions/cm^2; middle line: 2.4×10^{18} ions/cm^2; bottom line: 2.4×10^{17} ions/cm^2. 13 μm f.s.

cess of 8×10^{16} ions/cm^2. Evidence that the SE signal in the SIM carries information from the bulk is provided by the fact that even after surface amorphization has occurred, crystallographic contrast persists unchanged in the SE images.

Direct information on the lattice orientations dependence of the sputtering yields can be obtained by writing on a particular surface structure with the ion beam in a line scan. An example of this procedure is shown in Fig. 8c) and d). In Fig. 8c) the sample is characterized by SE imaging. Then lines are written on the structure. The result is examined at high magnification in the SEM micrograph of Fig. 8d). For <100> channelling [dark crystallite in Fig. 8c)] writing requires a higher dose than for unchannelled ions [bright area in Fig. 8c)]. Specifically, a dose of 7×10^{17} ions/cm^2 is required for a visible etching in channelling conditions, while a dose of 2×10^{17} ions/cm^2 produces comparable damage in the region where channelling does not occur.

VI. DISCUSSION AND CONCLUSIONS

The observation of crystalline structures with the SIM has been shown to give information on the ion-channelling dependence of kinetic SE emission, SI emission and sputtering. Of course, the results of these preliminary observations agree in general with the results of previous systematic measurements on monocrystals, already available in the literature. From this standpoint, the use of the SIM to visualize such effects is to be regarded as a practical application of ion channelling which may be valuable in the study of materials. In particular, the large contrast effects intrinsic to the method have obvious potential for the sensitive detection of defects and impurities in crystals, in particular at better spatial resolution than presented in this pilot study.

There are, however, several unique aspects of the present approach as a method to investigate the ion-solid interaction proper. These originate in the capability to correlate directly on a local scale, different secondary processes. Thus far, we learned, as yet in a qualitative manner, relevant new information on two aspects of these processes. The observation of persistent crystallographic content in SE emission even after dis-

appearance of such contrast in SI emission favors a kinetic electron emission model where primary ion channelling information is transported to the surface irrespective of the conditions at the surface. A likely candidate for such energy transport is recoil-induced SE emission.[4,15] Another important new aspect is the discovery of the occasional anticorrelation between SE and SI emission, at variance with the known correlation between SE and sputtering yields in crystals.[16] Clearly this calls for a detailed investigation of the lattice orientation dependence of the secondary ion yields, as an issue separate from sputtering. The simultaneous observation of SE emission in the SIM should be valuable in separating primary ion channelling effects from, e.g., the possible effects of focusing collision sequences.

VII. ACKNOWLEDGMENTS

This work was supported by the Air Force Office of Scientific Research (Contract F 49620-80-C-0074) and the National Science Foundation Ceramics Program (Grant DMR-8007978). Dr. R. L. Seliger of Hughes Research Laboratories kindly provided several Ga liquid metal sources, which made this work possible. It is a pleasure to acknowledge Dr. Peter Sigmund for an illuminating discussion on our early observations. The assistance of my collaborators, Dr. Timothy R. Fox and Mr. Kin Lam, is gratefully acknowledged. Thanks are due to Mr. Keith Evans for help in the operation of the SIM and Mr. Jorge Baralt for the photographic reproductions. The Material Research Laboratory of the James Franck Institute at the University of Chicago provided the opportunity to use the Coates and Welter SEM.

VIII. REFERENCES

1. R. Levi-Setti. "High resolution scanning transmission low energy ion microscopes and microanalyzers," in *Advances in Electronics and Electron Physics, Supp. 13A, Applied Charged Particle Optics,* ed. A. Septier (Academic Press, New York, 1980), pp. 261-320.
2. R. L. Seliger, J. W. Ward, V. Wang and R. L. Kubena, "A high-intensity scanning ion probe with submicrometer spot size," *Appl. Phys. Lett.* 34, 210-212 (1979).
3. T. R. Fox, R. Levi-Setti and K. Lam, "Magnetic prism analysis of a

practical gallium ion probe from a liquid metal source," *Proc. 28th Int. Field Emission Symposium,* eds. L. Swanson and A. Bell (The Oregon Graduate Center, Beaverton, Oregon, 1981), pp. 92-94. See also: K. Lam, T. R. Fox and R. Levi-Setti, "Scanning microscopy with gallium ions from a liquid metal source," *ibid.*, pp. 59-61.

4. G. Holmen, B. Svenson, J. Schou and P. Sigmund, "Direct and recoil-induced electron emission from ion-bombarded solids," *Phys. Rev. B* 20, 2247-2254 (1979).
5. D. Onderdelinden, "Single crystal sputtering including the channelling phenomena," *Can. J. Phys.* 46. 739-745 (1968).
6. H. E. Roosendaal, "Sputtering yields of single crystalline targets," in *Sputtering by Particle Bombardment I,* ed. R. Berisch (Springer-Verlag, Berlin-Heidelberg, 1981), pp. 219-256.
7. D. B. Medved and Y. E. Strausser, "Kinetic ejection of electrons from solids," in *Advances in Electronics and Electron Physics, Vol. 20,* (Academic Press, New York, 1965), pp. 101-179.
8. N. Colombie, B. Fagot and C. Fert, "Emission electronique cinetique des cibles monocrystallines metalliques," *Rad. Effects* 2, 31-39 (1969).
9. B. Fagot and C. Fert, "Microscopie electronique a emission secondaire sous bombardment ionique: Contrast des images," *J. Microscopie* 4, 21-32 (1965); *ibid.* 5, 389-408 and 409-420 (1966).
10. J. Lindhard, V. Nielsen and M. Scharff, *K. Dan. Vidensk. Selsk. Mat. Fys. Medd.* 36, No. 10 (1968).
11. R. S. Nelson, *The Observation of Atomic Collisions in Crystalline Solids* (J. Wiley & Sons, New York, 1968), p. 66.
12. J. Lindhard, "Influence of crystal lattice on motion of energetic charged particles," *K. Dan. Vidensk. Selsk. Mat. Fys. Medd.* 34, No.14 (1965).
13. L. Francken and D. Onderdelinden, "Influence of planar channelling on single crystal sputtering," in *Atomic Collision Phenomena in Solids,* eds. D. W. Palmer, M. W. Thompson, and D. P. Townsend (North-Holland, Amsterdam, 1968), pp. 266-277.
14. R. Levi-Setti, T. R. Fox and K. Lam, "Ion-channelling effects in scanning ion microscopy and ion beam writing with a 60 keV Ga^+ probe," in

Submicron Lithography, S.P.I.E. Proceedings Vol. 333, in press.

15. P. Sigmund and S. Tougaard, "Electron emission from solids during ion bombardment: theoretical aspects," in *Inelastic Particle-Surface Collisions,* Springer Series in Chem. Phys., Vol. 17, eds. E. Taglauer and W. Heiland (Springer-Verlag, Berline-Heidelberg, 1981), pp. 2-37.
16. E. S. Mashkova, V. A. Molchanov and D. D. Odintsov, "Anisotropy of the sputtering ratio and of the ion-electron emission coefficent in single crystals," *Sov. Phys.-Solid State* 5, 2510-2518 (1964).

ANOMALIES IN THE THICKNESS DEPENDENCE OF THE ENERGY LOSS OF HELIUM AND NITROGEN IONS IN VERY THIN CARBON FOILS

J. P. Biersack and P. Mertens

Hahn-Meitner-Institute, Glienicker Str. 100
1000 Berlin 39, W.-Germany

Energy losses of 300 and 610 keV He^+ and of 300 keV N^+ ions were measured in transmission experiments using carbon foils of 100 to 700 Å thickness. This range of thicknesses is well below that of W. Lennard et al. (1), who studied energy losses of Na^+ in carbon foils of up to about 3500 Å thickness. The energy losses were determined either by a magnetic spectrometer calibrated by proton resonance or by an electrostatic analyzer. The targets were kept at $4 \cdot 10^{-8}$ torr during beam exposures of less than 20 nC. The good vacuum and low ion dose helped to keep the targets unaffected during repeated measurements.

The carbon foils were prepared by vapor deposition in ultra-high vacuum using a quartz oscillator for relative thickness measurements. Independent thickness calibrations and purity tests were performed by Rutherford backscattering with the 300 keV H^+ beam in the final target chamber. In addition, down to thicknesses of about 80 Å, proton energy losses were found to be well proportional to the thickness as determined by the two previous methods, so that they may serve for thickness measurements as well. More details of the experimental work may be found in ref. (2).

The results of energy loss measurements of helium and nitrogen ions in dependence of the foil thickness are compiled in Figs. 1, 2 and 3. The ion energies are indicated on each graph. The dashed lines are least square fits to the experimental data points. In all cases they intersect the ΔE axis at positive values of about 2 to 3 keV (or correspondingly the Δx axis at -40 to -70 Å). This indicates - beyond statistical errors - that the initial stopping power, immediately after the ion enters the target, is higher than the equilibrium value which is observed as a constant slope of the dashed line which connects all data points between 100 and 800 Å foil thickness. In other words, in the region between the origin and an unknown thickness of less than 150 Å - which is not accessible by experiments - a step or steeper slope occurs (tentatively depicted by a dotted line in the figures). This enhancement of electronic stopping near the surface cannot be understood by the time

retardation in building up the wake configuration of free electrons, nor by a time delay in reaching the equilibrium state in excitation and ionization of the ion, as both effects would act in the opposite direction. For example, the initial charge state +1 of the helium projectiles will increase to its equilibrium value of +1.2 within about 10^{-15} sec or roughly 60 Å at the present energy (300 keV He). The higher (average) excitation and charge state would naturally increase - not decrease - the stopping over the first 60 Å flight path. Also, any additional stopping by adsorbed surface impurities on the foils, can be ruled out according to the Rutherford backscattering spectra. Energy loss processes which occur at or near the surface, such as collective excitations (surface plasmons, surface phonons, surface excitons), are estimated to cause energy losses well below 100 eV and can not account for the observed 2 to 3 keV.

In conclusion, our experimental data indicate an additional or enhanced electronic stopping near the surface which decreases to "normal" values at the experimentally accessible depths ($\geq$ 100 Å). The physical reasons are not yet understood.

Acknowledgments

We thank T. Krist, I. Reid, P. Scanlon, C. W. Cheng and K. Barfood for their cooperation and R. Ritchie for his theoretical estimates on surface energy losses.

REFERENCES

1. W. N. Lennard, H. R. Andrews, I. V. Mitchell, D. Phillips and D. Ward, "Energy Loss of Heavy Ions as a Function of Target Thickness: Na → C", Proceedings of the United States – Japan Seminar on Charged-Particle Penetration Phenomena, this ORNL report (1982).
2. P. Mertens and Th. Krist, "The Energy Loss of 300 keV He^+ and N^+ in 150 to 800 Å Carbon Foils", Nucl. Instr. Methods (1982), in press.

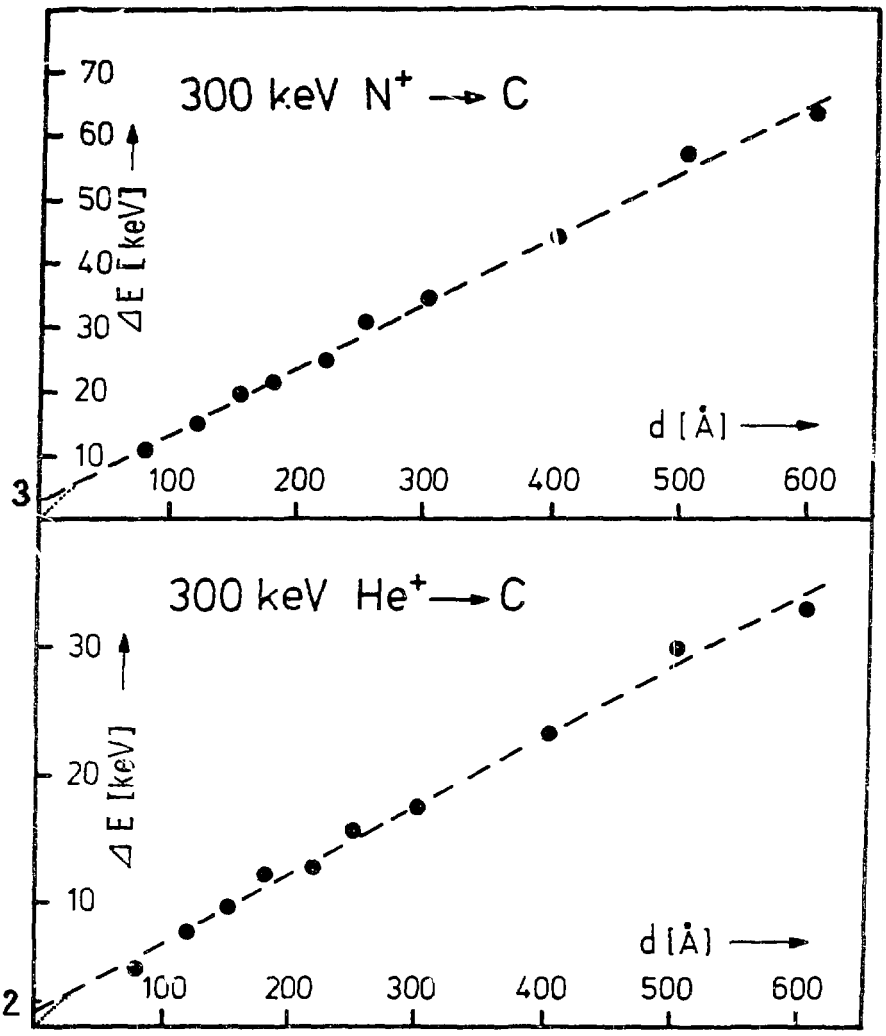

Fig. 1 Energy loss of 300 keV N^+ and He^+ ions in carbon foils as a function of foil thickness measured by a magnetic spectrometer. The foil thickness was determined by a quartz oscillator.

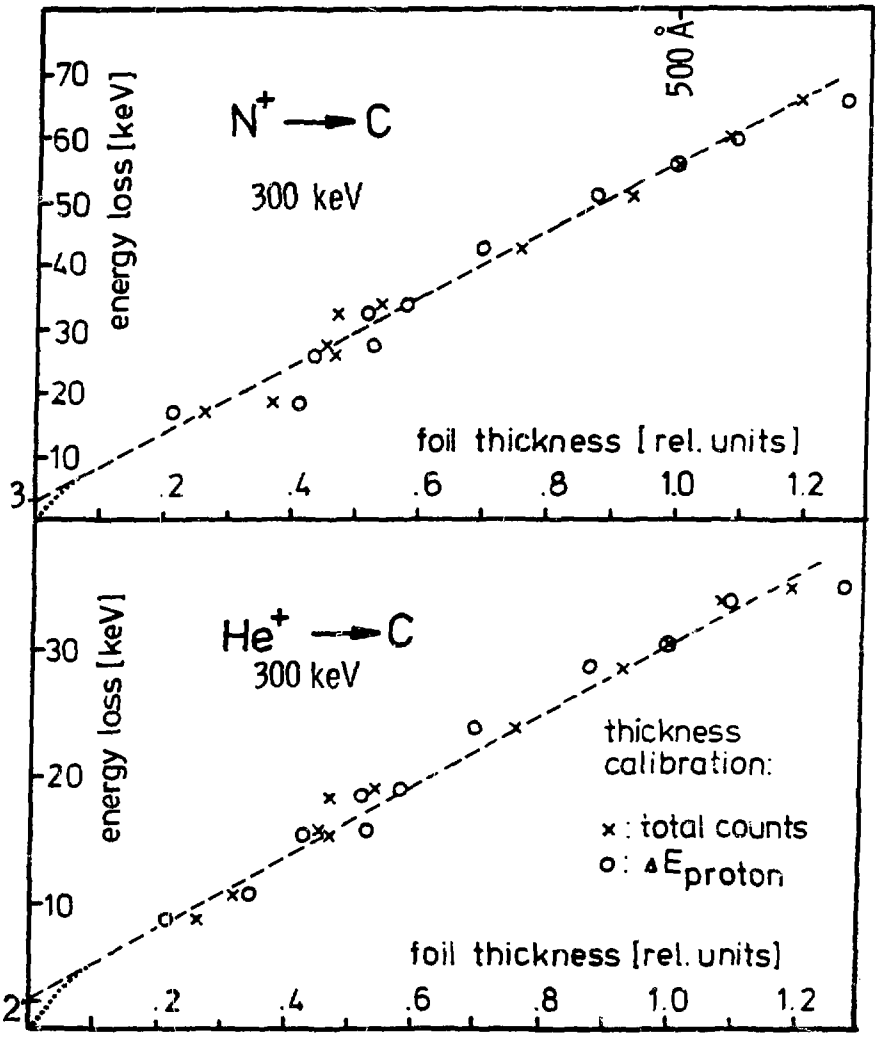

Fig. 2 Energy loss of 300 keV N^+ and He^+ in carbon as a function of foil thickness measured by a magnetic spectrometer. The foil thickness was determined by Rutherford backscattering with 300 keV H^+ (x) and by proton energy loss measurements (o).

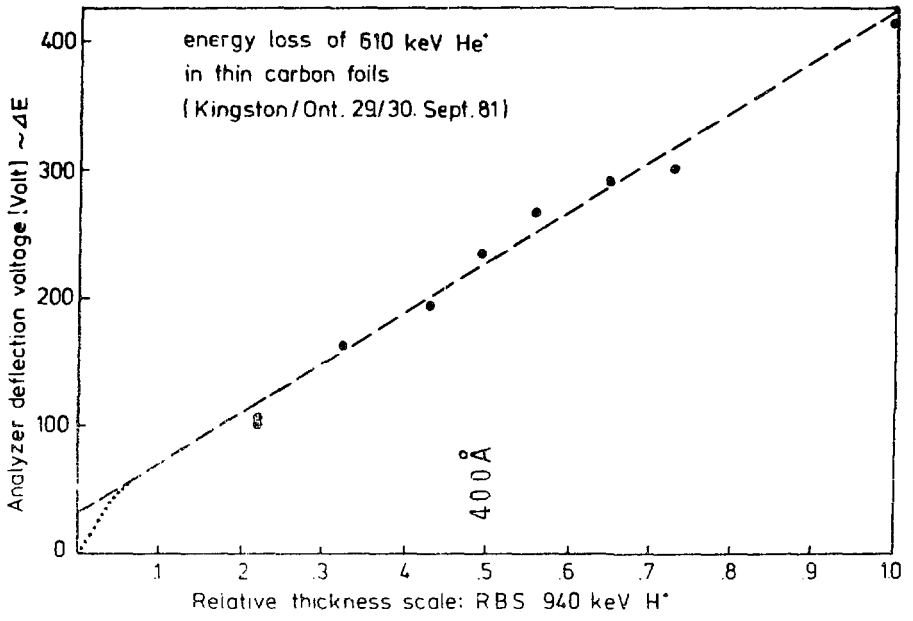

Fig. 3 Energy loss of 610 keV He^+ in carbon as a function of foil thickness as measured with an electrostatic energy analyzer. The foil thickness was determined by Rutherford backscattering with 940 keV H^+.

ENERGY LOSS OF HEAVY IONS AS A FUNCTION OF TARGET THICKNESS: Ne → C

W.N. Lennard, H.R. Andrews, I.V. Mitchell, D. Phillips and D. Ward
Atomic Energy of Canada Limited Research Company
Chalk River Nuclear Laboratories
Chalk River, Ontario, Canada K0J 1J0

Abstract

We report on extensive measurements to determine the target thickness dependence of heavy ion energy loss (dE/dx) for the Ne → C system. For ions transmitted with zero net deflection at velocities $0.75 \leq v/v_0 \leq 1.05$, a significant dependence of dE/dx on foil thickness has been observed which, parametrized through the Meyer-Klein-Wedell theory, identifies an inelastic component in the energy loss for scattered particles. A discussion is given of some of the precautions that have proved necessary in applying time-of-flight techniques to these energy loss measurements.

1. INTRODUCTION

When energetic heavy ions pass through a solid they lose energy by a variety of complex processes. Generally it is supposed that the specific energy loss, (dE/dx), comprises an electronic part arising from collisions with zero deflection, $(dE/dx)_e$, and a part which originates in atomic collisions with deflection, $(dE/dx)_c$, usually identified with the nuclear energy loss, $(dE/dx)_n$. Provided the multiple scattering process can be taken into account, it should be possible to separate experimentally $(dE/dx)_e$ and $(dE/dx)_c$ by measuring stopping powers either as a function of angle or of foil thickness. The importance of multiple scattering in treating these effects is very clear; for example, it is multiple scattering that, through the collision term, introduces a dependence of (dE/dx) on foil thickness.

The most comprehensive study of the dependence of (dE/dx) on foil thickness has been performed by Högberg (1), who found that (dE/dx) for heavy ions in carbon decreased strongly with decreasing foil thickness. It was argued that because of the small acceptance angle of

the detector set at zero degrees there could be no contribution from $(dE/dx)_n$ for a foil of zero thickness; hence the extrapolated (dE/dx) should be identified with $(dE/dx)_e$ and the excess for foils of finite thickness be identified with $(dE/dx)_n$.

A new treatment of the stopping problem has been given by Meyer, Klein and Wedell (2) (MKW) in which they developed approximate procedures to calculate the full energy-angle distribution, taking into account multiple scattering. In their treatment, the term $(dE/dx)_C$ is not taken to be $(dE/dx)_n$ since they wish to allow explicity for inelastic atomic collisions, $(dE/dx)_i$, i.e. they set

$$(dE/dx) = (dE/dx)_e + (dE/dx)_i + (dE/dx)_n \qquad [1]$$

In their work they consider that the electronic stopping power should be the sum of the first two terms; hence, they regard the interpretation given by Högberg as incorrect in that $(dE/dx)_i$ was not allowed to contribute to the electronic stopping in a foil of zero thickness. To some extent this is a matter of definition for it is equally useful to associate $(dE/dx)_i$ with $(dE/dx)_n$ and refer to a collisional stopping power, $(dE/dx)_C$, particularly since in MKW theory these terms are assumed to have the same angle dependence.

To date MKW theory has been applied to measurements made on carbon foils in the velocity range $0.2 < v/v_0 < 0.5$ by Högberg (1), Ormrod and Duckworth (3) and by Beauchemin and Drouin (4) (v_0 is the Bohr velocity). The magnitude of $(dE/dx)_i$ was generally found to be comparable to $(dE/dx)_n$. That is, treatments including only elastic scattering effects, $(dE/dx)_n$, considerably underestimate the observed angle and thickness variation. At higher velocities $v/v_0 \sim 1$, we concluded from a MKW analysis (5) of our previous sparse data on thickness dependence of (dE/dx) for Ne ions in nickel, silver and gold foils (6) that $(dE/dx)_i$ must be $\sim$5-10 times greater than $(dE/dx)_n$.

The present experiments were undertaken to examine in a systematic and more detailed way the dependence of (dE/dx) on foil thickness

in the velocity range $0.75 \leq v/v_0 \leq 1.1$. Measurements were carried out for ^{20}Ne ions stopping in carbon foils.

2. EXPERIMENTAL

The CRNL High Voltage Mass Separator provided primary beams of ^{20}Ne and ^{4}He for these experiments. These beams were then scattered by a thin gold foil (~ 70 μg cm^{-2}) to provide a low intensity flux into the time-of-flight apparatus aligned at 32° to the incident separator beam. An advantage of this setup was that beam induced damage and contamination of the samples were avoided. Energy losses were measured in transmission geometry by interposing thin sample foils of carbon into the scattered beam. The energy loss was determined by measuring the ion velocities with and without the samples in position.

Energies were deduced by timing the passage of the ions between two carbon foils, C_1 and C_2, separated by a flight path of 0.940 m. Electrons liberated at these foils, due to the passage of an ion, were accelerated through ~ 1 kV into microchannel plates from which timing signals were derived. Several improvements have been incorporated since the apparatus was described in ref. 6, see ref. 7: (i) the start and stop detectors were mounted perpendicular to the ion trajectories (cylindrical symmetry) rather than at 45°, which considerably reduced the dispersion in flight times arising from different trajectories, and (ii) the polarity of the microchannel plates was reversed making the front face positive with the carbon foil at ground potential. This latter step was taken to avoid possible systematic effects inherent in the previous electrical configurations in which the carbon foils were biassed at ~ -4 kV. With that configuration it was possible to change the energy of ions traversing the first foil C_1 if there were a shift in the mean charge state of the ions on passing through the foil. From charge state measurements by Lennard and Phillips (8), we could conclude that this systematic effect in our previous data (6) translated to an uncertainty $\sim 2\%$ in the derived stopping powers. Nevertheless, we felt it was worthwhile to eliminate the effect entirely.

3. EXPERIMENTAL PROCEDURES

Procedures for calibrating the time-of-flight system and for taking data are described in ref. 7. The sample holder held five foils with an additional blank position. The thicknesses of the foils were determined by measuring the energy loss of ^{4}He ions at $\sim$700 keV incident energy and assuming the stopping power values recommended by Ziegler (9).

The energy loss measurements for ^{20}Ne ions were performed at several incident energies, varied according to the foil thicknesses, in order that the final results could be interpolated to common velocities, v/v_0 = 0.75, 0.85, 0.95 and 1.05.

4. ANALYSIS

We have chosen to define energy losses in terms of their most probable values. Since the observed peaks were not symmetric but skewed to larger energy loss, this did not correspond with analysis in terms of mean energy losses. However, in those cases where we have compared with a centroid analysis of the obvious peak region, the differences in the final stopping powers between most probable and centroid analyses were found to be less than 1%. In a true centroid analysis it would be necessary to include events down to zero energy. Such an analysis was considered impractical for our purposes.

The most probable channel numbers were determined by a computer program which fitted a Gaussian shape to the peak. The channel limits for the fit were determined through an iterative procedure, setting the limit on the 'Gaussian side' (shorter times) of the peak to twice the fitted standard deviation (2σ) from the fitted mean and on the 'skewed side' (longer times) to 1σ from the mean. This procedure was convenient for determining peak shifts in a consistent and objective way. A typical example is shown in Figure 1.

The beam velocity was defined by a 'sample out' time-of-flight measurement and no direct use has been made of the accelerator energy calibration. A small correction to the observed velocity was made for the energy loss in the $\sim$7 μg cm^{-2} carbon foil at the first channel

plate. (The stopping powers for ^{20}Ne in C reported in ref. 6 were used for this purpose.) An additional correction was introduced to derive the most probable energy from the measured most probable flight time. This was a very small effect (<1%) and was calculated with good precision taking the width parameter of the Gaussian derived from the fit to the raw data.

To interpolate the (dE/dx) values to common velocities for all foil thicknesses, a computer code was developed which fitted by least squares a polynomial of arbitrary order to the velocity dependent measurements. In all cases the data were found to be roughly linear over the range $0.7 < v/v_0 < 1.1$ (but with intercepts not generally zero); however, examination of the chi-squared values showed that the addition of a small quadratic term generally gave a significantly better fit.

Since we were concerned with the dependence of (dE/dx) on foil thickness, it was essential to give careful consideration to the treatment of the finite energy loss. The data showed that (dE/dx) was nearly linear in velocity; therefore we have used the following definitions:

$$(dE/dx)_v = (E_{in} - E_{out})/t \qquad [2]$$

with

$$v = (v_{in} + v_{out})/2 \qquad [3]$$

E_{in} (v_{in}) is the most probable incident energy (velocity), E_{out} (v_{out}) is the most probable exit energy (velocity), and t is the target thickness. Results of this treatment were compared with more elaborate procedures involving integration through the foil thickness taking into account the quadratic parameterization of (dE/dx) versus velocity. The results were found to agree with equations [2] and [3] at the level of <1% even for the thickest foils.

The final values for (dE/dx) as a function of foil thickness are shown in Figure 2. The statistical uncertainties in the thickness determinations are included. There is a further uncertainty ($\sim 4\%$) in the absolute values arising from the assumed ^{4}He stopping powers (9) but this has not been included since it represents an overall scaling of the thickness dependence.

5. COMPARISON WITH MKW THEORY

A full description of MKW theory may be found in the original paper (ref. 2); a convenient summary of the main results has been given by Beauchemin and Drouin (4). For a single collision MKW write the energy loss as:

$$q(\eta) = c_0 + (c_2 + c_n)\eta^2 \qquad [4]$$

where η is a reduced scattering angle, c_2 and c_n are coefficients describing the inelastic and elastic energy losses respectively and c_0 is the energy loss associated with zero angular deviation. For passage through a foil of thickness t, the most probable energy loss at zero degrees has a similar form:

$$Q_m(0) = nc_0 + (c_2 + c_n)\,\vartheta_m(0) \qquad [5]$$

where n is the number of collisions, assumed to be equal to the number of atomic layers in the foil through the relation

$$n = \frac{\pi}{4} N^{1/3} \frac{t}{\rho} \qquad [6]$$

Here N is the number of atoms per cm^3, ρ is the density (g cm^{-3}) and t is the target thickness (g cm^{-2}). For carbon n = 16.87 when ρ = 2.25 g cm^{-3}. The quantity $\vartheta_m(0)$ in equation [5] is the most probable reduced energy loss for observation at zero

degrees. It is tabulated by MKW as a function of the reduced foil thickness, τ, where

$$\tau = \pi a^2 N \frac{t}{\rho} \qquad [7]$$

Here, a is the usual screening parameter given by $a = 0.8853\ a_0 [Z_1^{2/3} + Z^{2/3}]^{-1/2}$. For Ne in carbon, $\tau = 0.435\ t$ (t in $\mu g\ cm^{-2}$).

It can be seen that the form of equation [5] corresponds exactly with that of equation [1]. The quantity nc_0 is the electronic energy loss and $(c_2 + c_n)\ \mathcal{Q}_m(0)$ is the collisional energy loss made up of elastic (nuclear) and inelastic components. These same parameters in MKW theory also give the energy loss in a single atomic collision by eq. [4].

To analyze the thickness dependence, the data were least squares fitted to equation [5] with c_0 and $(c_2 + c_n)$ as free parameters. The results are shown in Figure 2. Unfortunately MkW tabulate $\mathcal{Q}_m(0)$ only to $\tau = 15$ so that only data for thicknesses $< 35\ \mu g\ cm^{-2}$ were used to obtain the fitted values. Extrapolated values of $\mathcal{Q}_m(0)$ were used to extend the fitted curves to larger thicknesses; these are the dashed portions of fig. 2. Overall the fits were good with normalized chi-squared values ~2-6. This indicates that the uncertainties (calculated from the statistical errors of the peak fitting) correspond to a scatter in the data of about half that observed. The quantity c_n is calculated from

$$c_n = \frac{4 M_1}{E M_2} \left(\frac{Z_1 Z_2 e^2}{a}\right)^2 \qquad [4]$$

Results for c_0, c_2 and c_n are shown in Table 1.

6. DISCUSSION

Stopping powers for the Ne → C system show marked thickness dependence. In all cases the MKW fits reproduce the shape of this dependence reasonably well. The extracted MKW parameters in carbon show that the contribution of inelastic collisions, c_2, to the total energy loss exceeds that of the nuclear scattering, c_n, by a factor of 3-4. There are no points of energy overlap where we might compare our data with that of other workers. The values obtained by Beauchemin and Drouin (4) for Ne and Ar in carbon were obtained at a smaller velocity. If the experiments may be compared, then apparently the coefficient c_2 must remain constant between their highest velocity, $v/v_0 = 0.47$ up to $v/v_0 = 0.75$, where our data begin.

We observed that the values of c_0 appear to increase roughly linearly with velocity. According to the theory of Lindhard, Scharff and Schiott (LSS) (11), the electronic stopping power should have the form $S_e = k(v/v_0)$ where $k = 3.78$ (keV cm^2 µg^{-1}). In general, our values for nc_0, which is to be identified with S_e, are 17% lower than the LSS prediction although they have approximately the same velocity dependence. Our c_0 value for ^{20}Ne → C at $v/v_0 = 0.85$ is ∿ 11% lower than extracted from ref. 4 extrapolated to the same velocity.

A further test of MKW theory would be to measure both the angle and thickness dependence for the same system. To date this has been done only by Högberg (1). The MKW parameters derived from the angular dependence for ^{14}N → C at 32.5 keV agreed roughly with those derived from the thickness dependence (2); however, as noted above, the fit to the thickness dependence was unsatisfactory. It would be desirable to examine whether or not the angle dependence for the Ne → C system studied here could be reproduced with the present parameter values.

Mertens and Krist (12) have recently measured energy losses (ΔE) for 300 keV ^{4}He, ^{14}N in C. They find a linear dependence of ΔE on the foil thickness for both projectiles, where the target thicknesses were obtained from, separately, quartz microbalance measurements, proton

energy loss data, and Rutherford backscattering data, the latter two using 300 keV ^{1}H particles. They hypothesized that particles heavier than protons and penetrating a solid experienced increased "pre-equilibrium" stopping. They conclude that dE/dx for $^{14}N \rightarrow C$ is larger for the first few atomic layers than throughout most of the foil, since the $\Delta E(^{14}N)$ versus target thickness (t) straight line plot has a positive intercept for t = 0. A straight line extrapolation of our $^{20}Ne \rightarrow C$ data to t = 0 yields a negative intercept, in disagreement with their result. Further measurements are in progress to determine our target thickness using the energy loss of protons.

7. SUMMARY

We have measured the thickness dependence of the most probable energy loss for Ne ions in carbon in the velocity range $0.75 \leq v/v_0 \leq 1.05$. Our data have been analyzed within the framework of the MKW theory, and show that there is indeed a thickness dependence that is too large to be explained by elastic (nuclear) energy loss alone. We find that we need a term that is 3-4 times larger than the elastic term to explain the data. Our data are consistent with another recent experiment on the same system that measured the energy loss as a function of angle at lower velocities (ref. 4). Our results are not in agreement with those of Mertens and Krist (12) for a similar system. Further careful experiments are necessary to resolve the disagreement.

REFERENCES

1. G. Högberg, "Electronic and Nuclear Stopping Cross Sections in Carbon for Light Mass Ions of 4.5-46 keV Energy", Phys. Stat. Sol. (b) 48 (1971) 829.
2. L. Meyer, M. Klein and R. Wedell, "The Energy-Angle Distribution of Heavy Particles Penetrating Solids", Phys. Stat. Sol. (b) 83 (1977) 451.
3. J. Ormrod and H. Duckworth, "Stopping Cross Sections in Carbon for Low-Energy Atoms with $Z \leq 12$", Can. J. Phys. 41 (1963) 1424.

4. G. Beauchemin and R. Drouin, "The Energy-Angle Distribution of Heavy Particles Pentrating Solids: Experimental Test of the Mayer-Klein-Wedell Theory for Ne and Ar Ions in Carbon Below 250 keV", Nucl. Instr. Meth. 160 (1979) 519.

5. H.R. Andrews, W.N. Lennard, I.V. Mitchell, D. Ward, D. Phillips and R.B. Walker, "Low Energy Stopping Powers Determined by Time-Of-Flight Techniques", IEEE Trans. Nucl. Sci. NS-26 (1979) 1326.

6. D. Ward, H.R. Andrews, I.V. Mitchell, W.N. Lennard, R.B. Walker and N. Rud, "Systematics for the Z_1-Oscillation in Stopping Powers of Various Solid Materials", Can. J. Phys. 57 (1979) 645.

7. W.N. Lennard, H.R. Andrews, M. Freeman, I.V. Mitchell, D. Phillips, D.A.S. Walker and D. Ward, "Time-Of-Flight System for Slow Heavy Ions", Nucl. Instr. Meth. (to be submitted).

8. W.N. Lennard and D. Phillips. "Mean Charge of Ions ($5 \leq Z_1 \leq 26$) Emerging from Carbon Foils: Evidence for the Effect of Inner-Shell Vacancies", Phys. Rev. Lett. 45 (1980) 176.

9. J.F. Ziegler, Stopping Powers and Ranges in All Elements, Vol. 4 (Pergamon Press, 1977).

10. P.R. Bevington, Data Reduction and Error Analysis for the Physical Sciences, (McGraw-Hill, Inc. 1969).

11. J. Lindhard, M. Scharff and H.E. Schiott, "Range Concepts and Heavy Ion Ranges", Kgl. Danske, Videnskab. Selskab., Mat.-Fys. Medd. 33, No. 14 (1963).

12. P. Mertens and T. Krist, "The Energy Loss of 300 keV He^+ and N^+ in 150-700 Å Carbon Foils", Nucl Instr. Meth. (1982, in press).

FIGURE CAPTIONS

Figure 1 - Gaussian fits to typical data to determine the peak (most probable) position.

Figure 2 - Results for the thickness dependence of stopping powers. The solid lines are fits to MKW theory. The dashed extensions of the curves are calculated with the fitted parameters and extrapolated values from the MkW tables (cf. text).

TABLE I

Summary of the coefficients c_0, c_2 and c_n extracted from the present work using MKW theory (units are keV).

v/v_0	c_0	c_2	c_n
0.75	0.138 ± 0.001	1.64 ± 0.20	0.65
0.85	0.156 ± 0.001	2.00 ± 0.12	0.50
0.95	0.182 ± 0.001	1.68 ± 0.13	0.40
1.05	0.210 ± 0.001	1.38 ± 0.14	0.33

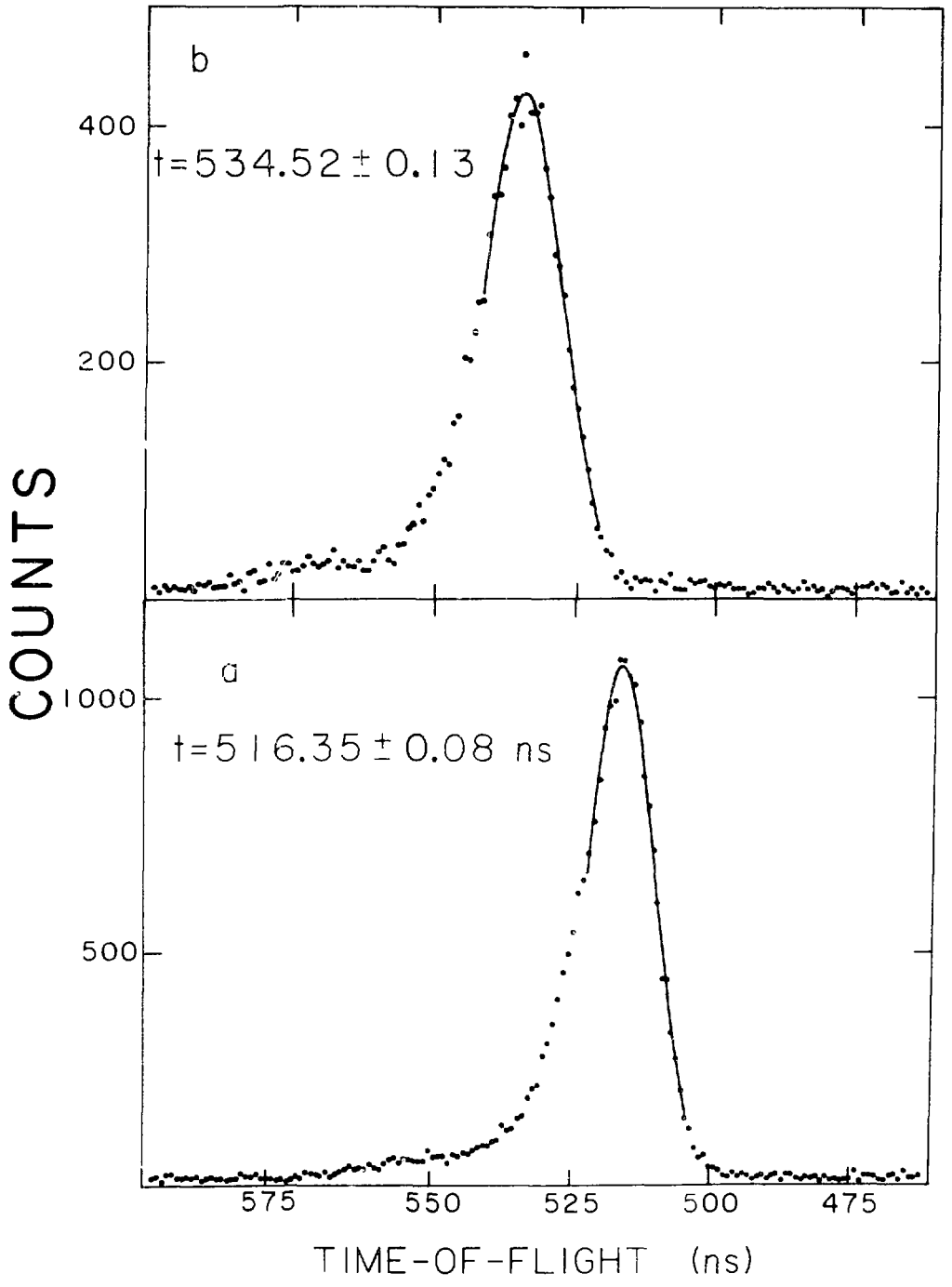
b
t=534.52±0.13
400
200
a
t=516.35±0.08 ns
1000
500
COUNTS
575
550
525
500
475
TIME-OF-FLIGHT (ns)

Figure 1

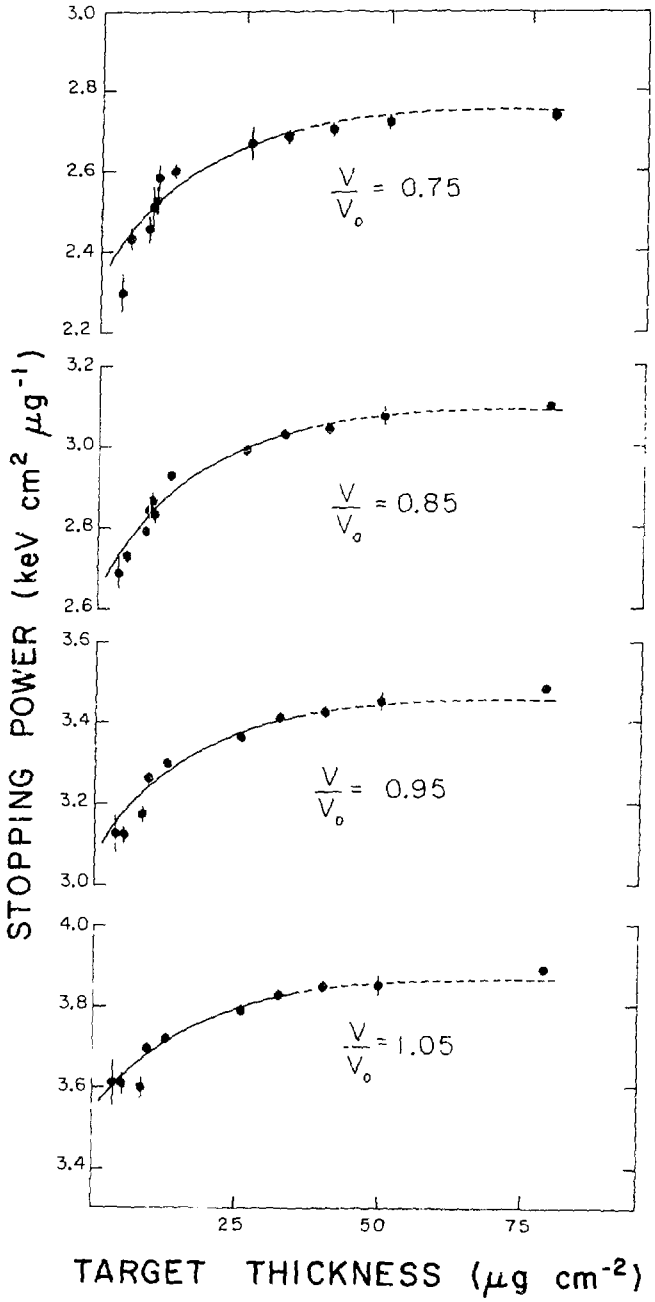
STOPPING POWER (keV cm² μg⁻¹)
TARGET THICKNESS (μg cm⁻²)
V/V₀ = 0.75
V/V₀ = 0.85
V/V₀ = 0.95
V/V₀ = 1.05
3.0
2.8
2.6
2.4
2.2
3.2
3.0
2.8
2.6
3.6
3.4
3.2
3.0
4.0
3.8
3.6
3.4
25
50
75

Figure 2

Estimation of Fluctuation in Restricted Energy Loss

Tadayoshi Doke*, Takayoshi Hayashi*
and Katsuaki Nagata**

*Science and Engineering Research Laboratory, Waseda University, Kikuicho-17, Shinjuku-ku, Tokyo, Japan

**Physics Laboratory, Faculty of Engineering, Tamagawa University, Machida-shi, Tokyo, Japan

1. Introduction

"Restricted Energy Loss (REL)" is defined as an energy loss $[(dE/dX)_{E_\delta \leq \omega}]$ that produced the δ-rays of energies less than some specified energy ω and is often used as a simple measure of track structure. For example, REL is a measure of track formation threshold in plastic track detector and the growth rate of track in chemical etching solution is considered to depend only on REL given along the track. Using a stack of plastic sheets, recently, it became possible to identify isotopes of incident particles. In that case, the limit of mass resolution is determined by fluctuation of REL in the length of etch pit produced along the path of particle.

In the middle of the 1970's, Badhwar[1] and Adams, Silberberg and Badhwar[2] made a computer program to calculate the probability distribution for energy deposition in absorber allowing for electron escape. In this calculation, it is assumed that all electrons with energies greater than a certain value ε_d escape. This means that this calculation directly gives the fluctuation of REL. Therefore, we tried to use the computer program developed by Adams et al.(ASB) to estimation of the ultimate mass resolution in plastic detector as mentioned above. In this paper, we show firstly the comparison of ASB's calculation with the experimental results obtained by a gas counter and next the results of estimation of ultimate mass resolution in plastic detectors.

2. Comparison of ASB's calculation with experimental results

Most resently, Nagata, Kikuchi, Doke and Gruhn measured the energy deposition in a gas proportional counter of effective length of 10 cm, filled with Ar + CH_4(7 %) gas mixture of various gas pressure, for high energy helium, carbon, neon, argon and iron ions[3, 4] and found that their deposited energy distribution are in good agreement with those calculated by ASB's computer program. Table 1 shows the experimental conditions in these measurements. In this table, $\kappa = \xi/\varepsilon_{max}$, where $\xi = 2\pi Z_1^2 e^4 Nx/mv^2$ ($Z_1 e$ and v ; nuclear charge and velocity of incident particle, e and m ; charge and mass of electron, N and x ; volume density of electrons in absorber and thickness of absorber) and ε_{max} is the maximum energy transferred to electron in absorber by an incident particle. The comparisons between fwhm-values of the deposited energy distributions

obtained by the calculation and by the experiment are shown in Fig. 1. Namely, Fig. 1 shows the variation of fwhm-value of deposited energy distribution as a function of the atomic number of the particle Z_1, measured for particles heavier than carbon ions under the condition $\kappa < 0.01$, as well as the theoritical curves for ε_d = 10, 15 and 20 keV obtained by ASB's calculation, where ε_d is the deposited energy of escaping electrons from absorber and is an adjustable parameter for fitting the calculated distribution to the experimental one. As seen in the figure, the expermental results shows the same tedency as those obtained by calculation and, except argon data , are on the calculated lines for ε_d = 10 and 15 keV, which correspond to the electron (extrapolated) ranges of 1/4 and 1/8 of the counter thickness. Fig. 2 also shows the variation of the fwhm-value of deposited energy distribution as a function of the counter gas pressure for helium(^{3}He) ions under the Vavirov region(κ = 0.03 ∿ 0.3). The black squaures represent the experimental data and the open circles represent the fwhm-values obtained from ASB's computer program assuming that ε_d equal to the energy corresponding to the electron range of 1/8 of the counter thickness . The agreement between the experimental value and the calculated ones is very good. As seen from the inserted figure, the deposited energy spectrum calculated for the low pressure counter has a bump in the high energy side. In this region, however, we do not yet ascertain whether the calculated spectrum is correct or not.

3. Application of ASB's calculation to estimation of fluctuation in REL

Here, let us apply ASB's calculation to estimation of REL fluctuation, which is required from a view-point of isotope-identification by a stack of plastic sheets. Firstly, we explain the outline of the isotope-identification method.

i) Outline of isotope-identification method

To identify the mass of heavy particles, a stack of plastic sheets as shown in Fig. 3 is used. After irradiation of heavy particles, the plastic sheets are etched in NaOH solution under the same condition. Then, the etch pits as shown in Fig. 3 appear on both side of each plastic sheet, excepting a final sheet, in which the particle stopped. If the cone length of etch pit L are plotted as a function of residual range R, we find a curve, which corresponds to a certain isotope, as shown in Fig. 4. Such a curve shifts toward the right-side with increase of mass and charge of particle. If the fluctuation of L is smaller than the gap between two adjacent curves, therefore, we can identify their two particles. For example, the vertical separation between ^{55}Fe and ^{56}Fe is about 2 % and therefore, if the fluctuation(r.m.s.) of length of etch pit, including measurement error, is less than 1 %, ^{55}Fe can be identified from ^{56}Fe. Recently, we found that the fluctuation of the track length(= 200 μm) of etch pit in CR-39 plastic produced by Fe ion of 100 MeV/n is roughly 1 %[5]. Next, we will estimate the fluctuation of L caused by the fluctuation of

REL under the same condition.

ii) Estimation of fluctuation of L

We can estimate the fluctuation of REL over a certain length by putting that $\varepsilon_d = \omega$, where ω depends upon the kind of plastic film, for example, ω = 200 eV for CR-39 plastic[5]. To obtain the fluctuation of L from the fluctuation of REL, we must know the relation between L and REL. If all plastic sheets in a stack are etched under the same condition, L is proportional to the growth rate of etch pit V_T. In general, V_T is a function of only REL and is given the following formula,

$$V_T(\propto L) = a(REL)^n.$$

For CR-39 plastic, n is given to be 2.2 in the present region. Therefore, we can estimate $\Delta L/L$ from $\Delta(REL)/REL$ using the relation of $\Delta L/L = 2.2\Delta(REL)/REL$, where Δ means the r.m.s. value of the fluctuation. Thus, we estimated $\Delta L/L$ for the etch pit length of 200 μm in CR-39 plastic irradiated by 100 MeV/n iron-ions. The results for the cases of ω = 100, 200, 300, 500 and 1000 eV are shown as a function of the energy of iron-ions. From the figure, we can obtain $\Delta L/L$ = 0.143 %. However, the actual fluctuation of L was 1%. The difference between the calculation and the experiment can not be explained even if the measurement error of ± 0.5 % is taken into consideration. Now, we consider that the main part of the fluctuation of L comes from the inhomogneity of sensitivity in plastic. If so and the inhomogeneity in CR-39 plastic is reduced to half, it is expected that the mass resolution of CR-39 plastic becomes comparable to that of semiconductor detector telescope.

References

1) G.D.Badhwar, Nucl. Instr. Meth. 109 (1973) 119
2) J.H.Adams, Jr.R.Silberberg amd G.D.Badhwar, Nucl. Instr. Meth. 124 (1975) 551
3) K.Nagata, J.Kikuchi, T.Doke and C.R.Gruhn, Nucl. Instr. Meth. 188 (1981) 217
4) K.Nagata, J.Kikuchi, T.Doke and C.R.Gruhn, Nucl. Instr. Meth. to be published.
5) T.Hayashi. R.Hamasaki and T.Doke, Nuclear Tracks, to be published.
6) D.L.Henshaw, N.Griffiths, A.L.Landen and E.V.Benton, Nucl. Instr. Meth. 180 (1981) 65

Table 1

Projectile	^3He	^3He	^3He	^{12}C	^{20}Ne	^{40}Ar	^{56}Fe
Energy(MeV/n)	40	40	40	450	670	1800	1870
Gas pressure (atm.)	0.10	0.21	0.49	0.10	0.10	0.10	0.10
κ	0.064	0.13	0.31	0.0061	0.0085	0.0053	0.0105

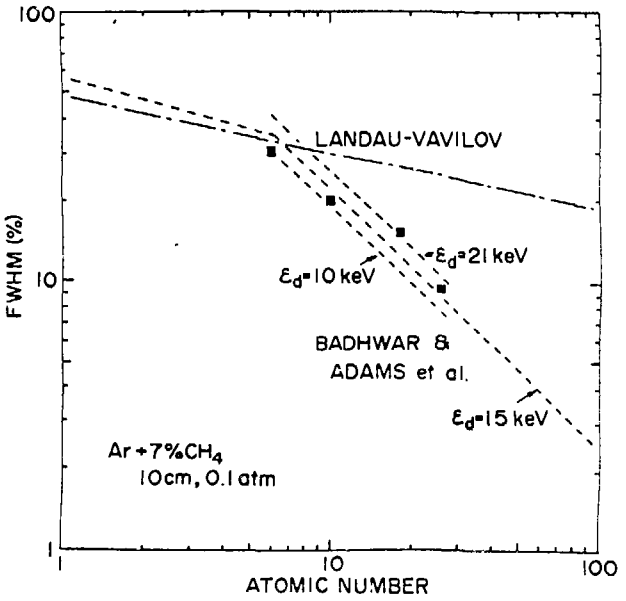

Fig. 1. Fwhm's value versus atomic number of thr particles. Squares show experimental results, the chain line shows the theoretical fwhm's of the Landau-Vavirov distribution, and the broken lines show the fwhm's values obtained by ASB's calculation.

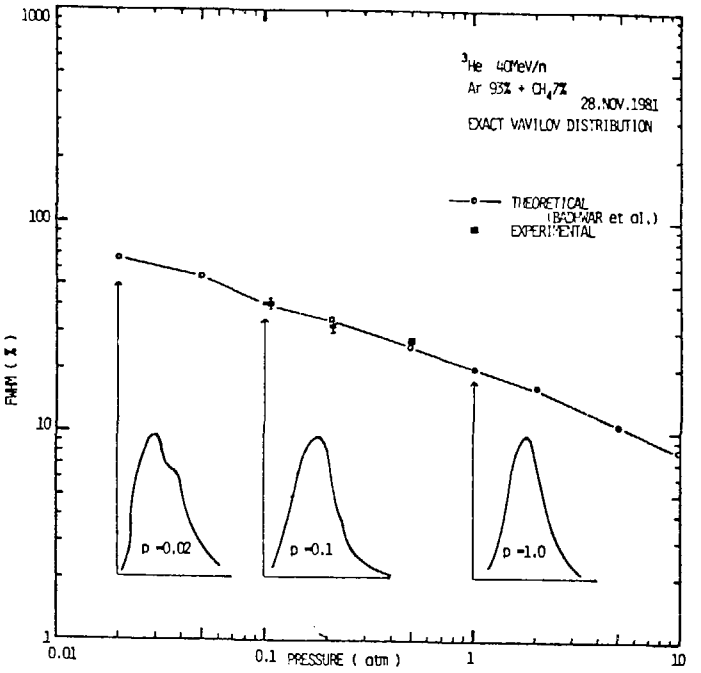

Fig. 2. Fwhm's value for 40 MeV/n ^{3}He ions versus the counter gas pressure. Squares show experimental results, open circles show the fwhm's values obtained by ASB's calculation for ε_d corresponding to the electron range of 1/6 × the counter thickness. The inserted figures show the deposited energy distributions obtained by ASB's calculation.

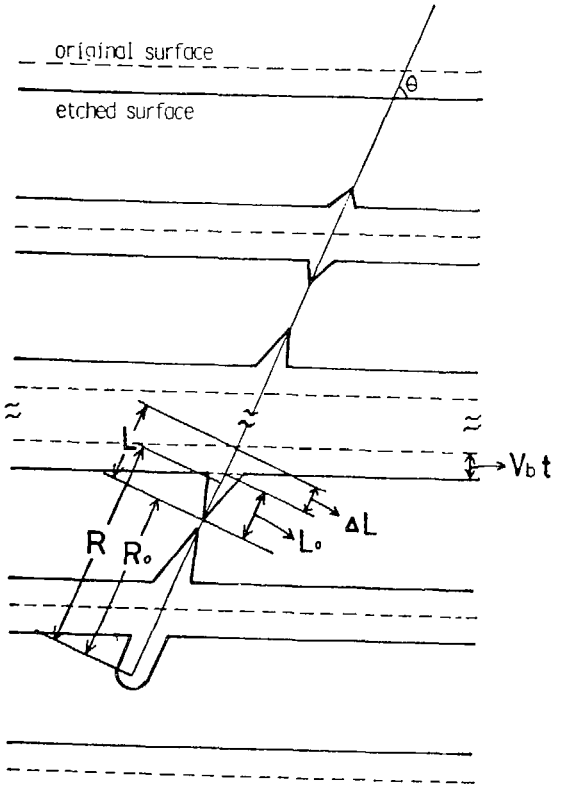

Fig. 3 Method of particle identification by measuring etch pit lengths L at residual ranges R.

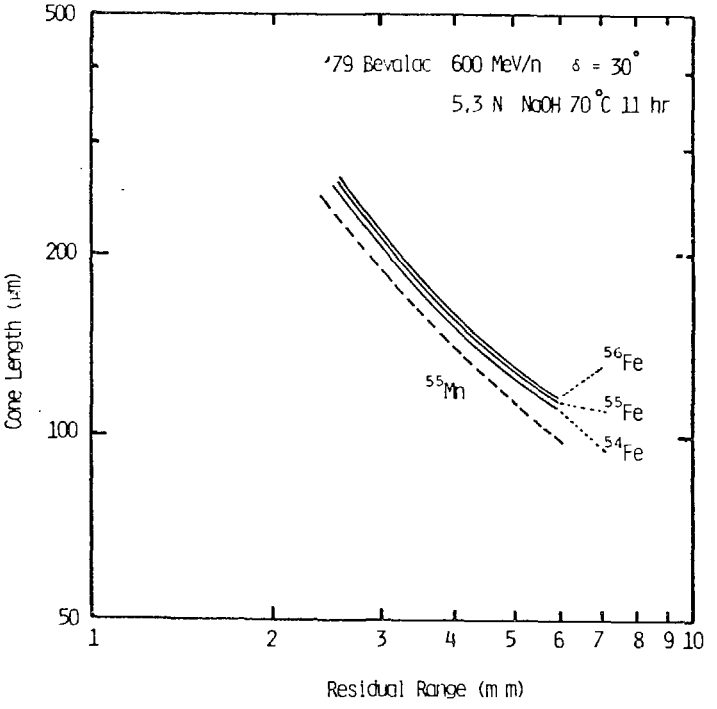

Fig. 4 The variation of etch pit length L in plastic sheets etched under the same condition as a function of residual range R.

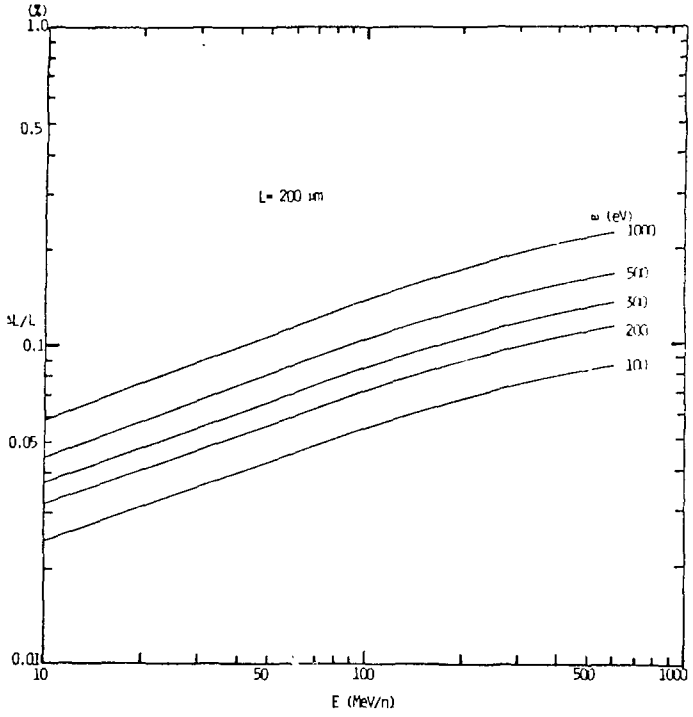

Fig. 5 The variation of $\Delta L/L(\%)$ as a function of iron particle energy for various values of ω.

INERTIAL-CONFINEMENT FUSION APPLICATIONS OF ION STOPPING THEORY

Richard M. More, Yim T. Lee, and David S. Bailey
University of California, Lawrence Livermore National Laboratory
Livermore, California 94550

Inertial-confinement fusion research has recently raised a variety of novel questions about range and energy-loss of fast ions in hot matter.

In part, our interest in ion energy-loss is stimulated by proposals for a hypothetical future accelerator which would have sufficiently intense beams for use as a target irradiation facility. This approach is regarded as promising since accelerators offer efficient beam generation and appear to have good coupling of beam energy into a fusion target. For this application, the main scientific questions concern energy-deposition in hot targets.

Existing range-energy data refers to solid or low-temperature gas targets composed of neutral atoms or molecules; however, inertial fusion plasmas will have temperatures up to 1 keV resulting in highly-charged target ions. Theoretical calculations performed by Nardi, Peleg and Zinnamon[1] predict a significant shortening of ion ranges in heated targets. This effect is caused by thermal ionization; free electrons are better able to accept small energy-transfers. The calculated range-shortening would substantially improve the performance of certain concepts for heavy-ion fusion targets.

Even in current laser-fusion experiments we are strongly interested in the thermalization of charged particles resulting from thermonuclear reactions. The basic question here is whether the thermonuclear reaction will be self-sustaining; as the deuterium-tritium fuel reacts it must heat itself sufficiently to make up for various cooling mechanisms. The physics question thus concerns the range and stopping of α particles and protons both in the D-T fuel and also in possible target capsule materials.

From the theoretical side, we are also interested in methods employed in ion stopping theory. If one can accurately calculate the collisions of heavy atoms in the multi-keV energy-range for ion

stopping, then it is probable that similar methods can be applied to calculate ion encounters which occur at thermal energy in hot plasma targets.

We would therefore like to develop methods to calculate:

1) The stopping power of a hot plasma target,

2) The charge-state of a fast ion projectile,

3) The final disposition of the deposited energy.

The first issue refers to the stopping power for protons. As mentioned, the proton stopping power is altered in high-density or high-temperature targets, especially at velocities below the stopping peak.[1-4,10] The second issue concerns the application of a proton stopping curve to the arbitrary projectile. Much less is known on this subject. In particular, we are skeptical about the usefulness of the usual idea of an equilibrium charge state Q(v) that is independent of the target material or irradiation conditions. For example, very heavy ion projectiles (i.e., 10 GeV uranium ions) which enter the target in a neutral state probably do not strip to their equilibrium charge state before significantly slowing down. If the charge state is affected by charge-transfer from target atoms, it will change with their temperature. The third topic is more specialized to inertial fusion and concerns the partition of deposited energy between ion (nuclear motion) degrees of freedom and those corresponding to bound and free electrons. The question here is whether a thermal equilibrium plasma is produced.

THEORETICAL MODELS FOR ION ENERGY-LOSS PHENOMENA

In this talk we summarize a few results obtained from statistical models of the Thomas-Fermi family. These models are not necessarily the most elaborate or accurate, and in some cases there are substantial corrections to Thomas-Fermi predictions. We limit ourselves to the statistical models because they offer the simplest comprehensive picture of ion collision and range phenomena.

Three specific Thomas-Fermi models are found to be useful:

a) The isolated Thomas-Fermi groundstate ion. In this model a nucleus of charge Z is surrounded by a spherically symmetric cloud of

bound electrons. The net ion charge is Q. We are interested in the ion radius R(Z,Q), the ionization potential I(Z,Q), mean ionization-excitation potential $\bar{I}(Z,Q)$, dipole polarizability $\alpha(Z,Q)$, and cross-sections for recombination or ionization by free electrons.

b) A pair of Thomas-Fermi ions in collision. The physics model in this case is characterized by the nuclear and ion charges (Z_1, Q_1; Z_2, Q_2) and by the internuclear separation R. We are interested in the groundstate interaction potential U(R), the nuclear stopping cross-sections, and possible charge-transfer or excitation-transfer cross-sections. Specifically, we would like to generalize the well-known results of Lindhard, Nielssen and Scharff[5] and Firsov[6] to collisions involving ions.

c) Thomas-Fermi plasma or fluid. This model describes a homogeneous fluid or plasma state having a finite density and temperature,[7-9] and is used to describe the heated target material. The finite-temperature Thomas-Fermi equation is solved in a spherical cell centered on one nucleus; the cell radius is determined by the plasma density ρ. In each cell, there are enough free electrons to guarantee electrical neutrality. This model is often used to calculate the average charge $Q(\rho,T)$ of equilibrium target ions and also bulk thermodynamic properties such as the pressure or energy-density. We use this model as a basis for numerical calculations of the electronic stopping-power of hot plasmas.[10]

ISOLATED THOMAS-FERMI IONS

The isolated Thomas-Fermi ion represents a textbook model for atomic/ionic structure.[11] The model is based upon the Poisson equation for the self-consistent electrostatic potential V(r) within the atom and the Fermi-gas formula for the electron density n(r) in a zero-temperature (fully degenerate) state. These equations are solved numerically. One of the most useful and interesting features of the Thomas-Fermi model is a scaling law which relates properties of any two atomic species. For example, the ion radius obeys the scaling law $R = Z^{-1/3}R_0(Q/Z)$, where Q/Z is the fractional degree of ionization (= 0 for neutral atoms). Thus the single function $R_0(x)$ describes

the Thomas-Fermi radii of all possible ions. Similar scaling-laws apply to all atomic properties including the total binding energy $E_{TOT} = Z^{7/3} E_0(Q/Z)$ and the ionization potential $I = Z^{4/3} I_0(Q/Z)$, defined as the derivative of E_{TOT} with respect to Q.

The actual ionization potential should be distinguished from the mean or effective ionization potential which enters the high-velocity Bethe-Bloch stopping formula. This quantity may be defined as the logarithmic average of the local plasma frequency within the atom; following this (traditional) definition, the scaling law is $\bar{I} = Z\bar{I}_0(Q,Z)$ as originally discovered by Bloch. Comparison of the ionization potential with this mean excitation-ionization energy shows that they are not very similar (Table I).

Another interesting property of the Thomas-Fermi ion is its dipole polarizability $\alpha = 1/Z\ \alpha_0(Q/Z)$. This is the ratio of the induced dipole moment $\vec{p}$ to the applied field $\vec{E}(\infty)$ in the case where a weak uniform field is applied to the ion. We may also ask how much of this applied field penetrates to the region close to the nucleus of our ion; this is measured by a ratio $\beta = \vec{E}(0)/\vec{E}(\infty)$, where $\vec{E}(0)$ is the portion of the total electric field having P_1 symmetry close to the nucleus. By a very pleasing theorem, the ratio is exactly Q/Z.[12]

The ion scaling functions are given in Table 1 (many of these quantities have been calculated previously). We should caution the reader that the neutral atom ($Q \to 0$) is a limit for which the Thomas-Fermi theory is relatively inaccurate. However, for the arbitrarily ionized atom, the Thomas-Fermi data represents a convenient body of useful information.

THOMAS-FERMI IONS IN COLLISION

Collisions of neutral Thomas-Fermi atoms were studied by Firsov[6] and Lindhard, Nielsen and Scharff,[5] who calculate an interaction potential U(R) defined as the groundstate energy for internuclear separation R minus the groundstate energies of the separate atoms. Our immediate practical interest is to generalize this potential to the case of colliding ions.

We expect that the potential U(R) between ions can be represented as a modification of the LNS-Firsov potential:

$$U(R) = \begin{cases} \dfrac{Z_1 Z_2 e^2}{R}\,\tilde{\phi}_0(R/a) & \text{small } R \\ \dfrac{Q_1 Q_2}{Z_1 Z_2} & \text{large } R \end{cases} \qquad (1)$$

In this equation, we assume that the LNS-Firsov screening is appropriate for small internuclear distances whereas a Coulomb potential of usual form applies at larger separations. However, we must decide where to switch between the two forms.

One conjecture is that the form changes at the internuclear separation for which the ions just touch; i.e., $R = R_1 + R_2$. This idea appears to be substantially incorrect (i.e., changing form at this radius does not give a smooth connection). Instead, it is more accurate to employ, at each radius, the larger of the two screening functions defined in eq. (1).

In order to settle this question, we require a method for calculation of interionic potentials. We have adopted a simple procedure which appears to be quite accurate. We calculate the force between ions $F(R)$ at separation R as a surface integral taken over a surface separating the ions (e.g., the midplane for a symmetric collision). The integrand is a stress tensor consisting of an electron pressure tensor and an electromagnetic stress-tensor. This method was proposed by Lee, Longmire and Rosenbluth[13] in an unpublished report (see also Refs. 9, 10). Lee, et al. calculate the potential $U(R)$ for a self-consistent two-center Thomas-Fermi problem. They obtain the potential for seven values of the spacing between neutral atoms. We have applied the stress-tensor method to the simpler charge density obtained by superposing undistorted charge densities of the two ions: $n(r) = n_1(r - R_1) + n_2(r - R_2)$. Our results agree to a few percent with those of Lee, Longmire and Rosenbluth for the neutrals (and to a similar accuracy with results obtained by the LNS prescription), except at large separations.

When generalized to interaction of charged ions, the stress-tensor method confirms the assumed potential (of course, it yields a smooth transition between the limiting forms of eq. (1)).

Concerning the potential U(R), we must point out that there are interesting objections to its use for the case of ion interactions; the same objections also apply to the more usual case of fast ions interacting with neutral target atoms. Consider a high-energy collision of a highly stripped nickel ion with a neutral nickel target atom. On classical reasoning, it appears that a substantial charge-transfer would occur if the ions reach a small enough separation. Indeed, if the instantaneous electron distribution is approximately the groundstate distribution for small internuclear separation, then the two ions must separate in essentially equal ionization states. In this case, the potential governing the approach of the particles must differ from that governing their recession. Likewise, to give a realistic physical description, we must make allowance for excitation and radiation by electrons during the collision.

Using the potential of eq. (1) it is straightforward to generalize the LNS nuclear collision cross-section to the case of ion collisions. The recoil cross-section reduces to a function of the single variable $\zeta \propto (E \cdot T)^{1/2}$, where E = laboratory collision energy and T = recoil energy of the target nucleus. This reduction is justified in the present case by the fact that the distance of closest approach R_{min} is a function of ζ for the low-energy collisions ($\zeta << \zeta_{max}$).

This theory predicts an increase in the production of low energy ion recoils. The long-range Coulomb potential $U = Q_1 Q_2 e^2/R$ produces large numbers of low-energy recoil ions which are not produced if the target atoms are neutral. The effect is accentuated by the substantial decrease of low-energy electronic stopping in hot targets.

THOMAS-FERMI FLUID

In a previous workshop, we have described the application of the Thomas-Fermi fluid model in calculations of electronic energy-loss S(E) for hot and/or dense plasmas.[10]

The calculations cited apply the finite-temperature electron-gas stopping theory developed by Skupsky[2] and Arista and Brandt[3]. These calculations give approximate forms for the finite temperature stopping number $L_0(n, T; v)$ per electron for a uniform electron gas of density n, temperature T for protons of velocity v. The theories are based on the random-phase approximation.

In the Thomas-Fermi fluid picture, the atomic calculation yields a temperature-dependent electron density n(r) reflecting thermal ionization and the plasma density. This then gives an atomic stopping number

$$L_{atom} = \int n(r)\ L_0(n, T; v)\ d^3r$$

on the basis of the usual inhomogeneous electron gas model.[14]

The statistical-model calculations described here do not exhaust the range of interesting questions and we believe that a large amount of additional scientific study will be required before we have a satisfactory understanding of ion range phenomena in plasma targets.

Table I. Properties of Thomas-Fermi groundstate ions. The numbers are scaled to Z = 1.

Q/Z	$\bar{I}_0$ (eV)	I_0 (eV)	E_0 (eV)	R_0 (Å)	α_0 (Å^3)
0.1	8.951	0.280	-20.908	5.141	36.006
0.2	11.526	0.882	-20.852	3.267	7.581
0.3	14.374	1.826	-20.720	2.365	2.390
0.4	17.694	3.210	-20.472	1.795	0.861
0.5	21.744	5.206	-20.058	1.383	0.318
0.6	26.953	8.147	-19.400	1.061	0.112
0.7	34.190	12.736	-18.374	0.791	0.0342
0.8	45.664	20.851	-16.739	0.552	7.608×10^{-3}
0.9	69.991	40.336	-13.859	0.321	7.362×10^{-4}

REFERENCES

1. E. Nardi, E. Peleg, and Z. Zinamon, "Energy Deposition by Fast Protons in Pellet Fusion Targets", Phys. Fluids 21, 574 (1978).

2. S. Skupsky, "Energy Loss of Ions Moving through High-Density Matter", Phys. Rev. A16, 727 (1977); S. Skupsky, Phys. Rev. Lett. 44, 1760 (1980).

3. N. Arista and W. Brandt, "Energy Loss and Straggling of Charged Particles in Plasmas of All Degeneracies", Phys. Rev. A 23, 1898 (1981).

4. Thomas A. Mehlhorn, "A Finite Material Temperature Model for Ion Energy Deposition in Ion-Driven Inertial Confinement Fusion Targets", J. Appl. Phys. 52, 6522 (1981).

5. J. Lindhard, V. Nielsen and M. Scharff, Det Kong Danske Vidensk Selsk 36, 10 (1968).

6. O. Firsov, Soviet Physics JETP 5, 1192 (1957); ibid. 6, 534 (1958); ibid. 7, 308 (1958).

7. R. Feynman, N. Metropolis and E. Teller, Phys. Rev. 75, 1561 (1949).

8. R. Latter, Phys. Rev. 99, 510 (1955); R. Latter, Phys. Rev. 99, 1854 (1955); R. Latter, J. Chem. Phys. 24, 280 (1956).

9. R. M. More, "Quantum Statistical Model for High-Density Matter", Phys. Rev. A 19, 1234 (1979).

10. R. M. More, "Atomic Physics in Inertial Confinement Fusion", Applied Atomic Collision Physics, Vol. II, (Academic Press); also Lawrence Livermore National Laboratory Preprint UCRL-84991 (1981).

11. H. A. Bethe, R. W. Jackiw, Intermediate Quantum Mechanics, 2nd Edition (W. A. Benjamin, Inc., New York, 1968).

12. D. Liberman, private communication, and R. Sternheimer, "Electronic Polarizabilities of Ions from the Hartree-Fock Wave-Functions", Phys. Rev. 96, 951 (1954)

13. C. Lee, C. Longmire and M. Rosenbluth, "Thomas-Fermi Calculation of Potential between Atoms", Los Alamos National Laboratory Report, LAMS-5694 (1974).

14. J. F. Ziegler, this conference.

*Work performed under the auspices of the U.S. Department of Energy by Lawrence Livermore National Laboratory under contract #W-7405-Eng-48.

ENERGY LOSSES TO SURFACE PLASMONS BY CHARGED PARTICLES*

R. H. Ritchie and J. C. Ashley
Health and Safety Research Division
Oak Ridge National Laboratory
Oak Ridge, Tennessee 37830 USA

Experimental work reported by Biersack at this Seminar indicates that appreciable energy loss specific to the surface of a stopping medium may occur when a charged particle traverses condensed matter. Some time ago the authors[1] made an estimate of the magnitude of such losses for a surface plasmon model in another connection.

Here we review briefly the theory of charged particle energy loss to the surface plasmon field for a swift charged particle incident on a model metallic system. We estimate the expected energy loss for some representative cases.

To establish the order of magnitude of the surface effect, a schematic model is sufficient. A swift ion with charge Ze crosses the surface of a plane-bounded, semi-infinite electron gas that is characterized by a dispersionless surface plasmon mode with eigenfrequency ω_s. The velocity vector, $\vec{v}$, of the ion makes an angle θ with the surface normal. It is a good approximation[2,3] to write the probability, P_s, of exciting a surface plasmon during the crossing as

$$P_s \sim \frac{C Ze^2}{\hbar v \cos\theta} = \frac{C' Ze^2}{\hbar v_\perp} \qquad (1)$$

where C is a constant of the order of one and $v_\perp$ is the component of the ion velocity perpendicular to the surface.

* Research sponsored by the Office of Health and Environmental Research, U.S. Department of Energy, under contract W-7405-eng-26 with Union Carbide Corporation.

A disturbing aspect of Eq. (1) is that P_s may be greater than 1. This defect is due to the fact that Eq. (1) was derived under the assumption that no depletion of the initial state is allowed. Approximate accounting for this is accomplished by writing[4]

$$P_n^{(s)} = \frac{(P_s)^n}{n!} e^{-P_s}$$

where $P_n^{(s)}$ is the probability of creating n surface plasmons in a crossing of the surface. This Poisson distribution of losses has the property that $\sum_{n=0}^{\infty} P_n^{(s)} = 1$, as it should.

Then the total energy, E_s, lost to the surface plasmon field must be given by

$$E_s = \sum_{n=1}^{\infty} n\hbar\omega_s P_n^{(s)} = \hbar\omega_s P_s = \frac{q^2 Z e^2 \omega_s}{v_\perp}$$

For a 30-keV proton incident on a metallic surface at $\theta = 89.5°$ with the normal, $P_s \sim 10$ and

$$E_s \sim 200 \text{ eV}$$

for a representative value of $\hbar\omega_s = 20$ eV. On the other hand, if a 30-keV proton is incident normally, $P_s \sim 1$ and $E_s = 20$ eV.

Hence, one expects a rather small contribution from surface plasmon creation to the energy loss by ions compared with the losses experienced in the bulk of foils with ordinary thicknesses. For example, a 30-keV proton should lose $\sim$ 12 keV to bulk processes in traversing a carbon foil only 1000 Å thick.

It should be pointed out that the description of surface losses given above will result in an overestimate of their contribution to the

energy loss of a charged particle. This is due to the fact that the losses to surface modes described above are partially compensated for by a decrease in loss to bulk modes near the surface.[2] The latter is attributable to orthogonality of the eigenfunction of the surface modes to those of the bulk modes.[4]

Peferences

1. J. C. Ashley and R. H. Ritchie, *Phys. Rev.* B5, 3485 (1972).

2. R. H. Ritchie, *Phys. Rev.* 106, 874 (1957).

3. E. A. Stern and R. A. Ferrell, *Phys. Rev.* 120, 130 (1960).

4. A. A. Lucas, E. Kartheuser and R. G. Badro, *Phys. Rev.* B2, 2488 (1970).

STOPPING OF SWIFT IONS IN CONDENSED MATTER: THE THEORY OF EFFECTIVE CHARGE

George Basbas
Physical Review Letters
Post Office Box 1000
Ridge, N.Y. 11961

Abstract

The stopping power of a dielectric medium for a swift ion is calculated for a prescribed electronic structure on the projectile. The electronic charge carried by the projectile in traversing the medium is dictated by a stripping criteria. From the resulting stopping power an effective charge may be inferred. This charge successfully predicts the energy loss for a variety of ions and targets encountered in the laboratory.

I. INTRODUCTION.

The energy loss of swift ions in matter is often discussed in terms of an effective charge which allows the ion to be viewed as a point charge devoid of electronic structure. In the Bethe stopping-power theory, and in the linear dielectric response theory, the energy loss of a bare particle is proportional to the square of its charge. The concept of the effective charge brings the theory for ions into contact with the successes of the theory of material stopping powers for bare particles. Indeed the definition of the stopping power for an ion as the square of its effective charge times the proton stopping power is an ansatz for ef-

fective charge. In this approach the study of the physical phenomena responsible for the energy loss of swift ions is concentrated in the question of the effective charge for a projectile while traversing the stopping medium.

The problem is to determine the effective charge. The research of Brandt and coworkers [1] has been directed at this tantalizing, important and controversial problem. Recent developments [2] have led to an organization and clarification of this issue in the study of the energy loss of swift ions in condensed matter. It is the purpose of this report to describe the theory of effective charge which has emerged.

The key feature advanced by Brandt and Kitagawa [2] is the assertion that the energy loss of a swift ion depends upon the solution to two separate problems. One is the determination of the ionic (real) charge state of the projectile in the stopping medium. The other is the calculation via linear dielectric response theory of the stopping power of a projectile with the electronic charge density which corresponds to the ionic charge state. It is the identification of these physical components, and their subsequent analysis, which ushers the concept of effective charge into the realm of systematic evaluation. The treatment given by Brandt and Kitagawa of these two features is discussed below.

II. CHARGE STATE OF AN ION PENETRATING CONDENSED MATTER.

In the reference frame of a projectile the conduction or valence electrons of the target appear to be streaming by at the beam velocity v_1. The maximum energy which can be delivered to a target electron from the medium is the energy of an electron with velocity v_1. Only projectile electrons bound with less energy can be removed by collisions with the target electrons. This leads to a stripping criterion which determines the charge state of the projectile: $v_e < v_1$. Only electrons with velocities which satisfy this inequality can be lost by the projectile. Here v_e is the velocity of a bound electron in the projectile frame of reference. If the velocity distribution which characterizes the electronic structure of the incident projectile is known, then the number of electrons satisfying the stripping criterion can be calculated. The ionic charge state, Q_1, can be inferred from the relation

$$Q_1 = Z_1 - N_1. \qquad (1)$$

The projectile atomic number is Z_1, and N_1 is the number of electrons which remain on the projectile after stripping. Atomic units are used throughout.

This simple picture of how the ionic charge state is determined has the compelling virtue of transparent physics.

If one prefers a more detailed description of the capture and loss processes which contribute to the charge state, how equilibrium is approached and what the charge state distribution might be, the theory of effective charge presented here does not prevent it. The models used in this discussion are introduced for the purpose of laying clear the theoretical grounds upon which effective-charge theory is built.

III. STOPPING POWER FOR A SWIFT ION WITH ELECTRONIC STRUCTURE.

In linear dielectric response theory the electromagnetic fields induced in the medium by the penetrating charges are calculated and used to compute the power dissipated per unit volume. The integration over space and time yields the stopping power. The key ingredients are the charge density of the projectile and the dielectric response function of the medium. The charge density of a moving nucleus with electronic density ρ_e is

$$\rho = Z_1 \delta(\underline{r} - \underline{v}_1 t) - \rho_e(\underline{r} - \underline{v}_1 t), \qquad (2)$$

where $\underline{r}$ refers to an arbitrary point in the stopping medium and the projectile is taken to move in a straight line. Maxwell's equations are solved by the method of Fourier transforms in which the space and time variables are re-

placed by wave number, k, and frequency, ω, variables. The following expression for the stopping power results:

$$S = \frac{2}{\pi v_1^2}\int_0^\infty \frac{dk}{k}\left|\tilde{\rho}(k)\right|^2 \int_0^{kv_1} \omega\, \mathrm{Im}\left[-\frac{1}{\epsilon(k,\omega)}\right] d\omega. \qquad (3)$$

This expression is valid for any dielectric response function $\epsilon(k,\omega)$, and for any charge density. (The Fourier transform of the charge density is indicated in Eq. (3).) Only the restrictions of linear response theory apply. According to Brandt's program for calculating the effective charge, the electronic charge density has a total charge N_1,

$$\int \rho_e \, dV = N_1. \qquad (4)$$

The determination of N_1 was discussed in the previous section.

The presentation of the theory is now complete. With choices for N_1, ρ_e, and $\epsilon(k,\omega)$, the stopping power for an ion in a particular medium can be calculated.

It should be pointed out that for the practical needs of energy loss calculations no more need be done. Explicit determination of the effective charge is not necessary. On the other hand, to obtain insight into the rich variety of penetration phenomena that have been the constant topic of these several workshops requires that the effective charge be extracted from the theoretical formalism and its proper-

ties elucidated. In the next section examples are cited from the instructive analysis of effective charges given by Brandt and Kitagawa.

IV. MODEL CALCULATION OF EFFECTIVE CHARGE.

In order to obtain analytical results for close inspection of the phenomenon, Brandt and Kitagawa choose an electronic charge density for the projectile in the form

$$\rho_e = \frac{N_1}{4\pi\Lambda^3}\frac{\Lambda}{R}e^{-R/\Lambda}. \qquad (5)$$

The screening length Λ is determined by minimizing the internal energy of the projectile. Reference [2] gives the details and an assessment of the accuracy of Eq. (5).

The present discussion is confined to results obtained for high velocities. The plasmon-pole approximation for the dielectric function is employed to evaluate Eq. (3) and yields an expression in closed form for the stopping power [2]. This leads immediately to a formula for the the effective charge, Z^*, via the definition:

$$Z^* = (S/S_p)^{1/2}, \qquad (6)$$

where S_p is the topping power for protons. In the high

velocity limit the result is

$$Z^{*2} = (1/2)\, Z_1^{\,2} + (1/2)\, Q_1^{\,2} \,. \quad (7)$$

A partition rule is apparent since the Z_1-squared term corresponds to the bare charge which gives the scattering interaction strength in close collisions for which the projectile's electronic structure gives no screening of the nuclear charge. The contribution from distant collisions is the Q_1-squared term. These collisions are governed by the interaction strength of the nuclear charge screened by all the projectile electrons (cf. Eq. (1)). The contributions are equal (the factor 1/2 is common to both) but weighted by the charge, Z_1 or Q_1, appropriate to the collision distance. For a fully stripped particle ($Q_1 = Z_1$) the distant and close collisions contribute exactly the same to stopping. This is the equipartition theorem.

Equation (7) provides another theorem in the case of neutral projectiles ($Q_1 = 0$). The stopping power of the medium for neutrals is half that for bare nuclei. The effective charge of a neutral atom is 0.7 of its nuclear charge.

V. SUMMARY AND CONCLUSION.

This report gives a qualitative discussion of the theory of effective charge developed by Brandt and coworkers. A thorough treatment is found in the paper by Brandt and Kitagawa and in the report to this conference by Kitagawa. These articles also convey the substantial relationship between the theory of effective charge and results of experiments designed to elucidate the phenomena of swift ions in condensed matter [3]. The success of the theory in accounting for discoveries in the laboratory demonstrates the utility of Brandt's approach to the calculation of stopping powers, and the efficacy of the concept of effective charge.

REFERENCES.

[1] W. Brandt, ''Effective Charges of Ions and the Stopping Power of Dense Media'', to be published in Nucl. Instr. Meth. Phys. Res., and ''Modern Problems of Low-Velocity Stopping Powers'', Nucl. Instr. Meth. Phys. Res. 191, 453 (1981).

[2] W. Brandt and M. Kitagawa, ''Effective Stopping Power Charges of swift ions in condensed matter'', Phys. Rev. B 25 (May) (1982).

[3] See also the report to this conference by F. Schulz.

Effective Charge of Energetic Ions in Metals*

M. Kitagawa
Department of Electronics North Shore College
Atsugi 243, Japan
and
Werner Brandt
Department of Physics, New York University
4 Washington Place, New York, N.Y. 10003, USA

Effective charge of energetic ion, as derived from stopping power of metals, is calculated by use of a dielectronic-response function method. The electronic distribution in the ion is described through the variational principle in a statistical approximation. The dependences of effective charge on the ion velocity, atomic number and r_s-value of metal are derived at the low-velocity region. The effective charge becomes larger than the real charge of ion due to the close collisions. We obtain the quasi-universal equation of the fractional effective electron number of ion as a function of the ratio between the ionic size and the minimum distance approach. The comparison between theoretical and experimental results of the effective charge is performed for the cases of N ion into Au, C and Al. We also discuss the equipartition rule of partially ionized ion at the high-velocity region.

1. Introduction

The researches of effective charges of ions, esprcially for experimental analyses relating to the stopping power at the low-velocity region, have taken a position of the basic themes in the field of ion-matter interactions for a long time. Northcliffe[1], and Betz[2] have reported general reviews of this field from the experimental and theoretical standpoints of view at each past moment. Recently, Ziegler[3] has collected the stopping power data covering over the wide range of the light to heavy ions based on numerical analyses. On the other hand, since the theoretical works performed by Lindhard, Scharff and Shiøtt[4], Firsov[5] and Lindhard and Winther[6] at the first half period of 1960, it has become possible to make comparisons between theoretical and experimental data quantitatively.

However, the agreements of various parameters between them, those are, the velocity v_1 and atomic number Z_1 of ion, r_s-value of metal, and the atomic number Z_2 of target atom, are not so enough. As far as the effective charge of heavy ion concerns, the analyses of experimental data by universal scaling due to $v_1/Z_1^{2/3}$ have been performed by Brandt[7,8] and Moak[9], since the velocity, or energy criteria of effective charge of heavy ion have been proposed by Bohr[10], or Lamb[11]. Here $Z_1^{2/3}$ means the avaraged velocity of electron given by the statistical treatment in Hartree atomic unit. For He ion case, in order to explain the effective charge, the avaraged relative velocity between ion and electrons in metal, v_r, has been introduced[12]. Recently, Ferrell and Ritchie[13] have improved the stopping power calculus of He ion by taking into account of 1s-type electronic distribution bound in it. In this manuscript, we develop the theory of effective charge, which is derived from stopping power, by taking into account of the structure of electronic distribution bound in ion, according to the variational principle of statistical treatment, which is derived in Sec.II. In Sec.III, we calculate the fractional effective charge ζ at high- and low-velocity regions, and formulate the equipartition rule[6] in the case of the partially ionized ion. The comparisons between theoretical and experimental results are also made in Sec.III.

II. Electronic Distribution of Ionic Projectile

We consider the stopping power of a medium for the ion with velocity v_1, in which N electrons are bound in its ionic state. The number of electrons bound in ion, N, depends on the ion velocity relative to electrons in metal. In such a case, the charge density of ion is written

$$\rho_{ne}(\vec{r}-\vec{v}_1 t) = Z_1\delta(\vec{r}-\vec{v}_1 t) - \rho_e(\vec{r}-\vec{v}_1 t) \quad . \tag{1}$$

In the above, $Z_1\delta(\vec{r}-\vec{v}_1 t)$ and $\rho_e(\vec{r}-\vec{v}_1 t)$ are the nuclear and electronic charge densities of ion, and for all results in this manuscript, we use Hartree atomic unit ($\hbar=e=m_e=1$).

The stopping power S for partially ionized ion is calculated according to the classical electro-magnetic approach as follows

$$S = \frac{\vec{v}_1}{v_1} \int \rho_{ne}(\vec{r},t)\vec{E}(\vec{r},t)d\vec{r} \ , \tag{2}$$

where $\vec{E}$ is the electric field acting the ion, which is derived through the following electro-magnetic equations in Fourier space

$$\left.\begin{aligned} k^2\varepsilon(k,\omega)\phi(k,\omega) &= 4\pi\rho_{ne}(k)\delta(\omega-\vec{k}\vec{v}_1) \\ \vec{E}(k,\omega) &= -i\vec{k}\phi(k,\omega) \end{aligned}\right\} . \tag{3}$$

In Eq.(3), $\varepsilon(k,\omega)$, $\phi(k,\omega)$ and $\vec{E}(k,\omega)$ are Fourier components of the dielectric function, the scalar potential and the electric field, respectively. $\rho_{ne}(k)$ is defined through Fourier component of the ionic charge density, $\rho_{ne}(k,\omega)$, as $\rho_{ne}(k,\omega) = 2\pi\rho_{ne}(k)\delta(\omega-\vec{k}\vec{v}_1)$. $\rho_{ne}(k)$ corresponds to Fourier component over the space coordinate of the rest system of ion, $\vec{R}$. Using Eqs.(2) and (3), we obtain

$$S = \frac{2}{\pi v_1^2} \int \frac{dk}{k} |\rho_{ne}(k)|^2 \int_0^{kv_1} d\omega \ \omega \mathrm{Im}(-\varepsilon^{-1}(k,\omega)) \ . \tag{4}$$

In order to calculate the stopping power by use of Eq.(4), we derive the electronic distribution, $\rho_e(R)$ $(\vec{R}=\vec{r}-\vec{v}_1 t)$, bound in the ion through the variational principle of the statistical treatment according to the following approximation.

$$\rho_e(R) = \frac{N\alpha^2}{4\pi R} e^{-\alpha R} \tag{5-a}$$

$$\varepsilon(N,Z_1,\alpha(N,Z_1)) = E_{ne} + \lambda E_{ee} + E_{kin} \tag{5-b}$$

$$E_{ne} = -Z_1 \int d\vec{R}\rho_e(R)/R = -Z_1 N\alpha \tag{5-c}$$

$$E_{ee} = \frac{1}{2} \int d\vec{R} \int d\vec{R}' \ \rho_e(R)\rho_e(R')/|\vec{R}-\vec{R}'| = N^2\alpha/4 \tag{5-d}$$

$$E_{kin} = \frac{3}{10} \int d\vec{R} \ \rho_e(R)(3\pi^2\rho_e(R))^{2/3} = C_0 N^{5/3}\alpha^2 \tag{5-e}$$

$$\partial E/\partial\alpha = 0, \quad \partial E/\partial N|_{N=Z_1} = 0 \tag{5-f}$$

where E_{ne}, E_{ee} and E_{kin} are the potential energies between nucleus-electron and electron-electron, and the kinetic energy of electron in the ionic system. $C_0 = \frac{1}{2}(\frac{3\pi}{4})^{2/3}(\frac{3}{5})^{5/3}\Gamma(\frac{4}{3}) \simeq 0.240$, where $\Gamma(z)$ is the Gamma function. Eq.(5-f) denotes the variational principle. The second equation in Eq.(5-f) gives the condition that the total electronic energy of neutral atom (Z_1=N) gives a minimumized one in comparison with those of the ionic cases. According to the above calculus, we have

$$\left.\begin{aligned} \alpha(Z_1, N/Z_1) &= \frac{Z_1^{1/3}(1-(\lambda/4)(N/Z_1))}{2C_0(N/Z_1)^{2/3}} \\ E &= -Z_1^{7/3}(N/Z_1)^{1/3}(1-(\lambda/4)(N/Z_1))^2/4C_0 \\ \lambda &= 4/7 \end{aligned}\right\} . \qquad (6)$$

In Figs.(1) and (2), we show $\alpha/Z_1^{1/3}$ and $E/Z_1^{7/3}$ as functions of Q ($=1-\frac{N}{Z_1}$), plotting together with the results of the case that we use Lenz-Jensen distribution[14] for $\rho_e(R)$. Q denotes the fractional degree of ionization. The values of $E/Z_1^{7/3}$ at the point of Q=0 in Fig.(2) correspond the numerical results of ours, Lenz-Jensen(L-J) and Thomas-Fermi(T-F) models. The agreement between our and Lenz-Jensen models is well. Transforming Eq.(5-a) to Fourier space, we have the analytic representation of $\rho_{ne}(k)$,

$$\rho_{ne}(k) = Z_1(1 - \frac{N}{Z_1}\frac{\alpha^2}{k^2+\alpha^2}) . \qquad (7)$$

Using Eqs.(4),(7) and the imargi ary part of the dielectric function $Im(-\varepsilon^{-1}(k,\omega))$, we can derive the stopping power and the fractional effective charge ζ which is defined as

$$\zeta = Z_1^*/Z_1 = [S/S_{N=0}]^{1/2} , \qquad (8)$$

where $S_{N=0}$ indicates the stopping power for bare nucleus.

III. Effective Charge Derived from Stopping Power

a) High-velocity case

At the high-velocity region, covering the Bethe-Bloch region and below it, but not including the relativistic one, we can use the approximate representation of the dielectric function firstly proposed by Hedin and Lund-

quist[15], and used for the calculation of the wake potential by Ritchie et al.[16], for the free-electron gas system,

$$\varepsilon(k,\omega) = 1 + \frac{\omega_p^2}{\omega_g^2+\beta^2k^2+k^4/4-\omega(\omega+i\delta)} \quad . \tag{9}$$

In Eq.(9), ω_p and ω_g denote the plasmon energy and energy of band-gap in the case of semiconductor. $\beta=(3/5)^{1/2}k_F$ indicates the phase velocity of plasmon, and the term of 4th-power of k in the denominator denotes the contribution of the single-electron excitation. Using Eq.(9), we have

$$\mathrm{Im}(-\varepsilon^{-1}(k,\omega)) \underset{\delta\to 0}{\simeq} \frac{\pi\omega_p^2}{2A}\delta(\omega-A), \tag{10}$$

where $A = [\Omega_p^2+\beta^2k^2+k^4/4]^{1/2}$ and $\Omega_p^2=\omega_p^2+\omega_g^2$.

From Eqs.(4) and (10), we obtain the upper and lower values of k which correspond to the maximum and minimum momentum transfers, k_+ and k_-,

$$\left.\begin{aligned} k_+ &= [2(v_1^2-\beta^2)+2\sqrt{(v_1^2-\beta^2)^2-\Omega_p^2}]^{1/2} \\ k_- &= [2(v_1^2-\beta^2)-2\sqrt{(v_1^2-\beta^2)^2-\Omega_p^2}]^{1/2} \end{aligned}\right\} , \tag{11}$$

and

$$S = \frac{\omega_p^2}{2v_1^2}\int_{t_-}^{t_+} dt(\rho_{ne}(t))^2/t \quad (t=k^2) \ . \tag{12}$$

Using Eqs.(7),(8),(11) and (12), we obtain ζ as follows

$$\zeta^2 = Q^2+(1-Q)[(1-Q)(1/(u_+^2+1)-1/(u_-^2+1)) + (1+Q)\ln\{(u_+^2+1)/(u_-^2+1)\}]/2L \quad , \tag{13}$$

where $L=\ln(u_+/u_-)$, and $u_+=k_+/\alpha$ and $u_-=k_-/\alpha$.

For the limiting case connecting to Bethe-Bloch region ($v_1>>\beta,\sqrt{\Omega_p}$), we have

$$k_+\simeq 2v_1 \text{ and } k_-\simeq\Omega_p/v_1 \tag{14-a}$$

$$L\simeq\ln(2v_1/\Omega_p) \text{ and } \zeta^2\simeq 1/2+Q^2/2 \quad , \tag{14-b}$$

where L becomes the L-factor derived by Lindhard and Winther[6]. The first and second terms of ζ^2 in Eq.(14-b) correspond to the contributions due to the close and distant collisions. Although, strictly speaking, the contri-

butions due to the core electrons of the target should be taken into account, the stopping power for neutrally fast projectile becomes smaller as 1/2 than that for the bare neuclus in free electron gas, which is the extended equipartition rule corresponding that for the bare nuclus derived by Lindhard and Winther[6]. From the condition of $(v_{th}^2-\beta^2)^2-\Omega_p^2=0$ in Eq.(11), we have the threshold velocity, $v_{th}=(\beta^2+\Omega_p)^{1/2}$, below which the plasmon contribution diminishes. This gives the almost same value used by Ashley[17].

b) Low-velocity case

The imarginary part of the dielectric function at the low-velocity region is obtained as an approximate formula by taking into account of the Debye type screening effect due to free electrons[6,18],

$$\mathrm{Im}(-\varepsilon^{-1}(k,\omega)) \simeq \begin{cases} 2k\omega/(k^2+k_D^2)^2 & (k\leq 2k_F) \\ 0 & (\text{otherwise}) \end{cases} . \tag{15}$$

Integrating over ω in Eq.(4), we have S and ζ by use of Eq.(7),

$$S = \frac{2v_1}{3\pi} Z_1^{*2} I_0(\pi k_F) \quad , \tag{16}$$

and

$$\zeta^2 = (1-(1-Q)/C_D)^2+[(1-Q)/C_D]^2 I_0(\gamma^2)/I_0(\pi k_F) + 2[(1-Q)/C_D][1-(1-Q)/C_D]\Xi_0(\alpha,k_F)/I_0(\pi k_F) \tag{17}$$

where $C_D=1-k_D^2/\alpha^2$, $k_D^2=4k_F/\pi$, $\gamma=2k_F/\alpha$ and

$$\left.\begin{aligned} I_0(z) &= \ln(1+z)-z/(1+z) \\ \Xi_0(\alpha,k_F) &= [\ln(1+\gamma^2)-k_D^2\ln(1+\pi k_F)/\alpha^2]/C_D \end{aligned}\right\} . \tag{18}$$

In the above, k_F is the Fermi wave number. γ gives the ratio between the ionic radius $(1/\alpha)$ and the minimum distance approach $(1/2k_F)$ corresponding to the maximum momentum transfer at the low-velocity region. Expanding ζ as a function of Q and k_F in terms of γ, we have more simplified relation between ζ and Q,

$$\zeta \simeq Q+C(k_F)(1-Q)\ln(1+\gamma^2) \tag{19}$$

$$C(k_F) = \pi k_F/[(1+\pi k_F)I_0(\pi k_F)]-2/\pi k_F \quad . \tag{20}$$

Introducing an effective number of electrons bound in the ion, $N^*=Z_1-Z_1^*$,

and using the relation of $1-N^*/N=(\zeta-Q)/(1-Q)$, we have

$$1-N^*/N \simeq C(k_F)\ln(1+\gamma^2) \quad . \tag{21}$$

In Tab.(1), we show the values of $C(k_F)$ for the cases of Au, C, Al and Cs. The dependence of $C(K_F)$ on k_F, or r_s is weaker than the variation of k_F, or r_s. In Fig.(3), we show the numerical results. Solid curves correspond to each metal (eg. Au, C, Al and Cs). The plots described as • are exact numerical calculations estimated from Eq.(17) under the various combinations between projectiles (C, N, Ar, I and U ions) and targets (Au, C, Al and Cs), in which we take the values of Q=0, 0.197, 0.447 and 0.852. The k_F-, or r_s-values are referred from Ref.(19). In drawing each solid curve, we have to take into account of the available criterion of the statistical treatment of γ_0. For the upper limit of each curve, we choose it as the case of Z_1=4. The dependence on k_F, or r_s value of metal appearing in solid curve is weak, and the agreements between solid curves and numerical plots are quite well. Then, Eq.(21) gives a quasi-universal equation between $1-N^*/N$ and γ.

In order to make a comparison with the experimental data, we calculate the fractional effective charge ζ based on the theoretical results discussed here. Using the velocity criterion for Q, developed by Bohr[10] and Lindhard[7], and recently improved by Brandt et al.[12] by introducing the averaged relative velocity v_r between the projectile and the electron in metal, we estimate[20]. In Fig.(4), we show the numerical results for the cases of C ion into Au, C and Al, together with the experimental data performed by Schulz et al.[21]. In Fig.(4), the dashed curves denote the numerical results obtained from Eq.(19), and the solid curves mean the results of the double numerical integration of Eq.(4). In such a numerical integration, we use the Lindhard dielectric function[6]. Also the solid curve is the scaling curve as a function of $y_r(=v_r/Z_1^{2/3})$, which is well established for the fractional degree of ionization of heavy ions[7-9,12]. The small discrepancies due to the analytical approximation for Eq.(4) appear at the higher region of y_r. There appear the deviation from the universal scaling and the r_s-, or k_F-dependence in γ as calculated here. The experimental data for N ion into Au, C and Al indicated by open symbols support the eff-

ective charge theory as presented within the dielectric function method here.

IV. Concluding Remarks

Making use of the dielectric-response function method, we calculated the effective charge of partially ionized ion passing through metals, as derived from the stopping power. The distribution of electron bound in the ion was derived through the variational principle in the statistical approximation. The ionic radius α^{-1} and the total electronic energy E of the ion of our model well agreed to those obtained from the case that we used Lenz-Jensen distribution. The dependences of effective charge on the ion velocity relative to those of electrons in metals, the atomic number of the ion, and the r_s-value of metal were estimated. The analytical expressions of the fractional effective charge were derived at the low- and high-velocity regions.

The effective charge Z_1^* becomes larger than the real charge of the ion, Z_1-N, due to the close collisions because of the fact that the ionic radius usually becomes larger than the minimum distance approach of the scattering between the ion and the electrons in metals. At the low-velocity region, we obtained the quasi-universal equation of the fractional effective electron number of the ion as a function of the ratio between the ionic radius and the minimum distance approach. On the other hand, at the high-velocity region, we also derived the extended equipartition rule of the partially ionized ion within the free electron gas model. In the case of neutrally fast projectile, the fractional effective charge ζ becomes smaller as $1/\sqrt{2}$ than that of bare nucleus, which indicates the stopping power for neutrally fast projectile becomes smaller as 1/2 than that for the bare nucleus. The threshold velocity was also obtained, below which the plasmon contribution diminishes.

The comparisons between the theoretical and experimental results were performed for the case of N ion into Au, C and Al by use of the velocity criterion of the fractional degree of ionization Q by introducing the avaraged relative velocity between the ion and the electrons in metal. Theoretical results gave the r_s-dependences shown in Fig.(4). Such a kind of r_s-dependences were also pointed out in the case of He ion into Au, C, Al

and Cs[12]. The experimental data supported the effective charge theory as presented here. Such kinds of results were also obtained for the cases of Ne and Ar ions[21]. From the velocity dependence of the effective charge, it will be able to derive the deviation from the linear velocity dependence of stopping power for the cases of heavy ions in the low velocity region[22].

Acknowledgment

The authors thank Dr. F. Schulz for his valuable discussions. One of the authors (M.K.) thanks the U.S. Department of Energy, North Shore College and Private University Research Fund of Japan for financial supports for this work performed at New York University. The helpful discussions with the experimental group of New York University are also acknowledged.

References

* Work supported by the U.S. Department of Energy, North Shore College and Private University Research Fund of Japan.

1 L.C. Northcliffe and R.F. Schilling, Nucl. Data, Sect. A7 233 (1970).

2 H.D. Betz, Rev. Mod Phys. 44 74 (1972).

3 For example, J.F. Ziegler, Helium Stopping Powers and Ranges in All Elements (Pergamon Press, New York, 1977).

4 J. Lindhard, M. Scharff and H.E. Shiøtt, Kgl. Danske-Videnskab. Selskab. Mat.-Fys. Medd. 33 No.14 (1963).

5 V.B. Firsov, Zh. Eksp. Teor. Fiz. 36 15 (1959).

6 J. Lindhard and A. Winther, Kgl. Danske-Videnskab. Selskab. Mat.-Fys. Medd. 34 No.4 (1964).

7 W. Brandt, in Atomic Collisions in Solids (Plenum, New York, 1973), Vol.1, p261.

8 B.S. Yarlagadda, J.E. Robinson and W. Brandt, Phys. Rev. B17 3473 (1978).

9 M.D. Brown and C.D. Moak, Phys. Rev B6 90 (1972).

10 N. Bohr, Phys. Rev. 58 654 (1940); 59 270 (1941).

11 W.E. Lamb, Phys. Rev. 58 696 (1940).

12 S. Kreussler, C. Varelas and W. Brandt, Phys. Rev. B23 82 (1981).

13 T.L. Ferrell and R.H. Ritchie, Phys. Rev. B16 115 (1977).

14 P. Gombas, Die Statistiche Theorie der Atoms und ihre Anwendungen

(Springer-Verlag, Vienna, 1949).
15 L. Hedin and S. Lundquist, Solid State Phys. 23 (1969).
16 R.H. Ritchie, W. Brandt and P.M. Echenique, Phys. Rev. B14 4808 (1976).
17 J.C. Ashley, Nucl. Instr. and Meth. 170 197 (1980).
18 M. Kitagawa and Y.H. Ohtsuki, Phys. Rev. B9 4719 (1974).
19 D. Issacson, Internal Report, Radiation and Solid State Laboratory, New York University (1975).
20 W. Brandt and M. Kitagawa, Phys. Rev. B, submitted.
21 F. Schulz, private communications. See also W. Brandt, Nucl. Instr. and Meth. (1982), to be published.
22 C.D. Moak, B.R. Appleton, J.A. Biggerstaff, M.D. Brown, S. Datz, T.S. Noggle and H. Verbeek, Nucl. Instr. and Meth. 132 95 (1976).

Figure and Table Captions

Fig.(1) $\alpha/Z_1^{1/3}$ as a function of Q. The solid and dashed curves show our results and those in the case of using Lenz-Jensen distribution.

Fig.(2) $E/Z_1^{7/3}$ as a function of Q. The solid and dashed curves have the same meanings as Fig.(1).

Fig.(3) $1-N^*/N$ as a function of γ for the cases of Au, C, Al and Cs bombared by C, N, Ar, I and U ions. The solid curves and plots (•) correspond to the results derived from Eq.(19) and calculated numerically from Eq.(17).

Fig.(4) Comparisons between the theoretical and experimental results for the cases of $_7N$ ion into Au, C and Al.

Tab.(1) $C(k_F)$ as a function of k_F, or r_s for the cases of Au, C, Al and Cs.

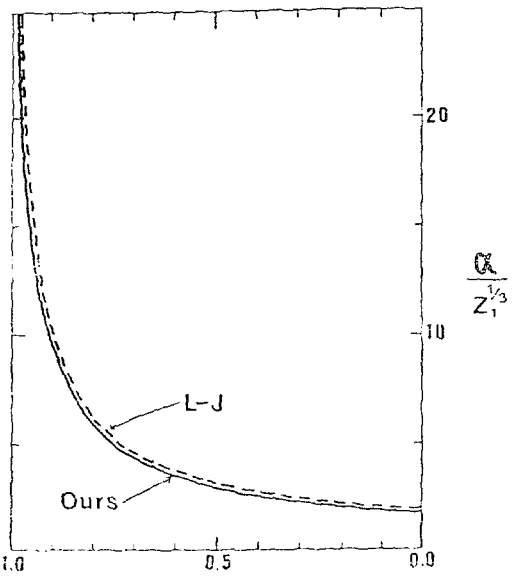
20
10
$\frac{\alpha}{Z_1^{1/3}}$
L-J
Ours
1.0
0.5
0.0
Q

Fig.(1)

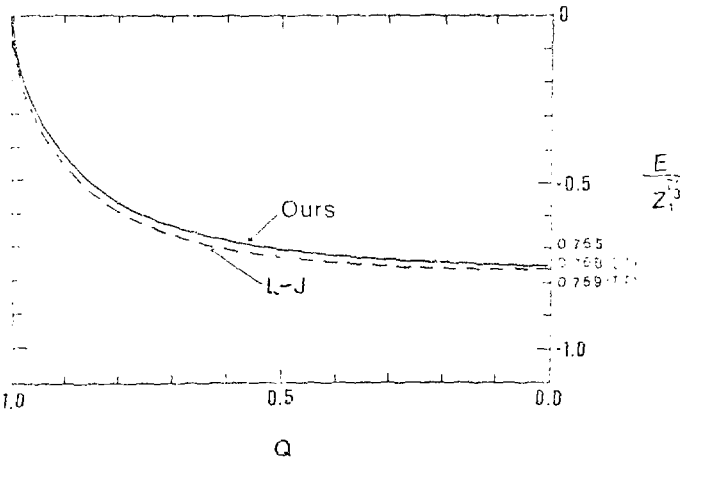
0
-0.5
-1.0
$\frac{E}{Z_1^{3}}$
Ours
L-J
1.0
0.5
0.0
Q

Fig.(2)

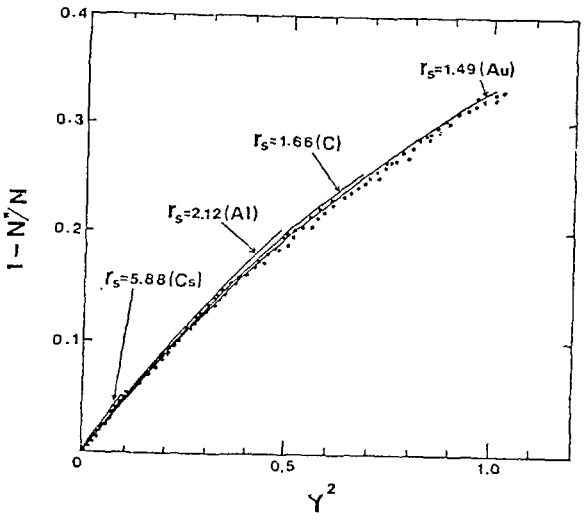
0.4
0.3
0.2
0.1
0
0.5
1.0
$1 - N^*/N$
Y^2
r_s=1.49 (Au)
r_s=1.66 (C)
r_s=2.12 (Al)
r_s=5.88 (Cs)

Fig.(3)

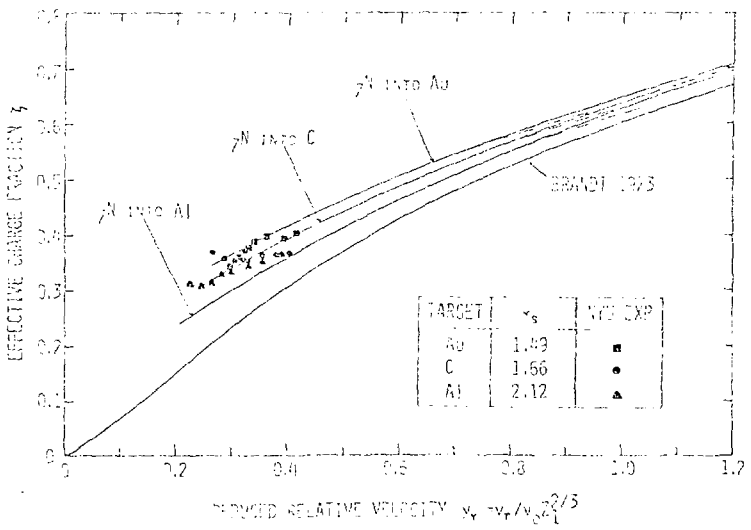
EFFECTIVE CHARGE FRACTION
REDUCED RELATIVE VELOCITY
BRANDT 1973
TARGET
r_s
Au
1.49
C
1.66
Al
2.12

Fig.(4)

	k_F	r_{Si}	$\epsilon(k_F)$
Al	1.24	1.49	0.487
Cr	1.14	1.66	0.43
Fe	0.96	2.12	0.3
Cu	0.926	5.8	0.5

Tab.(1)

EFFECTIVE CHARGE OF LOW-VELOCITY NITROGEN, NEON AND ARGON IONS IN CARBON, ALUMINUM AND GOLD

Friedrich Schulz
Gesellschaft für Strahlen- und Umweltforschung mbH, PTA
D-8042 Neuherberg, FR Germany
and
Werner Brandt
Radiation and Solid State Laboratory, New York University
4 Washington Place, New York, N. Y. 10003, USA

Stopping powers S of low-velocity nitrogen, neon and argon ions in carbon, aluminum and gold have been measured in order to deduce effective charge fractions $\zeta = Z_1^{-1}(S/S_p)^{1/2}$, *where* Z_1 *is the atomic number of the swift ion. The proton stopping powers* S_p *have been taken from literature data. The 'experimental' effective charge fractions are compared with the results of a new theory by Brandt and Kitagawa which involves the calculation of the stopping powers* S_Q *and* S_{Z_1} *for an ion of charge Q and the respective bare nucleus. It is found that the* ζ_{exp}*-values are in much better agreement with* ζ_{th} *than with the calculated mean degree of ionization of the swift ion in the target. However, the theory cannot fully account for all details of the experimental data. In particular, the observed* Z_1*-dependence of* ζ_{exp} *is more pronounced than predicted.*

I. INTRODUCTION

Calculations of the stopping power S of low-velocity heavy ions in solids are usually based upon an *ansatz* of the form

$$S \equiv S(Z_1^*, Z_2, v_1) = [Z_1^*(v_1, Z_1)]^2 S_p(v_1, Z_2). \qquad (1)$$

In Eq. (1) v_1 denotes the ion velocity, Z_1 and Z_2 the atomic numbers of the ions and the target atoms, respectively, and S_p the stopping power of the solid for bare protons at the same velocity v_1. Using Eq. (1), stopping power calculations are essentially reduced to the problem of evaluating the effective charge Z_1^*e of the swift ions. Previously, Z_1^*e

has been assumed to be identical with the mean electric charge, Qe, of the partially stripped ion.[1] More recently, Brandt and Kitagawa[2] have calculated Z_1^* in a dielectric-response approximation. In this approach, the density distribution of the N electrons bound to the swift ion is given by a variational statistical approximation. For an ionic charge $Q = Z_1 - N$, due to close collisions, Z_1^* is predicted to be a function of the ratio between the ion size and the mean electron spacing in the medium. In particular it is found[2] that Z_1^* is always larger than Q.

In order to compare the predictions of the Brandt-Kitagawa theory[2] with experimental data we define an effective charge fraction ζ. With reference to Eq. (1)

$$Z_1^*/Z_1 \equiv \zeta = Z_1^{-1}(S/S_p)^{1/2}. \qquad (2)$$

Since available experimental stopping powers for low velocity ions scatter by up to a factor of two, we have performed an elaborate study of the energy loss of He, N, Ne and Ar in C, Al and Au.[3,4] Particular attention has been devoted to elucidating detrimental effects introduced by the crystallinity of the target foils. Proton stopping powers required for evaluating ζ have been taken from the literature.[5]

II. EXPERIMENTAL

The stopping power measurements were performed using the New York Heavy Ion, 300 kV Dynatron accelerator. In order to improve vacuum conditions, the whole beam transport system was redesigned. The base pressure in the new target chamber was 2×10^{-5} Pa. Due to the improved conditions, which included the use of a LN cooled pressure step, carbon build-up on the targets was never observed.

Momentum analysis of the beam before and after passage through the target foils was achieved by two 90° magnetic spectrometers. The momentum resolution of the first spectrometer, which defines the velocity of the incident ion, was $\Delta p/p = 2.4 \times 10^{-4}$ (corresponding to $\Delta E/E \cong 5 \times 10^{-4}$). The resolution of the second spectrometer was $\Delta E/E \sim 10^{-3}$. The angular divergence of the incident beam was $< 0.05°$. Velocity spectra after passage of the ions through the target foil were measured with an angular

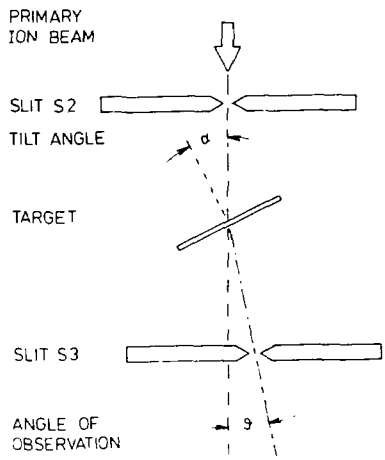

FIG. 1. Schematic of the experimental arrangement

resolution < 0.1° at angles of observation, ϑ , between 0° and 2° with respect to the incident beam direction (Fig. 1). As shown below, the ability to measure velocity spectra at scattering angles $\vartheta \neq 0$ is essential for discriminating between random and (partially) channeled loss components of a spectrum. A detailed description of the experimental set-up will be given elsewere.[3]

Carbon foils with a thickness of about 15 μg/cm^2 were provided by the Brookhaven National Laboratory. Foils of aluminum and gold were prepared at the Technological Laboratory of the Physics Department, University of Munich, with stated thicknesses of 24 μg/cm^2 ± 10 % and 150 μg/cm^2 ± 10 %, respectively. In an independent approach to determine the foil thicknesses we measured the energy loss of 300 keV He. The non-uniformity of the foils was found to be less than 2 % (probed area ~ 5 x 1 mm^2, beam size 0.3 x 0.2 mm^2). Assuming Ziegler's empirical He stopping power functions[6] to be correct at E_{in} = 300 keV, the thicknesses turned out to be 13.6, 26.0 and 130 μg/cm^2 for C, Al and Au, respectively. Judging from the scatter in the compilation of the literature data,[6] the foil thickness thus determined can be assumed to be uncertain to within ± 10 % or less.

III. EVALUATION OF THE MEAN ENERGY LOSS AND THE STOPPING POWER OF TRANSMITTED IONS

Figure 2 shows representative examples of velocity-loss spectra of 505 keV Ne in foils of C, Al and Au at two angles of observation $\vartheta = 0^{\circ}$ and $\vartheta = 1.3^{\circ}$. It is immediately evident that, in the case of Al and Au, a variation of the angle of observation results in pronounced changes of the shape of the spectra. Only in the carbon foils the spectra remain

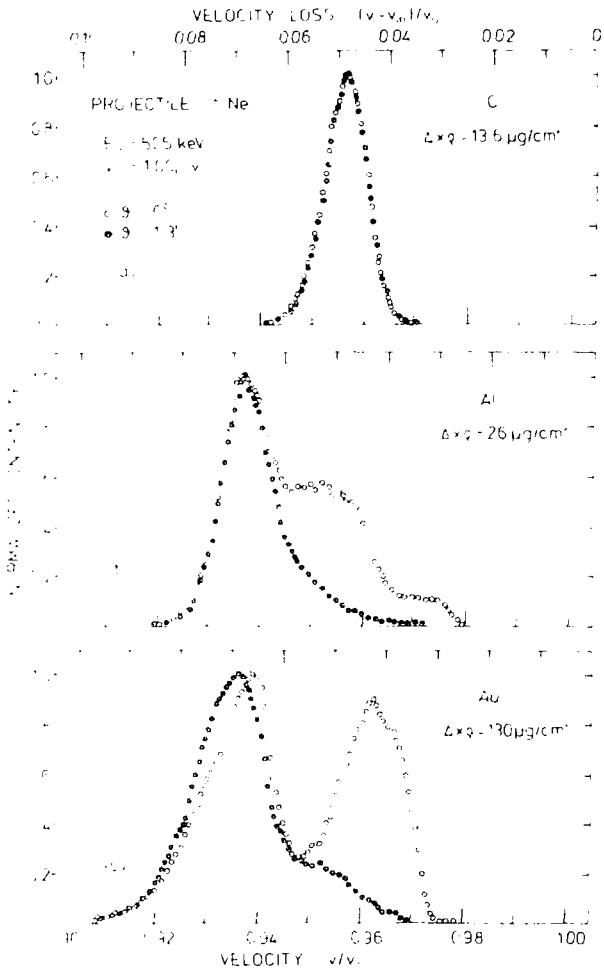

FIG. 2. Normalized velocity-loss spectra of 505 keV neon in (a) carbon, (b) aluminum and (c) gold. Parameter is the angle of observation ϑ, measured with respect to the direction of the incident beam. ($\alpha = 0$).

essentially unaffected by variations of ϑ. We attribute the low-loss (high-velocity) peaks in Fig. 2(b) and (c) to channeling effects. The effects seen in Fig. 2(b) and (c) cannot be removed by tilting the target with respect to the indicent beam (cf. Fig. 1). The only practicable way to circumvent these problems is to measure loss spectra at sufficiently large angles of observation. The same conclusions were reached by Mertens[7] who observed loss spectra similar to those of Fig. 2(b) and (c), but less well resolved.

The energy-loss component of interest here is the low-velocity peak observed for $\vartheta = 1.3^{o}$. This peak is considered to represent the random energy loss. From the velocity spectra we find the mean energy, $\bar{E}_{out}$, of ions transmitted through a foil of areal density $\Delta x\varrho$. The corresponding stopping cross section S is then defined as

$$S(E_1) = \frac{1}{n}\left.\frac{dE}{dx}\right|_{E_1} = \frac{A_2}{N_A}\,\frac{E_{in} - \bar{E}_{out}}{\Delta x \varrho} \qquad (3)$$

where $n(\text{atoms/cm}^3)$ and $\varrho(\text{g/cm}^3)$ are the number density and the density of the target, respectively. A_2 is the atomic weight of the target, N_A Avogadro's number, Δx(cm) the foil thickness and $E_1 = 0.25\ (E_{in}^{1/2} + \bar{E}_{out}^{1/2})^2$.

The position of the random loss peak could be determined with an uncertainty of 1 to 2 % for He and N , 2 to 3 % for Ne and 4 to 6 % for Ar, the better accuracy relating to the higher ion velocities. The total uncertainty in determining ΔE thus ranges from 3 to 8 %.

Experimental stopping cross sections for Ne in C, Al and Au are compiled in Fig. 3(a)-(c). As far as the results of the NYU experiments (Schulz et al.[4]) are concerned, both the raw data (+) and the corrected data (•) are given. The corrections for nuclear stopping are based upon the procedure introduced by Fastrup et al.[8] In our calculations[4] we used the 'average' potential after Wilson et al.[9] It is evident from Fig. 3 that the corrections become noticeable only at very low velocities. Comparison of our own results with those previously reported by other groups[8,10-15] shows that on the basis of the new data the scatter in the experimental stopping cross sections is reduced significantly. More detailed results will be reported elsewhere.[4]

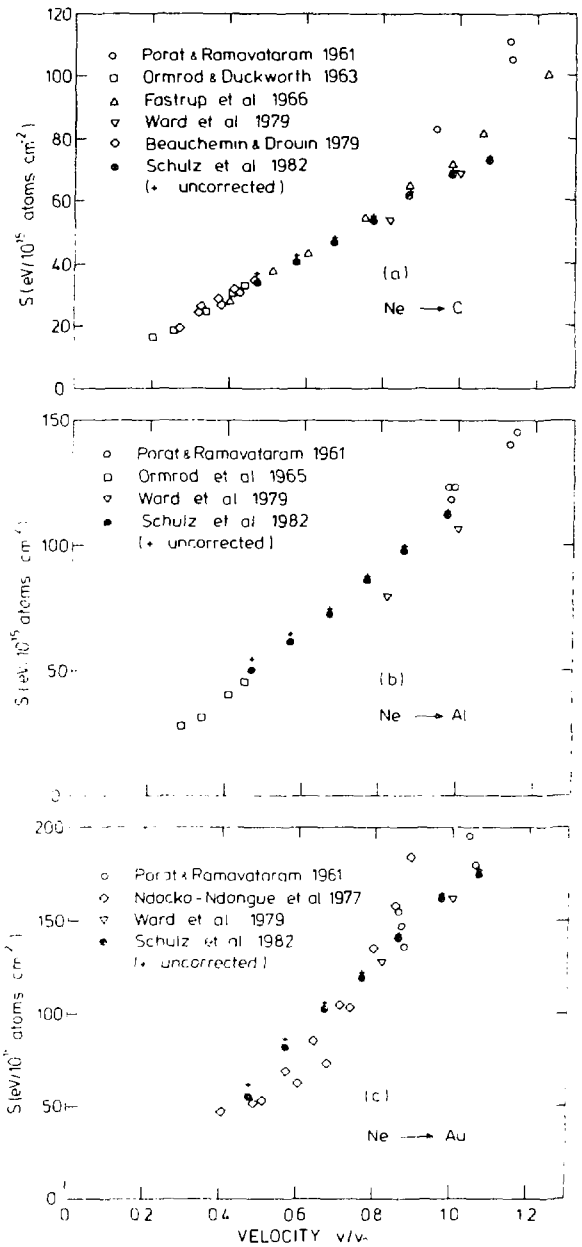

FIG. 1. Stopping cross sections for neon in (a) carbon, (b) aluminum and (c) gold.

IV. EFFECTIVE CHARGE FRACTIONS

'Experimental' and 'theoretical' effective charge fractions, ζ_{exp} and ζ_{th}, are presented in Fig. 4(a)-(c) as a function of the reduced relative ion velocity $v_r/v_o Z_1^{2/3}$, where v_r is the relative velocity between the projectile and the valence electrons in the respective medium.[2,16] It is seen that the effective charges are up to a factor of four larger than the degree of ionization q_{th} calculated by Brandt.[17] This discrepancy is much larger than any conceivable experimental error. The estimated uncertainty in ζ_{exp} is ± 15 %. Thus, the difference between ζ_{exp} and q_{th} seen in Fig. 4 is real.

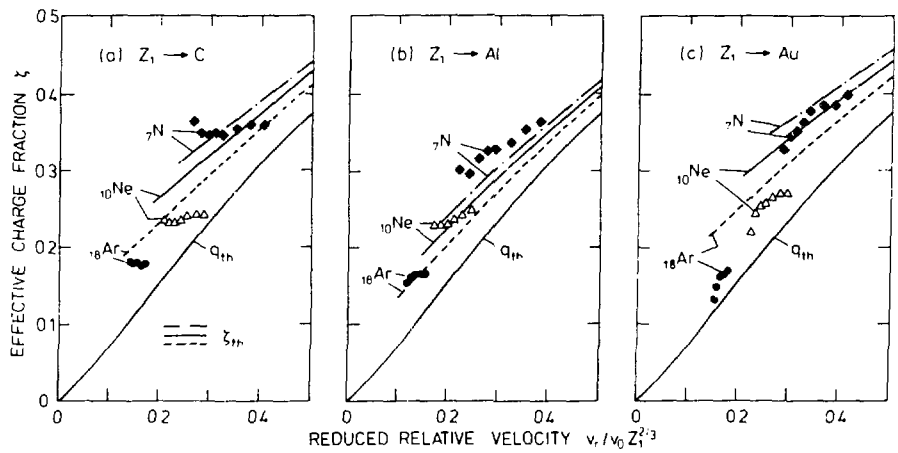

FIG. 4. Effective charge fractions of nitrogen, neon and argon ions in (a) carbon (b) aluminum and (c) gold versus the reduced relative velocity. The theoretical curves for ζ_{th} are derived from Ref. 2, q_{th} is due to Ref. 17.

By contrast, the agreement between ζ_{exp} and ζ_{th} is seen to be quite good. The theoretical and the 'measured' charge fractions differ from each other by at most 35 % with a relative root mean square deviation of 16 %, taking into account all 74 experimental data points.

Detailed inspection of Fig. 4 reveals certain trends which are not yet accounted for by the theory. (i) A v_r-velocity dependence of ζ_{exp} is evident only for $\zeta_{exp} > 0.25$; theory predicts a monotonic increase in ζ_{th}.

(ii) The influence of the target material on the effective charge is less pronounced than predicted. (iii) The empirical Z_1-dependence of ζ has the proper trend, but tends to be more pronounced than predicted.

V. CONCLUSION

The present study shows that effective charge fractions of low-velocity heavy ions in solids, derived from the ratio of stopping cross sections for the respective ions and protons of the same velocity, are fairly well described by the Brandt-Kitagawa theory. A firmer proton data base than employed here is required to improve the reliability of the empirical values. Refinements of the theory appear desirable in order to account for the strong Z_1-dependence of the experimentally determined effective charge fractions. There is also a need for more studies on the behaviour at very low velocities, $v_1/v_o Z_1^{2/3} < 0.2$.

Acknowledgements

This work was supported by the US Department of Energy and by the Gesellschaft für Strahlen- und Umweltforschung (GSF), Neuherberg, FRG. Collaboration with H. Halder (GSF) in designing essential parts of the experimental set-up is gratefully acknowledged. Thanks are due to C. Peterson and J. Shchuchinsky (NYU) for technical assistance during the experiments. One of us (F.S.) is indebted to all colleagues at the Radiation and Solid Laboratory and the Department of Physics for their kind hospitality during his stay at New York University (1979 - 80). F.S. is also grateful to K. Wittmaack for numerous discussions and many suggestions which were very helpful in writing this paper.

References

1. N. Bohr, "Scattering and stopping of fission fragments", *Phys. Rev.* 58, 654 (1940).
2. W. Brandt and M. Kitagawa, "Effective stopping power charges of swift ions in condensed matter", *Phys. Rev. B,* submitted.
3. F. Schulz, "Energy-loss of 50 - 600 keV helium and nitrogen ions in carbon, aluminum and gold foils", *Nucl. Instr. Meth.* submitted.

4. F. Schulz, W. Brandt and J. Shchuchinsky, to be published.

5. H.H. Andersen and J.F. Ziegler, *Hydrogen Stopping Powers and Ranges in All Elements,* (Pergamon Press, 1977).

6. J.F. Ziegler, *Helium Stopping Powers and Ranges in All Elements* (Pergamon Press, 1977).

7. P. Mertens, "Energy loss of light 300 keV ions in thin metal foils", *Nucl. Inst. Meth.* 149, 149 (1978).

8. B. Fastrup, P. Hvelplund and C.A. Sautter, "Stopping cross section in carbon of 0.1 - 1.0 MeV atoms with $6 \leq Z_1 \leq 20$", *Kgl. Danske Vidensk. Selsk., Mat.-Fys. Medd.* 35, No. 10 (1966).

9. W.D. Wilson, L.G. Haggmark and J.B. Biersack, "Calculation of nuclear stopping, range, and straggling in the low-energy region", *Phys. Rev. B* 15, 2458 (1977).

10. D.I. Porat and K. Ramavataram, "Differential energy loss and ranges of Ne, N and He ions", *Proc. Phys. Soc.* 78, 1135 (1961).

11. J.H. Ormrod and H.E. Duckworth, "Stopping cross sections in carbon for low-energy atoms with $Z \leq 12$", *Can. J. Phys.* 41, 1424 (1963).

12. D. Ward, H.R. Andrews, I.V. Mitchell, W.N. Lennard, R.B. Walker and N. Rud, "Systematics for the Z_1-oscillation in stopping powers of Various solid materials", *Can. J. Phys.* 57, 645 (1979).

13. G. Beauchemin and R. Drouin, "The energy-angle distribution of heavy particles penetrating solids: experimental test of the Meyer-Klein-Wedel theory for Ne and Ar ions in carbon below 250 keV", *Nucl. Instr. and Meth.* 160, 519 (1979).

14. J.H. Ormrod, J.R. MacDonald and H.E. Duckworth, "Some low-energy atomic stopping cross sections", *Can. J. Phys.* 43, 275 (1965).

15. V.B. Ndocko-Ndongue, A.J. Pape and R. Armbruster, "Low energy stopping powers of some heavy ions in gold", *Rad. Effects* 33, 91 (1977).

16. S. Kreussler, C. Varelas and W. Brandt, "Target dependence of effective projectile charge in stopping powers", *Phys. Rev. B* 23, 82 (1981).

17. W. Brandt, "Ion screening in solids", *Atomic Collision in Solids.* Vol. 1, ed. by S. Datz et al. (Plenum, New York, 1975).

CALCULATION OF THE EQUILIBRIUM MEAN CHARGE OF HELIUM IONS

T. Kaneko and Y. H. Ohtsuki

Department of Physics, Waseda University, 3-4-1 Ohkubo Shinjuku,
Tokyo 160, Japan

ABSTRACTS

Z_2-oscillation of the equilibrium mean charge of 1 MeV He ions discovered by experiments is confirmed by calculating both the electron-capture and -loss cross sections, employing two-state atomic expansion method and Born approximation, respectively. Our calculations are in good agreement with the experimental results.

§1. Introduction

In the MeV energy region of helium ions, negative charge states can be neglected. So we consider only the singly- and doubly-ionized helium ions. And also the cross sections of the double-electron-capture and -loss may be neglected in comparison with those of the single-electron-capture and -loss. Considering from the experimental data that the capture cross section is larger than the loss cross section in this energy range, the equilibrium mean charge $\bar{q}$ is given by

$$\bar{q} = 2 - \frac{\sigma_{21}}{\sigma_{21} + \sigma_{12}}. \tag{1}$$

It is important to know that only two cross sections, σ_{12} and σ_{21}, are needed to describe the $\bar{q}$.

§2. Electron-Capture Cross Section

Here we derive the electron-capture cross section of He^{2+} ions. The target materials have many electrons and all of them will contribute to the electron-capture cross section. We assume that when one electron in the target atom is captured, the others hardly influence the capture process except screening the target nuclear field. Namely each electron contributes independently. The electron to be captured is called the active electron. Also we employ two-state atomic expansion method for detailed calculations of the matrix elements.

The wave function of the active electron is governed by the time-dependent Schrödinger equation,

$$i \frac{\partial \Psi}{\partial t} = H\Psi$$

$$H = -\frac{1}{2}\Delta - \frac{Z_2}{r_2} - \frac{Z_1}{r_1}, \tag{2}$$

where $Z_2(Z_1)$ is the nuclear charge of the target (the projectile) and $r_2(r_1)$ the position vector of the active electron from the target nucleus (from the projectile). In eq. (2), the trajectory of the projectile is

assumed to be a straight line, so we neglect the scattering potential between the projectile and the target nucleus. In general, Ψ is expanded in terms of the "travelling eigenstates" both of the target and the projectile such as

$$\Psi = a(t)\phi_A(r_2)\exp[-i(\frac{\vec{v}}{2}\cdot\vec{r} + \frac{1}{8}v^2t + \varepsilon_A t)] + b(t)\phi_B(r_1)\exp[-i(-\frac{\vec{v}}{2}\cdot\vec{r} + \frac{1}{8}v^2t + \varepsilon_B t)], \quad (3)$$

where $\phi_A(\phi_B)$ and $\varepsilon_A(\varepsilon_B)$ are the eigen-function and the eigenenergy of the target (of the projectile) respectively. And, $\vec{v}$ is the projectile's velocity and $\vec{r}$ the position vector of the active electron with respect to the midpoint of the internuclear axis. The expansion coefficient a(t) (b(t)) is the probability amplitude of the active electron to find in the eigenstate of the target (of the projectile) at the time t.

From eqs. (2) and (3), we get the following differential equations,

$$\begin{aligned} i(1 - S^2)\dot{a}(t) &= a(t)(h_{AA} - S_{AB}h_{BA}) + b(t)(h_{AB} - S_{AB}h_{BB})e^{i\omega t} \\ i(1 - S^2)\dot{b}(t) &= b(t)(h_{BB} - S_{BA}h_{AB}) + a(t)(h_{BA} - S_{BA}h_{AA})e^{-i\omega t}, \end{aligned} \quad (4)$$

where

$$\begin{aligned} \omega &= \varepsilon_A - \varepsilon_B \\ S^2 &= S_{AB}\cdot S_{AB}^* \\ S_{AB} &= \int d\tau \phi_A^* \phi_B \exp(i\vec{v}\cdot\vec{r}) \\ S_{BA} &= S_{AB}^* \\ h_{AB} &= \int d\tau \phi_A^* (-\frac{Z_2}{r_2})\phi_B \exp(i\vec{v}\cdot\vec{r}) \\ h_{BA} &= \int d\tau \phi_B^* (-\frac{Z_1}{r_1})\phi_A \exp(-i\vec{v}\cdot\vec{r}) \\ h_{AA} &= \int d\tau \phi_A^* (-\frac{Z_1}{r_1})\phi_A \\ h_{BB} &= \int d\tau \phi_B^* (-\frac{Z_2}{r_2})\phi_B \end{aligned}$$

In the above, $d\tau$ is the volume element. S_{AB} and S_{BA} are the overlap integrals between travelling eigenstates, and $h_{AA}(h_{BB})$ the average

potential energy of the interaction between the active electron and the projectile (and the target nucleus).

To solve the eq.(4), we introduce new variables $d_A(t)$ and $d_B(t)$ by the following transformation,

$$\begin{aligned} a(t) &= d_A(t)\exp[-i\int_{-\infty}^{t} dt'\alpha(t')] \\ b(t) &= d_B(t)\exp[-i\int_{-\infty}^{t} dt'\beta(t')] \end{aligned} \tag{6}$$

where

$$\begin{aligned} \alpha(t) &= (h_{AA} - S_{AB}h_{BA})/(1 - S^2) \\ \beta(t) &= (h_{BB} - S_{BA}h_{AB})/(1 - S^2) \end{aligned} \tag{7}$$

Then we obtain the coupled equations from eq.(4).

$$\begin{aligned} i\,\dot{d}_A(t) &= d_B(t)(h_{AB} - S_{AB}h_{BB})/(1 - S^2)\exp[i\omega t + i\sigma(t)t] \\ i\,\dot{d}_B(t) &= d_A(t)(h_{BA} - S_{BA}h_{AA})/(1 - S^2)\exp[-i\omega t - i\sigma(t)t] \end{aligned} \tag{8}$$

where

$$\sigma(t) = \int_{-\infty}^{t} dt'\{\alpha(t') - \beta(t')\}. \tag{9}$$

By solving eq.(8) for the straight-line trajectory with the initial conditions ; $d_A(t = -\infty) = 1$, $d_B(t = -\infty) = 0$. We can obtain the electron capture probability $P_c(\rho)$ as a function of the impact parameter ρ from the equation;

$$P_c(\rho) = |d_B(t = \infty)|^2, \tag{10}$$

and also obtain the electron-capture cross section σ_{21} as follows,

$$\sigma_{21} = 2\pi N_A \int_0^{\rho_{max}} d\rho\cdot\rho\, P_c(\rho). \tag{11}$$

Where N_A is the number of the equivalent electrons in the shell of the target atom. ρ_{max} is the upper limit of the impact parameter.

We consider the case such as the projectile's velocity is larger than the Bohr velocity, S^2 may be negligible in comparison with unity. δ represents the distortion of the electron wave function in the nuclear field of the projectile and the target. This is also neglected because of the high velocity.

In the second equation of eq.(7), considering the initial conditions and neglecting S^2 and $\delta(t)$, the transition probability amplitude of the

electron is expressed as

$$d_B(t=\infty) = -i\int_{-\infty}^{\infty} dt \int d\tau \phi_B^*(\vec{r}_1)(-\frac{Z_1}{r_1} - h_{AA})\phi_A(\vec{r}_2) \times \exp[-i(\vec{v}\cdot\vec{r} + \omega t)]. \quad (12)$$

Neglecting the term h_{AA} in eq.(12) means Brinkman-Kramers approximation [1]. We use Hartree-Fock wave functions for neutral atoms to describe the electrons. The wave function ϕ_A is given by [2]

$$\phi_A = \begin{cases} \sum_i C_i N_i r^{n_i-1} \exp(-\zeta_i r) Y_{00}(\theta,\phi), & \text{for s-state} \\ \sum_i C_i N_i r^{n_i-1} \exp(-\zeta_i r) Y_{10}(\theta,\phi), & \text{for p-state} \\ \sum_i C_i N_i r^{n_i-1} \exp(-\zeta_i r) Y_{20}(\theta,\phi), & \text{for d-state} \end{cases} \quad (13)$$

$(n_i = 1, 2, \ldots\ldots)$

In the above, C_i and N_i are the expansion coefficient and the normalization constant, respectively. The relation between C_i and ζ_i is determined by the variational principle. $Y_{lm}(\theta,\phi)$ is the spherical harmonic function.

The wave function of the captured electron in the projectile takes the following form,

$$\begin{cases} \phi_B(r_1) = (\pi a_1^3)^{-1/2} \exp(-a_1^{-1} r_1) \\ a_1 = Z_1^{-1} \end{cases} . \quad (14)$$

If we neglect h_{AA} in equation (14), we get the form of the $d_B(\rho)$ as a function of the impact parameter ρ as follows,

$$d_B(\rho) = iZ_1^{5/2} \frac{4}{v} \sum_i C_i N_i [\frac{\partial}{\partial(-\zeta_i)}]^{m_i} I_1, \text{ for s-state} \quad (15)$$

and

$$d_B(\rho) = 8\sqrt{3}\, Z_1^{5/2} \frac{1}{v} (\frac{v}{2} + \frac{\omega}{v}) \sum_i C_i N_i [\frac{\partial}{\partial(-\zeta_i)}]^{m_i} I_2, \text{ for p-state} \quad (16)$$

and for d-state,

$$d_B(\rho) = 16\sqrt{5}i\, Z_1^{5/2} \frac{1}{v} \sum_i C_i N_i [\frac{\partial}{\partial(-\zeta_i)}]^{m_i} [I_2 - \{\zeta_i^2 + 3(\frac{v}{2} + \frac{\omega}{v})^2 I_3\}], \quad (m_i = 1, 2, \ldots\ldots) \quad (17)$$

where

$$I_1 = \{K_0(\alpha\rho) - K_0(\beta_i\rho)\}/X,$$
$$I_2 = (1_1/X) - \{\rho K_1(\beta_i\rho)/2\beta_i X\}$$

$$
\begin{aligned}
I_3 &= (I_2/X) - \{\rho^2 K_0(\beta_i\rho)/8\beta_i{}^2 X\} - \{\rho K_1(\beta_i\rho)/4\beta_i{}^3 X\} \\
X &= \beta_i{}^2 - \alpha^2 \\
\alpha^2 &= Z_1{}^2 + (\frac{v}{2} - \frac{\omega}{v})^2 \\
\beta_i{}^2 &= \zeta_i{}^2 + (\frac{v}{2} + \frac{\omega}{v})^2 .
\end{aligned}
\tag{18}
$$

In eq.(18), K_0 and K_1 are the modified Bessel functions of the second kind. The impact parameter dependence of the capture probability appears in terms of the arguments of K_0 and K_1. The variables, α and β_i, depend on the projectile's velocity v, while X is independent of the velocity.

§3. Electron-Loss Cross Section

The cross section for the electron-loss can be calculated to be the ionization cross section of He^+ ion. When the projectile with the nuclear charge Z_1 and with only one electron collides with the neutral target with nuclear charge Z_2, the total Hamiltonian H is given by

$$
\begin{aligned}
H &= -\frac{1}{2M}\Delta_R + \frac{Z_1 Z_2}{R} + H_t + H_i + V_{int} \\
H_t &= \sum_i (-\frac{1}{2}\Delta_{r_{2i}} - \frac{Z_2}{r_{2i}}) + \frac{1}{2}\sum_{i\neq j}\frac{1}{|\vec{r}_{2i} - \vec{r}_{2j}|} \\
H_i &= -\frac{1}{2}\Delta_{r_1} - \frac{Z_1}{r_1} \\
V_{int} &= \sum_i (-\frac{1}{|\vec{r}_{2i} - \vec{R}|}) - \frac{Z_2}{|\vec{r}_1 + \vec{R}|} + \sum_i \frac{1}{|\vec{r}_{2i} - \vec{r}_1 - \vec{R}|}
\end{aligned}
$$

In the above, M is the reduced mass in the laboratory system. And $\vec{r}_{2i}$ $(i = 1, \ldots, Z_2)$ is the position vector of the target electron from the nucleus and $\vec{r}_1$ is that of the electron from the projectile's nucleus and $\vec{R}$ the relative position vector of the projectile from the target nucleus. Δ_r is the Laplacian operator with respect to the variable r $(r = R, r_{2i}, r_1)$.

The wave function of the total system is expanded by the product of the eigen-functions of the target, Φ_A, and the projectile, ϕ_B, such as

$$
\psi = \sum_{A,B} F_{AB}(\vec{R})\, \Phi_A(\vec{r}_{21}, \ldots, \vec{r}_{2Z_2})\phi_B(\vec{r}_1) \tag{20}
$$

where $F_{AB}(\vec{R})$ is the expansion coefficient and Φ_A and ϕ_B satisfy the

following equations,

$$H_t \Phi_A = \varepsilon_A \Phi_A$$
$$H_i \Phi_B = \varepsilon_B \Phi_B \tag{21}$$

in the above ε_A and ε_B are the eigenvalues of the electron state A in the target and that of the electron state B in the projectile respectively. Inserting Ψ into the Schrödinger equation ;

$$H\Psi = E\Psi \tag{22}$$

we obtain the following differential equation ;

$$(\Delta + K_{AB}^2) F_{AB}(\vec{R}) = \sum_{A'B'} V_{ABA'B'} F_{A'B'}$$
$$V_{ABA'B'} = 2M \int \Phi_A^* \Phi_B^* \left(\frac{Z_1 Z_2}{R} + V_{int}\right) \Phi_{A'} \Phi_{B'} \prod_{j=1}^{Z_2} d\vec{r}_{2j} d\vec{r}_1$$
$$K_{AB}^2 = 2M(E - \varepsilon_A - \varepsilon_B). \tag{23}$$

The scattering amplitude g_{AB} of the transition from the ground state both of the target and of the projectile to the state A of the target and the state B of the projectile, is

$$g_{AB} = - \frac{2M[Z_2 \delta_{A0} - f_{A0}^t(\vec{Q}_{AB})][Z_1 \delta_{B0} - f_{B0}^p(-\vec{Q}_{AB})]}{Q_{AB}^2} \tag{24}$$

where

$$\vec{Q}_{AB} = \vec{K}_{AB} - \vec{K}_{00}$$
$$f_{A0}^t(\vec{Q}) = \int \Phi_A^* \left\{ \sum_{j=1}^{Z_2} \exp(i\vec{Q}\cdot\vec{r}_{2j}) \right\} \Phi_0 \prod_{j=1}^{Z_2} d\vec{r}_{2j}$$
$$f_{AB}^p(\vec{Q}) = \int \phi_B^* \exp(i\vec{Q}\vec{r}_1) \phi_0 d\vec{r}_1. \tag{25}$$

In the above, $\vec{K}_{00}$ and $\vec{K}_{AB}$ are the wave vectors in the initial and in the final state respectively. The cross section of this transition is obtained by integrating over the solid angle $d\Omega$,

$$\sigma_{AB} = \int \frac{K_{AB}}{K_{00}} |g_{AB}|^2 d\Omega. \tag{26}$$

Because the electron-loss is considered as the ionization of the projectile, the state B of the projectile is in a continuous state.

First, in the case that the state A is in the ground state, the target remains in the ground state and so the ionization is caused by the total potential of the target atom. The cross section of this process is given by

$$\sigma_{el} = 8\pi\left(\frac{Z_2}{Z_1\eta}\right)^2 \int_{q_{min}}^{q_{max}} \frac{dq}{q^3} \left\langle \left| 1 - \frac{1}{Z_2} f_{00}^{t}(-Z_1\vec{q}) \right|^2 \right\rangle \times \int_0^{\kappa_{max}(q)} d\kappa\, I(q, \kappa) \tag{27}$$

$$\kappa_{max}(q) = (2q\eta - 1)^{1/2},$$

where κ is the wave vector of the ionized electron and η the ratio of the projectile's velocity v to the orbital velocity Z_1 of the electron of the projectile, that is to say $\eta = v/Z_1$. In eq.(27),

$$I(q,\kappa) = \frac{2^8 q^2 \kappa [q^2 + \frac{1}{3}(1 + \kappa^2)]}{[1 + (\kappa + q)^2]^3 [1 + (\kappa - q)^2]^3} \frac{\exp(-\frac{2}{\kappa}\tan^{-1}\frac{2\kappa}{1 + q^2 - \kappa^2})}{1 - \exp(-\frac{2\pi}{\kappa})} \tag{28}$$

and

$$q_{min} = \frac{1}{2v}, \quad q_{max} = \infty.$$

Moreover, $\langle \cdots\cdots \rangle$ means the average over the direction of the momentum-transfer vector $\vec{q}$ and it is reduced to a scalar function.

We use the Hartree-Fock wave functions for calculation of the form factor $f_{00}^{t}(-Z_1\vec{q})$ as well as the capture process. The target form factor is the sum of each electron's form factor;

$$f_{00}^{t}(-Z_1\vec{q}) = \sum_i f_{00}^{i}(-Z_1\vec{q}) \cdot N_i$$

where N_i is the number of the equivalent electrons in the i-th shell of the target atom and $f_{00}^{i}(-Z_1\vec{q})$ the i-th electron's form factor.

§4. Numerical Calculations and Discussions

First we calculated the electron-capture probability $P_c(\rho)$ as a function of the impact parameter ρ for the carbon and the calcium targets, which results are shown in Figs.1 and 2 respectively. For the carbon target, we can see that 2p-state electrons have the largest contribution. On the other hand, for the calcium target 3p-state contributes mainly to the capture process. In both cases, the dips of $P_c(\rho)$ are caused by the node of the wave functions in the state. So we can conclude that for the calcium target, the M-shell has the dominant contribution than any other shells, while the L-shell contributes dominantly for the carbon target.

Next, we calculated the electron-capture cross section

σ_{21} for various targets from the values of $P_c(\rho)$. As shown in Fig. 3, we can see the oscillatory behavior. The peaks are marked at the positions where Z_2 equals 4, 10, and nearly equals 22 and 45 for 1 MeV He^{2+}. These positions reflect the dominant contributions of the K, L, M and N shells respectively. This is explained by the fact that the Hatree-Fock energy levels of target electrons which has the most dominant contribution at the peak positions, nearly equals to the ground state energy level of the electron which is bounded in the He^{2+}. The broad peak in the capture cross section of the targets which have the atomic number between twenty and thirty is due to the fact that the energy levels of 2p- and 3p-states increase gradually with the atomic number. Therefore these levels are near the 1s-state energy level of He^{2+} over the broad Z_2.

When the energy of He^{2+} becomes 2 MeV, the absolute values of the capture cross section decrease and the peak positions tend to shift a little to the larger atomic number. According to the results on the classical basis, those electrons whose orbital velocities are comparable with the ion velocity have the dominant contribution to the capture process. But our quantum-mechanical calculations lead us to the result that the orbital electrons which satisfy the condition: $|\varepsilon_A - \varepsilon_B| \ll (1/2) m v^2$, play a dominant role in the capture process.

In Fig. 4, we show the calculated results for the electron-loss cross section. In Fig. 5, we show the equilibrium mean charge of helium ions by using our computational values of the electron-capture and -loss cross sections. The overall feature of the Z_2-dependence is in good agreement with the experimental (gas and solid) data of Fukuzawa's group.

REFERENCES

[1] C. D. Lin, S. C. Soong and L. N. Tunnell, Phys. Rev. A17, 1646 (1978).

[2] E. Clementi and C. Roetti, Atom. Dat. Nucl. Dat. Tables, 14, 177 (1974).

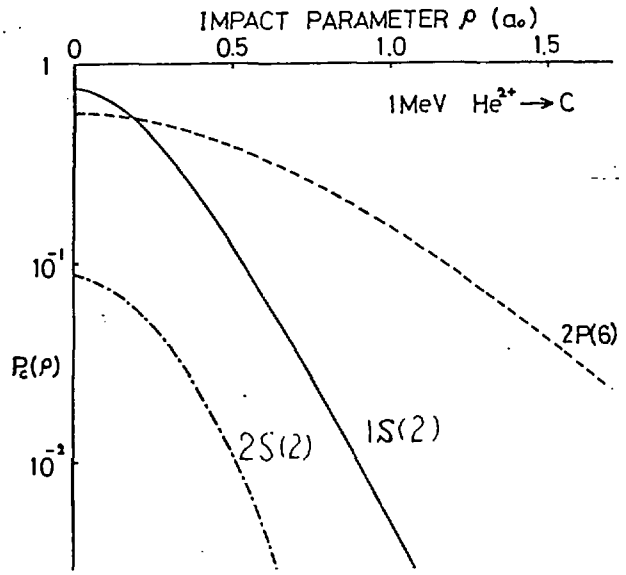

Fig. 1 One-electron capture probability $P_c(\rho)$ of 1 MeV He^{2+} for the carbon target as a function of the impact parameter ρ.

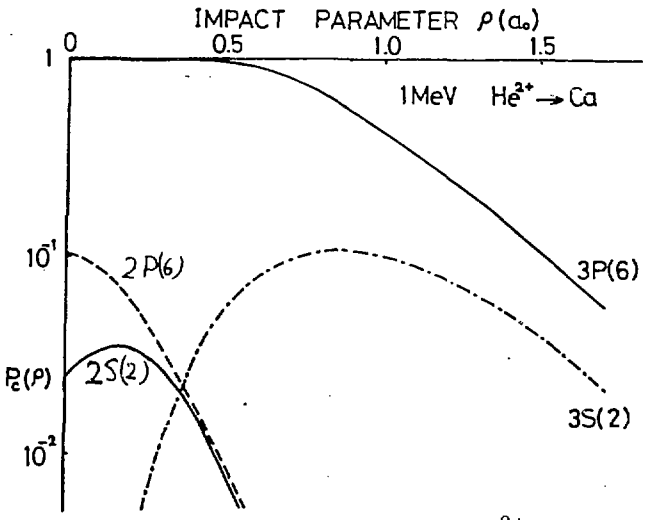

Fig. 2 One-electron capture probability $P_c(\rho)$ of 1 MeV He^{2+} for the calcium target as a function of the impact parameter ρ.

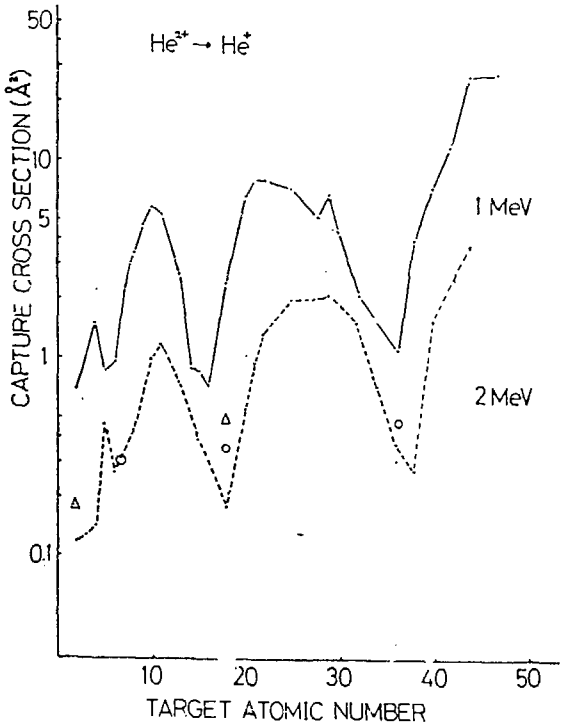

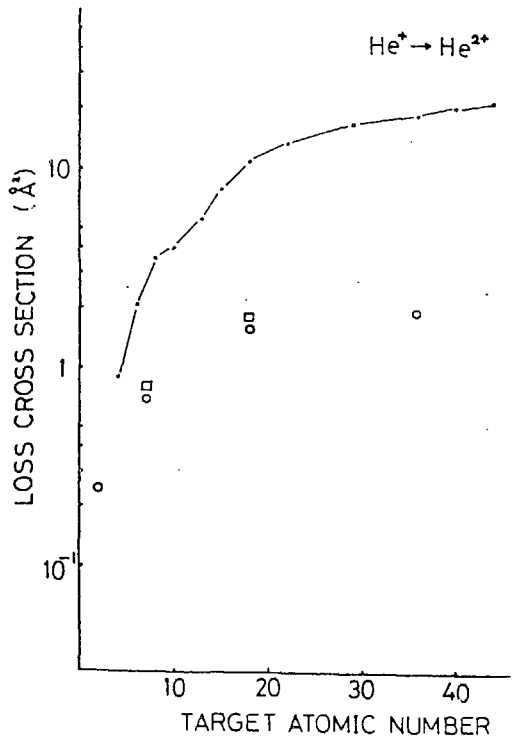

Fig. 3 Target atomic number dependence of one-electron capture cross section σ_{21} of 1- and 2-MeV He^{2+}. —·— (1 MeV He^{2+}), ---·--- (2 MeV He^{2+})

Fig. 4 Target atomic number dependence of one-electron loss cross section σ_{12} of 1 MeV He^{+}.

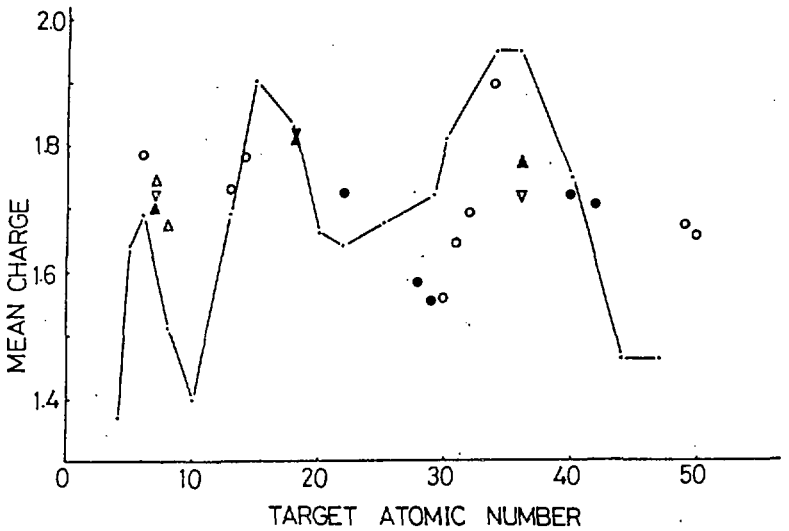

Fig. 5 Target atomic number dependence of the equilibrium mean charge of 1 MeV helium ions.

MEDIUM DEPENDENCE OF CHARGE STATE FRACTIONS OF MeV He BEAM

Fumio Fukuzawa

Department of Nuclear Engineering,
Kyoto University, Kyoto 606, Japan

We have measured the charge state fractions of He ions in the energy range 0.5-2.3 MeV by means of backscattering method. The charge states and energies of scattered He ions were analyzed with the combination of magnetic deflection and a position sensitive solid state detector [1]. In this method we can use thick targets and therefore we can easily obtain the data over various kinds of target materials. In addition to the benefit for preparing the target without difficulty, thick targets can be treated easily such that they can be heated up and also evaporated on the surface without destroying the condition of data aquisition.

In our apparatus, the collision chamber was evacuated with oil diffusion pumps with liquid nitrogen traps and attained only to the pressure of 10^{-7} Torr. Very small amount of contaminating substances on the target surface can affect drastically the charge state fractions of He ions scattered from the target, giving the same result for different target materials [2].

In order to prepare clean surface, two methods were employed; raising target-temperature and continuous evaporation during measurement.

By raising target-temperature, as can be seen in Fig. 1, the mean charge calculated with measured charge state fractions shows abrupt change at about 500°C, and saturates above 800°C. This saturation value is thought to be characteristic to the target material itself [3].

In the case of continuous evaporation, as shown in Fig. 2, the characteristic mean charge was obtained at high evaporation rate compared to the sticking rate of residual gas molecules on the target surface [4].

These two kinds of data are summarized in Fig. 3 together with the gas target data for the mean charge of 1 MeV He ion for various targets. It is clearly seen that the mean charge oscillates as a function of target atomin number.

The solid curve in this fifure is calculated by the following formula,

$$\bar{q} = (\sigma_{21} + 2\sigma_{12})/(\sigma_{21} + \sigma_{12}).$$

The electron loss cross sections σ_{12} were determined empirically by connecting available experimental data. The electron capture cross sections σ_{21} were calculated on the basis of Bohr-Lindhard model [8]. In the present calculation, we have taken into the discrete orbital velocities and orbital radii of all subshell electrons in the target atom. They were estimated from the binding energies [9] and radial distributions [10] of subshell electrons. Two fitting parameters have been introduced in order to correct the capture probability of the released electron and to take into account finite release time of the target electron. Calculated mean charge reproduces satisfactorilly the experimental oscillatory behaviour.

It is interesting to note that the period of this Z_T-oscillation is just the same as that of stopping cross section [11].

REFERENCES

1. F. Fukuzawa, " Measurement of Equilibrium Charge Distribution with a Thick Target", Phys. Lett. 43A, 147-148 (1973)
2. Y. Kido, M. Asari, A. Nakata and F. Fukuzawa, "Equili-

brium Charge State Distributions of ^{14}N and ^{20}Ne Ions Emerging from Solids", Nucl. Instr. and Meth. 143, 601-604 (1977)

3. Y. Kido, Y. Kanamori and F. Fukuzawa, "Target Temperature Dependence of Charge State Distributions of Fast He Ions Emerging from Solids", Nucl. Instr. and Meth. 164, 565-570 (1979)
4. Y. Haruyama, Y. Kanamori, T. Kido and F. Fukuzawa, "Equilibrium Charge State Distributions of MeV He Ions Backscattered from Continuously evaporated Targets", to be published in J. Phys. B (1982)
5. A. Itoh and F. Fukuzawa, "Equilibrium Charge Distributions of Helium Beams in Various Gases", J. Phys. Soc. Jpn. 50, 632-637 (1981)
6. L. I. Pivovar, V. M. Tubaev and M. T. Novikov, "Electron Loss and Capture by 200-1500 keV Helium Ions in Various Gases", Sov. Phys.-JETP 14, 20-24 (1962)
7. V. S. Nikolaev, I. S. Dmitriev, L. N. Fateevaand Ya. A. Teplova, "Investigation of the Equilibrium Charge Distribution in a Fast Ion Beam", Sov. Phys.-JETP 12, 627-633 (1961)
8. N. Bohr and J. Lindhard, "Electron Capture and Loss by Heavy Ions Penetrating through Matter", K. Dan.Vidensk. Selsk. Mat.-Fys. Medd. 28, Nr. 7, 1-31 (1954)
9. W. Lotz, "Electron Binding Energies in Free Atoms", J. Opt. Soc. Am. 60, 206-210 (1970)
10. J. P. Desclaux, "Relativistic Dirac-Fock Expectation Values for Atoms with Z=1 to Z=120", At. Data Nucl. Data Tables 12, 311-406 (1973)
11. J. F. Ziegler and W. K. Chu, "Stopping Cross Sections and Backscattering Factors for ^{4}He Ions in Matter", At. Data Nucl. Data Tables 13, 463-489 (1974)

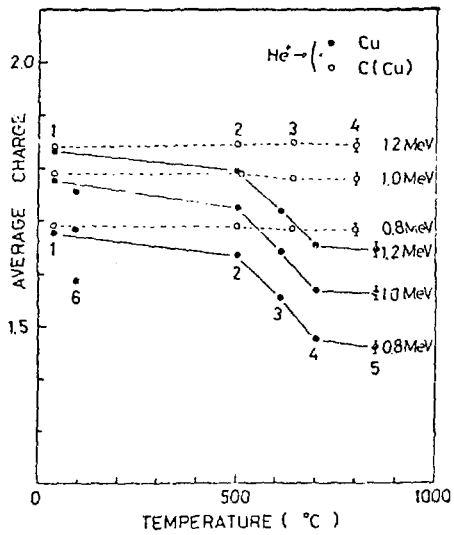

Fig. 1. Temperature dependence of mean charge of 0.8, 1.0 and 1.2 MeV He ions emerging from Cu and C (C evaporated on Cu plate) Targets.

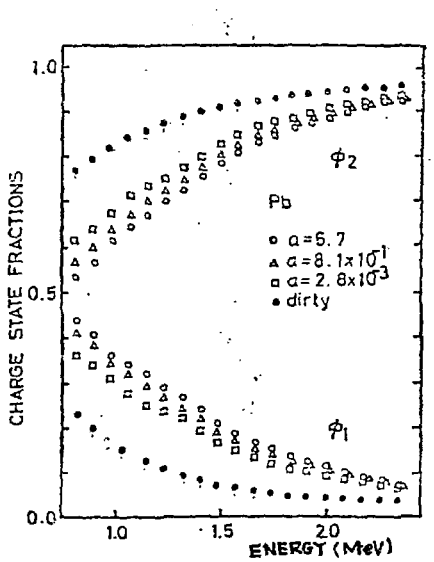

Fig. 2. Charge state fractions of He ions emerging from Pb. The surface cleanliness parameter α is defined as the ratio of number of evaporated metal atoms to the number of residual gas molecules on the target surface.

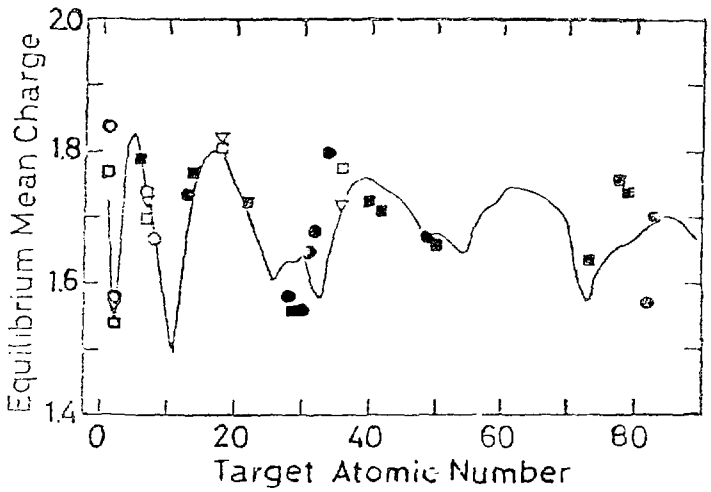

Fig. 3. Mean charges of 1 MeV He ions for various targets. Experimental gas and solid data are represented by open and closed symbols, respectively; ▣ [3] ● [4] ○ [5] □ [6] ▽ [7]. The solid curve was calculated on the basis of Bohr-Lindhard model.

Charge State Distribution of Light Ions at Glancing Collision with Solid Surface

M. Mannami, K. Kimura and N. Kuwata
Department of Engineering Science, Kyoto University, Kyoto 606

I. Introduction

Many experimental results have suggested that the charge state distribution of ions having penetrated through solid is different from that inside the solid. It is important to clarify the physical process taking place at solid surface in order to know the states of ions inside the solid from those observed outside the solid.

In the present paper, we report our measurement of charge state distributions of He^+ and H_2^+ ions having been scattered in small angles (less than 4°) at surfaces of Au, Ag and C. One of the advantages of the use of the glancing collision of ions at solid surface for the study of ion-surface interaction is that the dwell time of ion near solid surface can be made more than 100 times longer than that in normal transmission experiments. The longer dwell times may alter any contribution of solid surface to electron capture and loss of ions. Although new experimental evidences have been obtained on the anisotropic excitation of ions at tilt foil experiments, which could be interpreted as the anisotropic electron capture into excited magnetic states, the understanding of interaction between fast ion and solid surface has little progress.

2. Experimentals

For the glancing collision experiment, it is important to have atomically smooth surface. This is difficult to prepare in usual experimental conditions. Therefore we evaporatd Au, Ag and C on freshly cleaved surfaces of mica. The evaporated Au and Ag were polycrystalline and the average grain size were 20 nm as observed by transmission electron microscope. The evaporated carbon was amorphous.

The experimental set-up is shown in Fig. 1. The mica plate was mounted on a goniometer in vacuum of 10^{-7} torr. The mica plate was surrounded by plate cooled by liquid nitrogen so as to avoid the

contamination of surface by the beam irradiation. The beam of ions from 4 MV Van de Graaff accelerator was collimated by apertures to the divergence angle less than 0.05° and the beam diameter about 0.5 mm. The scattered ions was analysed into their charge states by the use of an electrostatic deflector and counted by a solid state detector. The incident beams of ions used in the experiment were 1 MeV and 1.5 MeV He^+ and 700 keV H_2^+. The beam intensity and the purity of incident beam were monitored by a solid state detector accepting the ions scattered at 90°.

3. Results

The characteristic features of the energy spectrum of scattered ions can be seen in Fig. 2, where the incident angle θ_i of 1.5 MeV He^+ was 15' and the scattered angle θ_s was 30'. The spectrum is sharply peaked at the energy slightly less than the incident energy. This peak becomes narrower and the peak energy becomes larger for smaller θ_i and θ_s. Thus for ions scattered at small angles, the energy spectra of each charge states can be measured easily by the experimental set-up shown in Fig. 1, where the scattered angle θ_s can be selected by the aperture in front of deflector and all the ions in a charge state can be accepted by the detector set at a suitable position and with a suitable electrostatic potential applied to the deflector.

From the energy spectra, $I_{A_f}(E_o,\theta_i,\theta_s,E)$, of each charge states of scattered ions A_f at angle θ_s, the energy dependent fraction of A_f ions, $F_{A_f} = F_{A_f}(E_o,\theta_i,\theta_s,E)$, in the scattered beam at θ_s when the beam of A_i ions incident on the target at an angle θ_i can be obtained as a function of incidnet energy E_o, θ_i, θ_s, and E. Figure 3 shows an example of charge state fraction of scattered He ions when the incident beam was 1000 keV He^+ with θ_i = 30' and θ_s = 36'. Scattered yields of ions of energies near the incident energy were small and no reliable fractions could be determined at these energy region. For ions of energy less than about 990 keV (energy loss larger than about 10 keV), the fractions of He°, He^+ and He^{++} do not show any anomaly and they agreewell with the data found in literature shown by solid lines. This result was independent of the target material.

Figure 4 shows the energy dependent H° fraction, where the incident

700 keV H_2^+ beam was scattered at Au target when $\theta_i = 2.0°$ and $\theta_s = 2.9°$, where the twice of the fraction $\phi_{H_2^+ \to H^o}(E_i=700keV, \theta_i=2°, \theta_s=2.9°, E)$ is shown. The energy spectrum of non-analysed H ions is also shown in the figure. At the energies less than about 350 keV, which is a half of the energy of incident H_2^+ ions, H^o fraction is constant independent of energy E, while it is a decreasing function of E at lower ion energies. The fraction of H^o observed in the case of normal transmission of H^+ beam through carbon is shown by the solid line for comparison. The scatter of the data found in literature is shown by an error bar. The H^o fraction observed in the present experiment is larger than that observed for H^+ incidence.

For smaller incident and scattered angles, the energy spectra become narrower. For these cases, we calculated the charge fractions of ions scattered at a given direction,

$$\phi_{H_2^+ \to H^o}(E_i, \theta_i, \theta_s) \simeq \frac{\int dE\ I_{H^o}(E_i, \theta_i, \theta_s, E)}{\int dE\ I_{H^o}(E_i, \theta_i, \theta_s, E) + \int dE\ I_{H^+}(E_i, \theta_i, \theta_s, E)} .$$

An example of dependence of the H^o fraction on scattered angle θ_s is shown in Fig. 5. The energy at the peak of the spectrum is also shown. H^o fraction is a few tens percent larger than that at normal transmission in the angular range of scattered ions observed in the present experiment.

At 700 keV in the energy spectra, the reflected incident H_2^+ ions and D^+ ions, which could not be eliminated from the incident H_2^+ beam, were detected. The dependence of this reflected ions on the scattered angle is shown in Fig. 6. H_2^+ fraction is a decreasing function of θ_s and becomes a constant at angles larger than about 1°. This constant value is supposed to be D^+, estimated from the D concentration of incident beam measured by 90° scattering.

4. Discussion

No anomaly in the charge state distribution in the scattered He ions was observed, i.e. the observed fractions agree very well with the data found in literature for the case of transmission. The low energy scattered H ions, which were formed by the dissociation of H_2^+ and have penetrated through the target more than 0.3 μm, also showed no anomaly

in their charge state fractions. Although the dwell times of these ions near solid surface were very long compared with that at normal transmission, i.e. the dwell time is inversely proportional to $\cos(\theta_i-\theta_s)$, no change in the charge state distribution was detected. This suggests the existence of electron capture process independent of dwell time of ion near solid surface or the negligible role of solid surface on the electron capture of ions in the energy range studied in the present experiment.[1]

The yields of scattered ions having energies almost equal to the incident energy were so small in the present ion-target geometry and we could not measure their charge state distributions. The minimum energy losses of the scattered ions we could observe were 5 keV and 10 keV for 700 keV H_2^+ and 1000 keV He^+ respectively. If the stopping powers of the bulk can be used for these ions, the dwell times of these ions in target were longer than 6 fs and 2 fs for 700 keV H_2^+(350 keV H^+) and 1000 keV He^+ respectively. These dwell times in target are longer than the life-times of the incident H_2^+ and He^+ observed in transmission 0° scattered ions through thin carbon foils [2-5] and thus the equilibrium of charge states is supposed to be attained for these observed ions. In fact, the agreement between the observed fractions and those found in literature for He^+ ions was satisfactory and this is consistent with the above statement. However, for the scattered H ions , which have suffered from energy losses less than about 50 keV, the observed charge state fractions showed the effects of dissociation of incident H_2^+ ions. This may be related to the observation by Gaillard et al.[2] that the transmitted H^o fractions for the cases of H_2^+ ion incidence are a few tens percent larger than those for proton of same velocity when the beams have transmitted through carbon foils (dwell time 2 - 15 fs). This overproduction of H^o is interpreted as due to the target electron capture into $2p\sigma_u$ orbit of clustered di-proton. Thus the present results may also be interpreted as due to the target electron capture by cluster as a whole, although it is surprising that the dissociated H fragments travel in solid as a cluster after being scattered at angles larger than 4°.

The scattered H_2^+ ions had energy equal to that of incident H_2^+ ions

within the experimental error. This suggests that the scattered H_2^+ ions may either be reflected at the surface or had dwelt in target not more than 0.1 fs. If latter the case, the dwell time is within so callled "red regime" and the observed H_2^+ ions are the result of molecular transmission. The observed transmitted fractions at 0.5° is 10^{-2} of the yield of 0° transmission. This decrease may be due to the effect of scattering in target and may be interpreted by the model proposed by Cue et al.[5]

[1]K. Kimura, A. Kyoshima, A. Itoh and M. Mannami, Radiat. Effects 41, 91 (1979).

[2]M. J. Gailllard, J. -C. Poizat, A. Ratkowski, J. Remillieux, and M. Auzas, Phys. Rev. Lett. A 16, 2323 (1977).

[3]N. Cue, N. V. de Castro-Faria, M. J. Gaillard, J. -C. Poizat, and J. Remillieux, Nucl. Instr. and Methods 170, 67 (1980).

[4]N. Cue, N. V. de Castro-Faria, M. J. Gaillard, J. -C. Poizat, J. Remillieux, D. S. Gemmell, and I. Plesser, Phys. Rev. Lett. 45, 613 (1980).

[5]T.R. Fox, Nucl. Instrum. and Methods 179, 407 (1981).

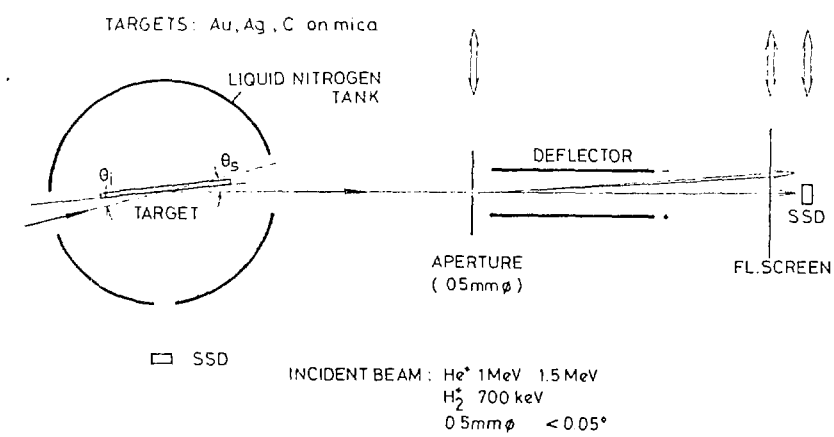

FIG.1 Experimental set-up

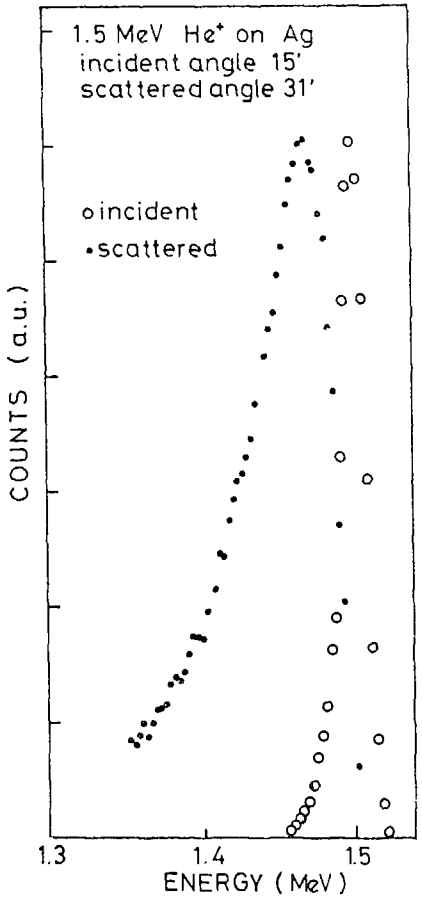

FIG.2 A typical energy spectrum of scattered ions.

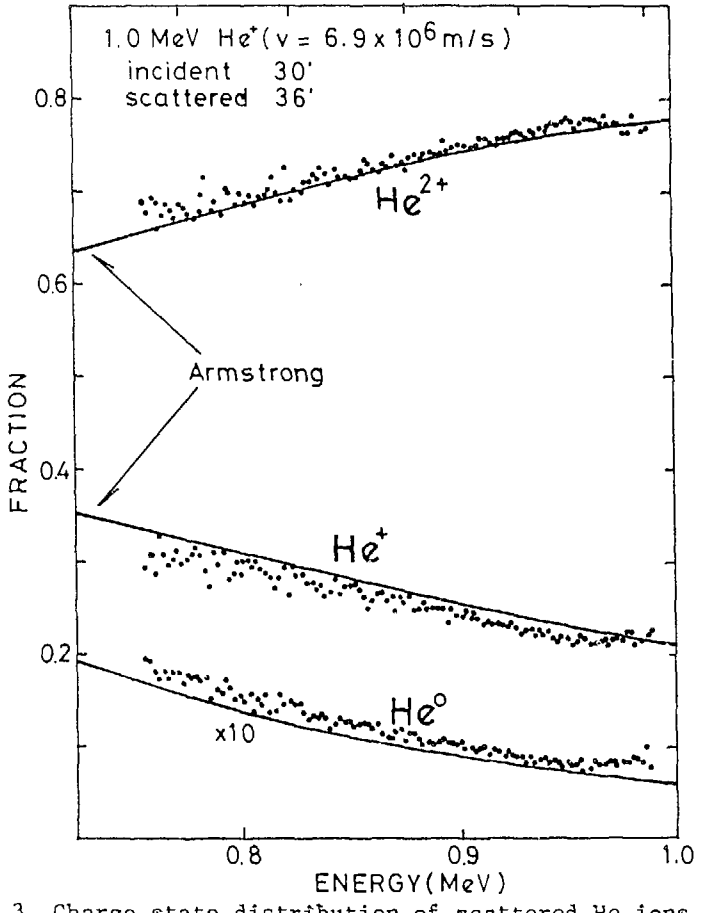

FIG. 3 Charge state distribution of scattered He ions Solid lines are the data by Armstrong et al.

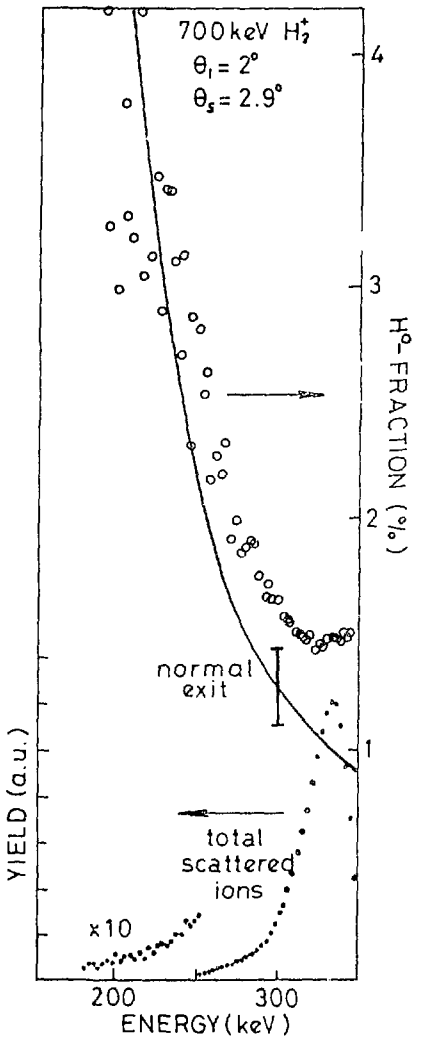

FIG. 4 Energy dependent H^o fraction when the incident beam of 700 keV H_2^+ was scattered at Au with θ_i=2.0° and θ_s=2.9°.

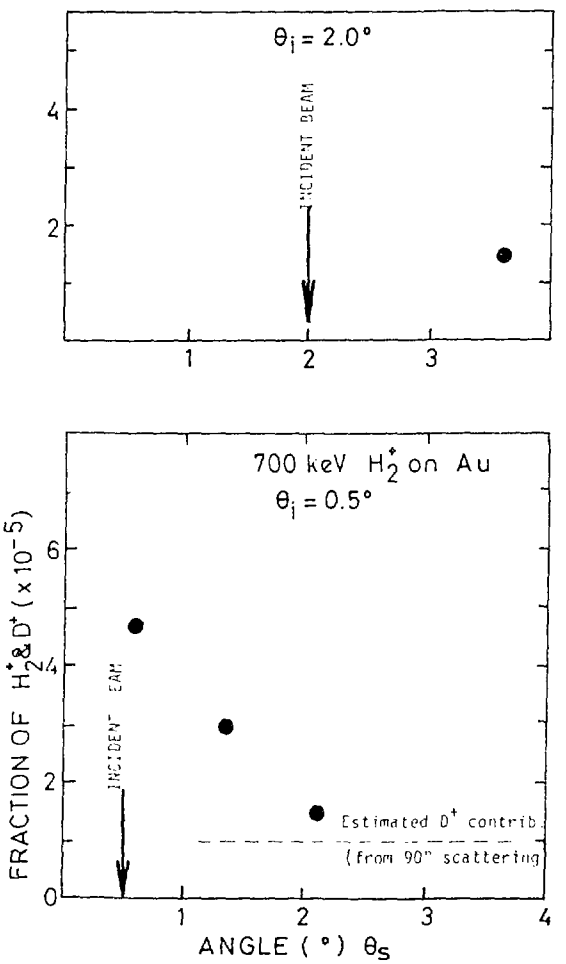

FIG.6 Dependence of H_2^+ fraction on scattered angle θ_s when 700 keV H_2^+ on Au.

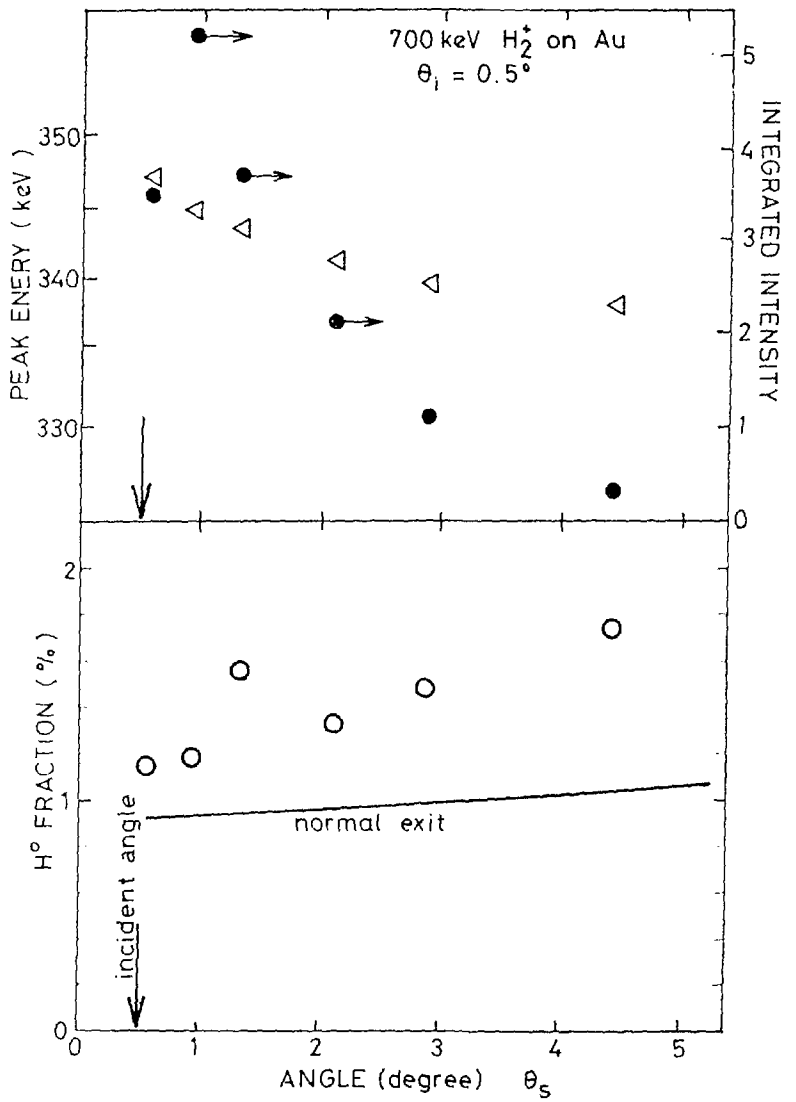

FIG. 5 H^o fraction as a function of scattered angle for 700 keV H_2^+ ions on Au target. Peak energy of the scattered ions and the total scattered intensity are also shown.

"Interactions of Fast Molecular Ions Traversing Thin Foils"
"The Contribution from Field-ionized Rydberg Atoms in Measurements on Convoy Electrons"

Donald S. Gemmell
Physics Division, D203
Argonne National Laboratory, Argonne, IL 60439

A) Interactions of Fast Molecular Ions with Matter

1. INTRODUCTION

Experiments with fast (MeV) molecular-ion beams offer many attractive possibilities for studying atomic collisions in solids. Of particular value in such experiments is the possibility of determining the force fields (primarily the induced electric field) that surround ionic fragments traversing a solid. One has the opportunity to evaluate these fields not just at the fragments themselves (as one would, for example, in stopping-power measurements with monatomic projectiles) but in the spatial regions extending out to several Angstroms from the fragment positions.

In this paper we give a brief introduction to the subject and present some recent results. For more detailed information, the reader is reminded of the existence of the published proceedings[1,2] of two recent workshops on these topics. There also exist several recent review articles [3-8] including one[8] on the use of the experimental techniques to determine the stereochemical structures of molecular-ion projectiles.

In a typical experiment with fast molecular ions, a tightly collimated magnetically analyzed beam of molecular projectiles is directed onto a thin target foil (most commonly carbon, in order to reduce multiple-scattering effects). In the front surface layers of the foil, some or all of the electrons on

each projectile are stripped off, so that, after a time typically about 10^{-16} sec (see, eg. ref. 3), there exists a cluster of fragment ions each with a well-defined equilibrium effective charge. These fragments separate in a "Coulomb explosion". The characteristic time for the Coulomb explosion to develop (a few femtoseconds) is usually comparable with the dwell time in the target. (For dwell times much less than 1 fsec, non-equilibrium effects are observed in which the emergent molecular fragments retain a memory of the initial electronic configuration of the projectile. Emerging from the foil, the fragments may capture sufficient electrons to reform a bound state of the initial projectile species (this is usually termed "transmission"), or some other species based on a combination of projectile fragments. Most commonly, a dissociative molecular state is formed which leads to individual monatomic fragment ions in various charge states and in varying degrees of excitation.

2. EXPERIMENTS WITH FAST LIGHT MOLECULAR PROJECTILES

a. Dissociation

Figure 1 shows results obtained for the joint energy-angle distributions of protons arising from the dissociation of 2-MeV HeH^+ ions in a thin carbon foil.[9,10] The observed "ring pattern" [e.g. fig. 1(c)] is readily understood in terms of the vector diagram shown in fig. 1(b), where the beam velocity $\underline{v}$ and the Coulomb explosion velocity $\underline{u}$ of the proton have magnitudes of about 10^9 cm/sec and 10^7 cm/sec, respectively. Figure 1(d) shows the result of a computer simulation. The diameter of the measured ring [fig. 1(c)] and the shape of the "rim" are well reproduced. The non-uniform distribution of proton intensity around the ring is a consequence of wake effects (see, eg. refs. 7 and 9) and is reproduced only qualitatively in this simulation. An improved simulation can be achieved by taking into account the rotational motion of the incident projectiles.[11] From an analysis of the shape of the rim of the ring, one can derive the distribution, $D(r_o)$, of initial internuclear separations[10].

Generally, computer calculations based on either a simple plasma wake model[7] or on a wake calculated using Lindhard's dielectric function [12], agree well with experiment, especially when rotational motion of the projectiles is taken into account and when multiple-scattering and straggling effects are small.

b. Transmission

Figure 2 shows a set of data on the transmission of fast molecular ions through thin foils. The phenomenon of molecular-ion transmission which was discovered by Poizat and Remillieux[15], has recently been quantitatively accounted for[16] using a model in which the molecular projectiles dissociate upon entering the target and then are reconstituted by capturing one or more electrons as they exit the target.

The following factors act to increase the transmission of molecular ions through foils:

i) Short dwell times. The internuclear separations and relative momenta of the fragments upon exit are then more likely to favor reconstitution of the projectile.

ii) A weak Coulomb explosion inside the foil. This can result from large values of r_o (the initial internuclear separation), low values of the effective charges inside the foil, and large values of the reduced mass of the projectile fragments.

iii) Multiple scattering. This is essential in order to provide a fraction of the beam that, after a long dwell time, has exit fragment separations and momenta suitable for molecular reconstitution.

iv) Low projectile velocity. This increases the electron capture probability upon exit.

v) The need to capture only a few electrons (e.g. one).

vi) Favorable spatial orientation of the exiting fragments. The data of Eckardt et al.[17] and Levi-Setti et al.[18] indicate that the transmission of low-velocity (~1 a.u.) H_2^+ is favored when one proton directly trails the other ("longitudinal" orientation).

The greatly increased transmission of H_2^+ as compared with HeH^+ is primarily due to factors ii) and v). The distribution $D(r_o)$ extends to much larger values of r_o for H_2^+ than for HeH^+. Similarly, the inability of experiments to detect transmission for O_2^+, CO^+, OH^+, etc. is mostly a result of factor v).

c. Reconstitution of other species

Figure 3 shows an example of the reconstitution of a diatomic species, D_2^+, from a triangular triatomic projectile, D_3^+. The process is evidently highly orientation-dependent--if it were not, the contour plot in fig. 5(d) would be circular with equal diameters in parallel and transverse velocities.[19] The data of fig. 3 indicate that leading or trailing deuteron pairs are more likely to pick up a binding electron than "sideways-going" pairs in which one deuteron trails another. In this latter orientation, capture of a binding electron only occurs when the third deuteron is far away.

d. Rare charge states

The ring patterns obtained for rare charge states frequently display strong orientation dependences. The "peculiar" distributions obtained for H^o produced from the bombardment of thin carbon foils with H_2^+ and HeH^+ are examples[10,13].

For H^- produced from the foil dissociation of HeH^+, the ring pattern is found to be indistinguishable in shape from that of the H^o fragments[13]. This strongly suggests that the H^- fragments arise from a molecular state formed upon foil exit in which the dissociation proceeds as in the H^o case (most probably

to form He^{++} and H^0) but now in the presence of either a loosely bound ("Rydberg") or continuum ("convoy") electron. This electron, although not much affecting the dissociation energy, has some probability of attaching to the H^0 fragment to yield H^-.

Similar evidence for processes of this type is to be found in the spectra of H^0 fragments from the foil-induced breakup of OH^+ projectiles[11].

e. Effects due to modification of $D(r_o)$

It is of interest to see to what extent the distribution $D(r_o)$ is affected by ion-source parameters such as source type, gas pressure, extraction voltage, gas mixture, etc. At Argonne, after much effort, we have succeeded in finding only one case where $D(r_o)$ can be easily and significantly modified. This is for HeH^+ produced from an r.f. source as contrasted with our more usual duoplasmatron source. Figure 4 shows how the higher vibrational excitations in HeH^+ ions from the r.f. source manifest themselves in various effects.

f. Cluster stopping powers

Following the discovery by Brandt, Ratkowski and Ritchie[21] of the influence of cluster effects upon the slowing down of ions in solids, there have been several experimental and theoretical investigations of this phenomenon (see, for example, the article by Arista[22] and references contained therein). Figure 5 shows some recent data on the slowing down of "longitudinally aligned" protons from 800-keV H_2^+. In general the cluster stopping powers for light projectiles like H_2^+ are fairly well described on the basis of wake models derived from Lindhard's dielectric function.

g. Extended measurements on wake potentials

To further test the applicability of various wake models, it is desirable to study fragment interactions over internuclear seprations comparable with wake wavelengths (typically several Angstroms). Going to thicker targets would permit this, but unfortunately multiple-scattering effects effectively blur out the experimental resolution and sensitivity. This difficulty can be largely overcome by employing channeling in a monocrystalline target (where multiple scattering is greatly reduced). Figure 6 shows results from a recent molecular-ion channeling measurement[24] indicating the feasibility of such experiments in relatively thick targets. (If one were to ignore the influence of the crystal upon the motion of the fragments, the proton and helium fragments in the experiment depicted in fig. 8 would be separated at exit by about 7 Angstroms, i.e. about 0.4 plasma oscillation wavelengths.)

3. EXPERIMENTS WITH SLOW HEAVY MOLECULAR PROJECTILES

It is of interest to see to what extent current wake theories are applicable to the case of slowly-moving heavy projectiles where the effective charges are significantly less than the nuclear charges. To this end, we have recently initiated at Argonne a series of measurements on the dissociation[25] and stopping power[23] of N_2^+ projectiles in the energy range 1.0 to 3.6 MeV.

a. Dissociation

Figure 7 shows ring patterns measured for N^+ and N^{4+} fragments emerging from a 73-Å carbon foil bombarded by 3-MeV N_2^+. The ring diameters can be fairly well understood in terms of a model in which the nitrogen fragments repel each other inside the foil with the same (not necessarily integral) effective charges that determine their individual stopping powers. Outside

the foil, the detected fragments (either N^+ or N^{4+} in this case) continue to Coulomb-explode away from their partners which can assume one of several possible integral charge states. Thus, although inside the foil the effective charges of the detected N^+ and N^{4+} are the same, the ring diameter measured for N^{4+} is larger than for N^+.

Figure 8 shows a comparison of these measured ring patterns with rings calculated using three different wake models. The calculations were performed with the "Fokker-Planck" technique described by Vager.[11] The distributions $D(r_o)$ were derived using Franck-Condon factors to estimate the population of vibrational levels in the X and A states of N_2^+. This gave a most probable value of $r_o = 1.12$ Å in good agreement with the value tabulated by Huber and Herzberg[26].

The three wake models tried were:

1) "Lindhard". Obtained by numerical integration of Lindhard's dielectric function for a Fermi gas of free electrons.

2) "Vager-Gemmell". A simple classical plasma wake[9] based on the high-frequency approximation to the dielectric function

$$\varepsilon(\omega) = 1 - \frac{\omega_p^2}{(\omega + i\gamma)^2} \quad ,$$

where γ is a damping parameter.

3) "Coulomb". Based on a polarization charge distribution derived from Coulomb wave functions

$$\rho_{pol}(\underline{r}) = ne(\langle|\psi_c(n,\underline{r})|^2\rangle_u - 1) \quad ,$$

as described by Faibis et al.[27].

It is clear that none of the computer simulations fits the experimental data very well. In particular, the "Lindhard" wake gives a very poor fit. This is no great surprise since a linear-response theory, in which the projectile charge is treated

as a perturbation in the electron gas, is not expected to be valid for these heavy ions.

Figure 9 shows the stopping power ratio, R, (defined as the average rate of slowing down for the two detected N^+ fragments from N_2^+ divided by the rate of slowing down for a monatomic N^+ beam of the same velocity) as a function of dwell time in a carbon target, for N_2^+ energies between 1 MeV (v = 1.2 a.u.) and 3.6 MeV (v = 2.28 a.u.). Only N^+ fragments from fragment pairs that were "longitudinally" aligned upon foil exit, were detected in these measurements. In contrast with most of the data for light molecular projectiles, the stopping power ratios thus determined for N_2^+ beams are all less than unity. (Crudely speaking, this is because much of the induced negative polarization charge now lies between the two ion fragments.)

As indicated in fig. 10, none of the calculations that have so far been performed, based on the three wake models described above, is able to reproduce the experimental R-values. In fact, the least bad fit is obtained with the "Lindhard" wake and the worst with the "Coulomb"--just the reverse from the situation in fitting the fragmentation patterns.

b. Validity of wake models for slow heavy molecular ions

It is clear that none of the wake models tested thus far is able to account simultaneously for both the fragmentation and the stopping power measurements. This failure is not unexpected. The main factors limiting the applicability of these wake models to the N_2^+ problem are:

i) A non-linear theory is clearly required. (Of the three models tested, only the "Coulomb" wake is not of a linear-response type.)

ii) Although the "Coulomb" wake was used successfully by Faibis et al.[27] to describe the dissociation of OH^+, it is expected to be of limited validity for N_2^+. This is because

two heavy ions are involved, whereas in the OH^+ case the proton can be treated as a perturbation.

iii) The fragments are not point charges. Although the point-charge approximation may be useful in describing the slowing down of monatomic heavy-ion beams, it has obvious limitations in describing the force fields away from the ion centers.

iv) The target foils are not uniform Fermi gases. This feature is expected to become more pronounced for heavy ions.

v) There are indications that strong re-orientation and wake-trapping effects play a significant role in the motions of the fragments within the foil. These effects have not yet been taken into account in calculations.

B) The Contribution of Field-ionized Rydberg Atoms in Measurements on Convoy Electrons

A prominent feature observed in the energy spectrum of electrons emitted in the forward direction from thin foils and gas targets under fast ion bombardment is a sharp cusp-like peak occurring at an energy where the electron velocity matches the velocity of the emerging ions. For fast protons or alpha particles, these "cusp" electrons (also called "convoy" electrons in the case of solid targets) are believed to originate predominantly from the capture of target electrons into continuum states of the projectile. Intense experimental and theoretical efforts[28] have been directed towards understanding the measured cusps in terms of the electron-capture-to-the-continuum (ECC) model and also in terms of a "wake-riding" model.[29] Many of the observed features lack satisfactory explanation. Adding to the difficulties in interpretation is the recent observation[30] of two components in the cusp peak--a feature not seen in previous measurements.

These difficulties prompted a group of us at Argonne[31] to wonder how much the presence of Rydberg atoms in the beam emerging from the target could be affecting observations on convoy electrons. If electron capture can occur into continuum states lying just above the ionization threshold of the projectile, there is no a priori reason why capture into bound states lying just below the ionization threshold cannot also occur with comparable probability. The level density for these quasi-classical Rydberg states increases very rapidly with excitation energy as the ionization limit is approached. There already exists some evidence that such states play a role for example in the delayed emission of Ly-α radiation from foil- and gas-excited fast ions[32] and in the "Coulomb-explosion" patterns observed for H^- arising from fast HeH^+ projectiles and for H^0 from fast OH^+ projectiles (see Section A, above).

The fate of Rydberg atoms emerging from a target can be expected to depend sensitively, and in ways difficult to predict, upon details of the experimental apparatus. Rydberg atoms have long radiative lifetimes, but they can be ionized in quite modest electric fields. Certainly the electric fields used in most electrostatic electron spectrometers (and the equivalent Lorentz field in most magnetic spectrometers) suffice to ionize a large fraction of Rydberg atoms entering the spectrometer. It is customary in measurements on convoy electrons to pass the projectiles emerging from the target through the spectrometer. Furthermore these weakly bound and spatially extended Rydberg atoms are fragile and susceptible to ionization by collision with residual gas in the vacuum chamber. If ECC electrons and Rydberg atoms were to emerge from the target in comparable numbers, the intensity and shape observed for the cusp peak would depend critically on experimental parameters such as the quality of the vacuum, the spectrometer fields (their magnitudes and directions), the distance from target to spectrometer, etc. In the experiments described below, we show that for fast H^+ and He^+ bombardment of

carbon and aluminum foils, Rydberg atoms do indeed contribute significantly to the cusp peak.

After acceleration in Argonne's 4.5-MV Dynamitron the ions were magnetically analyzed and collimated so that upon entering a vacuum chamber (2×10^{-7} Torr), the beam spot size was 1 mm and the angular divergence was ±0.15 mrad. In the chamber (Fig. 11) the beam first traversed a monitoring system consisting of a rotating chopper with a detector for scattered projectiles. The beam then passed consecutively through two sets of mutually orthogonal ("Y" and "X") electrostatic deflectors, a foil target, a further set of electrostatic deflectors ("X"), the entrance aperture of a 45° parallel-plate electron spectrometer, and finally through a hole drilled in the back-plate of the spectrometer. The spectrometer was located so as to view electrons emerging from the target parallel to the incident beam and was oriented so that analyzed electron trajectories lay in the "X-Z" plane. The foil target and the housings for the deflectors and spectrometer were all electrically grounded. The 3.7-mm diam. entrance nozzle of the spectrometer abutted the post-deflector housing and was located 15.8 cm downstream from the target.

Figure 12 shows electron distributions obtained with a 3-MeV He^+ beam and a 2-$\mu g/cm^2$ carbon target (qualitatively similar results were also obtained with energetic beams of H^+, H_2^+, HeH^+ and Ne^+ on both carbon and aluminum targets). The experimental procedure was as follows. Firstly, with all deflector plates grounded, an electron spectrum was recorded and the cusp peak identified. Then the yield of cusp electrons was maximized by applying voltages to the predeflectors, thereby fine-tuning the direction of the incident beam. (A limited angular distribution for the cusp electrons was obtained in this way.) Figure 12(a) shows the electron energy spectrum obtained after this alignment procedure. Next, a field was applied symmetrically to the postdeflector plates. Figure 12(b) shows the relative yield of

electrons detected as a function of the fields in the postdeflector and the spectrometer. The deflection of the emerging projectiles in these measurements was negligible (for He^{++} it was ~1/4000 of the deflection of electrons coming from the target).

Except for the cusp electrons, the electron yield varies with postdeflector field as expected for electrons originating from the target. The behavior of the cusp electrons, on the other hand, is quite different. There appear to be two components in the cusp. The first component varies with postdeflector field in the manner expected for target electrons. The second component behaves quite differently. It is much less affected by the postdeflector field and appears as a "ridge" in Fig. 12(b). Figure 13 shows the distribution that results when this ridge is subtracted.

Using a biased filament as a collimated monoenergetic source of 400-eV electrons at the target position, the response function of the detection system was measured in terms of the spectrometer and postdeflector fields. The result, which agreed well with calculations based on the known geometry of the apparatus, was then used together with a theoretical model[33] for the ECC electrons to derive the calculated curves shown in Figs. 3(b) and (c). Although our resolution in energy (~8%) and angle (~24 mrad) was not good enough to test details of the ECC theory, the calculated curves are consistent with a description of the cusp-like peaks in both energy and angle as being primarily due to ECC electrons. The narrow peak in angle agrees with that determined using the predeflectors. There have been few determinations of angular distributions for cusp electrons from foils. However, our results do show qualitative agreement with the narrow angular peaks observed by previous workers[34,35].

We identify the "ridge" electrons in Fig. 12(b) as arising from Rydberg atoms created at the exit surface of the

target foil when emerging helium projectiles capture target electrons into bound states. These atoms fly undeflected (He^{o}) or almost undeflected (He^{+}, He^{-}) into the electron spectrometer which, if set to record ~400-eV (cusp) electrons, contains a field of 170 Volt/cm. For hydrogenic Rydberg atoms, this field reduces the ionization lifetime to about 1 nsec for n = 50 (and, of course, shorter lifetimes for higher principal quantum numbers).[36] Since 3-MeV helium atoms travel about 1.2 cm in a nanosecond, we can expect that the spectrometer field will ionize all Rydberg atoms with n-values greater than about 50. The weaker electric field in the postdeflector [up to about 30 Volt/cm for the data shown in Fig. 12(b)] will only ionize Rydberg atoms with much higher principal quantum numbers. As expected, the "Rydberg ridge" decreases with increasing postdeflector voltage. At a postdeflector field of 170 Volt/cm, the ridge height is ~1/20 of its value at a field of 30 Volt/cm. The center of the Rydberg ridge is displaced upwards in apparent energy by about 18 eV from the energy at the peak of the cusp shown in Fig. 13(b). This upward shift in apparent energy is due to the ionization occurring after the Rydberg atoms penetrate on the average about 2 mm into the spectrometer field. This distance is reasonable when viewed in terms of the lifetimes quoted above and in terms of the spatial extent of the transition field at the entrance to the spectrometer.

Additional measurements in which a positive bias voltage was applied to the target confirm the origins of the two components--the apparent energy of the ridge electrons is unaffected while the electrons from the target are lowered in energy (see Fig. 14). Our experiments thus far have not permitted us to make an accurate determination of the ratio of Rydberg atoms to ECC electrons, but the data do indicate that they emerge from the target with comparable probabilties.

In further studies, we have observed similar effects for

gaseous as well as solid targets and for an extended range of beam velocities. The use of molecular-ion projectiles was also found to have a pronounced influence upon the relative numbers of Rydberg atoms reaching the spectrometer.

In comparing observations on ECC electrons either with theory or with results from other laboratories, it is clearly essential to consider the contribution of electrons stemming from the field-ionization of projectile Rydberg atoms during passage through the spectrometer. Such electrons which can influence the observed yield and shape of the cusp peak in a very significant manner, have not hitherto been taken into account.

These results have consequences in several areas of collision physics. For example it is interesting to speculate that the well-known and as yet unexplained differences in the charge-state distributions attained by fast heavy-ion beams after traversing gaseous and solid targets may be in large measure due to field ionization effects present at the exit surface of foils but absent in gases.

ACKNOWLEDGMENT

Much of the work described in this article was performed at Argonne in collaboration with E. P. Kanter and B. J. Zabransky together with several visiting scientists--N. Cue (SUNY, Albany), P. J. Cooney (Millersville State College), A. K. Edwards (U. Georgia), Y. Z. Gu (Fudan University), I. Plesser (Weizmann Institute), J. -C. Poizat (U. Lyon), D. Schneider (Hahn-Meitner Institute), M. F. Steuer (U. Georgia), and Z. Vager (Weizmann Institute). This work was supported by the U. S. Department of Energy, Office of Basic Energy Sciences, under Contract W-31-109-Eng-38.

REFERENCES

1. Proceedings of the Workshop on Physics with Fast Molecular-Ion Beams, Argonne National Laboratory, Argonne, IL, Aug. 20-21, 1979, D. S. Gemmell, Ed., Physics Division Informal Report ANL/PHY-79-3 (Aug. 1979).
2. Proceedings of the Bat-Sheva seminar on Molecular Ions, Molecular Structure and Interaction with Matter, Israel, Jan. 4-12, 1981. B. Rosner, Ed., Annals Israel Phys. Soc. 4, 1 (1981).
3. J. Remillieux, Nucl. Instr. Methods 170, 31 (1980).
4. D. S. Gemmell, Nucl. Instrum. Methods 170, 41 (1980).
5. R. Laubert, IEEE Trans. Nucl. Sci. NS-26, 1020 (1979).
6. E. P. Kanter, EIII Trans. Nucl. Sci. NS-28, 1162 (1981).
7. D. S. Gemmell and Z. Vager in "Heavy Ion Science" Ed. D. A. Bromley, Plenum Press, N.Y., to be published.
8. D. S. Gemmell, Chem. Rev., 80, 301 (1980).
9. Z. Vager and D. S. Gemmell, Phys. Rev. Lett. 37, 1352 (1976).
10. E. P. Kanter, P. J. Cooney, D. S. Gemmell, K.O. Groeneveld, W. J. Pietsch, A. J. Ratkowski, Z. Vager, and B. J. Zabransky, Phys. Rev. A20, 834 (1979).
11. Z. Vager, page 139 of Reference 2.
12. J. Lindhard, K. Dan. Vidensk. Selsk. Mat.-Fys. Medd. 28,8 (1954).
13. P. J. Cooney, D. S. Gemmell, W. J. Pietsch, A. J. Ratkowski, Z. Vager, and B. J. Zabransky, Phys. Rev. A 24, 746 (1981).
14. M. J. Gaillard, J.-C. Poizat, A. Ratkowski, and J. Remillieux, Nucl. Instrum. Methods 132, 69 (1976).
15. J.-C. Poizat and J. Remillieux, Phys. Lett. 34A, 53 (1971).
16. N. Cue, N. V. de Castro-Faria, M. J. Gaillard, J.-C. Poizat, J. Remillieux, D. S. Gemmell and I. Plesser, Phys. Rev. Lett. 45, 613 (1980).
17. J. C. Eckardt, G. Lantschner, N. R. Arista, and R. A. Baragiola, J. Phys. C 11, L851 (1978).

18. R. Levi-Setti, contribution to this seminar.

19. P. J. Cooney, N. Cue, A. K. Edwards, D. S. Gemmell, I. Plesser, and J.-C. Poizat (private communication).

20. E. P. Kanter, D. S. Gemmell, I. Plesser, and Z. Vager, private communication.

21. W. Brandt, A. Ratkowski, and R. H. Ritchie, Phys. Rev. Lett. 33, 1329 (1974).

22. N. R. Arista, Phys. Rev. B18, 1 (1978).

23. M. F. Steuer, D. S. Gemmell, E. P. Kanter, E. A. Johnson, and B. J. Zabransky, to be published.

24. D. S. Gemmell, E. P. Kanter and M. F. Steuer (private communication).

25. I. Plesser, D. S. Gemmell, and E. P. Kanter (to be published).

26. K. P. Huber and G. Herzberg "Molecular Spectra and Molecular Structure: IV Constants of Diatomic Molecules". Van Nostrand Reinhold, N.Y. 1979.

27. A. Faibis, R. Kaim, I. Plesser, and Z. Vager, Nucl. Instrum. Methods 170, 99 (1980).

28. For recent reviews, see I. A. Sellin et al., Annals of the Israel Phys. Soc. 4, 201 (1981); Proc. 12th Int. Conf. on Physics of Electronic and Atomic Collisions, Gatlinburg, Tenn., July 15-21 (1981), to be published.

29. V. N. Neelavathi, R. H. Ritchie, and W. Brandt, Phys. Rev. Lett. 33, 302 (1974); W. Brandt and R. H. Ritchie, Physics Letters 62A, 374 (1977).

30. A. Gladieux and A. Chateau-Thierry, Phys. Rev. lett. 47, 786 (1981).

31. Z. Vager, B. J. Zabransky, D. Schneider, E. P. Kanter, Y. Z. Gu and D. S. Gemmell, to be published.

32. H.-D. Betz, J. Rothermel and F. Bell, Nucl. Instrum. Methods 170, 243 (1980).

33. K. Dettman, K. G. Harrison, and M. W. Lucas, J. Phys. B 7, 269 (1974).

34. M. M. Duncan, and M. G. Menendez, Phys. Rev. A 13, 566 (1976).

35. W. Meckbach, K. C. R. Chiu, H. H. Brongersma, and J. Wm. McGowan, J. Phys. B 10, 3255 (1977).

36. P. M. Koch and D. R. Mariani, Phys. Rev. Lett. 46, 1275 (1981).

FIGURE CAPTIONS

Fig. 1. Results for protons arising from 2-MeV HeH^+ projectiles bombarding an 85-Å thick carbon target[9,10].

Fig. 2. Transmitted fractions, T, of fast beams of H_2^+, $^4HeH^+$, $^3HeH^+$, $^3He_2^+$ and D_3^+ through thin foils[13]. All of the data points except the one labelled "Al_2O_3" were obtained with carbon targets. The dashed curve for 2-MeV H_2^+ represents data taken by the Lyon group[14].

Fig. 3. (a), (b), and (c). Energy and angle distributions for D_2^+ arising from 3.6-MeV D_3^+ incident upon a 216-Å carbon foil. (c) A contour plot of the D_2^+ intensity as a function of transverse and parallel velocities (arb. units) in the c.m. The two velocity scales in (c) are equal[19].

Fig. 4. Comparison of effects seen for protons from the foil-induced dissociation of 2-MeV HeH^+ ions produced from an r.f. source and a duoplasmatron source[20]. a) angle spectrum, b) distribution $D(r_o)$, c) HeH^+ transmission and d) ring patterns for H^o.

Fig. 5. Stopping power ratio, R, (i.e. the average rate of slowing down for the two protons from H_2^+ compared with that for protons of the same velocity) for 800-keV H_2^+ in aluminum [open circles (experiment) and long-dashed line (calculation)] and in carbon [crosses (experiment) and short-dashed line (calculation)]. Only protons emerging in the beam direction from the target are counted[23].

Fig. 6. Ring pattern for protons emerging in the (111) planar direction from a gold crystal 950 Å thick bombarded by 3-MeV HeH^+ incident along the same (111) planar direction. In Fig. 6(d), the velocity scales are arbitrary, but equal. The angular coordinate in Figs. 6(a) and (c) is measured with respect to the beam direction in the (111) plane[24].

Fig. 7. Ring patterns for N^+ (a, b and c) and N^{4+} (d, e and f)

fragments arising from the bombardment of a 73-Å carbon foil by 3-MeV N_2^+ projectiles[25].

Fig. 8. Comparison of the experimental ring pattern (Fig. 7) for N^{4+} with patterns calculated on the basis of three different wake models as described in the text.

Fig. 9. Stopping power ratio (see text) for N_2^+ projectiles of various energies penetrating carbon foils[23]. Only N^+ fragments from "longitudinally" oriented fragment pairs are detected.

Fig. 10. Comparison of the measured R-values for 3-MeV N_2^+ projectiles with calculated values based on the various wake models described in the text. The data pertain to the case of "longitudinally" aligned projectiles[23].

Fig. 11. Schematic arrangement of the elements of the experimental set-up within the target chamber.

Fig. 12. Electron distributions measured for 3-MeV He^+ incident on a 2-$\mu g/cm^2$ carbon foil.

(a) Electron energy distribution obtained in the forward direction. The peaks corresponding to cusp electrons and to binary encounters with target electrons are marked.

(b) Distribution of electrons detected as a function of the postdeflector and spectrometer fields. The energy scale applies to electrons from the target. The angle scale applies only to convoy electrons (~400 eV) coming from the target.

The distribution in Fig. 12(a) was derived by dividing the measured electron count rates by the electron energies in order to take into account the energy dependence of the spectrometer acceptance. This correction has not been applied in Fig. 12(b).

Fig. 13. a) Distribution as in Fig. 12(b), but with the "Rydberg ridge" subtracted out. Since all of the electrons in the remaining distribution are assumed to emerge from the

target, the data are plotted in terms of electron energy and angle of emission.

b) and c) orthogonal cuts made at the peak position and parallel to the two axes of Fig. 13(a). The solid curves are energy and angle distributions calculated for convoy electrons. As in Fig. 12(a), the distribution shown in Fig. 13(b) has been divided by the electron energy.

Fig. 14. Electron distribution for 750-keV H^+ incident on a 2 $\mu g/cm^2$ carbon foil upon which a positive bias of 60 Volts has been placed. The number of detected electrons is shown plotted as a function of their apparent energy (as determined from the spectrometer field) and of the field on the post-deflector plates.

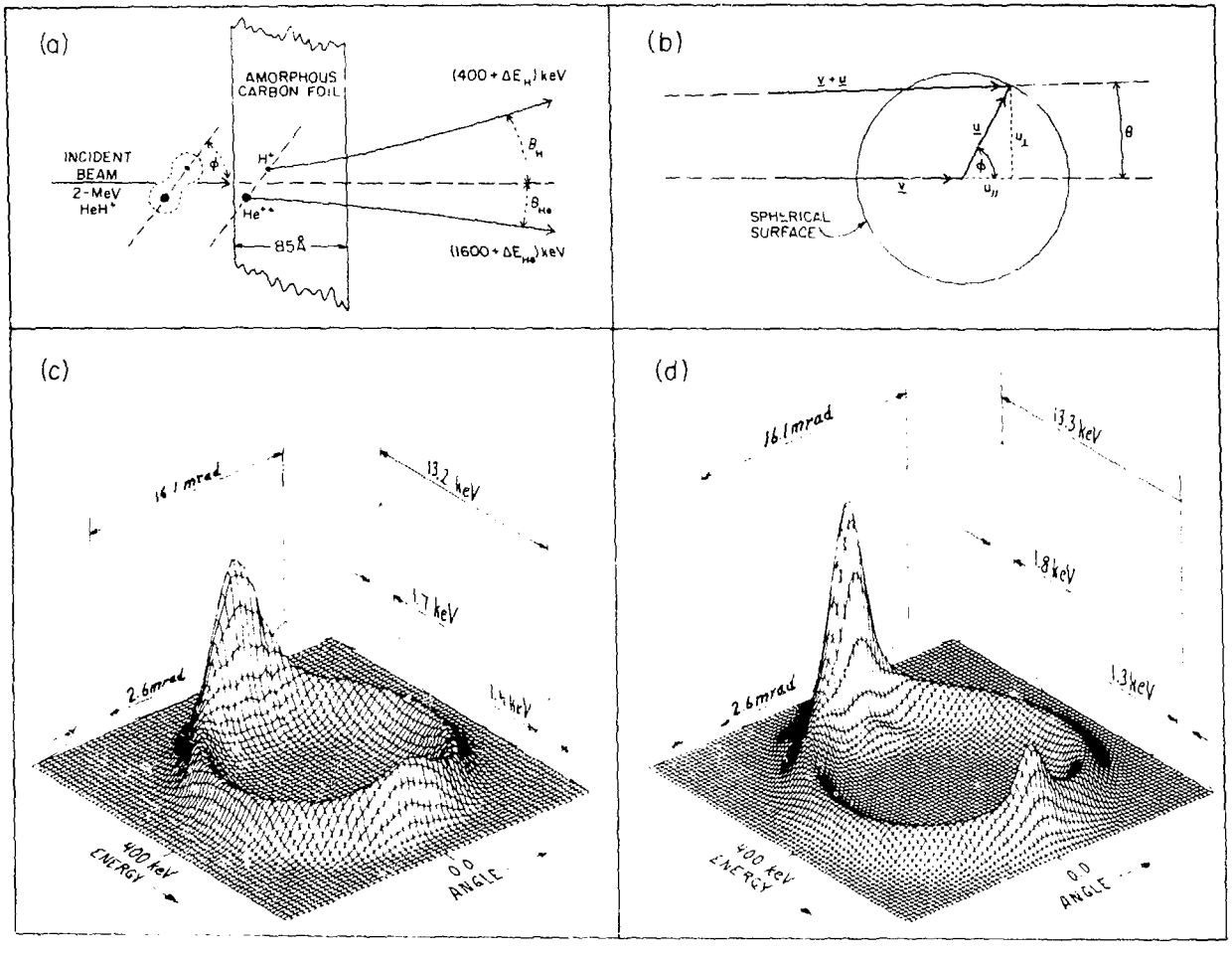
(a)
AMORPHOUS CARBON FOIL
(400 + ΔE_H) keV
INCIDENT BEAM
2-MeV HeH+
φ
H+
θ_H
He++
θ_He
85 Å
(1600 + ΔE_He) keV
(b)
v + u
u
u⊥
θ
φ
v
u∥
SPHERICAL SURFACE
(c)
16.1 mrad
13.2 keV
1.7 keV
2.6 mrad
1.4 keV
400 keV ENERGY
0.0 ANGLE
(d)
16.1 mrad
13.3 keV
1.8 keV
2.6 mrad
1.3 keV
400 keV ENERGY
0.0 ANGLE

Figure 1

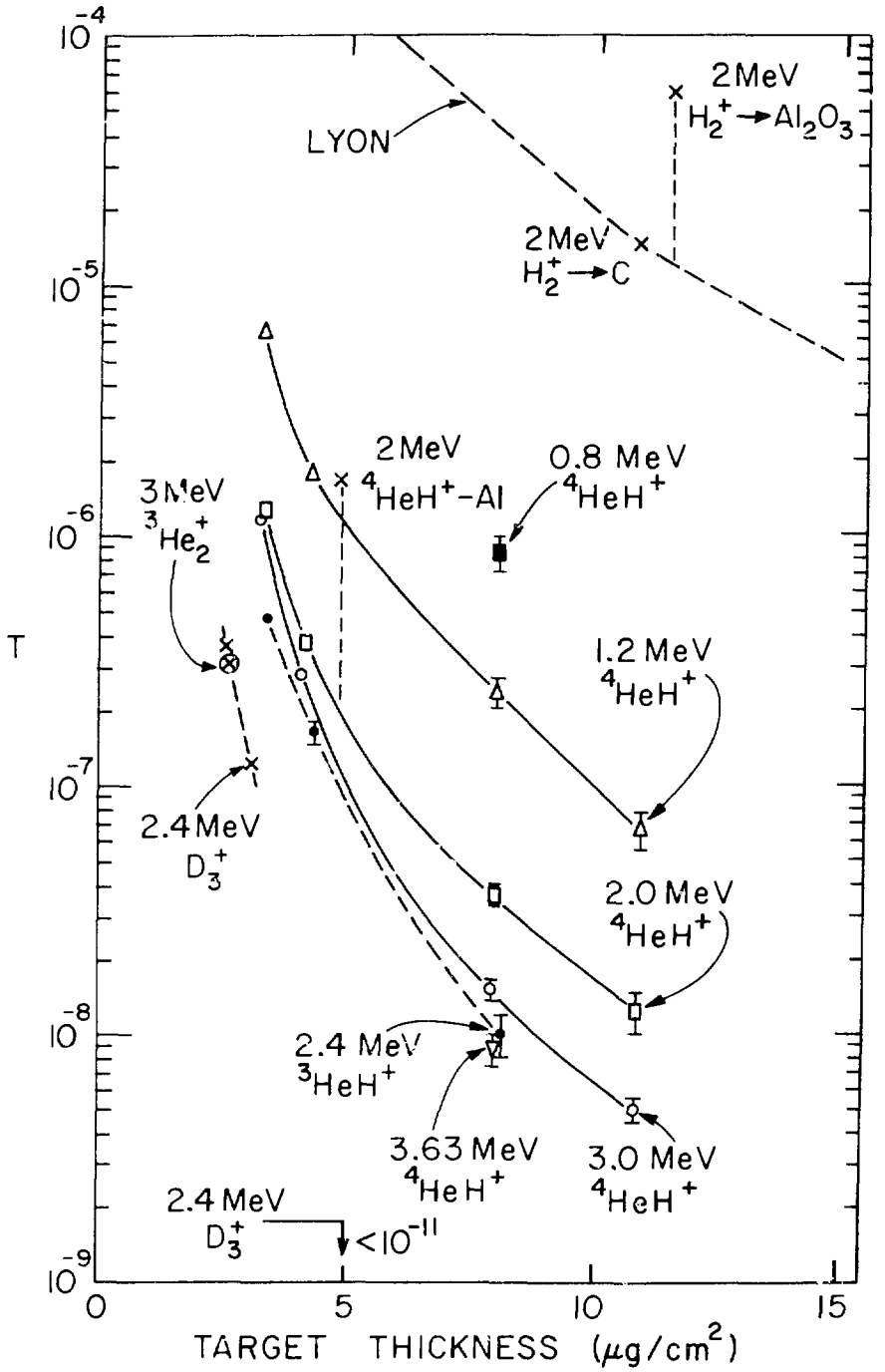
LYON
2MeV
$H_2^+ \rightarrow Al_2O_3$
2MeV
$H_2^+ \rightarrow C$
2MeV
$^4HeH^+$-Al
0.8 MeV
$^4HeH^+$
3MeV
$^3He_2^+$
1.2 MeV
$^4HeH^+$
2.4MeV
D_3^+
2.0 MeV
$^4HeH^+$
2.4 MeV
$^3HeH^+$
3.63 MeV
$^4HeH^+$
3.0 MeV
$^4HeH^+$
2.4 MeV
D_3^+
$<10^{-11}$
T
10^{-4}
10^{-5}
10^{-6}
10^{-7}
10^{-8}
10^{-9}
0
5
10
15
TARGET THICKNESS ($\mu g/cm^2$)

Figure 2

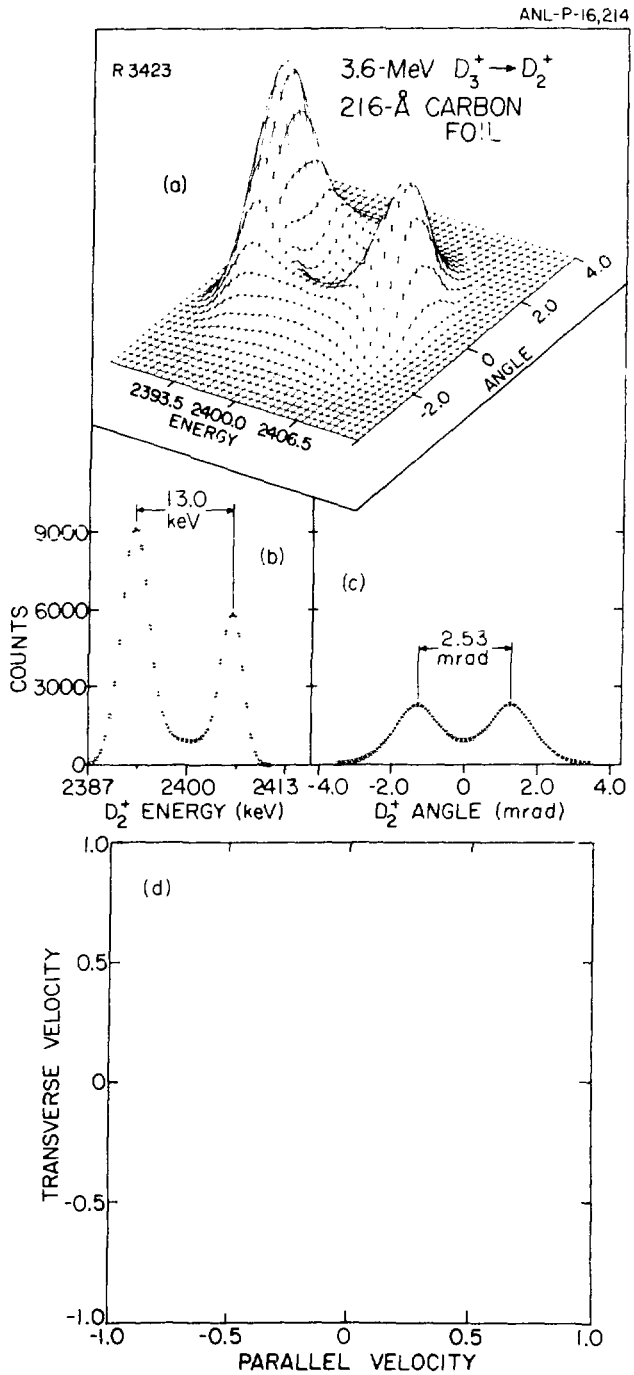
ANL-P-16,214
R 3423
3.6-MeV $D_3^+ \rightarrow D_2^+$
216-Å CARBON FOIL
(a)
2393.5 2400.0 2406.5
ENERGY
-2.0 0 2.0 4.0
ANGLE
13.0 keV
(b)
(c)
2.53 mrad
COUNTS
9000
6000
3000
0
2387 2400 2413
D_2^+ ENERGY (keV)
-4.0 -2.0 0 2.0 4.0
D_2^+ ANGLE (mrad)
(d)
TRANSVERSE VELOCITY
1.0
0.5
0
-0.5
-1.0
-1.0 -0.5 0 0.5 1.0
PARALLEL VELOCITY

Figure 3

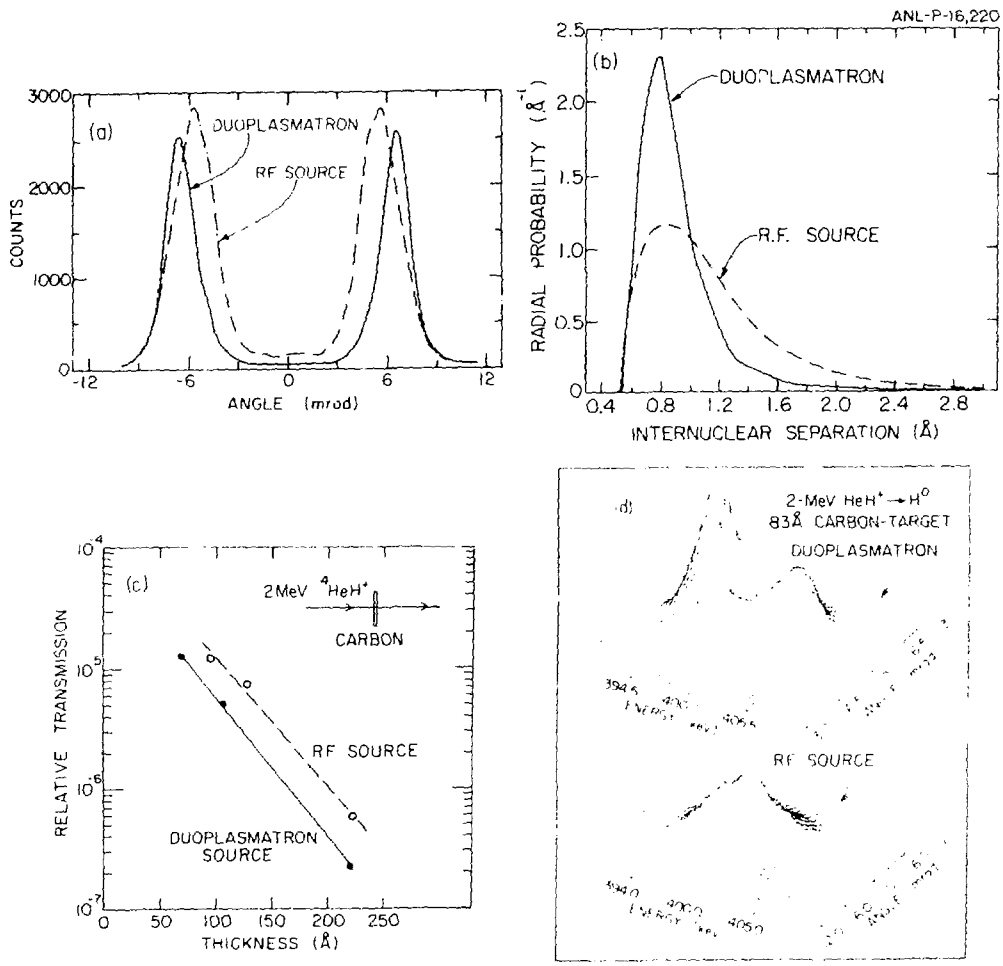
ANL-P-16,220
(a)
DUOPLASMATRON
RF SOURCE
COUNTS
ANGLE (mrad)
(b)
DUOPLASMATRON
R.F. SOURCE
RADIAL PROBABILITY (Å⁻¹)
INTERNUCLEAR SEPARATION (Å)
(c)
2MeV ⁴HeH⁺
CARBON
RF SOURCE
DUOPLASMATRON SOURCE
RELATIVE TRANSMISSION
THICKNESS (Å)
(d)
2-MeV HeH⁺ → H⁰
83Å CARBON-TARGET
DUOPLASMATRON
RF SOURCE

Figure 4

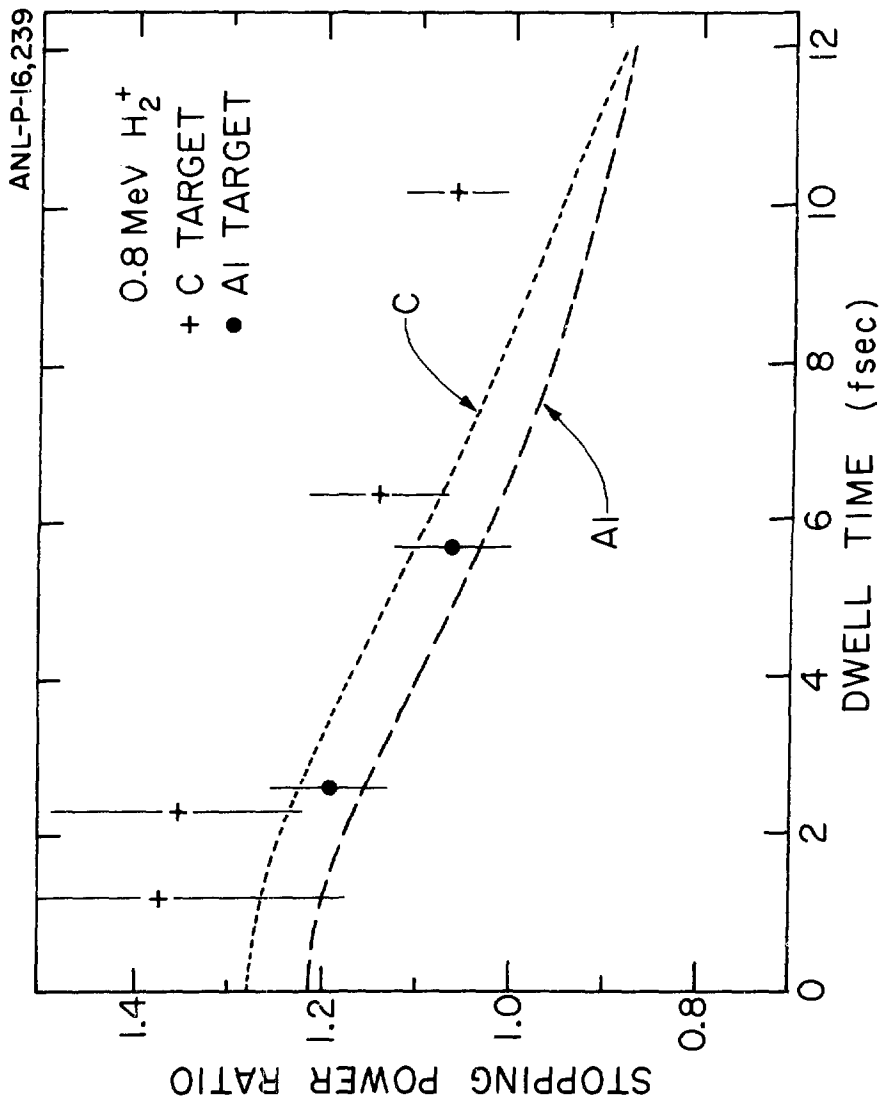
ANL-P-16,239
0.8 MeV H_2^+
+ C TARGET
• Al TARGET
C
Al
STOPPING POWER RATIO
DWELL TIME (fsec)
0.8
1.0
1.2
1.4
0
2
4
6
8
10
12

Figure 5

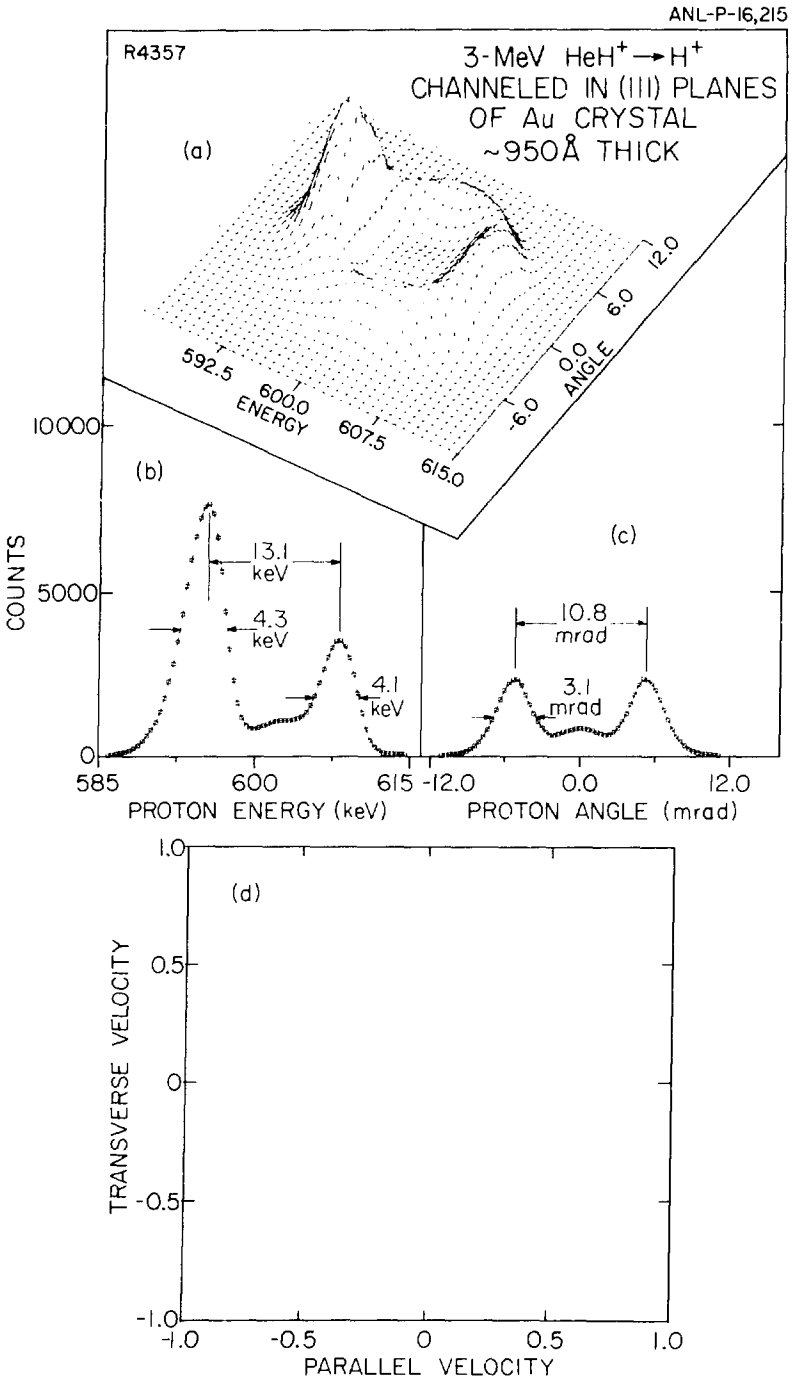
ANL-P-16,215
R4357
3-MeV HeH+ → H+
CHANNELED IN (111) PLANES
OF Au CRYSTAL
~950Å THICK
(a)
592.5
600.0
607.5
615.0
ENERGY
12.0
6.0
0.0
-6.0
ANGLE
10000
5000
0
COUNTS
(b)
13.1 keV
4.3 keV
4.1 keV
(c)
10.8 mrad
3.1 mrad
585
600
615
PROTON ENERGY (keV)
-12.0
0.0
12.0
PROTON ANGLE (mrad)
(d)
1.0
0.5
0
-0.5
-1.0
TRANSVERSE VELOCITY
-1.0
-0.5
0
0.5
1.0
PARALLEL VELOCITY

Figure 6

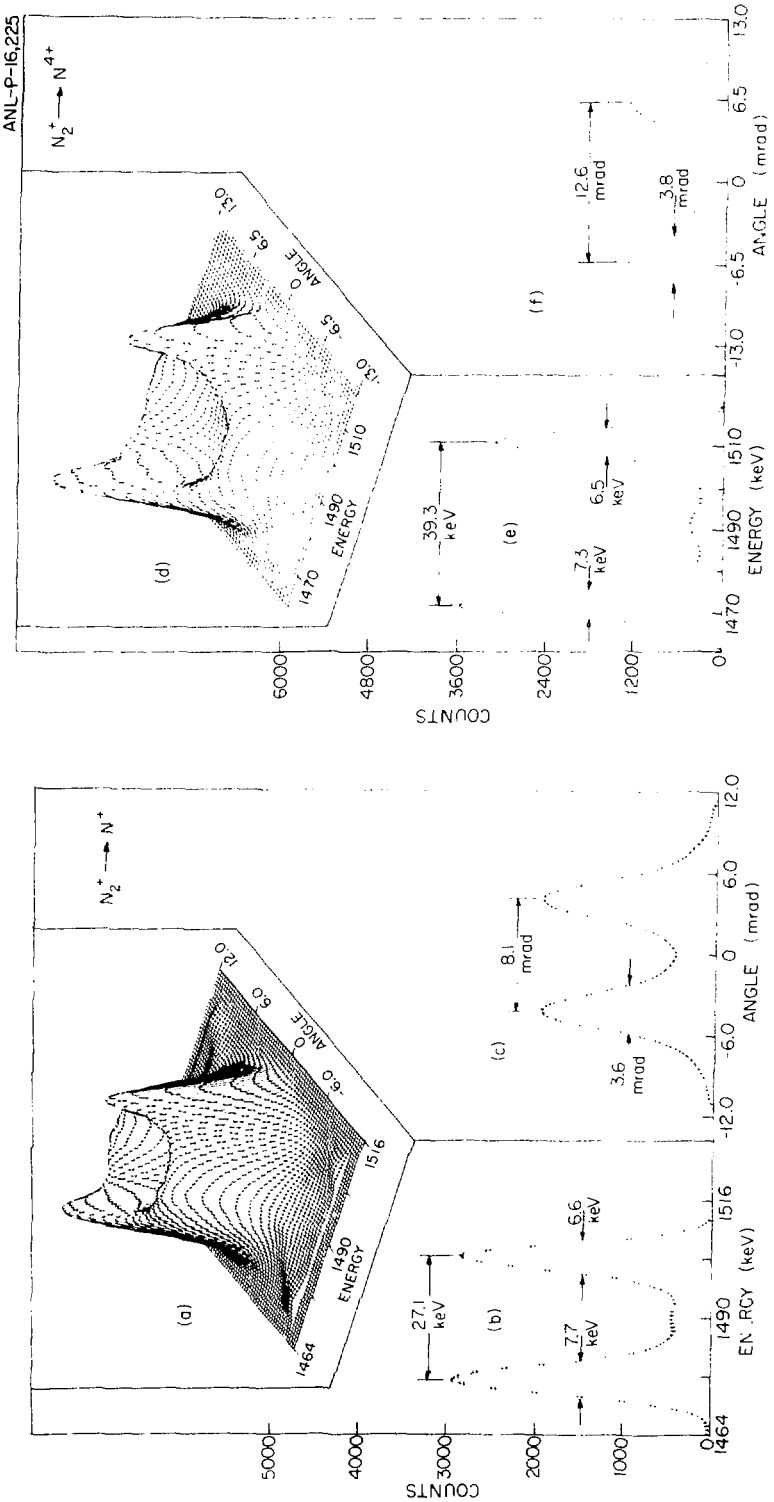
ANL-P-16,225
$N_2^+ \rightarrow N^+$
$N_2^+ \rightarrow N^{4+}$
(a)
(b)
(c)
(d)
(e)
(f)
COUNTS
ENERGY (keV)
ANGLE (mrad)
1464
1490
1516
1470
1510
27.1 keV
7.7 keV
6.6 keV
8.1 mrad
3.6 mrad
39.3 keV
7.3 keV
6.5 keV
12.6 mrad
3.8 mrad

Figure 7

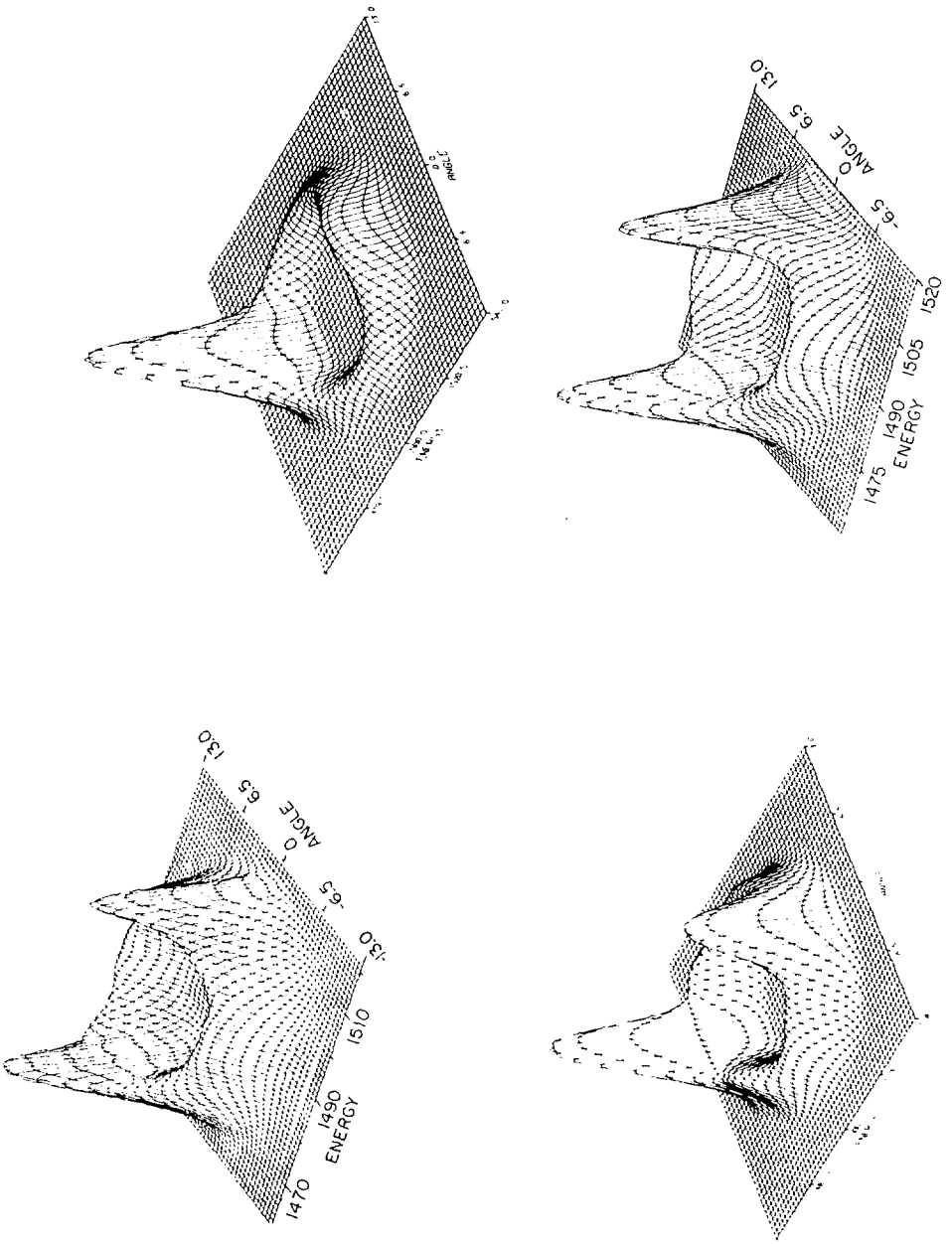

Figure 9

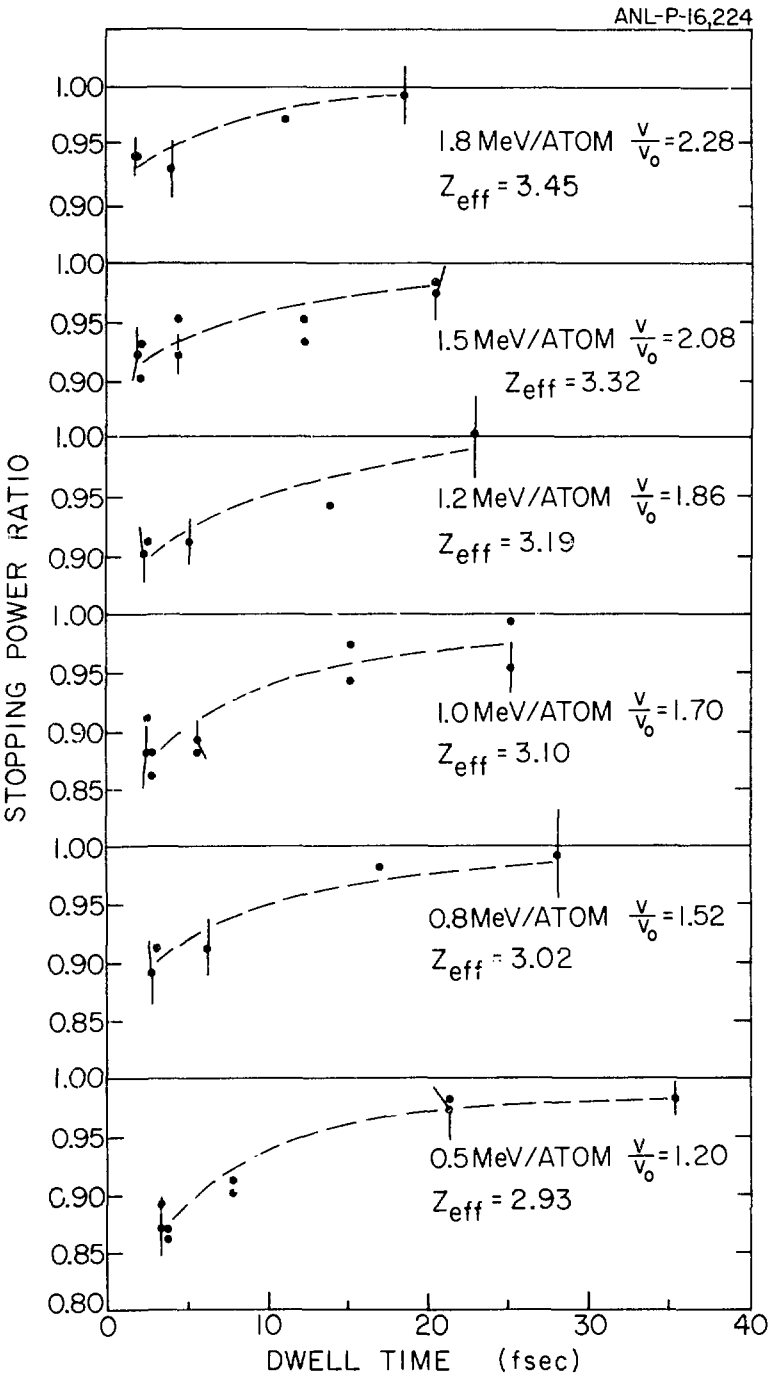
ANL-P-16,224
STOPPING POWER RATIO
1.8 MeV/ATOM $\frac{v}{v_0}$=2.28
Z_{eff} = 3.45
1.5 MeV/ATOM $\frac{v}{v_0}$=2.08
Z_{eff} = 3.32
1.2 MeV/ATOM $\frac{v}{v_0}$=1.86
Z_{eff} = 3.19
1.0 MeV/ATOM $\frac{v}{v_0}$=1.70
Z_{eff} = 3.10
0.8 MeV/ATOM $\frac{v}{v_0}$=1.52
Z_{eff} = 3.02
0.5 MeV/ATOM $\frac{v}{v_0}$=1.20
Z_{eff} = 2.93
DWELL TIME (fsec)

Figure 9

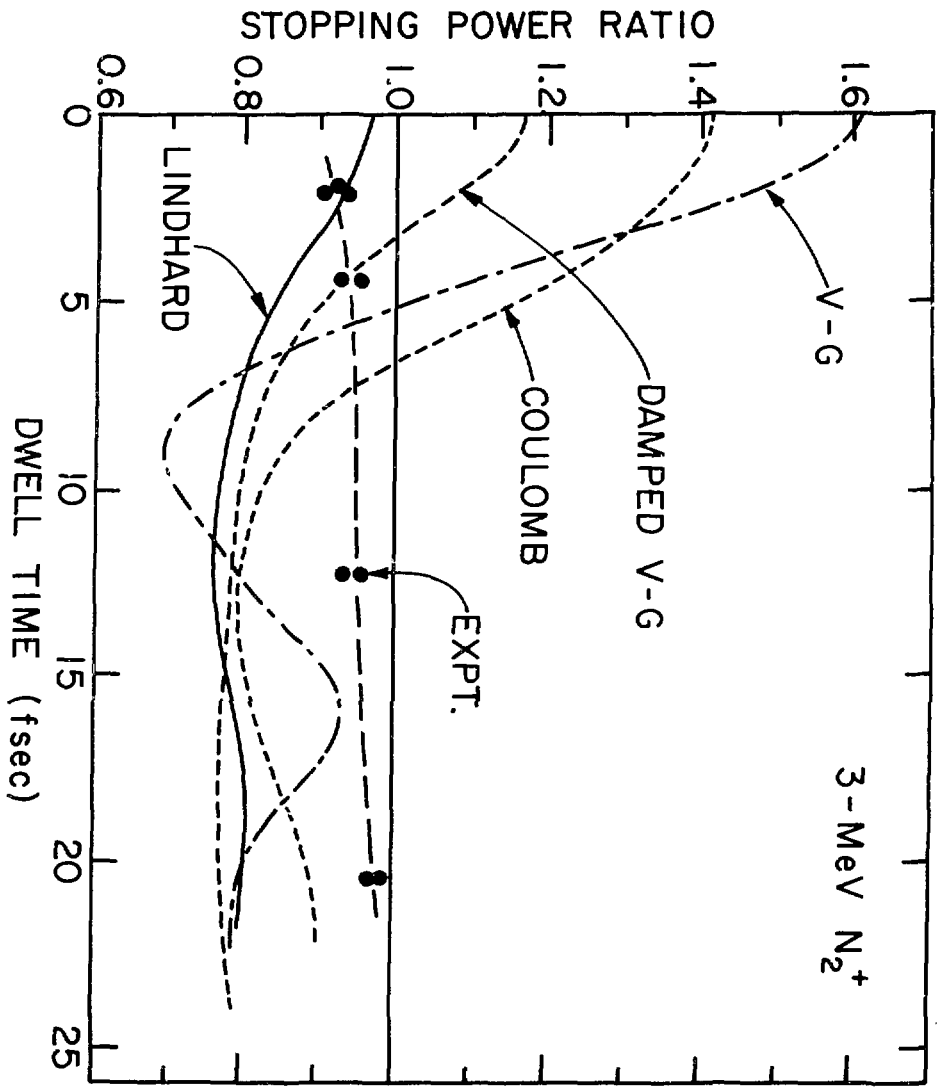
STOPPING POWER RATIO
0.6
0.8
1.0
1.2
1.4
1.6
0
5
10
15
20
25
DWELL TIME (fsec)
LINDHARD
V-G
DAMPED V-G
COULOMB
EXPT.
3-MeV N_2^+

Figure 10

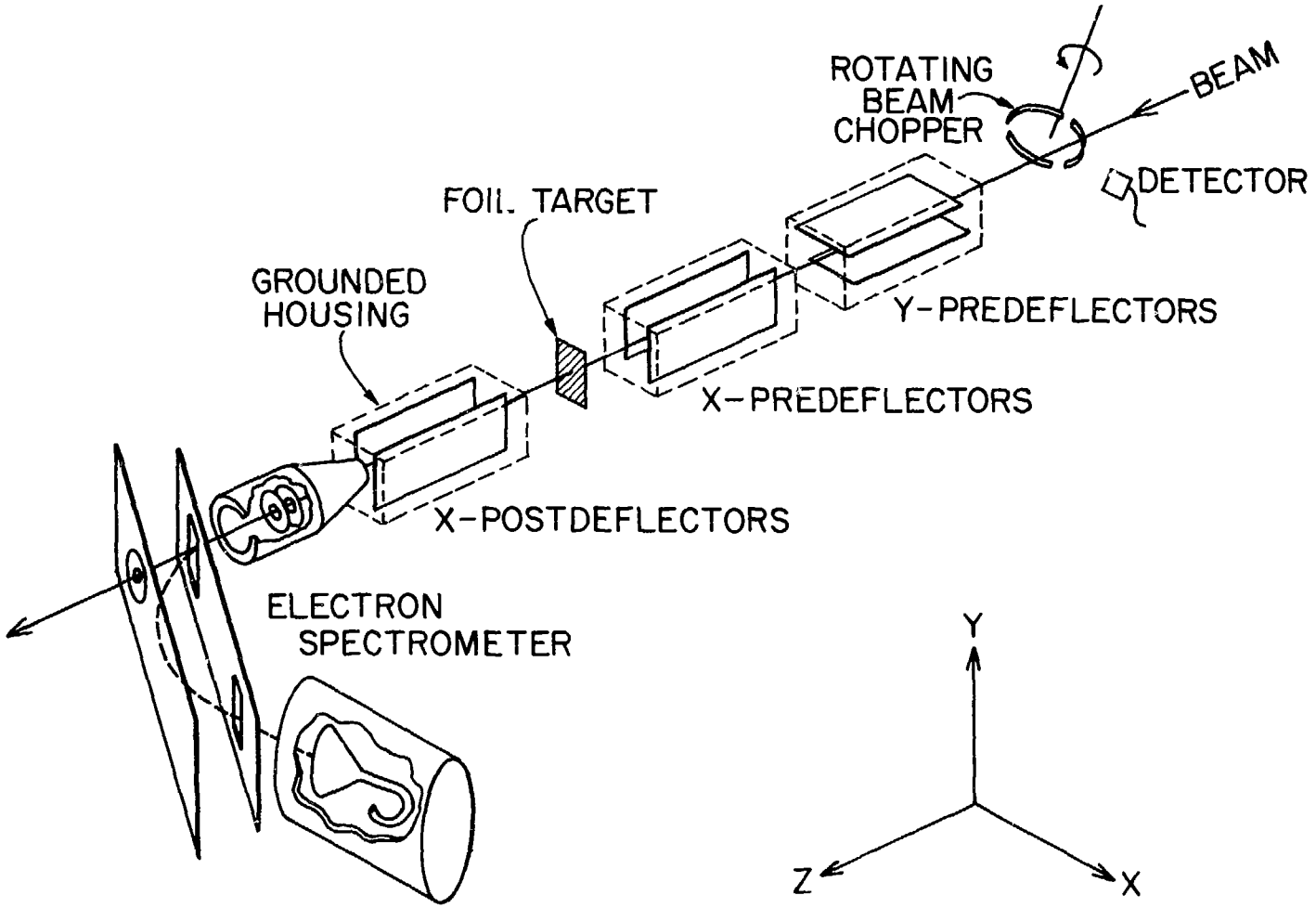
ROTATING
BEAM
CHOPPER
BEAM
DETECTOR
FOIL TARGET
GROUNDED
HOUSING
Y-PREDEFLECTORS
X-PREDEFLECTORS
X-POSTDEFLECTORS
ELECTRON
SPECTROMETER
Y
Z
X

Figure 11

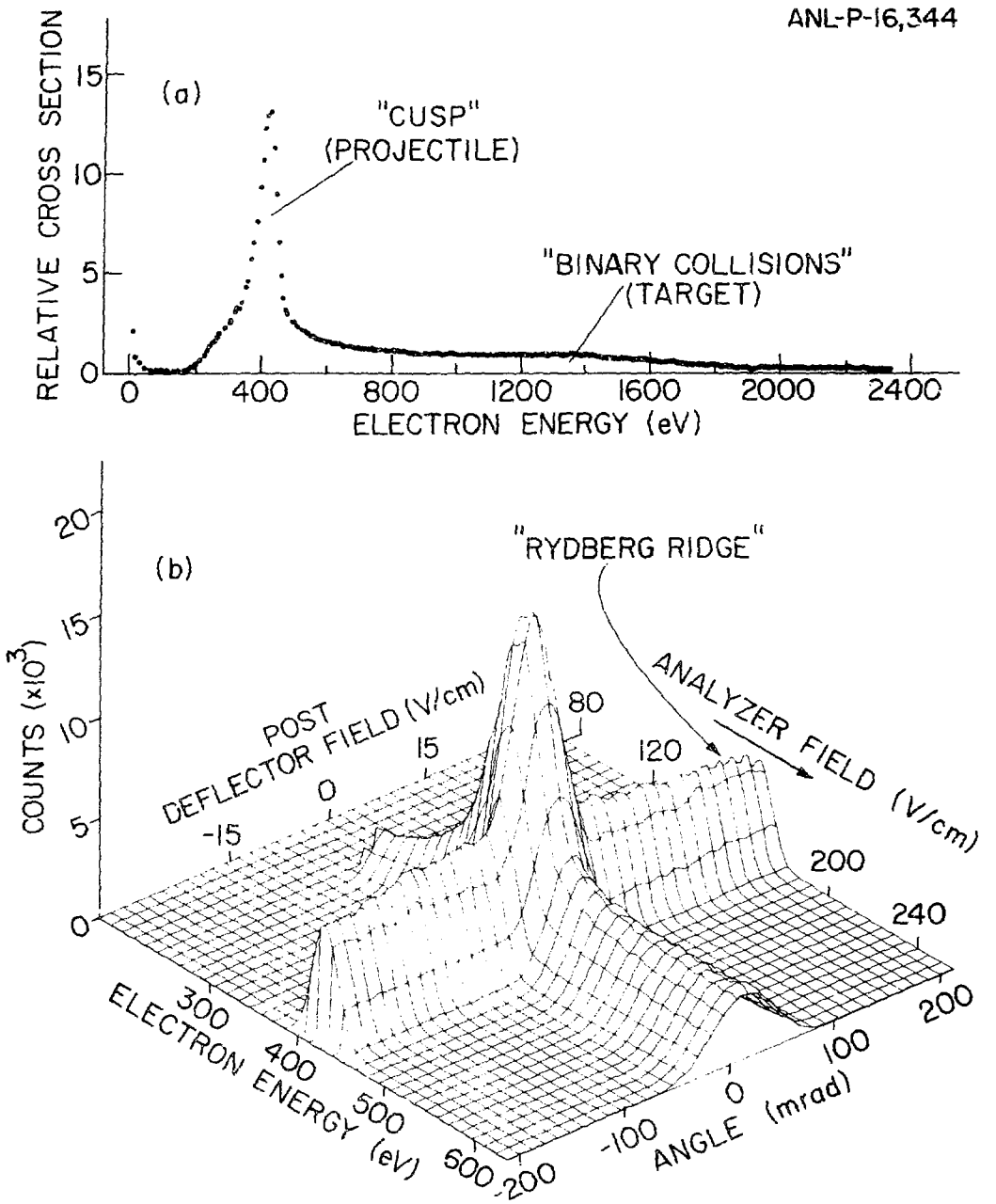
ANL-P-16,344
(a)
"CUSP"
(PROJECTILE)
"BINARY COLLISIONS"
(TARGET)
RELATIVE CROSS SECTION
ELECTRON ENERGY (eV)
(b)
"RYDBERG RIDGE"
ANALYZER FIELD (V/cm)
POST
DEFLECTOR FIELD (V/cm)
COUNTS (x10^3)
ELECTRON ENERGY (eV)
ANGLE (mrad)

Figure 12

ANL-P-16,345

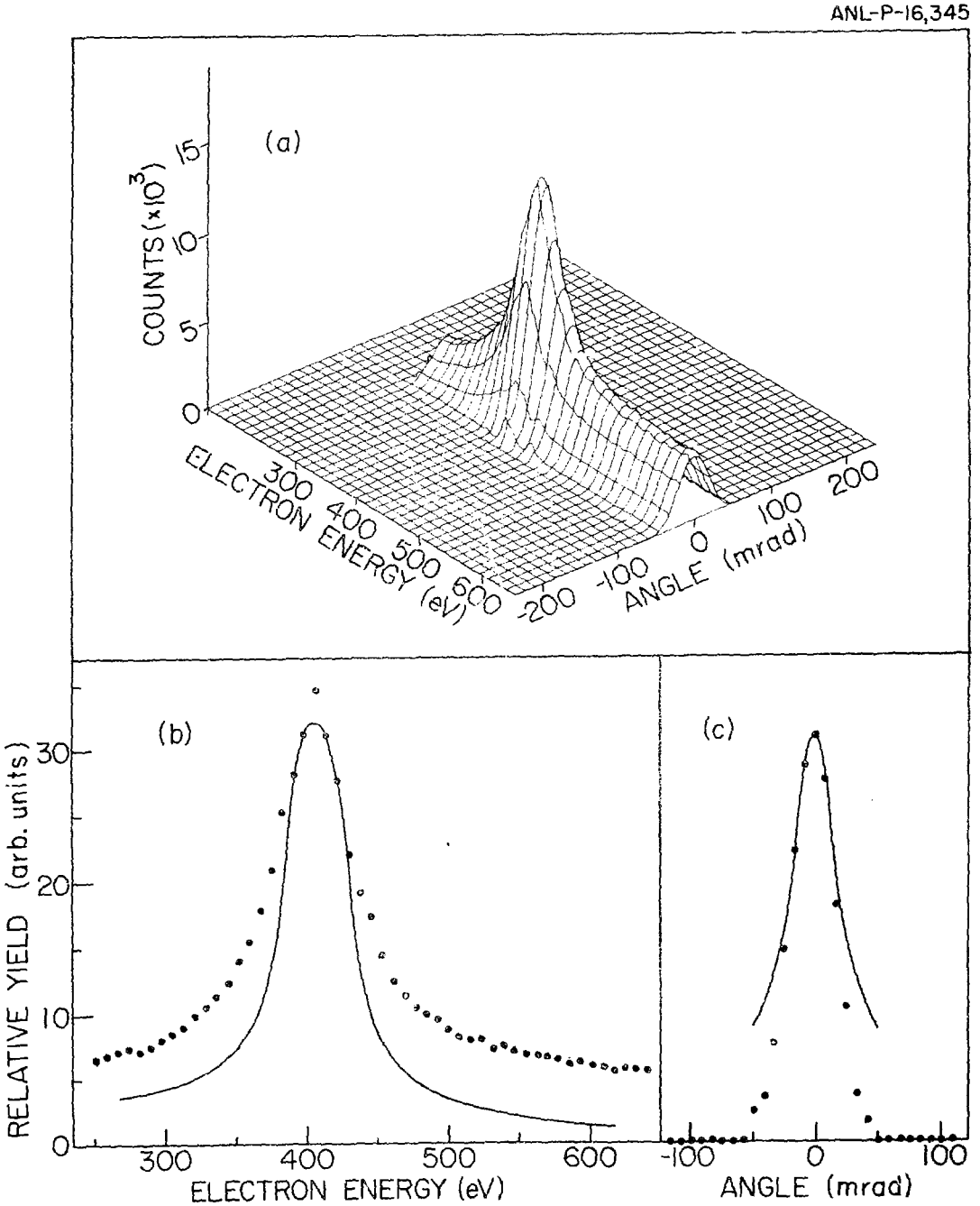

Figure 13

750 keV H^+ carbon target (+60 V bias) (RING5317)

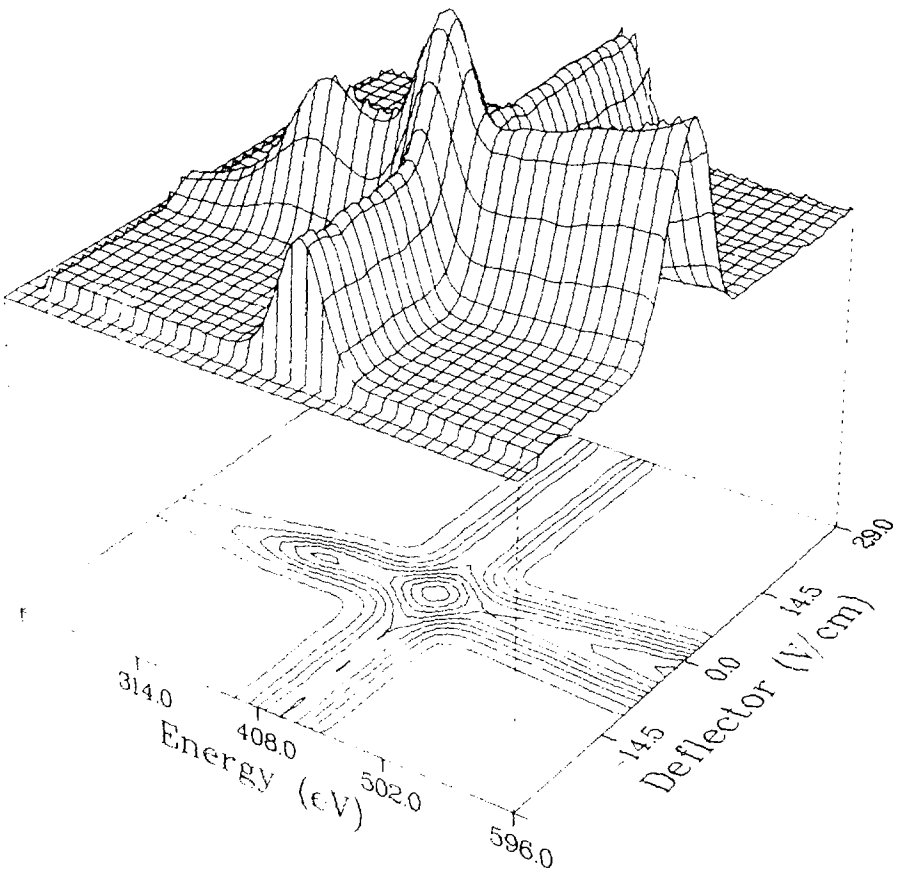

Figure 14

Interaction of Hydrogen Molecular Ions with Thin Foils

I Convoy Electrons

N.Oda, Y.Yamazaki, and Y.Yamaguchi

Research Laboratory for Nuclear Reactor, Tokyo Institute of Technology, Ookayama, Meguro-ku, Tokyo, 152, Japan

Doubly differential electron spectra from thin carbon foils(2-20 μg/cm^2) bombarded with 0.8 MeV/amu H^+, H_2^+, H_3^+, and $^3He^+$ ion beams have been measured in the angular range 15°-30°. A predominant group of electrons whose velocities are centered about the ion velocity(convoy electrons) is observed even at these large angles, for thinner foils with molecular ions H_2^+ and H_3^+. The yield of convoy electrons for H_3^+ is always larger than that for H_2^+ and both yields are strongly dependent on foil thickness. Our results for H_2^+ and H_3^+ are consistent with the model that the electron loss process is the dominant mechanism for producing convoy electrons.

1. Introduction

Most studies of the origin of the convoy electrons from solid foils have been carried out with atomic projectiles. Studies with molecular projectiles are very few and are all limited to the angular range near 0°.[1-4] In a previous paper, we measured energy and angular spectra of electrons emitted from carbon foils(4-20 μg/cm^2) for the angular range 20°-150° for 0.8 MeV/amu H^+, H_2^+, and H_3^+ projectiles[5] and found that the convoy electrons are clearly observed in backward angles for molecular projectiles(H_2^+, H_3^+) but not for an atomic projectile(H^+). We identified these convoy electrons as ones originating from the electron stripping (loss) process for the original electrons accompanied by incident molecular projectiles(H_2^+, H_3^+). However, at that time no definite explanation for the origin of convoy electrons emitted in forward angles for molecular projectiles was obtained. In this work, the previous measurement has been reexamined in the forward angluar range 15°-30° for 0.8 MeV/amu H^+, H_2^+, H_3^+, and $^3He^+$, extending the range of the foil thickness to much thinner thickness(~2 μg/cm^2), in order to obtain an information on the origin of the convoy electrons emitted angles larger than ~15° in molecular ion-foil collisions.

2. Experimental

The experimental arrangement is shown in Fig.1, which is almost the same as that previously described[5]. 0.8 MeV/amu H^+, H_2^+, H_3^+, and $^3He^+$ beams were collimated to 0.8 mm in diameter and 0.08° in divergence at the position of target foils and collected by a Faraday cup. The quality of primary beams was magnetically analyzed for the contaminations of primary beams by unwanted components. Emitted electrons were energy analyzed by a parallel plate electrostatic energy analyzer and detected by a channeltron. The energy resolution of the analyzer is $\Delta E/E(fwhm)=1.4\%$ and the angular acceptance is 2.1°. The collision chamber was maintained at a pressure of $\sim 10^{-9}$ Torr during measurements. Carbon foils of thickness ranging from 2 to 20 $\mu g/cm^2$ were mounted on a sample disk which can hold 15 samples and has an open window.

3. Results and discussions

In Fig.2, doubly differential electron spectra measured at 20°, $d^2n_e/dEd\Omega$, multiplied by the electron energy E are plotted as a function of electron energy, for four different thicknesses of carbon foils(2-20 $\mu g/cm^2$) perpendicularly bombarded by 0.8 MeV/amu H_3^+. Features seen in common in the four spectra are the existence of four groups of electrons; (1) the low energy electrons($0 \leq E \leq 100eV$), (2) carbon K Auger electrons(~270 eV), (3) peaks centered at about 400 eV, corresponding to convoy electrons, and (4) the high energy electrons with very broad peaks centered at about 1300 eV, due to knock-on collisions. These features for H_3^+ are qualitatively the same as those for H_2^+. The intensity of the knock-on electrons increases with the increase of the foil thickness and saturates for foils thicker than ~10 $\mu g/cm^2$. The reson for that is easily understood in terms of the escape lengths for the knock-on electrons. The intensity of the carbon K-LL Auger electrons does not change with the foil thickness for the range of the foil thickness used in the present experiment within experimental uncertainties. The intensity of the low energy electrons remarkably increases with the decrease of the foil thickness, but we do not go into details of this matter in the present paper. The most striking result is that the yield of the convory electrons drastically increases

with the decrease of the foil thickness; in other words, the large molecular enhancement for the yields of convoy electrons is observed with decreasing foil thickness. In Fig.3 are shown electron spectra measured at 20° for carbon foils(~2 and 20 $\mu g/cm^2$) bombarded by 0.8 MeV/amu H^+, H_2^+, and H_3^+. All the spectra are normalized to the number of protons detected by the Faraday cup; viz., measured spectra are divided by 2 and 3 for H_2^+ and H_3^+, respectively. An interesting feature seen in Fig.3 is that intensities of the Auger electrons and the knock-on electrons are almost independent on the species of projectiles; that is, no molecular effect for the productions of these electrons. This result may be interpreted on the basis of that the impact parameters responsible for knock-on collisions as well as collisions producing vacanicies in carbon K-shell are both much smaller than the internuclear distances of molecular ions, at the ion energy of 0.8 MeV/amu. The most interesting results are; i) a very large enhancement of yields of convoy electrons for molecular projectiles, H_2^+ and H_3^+, as compared with that for H^+, for a thinn foil(~2 $\mu g/cm^2$), where the yield for H_3^+ is larger than that for H_2^+, and ii) electron spectra for a thick foil(20 $\mu g/cm^2$) being all the same for H^+, H_2^+, and H_3^+ over the whole energy range, including convoy electrons. Notice that a convoy electron peak for H^+ is discernible, though small, for both thin and thick foils.

Hereafter, we are mainly concerned with the origin of the molecular enhancement of convoy electrons. Three kinds of processes have been so far proposed for the origin of convoy electrons: (1) electron(charge) transfer to the continuum(ETC or CTC)[1], (2) electron capture into the wake-riding (WR) states of a fast ion moving through a solid[6], and (3) electron loss (EL) to the continuum from electronic states carried along by the projectile.[5,7,8] The ETC and EL processes are possible for both ion-gas and ion-solid collisions but the WR process is possible only for ion-solid collisions.

What we are now looking for is such a process that can explain the molecular enhancement for yields of convoy electrons emitted at angles larger than 0°(15°-30°). Ponce *et al.*[4] interpreted the molecular enhancement for the yield of convoy electrons emitted in the forward direction near 0° in

terms of a correlated action of the emergent protons on the ETC process for H_2^+ projectile. The molecular enhancement ratio for convoy electron yields per proton observed at ~0° by Ponce *et al.* is at the most ~1.4 for 100 keV/amu H_2^+ and H^+ on 2 μg/cm^2 carbon foil, whereas our ratio for 0.8 MeV/amu H_2^+ and H^+ on 2 μg/cm^2 carbon foil is surprisingly large compared with that by Ponce *et al.*, as seen in Fig.3. Since the above molecular enhancement ratio is bound between the values 1 and 2 in terms of the ETC process[4], it is questionable whether the model proposed by Ponce *et al.* be applicable to our results. In the ETC theory[9], based on the second Born approximation, the yield of convoy electrons (the doubly differential yield) should be proportional to Z_1^3, where Z_1 is the effective charge of the projectile.

In order to see whether the molecular enhancement for the yield of convoy electrons can be explained by the ETC process, the electron spectrum for 0.8 MeV/amu H_2^+ on 2 μg/cm^2 carbon foil is compared with that for 0.8 MeV/amu $^3He^+$ on 20 μg/cm^2 carbon foil in Fig.4. The 20 μg/cm^2 carbon foil is thick enough to assure the eqilibrium charge state for 0.8 MeV/amu ^3He projectiles, where the population ratio of He^+ and He^{++} charge states is 2-3%.[10] Thus, the effective charge for ^3He projectiles is nearly 2 and that for H_2^+ projectiles is less than 2. Therefore, if the ETC process should be the origin of convoy electrons, the theoretical ratio of yields of convoy electrons for $^3He^+$ and H_2^+ projectiles would be much larger than 1. The experimental ratio is approximately 0.5, in great contrast to the theoretical value for the ETC process as seen in Fig.4. Therefore, it is concluded that the ETC process is not responsible for the molecular enhancement for convoy electrons. Although detailed discussions on the electron capture to the wake patential are not given here,[11] it is unlikely that the WR process can explain the experimental result shown in Fig.4.

Next, let us try to examine the possibility of the EL process as the origin of convoy electrons for molecular projectiles. The range of the dwell time t_D in the present experiment is from ~1 to ~20 fs(10^{-15}s), corresponding to foil thicknesses of ~2-20 μg/cm^2. This region of the dwell time just corresponds to the transition region, where the so-called *red*

regiem gradually changes to the *blue* regiem[12] and the molecular enhancement for the production of neutral hydrogens(H^0) is observed for the dwell times less than ~15 fs by Gaillard *et al.*[13] It is here assumed that convoy electrons are generated by the EL process taking place in the vicinity of the exit surface; then, the yields of convoy electrons for H_2^+ and H_3^+ projectiles as functions of t_D, $I(H_2^+, t_D)$ and $I(H_3^+, t_D)$, are proportional to (i) the electron loss cross section $\sigma_\ell(H^0)$ times the number of neutrals (H^0), $N_{H_2}+(H^0, t_D)$ and $N_{H_3}+(H^0, t_D)$, or (ii) the ionization(or electron loss) cross section $\sigma_\ell(H_2^+$ or $H_3^+)$ times the number of surviving molecular projectiles(H_2^+ and H_3^+), $N(H_2^+, t_D)$ and $N(H_3^+, t_D)$; that is,

$$\text{i)} \qquad \begin{aligned} I(H_2^+, t_D) &= A\, \sigma_\ell(H^0)\, N_{H_2}+(H_0, t_D), \\ I(H_3^+, t_D) &= A\, \sigma_\ell(H^0)\, N_{H_3}+(H_0, t_D), \end{aligned} \qquad (1)$$

or

$$\text{ii)} \qquad \begin{aligned} I(H_2^+, t_D) &= B\, \sigma_\ell(H_2^+)\, N(H_2^+, t_D), \\ I(H_3^+, t_D) &= B\, \sigma_\ell(H_3^+)\, N(H_3^+, t_D), \end{aligned} \qquad (2)$$

where A and B constants.

Referring to the data on the electron loss cross sections for H_2^+ and H_3^+,[10] we can conclude that the process (ii) has a negligible contribution to the production of convoy electrons as compared with the process (i).

If the process (i) is the case, the ratio of the yield of convoy electrons for H_3^+ to that for H_2^+, R, is given by the following relation as a function of t_D, using Eq.(1),

$$\begin{aligned} R(t_D) &= I(H_3^+, t_D) \,/\, I(H_2^+, t_D) \\ &= N_{H_3}+(H^0, t_D) \,/\, N_{H_2}+(H^0, t_D). \end{aligned} \qquad (3)$$

Convoy electron spectra per proton for H_2^+ and H_3^+ projectiles of the molecular origin, $d^2n_c^{\text{molec}}/dEd\Omega$, are derived by the subtraction of the electron spectrum for H^+, $d^2n_e(H^+)/dEd\Omega$, from the electron spectra for

H_2^+ and H_3^+, $d^2n_e(H_2^+ \text{ or } H_3^+)/dEd\Omega$. Hereafter, $d^2n_e/dEd\Omega$ and $d^2n_c/dEd\Omega$ are, for simplicity, expressed as n_e and n_c, respectively. Then the ratio of the yields of molecular convoy electrons for H_3^+ and H_2^+ projectiles, differential in electron energy, $r(E, t_D)$, becomes

$$r(E, t_D) = \frac{n_e(H_3^+) - n_e(H^+)}{n_e(H_2^+) - n_e(H^+)} = \frac{n_c(H_3^+)}{n_c(H_2^+)} . \qquad (4)$$

$n_c(H_3^+)$ and $n_c(H_2^+)$, and the ratio $r(E, t_D)$ are shown in Fig.5, for an emission angle 20°, and for t_D=1 fs. The difference of the relative populations of the n-states of neutral hydrogen(H^0) between H_2^+ and H_3^+(n is the principal quantum number)[14] may affect the electron loss cross sections $\sigma_\ell(H^0)$ for H_2^+ and H_3^+, which may also be reflected in the small difference of the shapes of convoy electron spectra between H_2^+ and H_3^+, as seen in Fig.5. If this difference is disregarded, $R(t_D)$ is regarded to be approximately equal to the value of $r(E, t_D)$ at the peak position of convoy electrons, $r(E_p, t_D)$. Then, from Eqs.(3) and (4), we have a relation

$$r(E_p, t_D) \simeq N_{H_3^+}(H^0, t_D) \; / \; N_{H_2^+}(H^0, t_D). \qquad (5)$$

The value of $r(E_p, t_D)$ is of the order of ~1.5-1.7 for t_D≃1 fs, slightly depending on emission angles, decreases slowly with foil thickness, and reaches a value of 1 for foil thickness ≳15 μg/cm^2.

It is here very interesting to consider the relations between the ratio $N_{H_3^+}(H^0, t_D)/N_{H_2^+}(H^0, t_D)$ and the ratio $\Phi_0^{H_3^+}(t_D)/\Phi_0^{H_2^+}(t_D)$ for the neutral fraction (H^0) per proton observed by Gaillard *et al.*[13] While the former ratio is for the neutral fraction (H^0) in the vicinity of the exit surface inside solid, the latter ratio is for that observed at a distance far away

from the exit surface. However, it should be noted that both ratios have almost the same magnitude and the same tendency as functions of the dwell time in the region, t_D=1~15 fs, though the values of $\Phi_0^{H_3^+}(t_D)/\Phi_0^{H_2^+}(t)$ for $t_D \lesssim 2$ fs are not definitely established in the data by Gaillard *et al.*[13] This fact strongly supports our model that the origin of the molecular enhancement for the production of convoy electrons is the electron loss process for the neutral fraction.

References

1. K.Dettmann, K.G.Harrison, and M.W.Lucas, "Charge exchange to the continuum for light ions in solids", *J.Phys.* B7, 269-287 (1974).
2. M.M.Duncan and M.G.Menéndez, "Measurements of beam-foil electrons emitted near 0° from H^+ and H_2^+ on carbon in the energy range 0.175-1.0 MeV/amu", *Phys.Rev.* A13, 566-571 (1976).
3. W.Meckback, K.C.R.Chiu, H.H.Brongersma, and J.Wm.McGowan, "Do present 'charge transfer to the continuum' theories correctly describe the production of $v_i=v_e$ electrons in ion beam-foil collisions?", *J.Phys.* B10, 3255-3270 (1977).
4. V.H.Ponce, E.González Lepera, W.Meckbach, and I.B.Nemirovsky, "Molecular Effects in Beam-Foil Electron Transfer to the Continuum", *Phys.Rev.Lett.* 47, 572-575 (1981).
5. N.Oda, F.Nishimura, Y.Yamazaki, and S.Tsurubuchi, "Energy and angular spectra of electrons emitted from foils by ion beams", *Nucl.Instr. Meth.* 170, 571-575 (1980).
6. V.N.Neelavathi, R.H.Ritchie, and W.Brandt, "Bound Electron States in the Wake of Swift Ions in Solid", *Phys.Rev.Lett.* 33, 302-305 (1974).
7. F.Drepper and J.S.Briggs, "Doubly differential cross sections for electron-loss in ion-atom collisions", *J.Phys.* B9, 2063-2071 (1976).
8. J.S.Briggs and M.H.Day, "The structure of the doubly differential cross section for electron loss to low-lying continuum states of the projectile in fast ion-atom collisions", *J.Phys.* B13, 4797-4810 (1980).
9. M.Rødbro and F.D.Andersen, "Charge transfer to the continuum for 15 to 1500 keV H^+ in He, Ne, Ar, and H_2 gases under single-collision conditions", *J.Phys.* B12, 2883-2903 (1979).
10. N.Cue, N.V.de Castro Faria, M.J.Gaillard, J.C.Poizat, and J.Remillieux, "Electron loss and capture cross section of 800 keV amu^{-1} H and He species in carbon foils", *Nucl.Instr.Meth.*, 170, 67-72 (1980).
11. Y.Yamazaki and N.Oda, "Electron capture process into wake potential", *Nucl.Inst.Meth.* (in press).
12. J.Remillieux, "Interaction of fast molecular ions with solids", *Nucl. Instr.Meth.* 170, 31-40 (1980).

13. M.J.Gaillard, J.C.Poizat, A.Ratkowski, J.Remillieux, and M.Anzas, "Nonequilibrium effects in the proton neutral fraction emerging from solids bombarded with MeV H^0, H^+, H_2^+, and H_3^+ beams", *Phys.Rev.* A16, 2323-2335 (1977).

14. K.Kobayashi and N.Oda, "Interaction of Hydrogen Molecular Ions with Thin Foils. II. Balmer Emission", a succeeding paper.

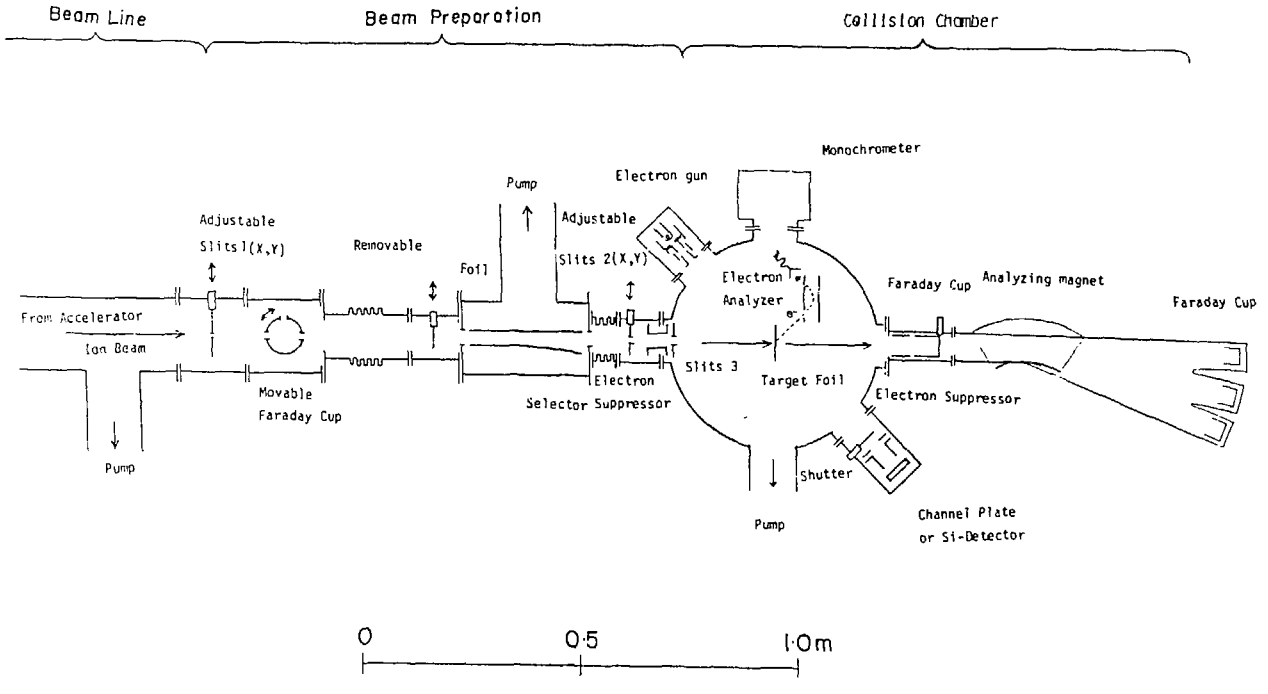

Fig.1 Experimental set-up to measure electron spectra from carbon foils with H^+, H_2^+, H_3^+, and $^3He^+$ beams.

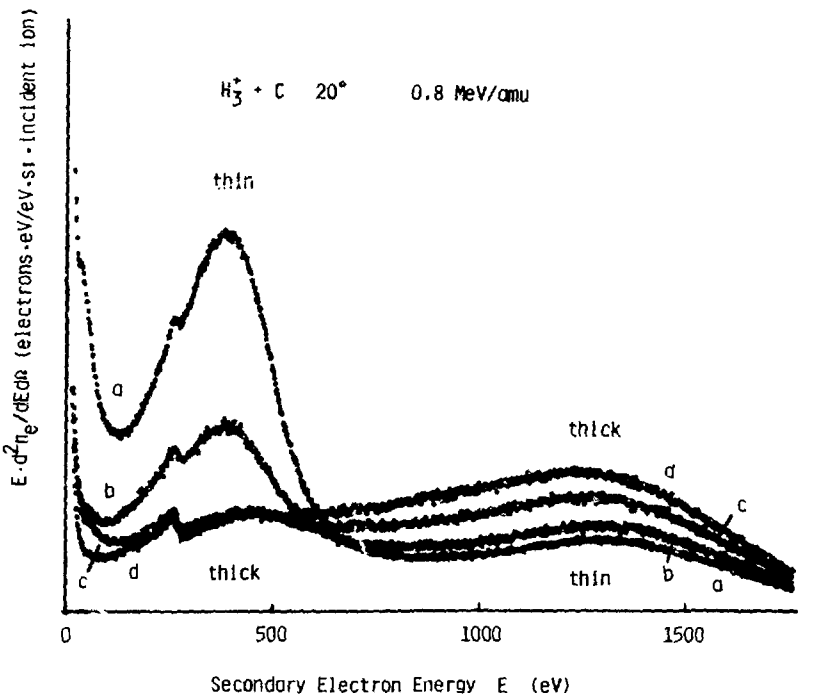

Fig.2 Doubly differential electron spectra $d^2n_e/dEd\Omega$ multiplied by electron energy E measured at 20° as a function of electron energy, with 0.8 MeV/amu H_3^+ beam. Spectra (a)-(b) correspond to four different carbon foil thicknesses from the thinnest (~2 μg/cm^2) to the thickest(~20 μg/cm^2).

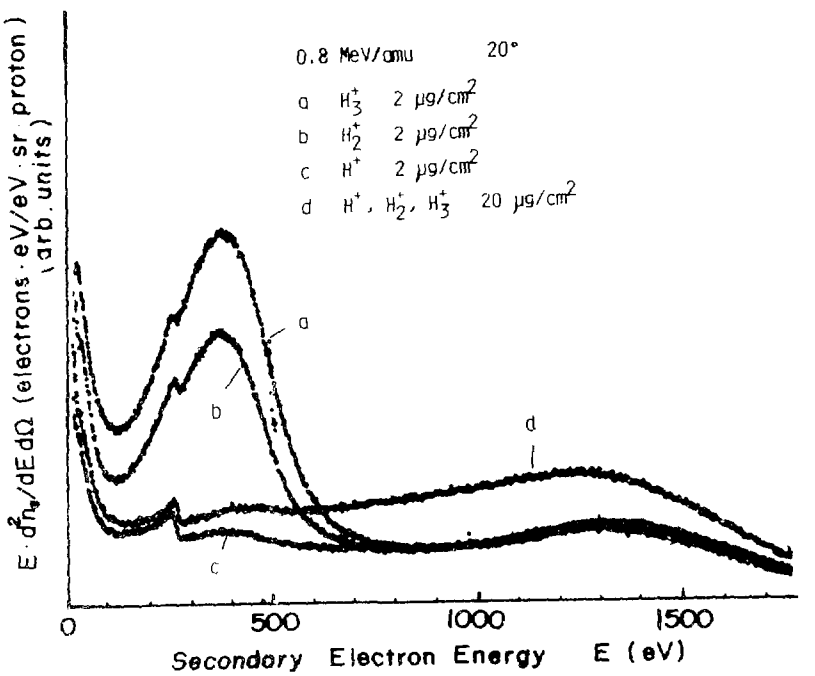

Fig.3 Doubly differential electron spectra $d^2n_e/dEd\Omega$ multiplied by electron energy E at 20°, normalized to the number of protons, with 0.8 MeV/amu H^+, H_2^+, H_3^+ beams on carbon foils: curve(a) H_2^+ on 2 μg/cm^2 foil; curve(b) H_2^+ on 2 μg/cm^2 foil; curve(c) H^+ on 2 μg/cm^2 foil; curve(d) H^+, H_2^+, H_3^+ on 20 μg/cm^2 foil.

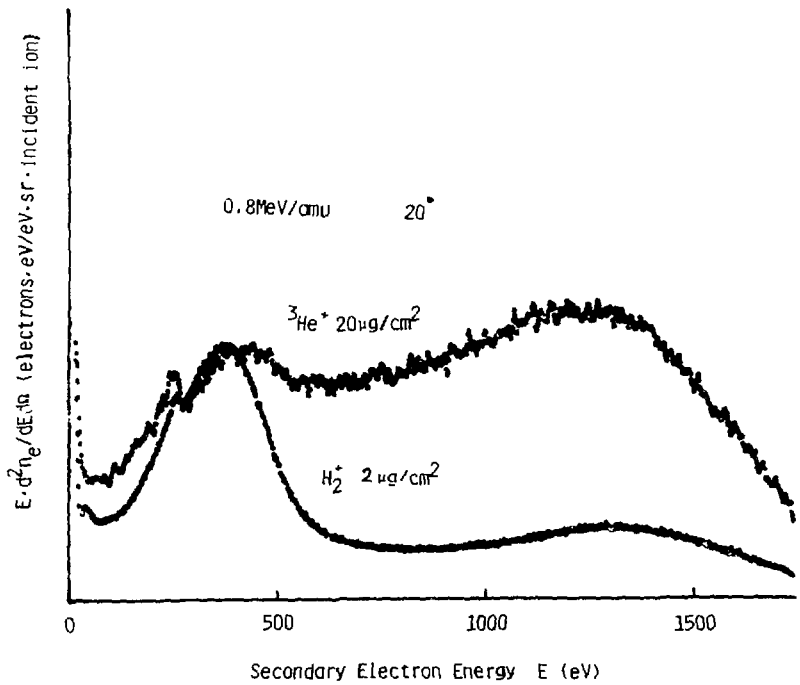

Fig.4 Doubly differential electron spectra $d^2n_e/dEd\Omega$ multiplied by electron energy E at 20° normalized to the number of incident projectiles; for 0.8 MeV/amu $^3He^+$ on 20 μg/cm^2 carbon foil and 0.8 MeV/amu H_2^+ on 2 μg/cm^2 carbon foil.

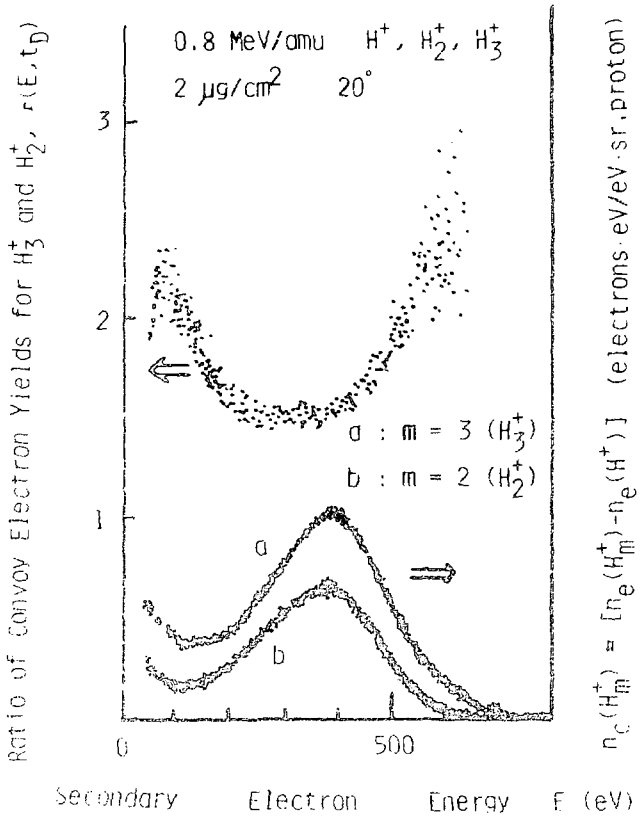

Fig.5 Convoy electron spectra per proton, $n_c(H_3^+)$ and $n_c(H_2^+)$, and ratio $r(E, t_D)$ of convoy electron yields for 0.8 MeV/amu H_3^+ and H_2^+ on 2 $\mu g/cm^2$ carbon foil(t_D=1 fs), for emission angle 20°, as a function of electron energy. For the definitions of $n_c(H_3^+)$, $n_c(H_2^+)$, and $r(E, t_D)$, see the text(Eq.4)

Interaction of Hydrogen Molecular Ions with Thin Foils

II Balmer Emission

H.Kobayashi* and N.Oda

Research Laboratory of Nuclear Reactors, Tokyo Institute of Technology, Meguro-ku, Tokyo 152, Japan

Relative emission yields of Balmer α, β, γ, and δ lines as functions of the dwell time, t_D, in thin carbon foils have been measured with beams of H^+, H_2^+, and H_3^+ impinging on thin carbon foils(2-37μg/cm^2) at 0.5 and 0.8MeV/amu. Large molecular enhancement of emission yields of Balmer lines has been observed for H_2^+ and H_3^+ beams, where (i) the molecular enhancement for H_3^+ is higher than that for H_2^+ over both the range of the corresponding principal quantum number(n=3,4,5,and 6) and the range of the dwell time measured(t_D=0.97-12.3fs), and (ii) the molecular enhancement for both H_2^+ and H_3^+ rapidly increases when the dwell time decreases to values less than ~2fs. Relative populations of n levels in hydrogen have been derived from the relative yields of Balmer lines as functions of n and the dwell time t_D. The molecular enhancement for relative populations is compared with the molecular enhancement for the other kind of quantity such as the neutral hydrogen yields.

1. Introduction

Observations of the yields of neutral hydrogen atoms generated by the transversals of fast H^+, H_2^+, and H_3^+ beams through thin carbon foils afford a very powerful tool to elucidate the mechanism of interactions of fast hydrogen molecular ions with thin foils. Gaillard *et al.*[1] measured the yields of the total neutral hydrogens H^0 and observed molecular enhancement for H^0 in a region of the dwell time, t_D=1-15fs(10^{-15}s). This region of the dwell time corresponds to the transition region, where the so-called *red* regiem gradually changes to the *blue* regiem[2] and, in other words, the *original* regiem transfers to the *reconstitution* regiem in terms of the transmission of H_2^+.[3] Neutrals H^0 observed by Gaillard *et al.* con-

---

*Permanent address: Institute for Atomic Energy, Rikkyo University, 2-5-1, Nagasaka, Yokosuka-shi, 240-01, Japan.

tain all the hydrogen atoms with n=1,2,$\cdots$, ∞, where n is the principal quantum number; thus, from their data we can obtain no information on the yields of hydrogens in excited states($n\geq 2$) for whose yields much higher molecular enhancement is expected.

The beam foil spectroscopy is the most useful method to obtain informations on the excited hydrogen atoms and several studies have been reported to date. Gabrielse[4] measured the Lyman α radiation yields as a function of the dwell time t_D in carbon foils(t_D=2-17fs) for H_2^+ and H_3^+ and observed the molecular enhancement of yields in a region of t_D less than ~9fs. Bukow *et al.*[5] derived the initial population ratios of $3p$ and $3d$ states to $3s$ state from the measurement of Balmer emission yields for H^+, H_2^+, and H_3^+ beams, for a relatively large values of t_D(7-11fs). Similarly, Andresen *et al.*[6] measured Balmer emission yields for larger dwell times(t_D=27 and 55fs) and estimated the molecular effect on the population of n-states($n\geq 3$), assuming the n^{-3} dependence of the transition probabilities.

While it is expected that the molecular enhancements for the emission yields are larger for the Balmer emission than for the Lyman emission and also are larger for shorter dwell times, the previous measurements of the Balmer emission were limited to the region of large dwell times.[5,6] We have recently measured the Balmer emissions for H^+, H_2^+, and H_3^+ beams impinging on thin carbon foils(2-37μg/cm^2) at 0.5 and 0.8MeV/amu,[7] where the range of the dwell time t_D is from 0.97fs to 12.3fs. In this report, relative populations of n levels(n=3,4,5,and 6) in hydrogen fragments are derived from the relative yields of Balmer lines as functions of n and t_D, and the molecular enhancement for relative populations is compared with those for the other kind of quantity such as the total neutral hydrogen yields.

2. Experimental

A schematic diagram of the experimental apparatus is shown in Fig.1. Hydrogen ions H^+, H_2^+, and H_3^+ accelerated to 0.5 and 0.8MeV/amu by the 3MV Pelletron accelerator, after mass analyzed, are collimated by a pair of slits(S1,S2), pass through the carbon foil(F1), and finally are collected by a movable Faraday cup(MFC). A movable foil(F2)(~20μg/cm^2), which is

set 13mm upstream from the target foil, serves as a stripper which produces a H^+ beam from the H_2^+ and H_3^+ beams, keeping the other experimental conditions the same. The quality of beams is checked with a charge-state selector(M). The thicknesses of carbon foils were measured with a quartz thickness monitor at the manufacturing stage of foils by evaporation and later by the optical interference method. After foils were attached on a foil holder, the foil thicknesses were further monitored with a foil thickness monitor utilizing the Rutherford scatterings during measurements in order to observe the uniformity of foils, the foil thickening effect by ion bombardments, and also the foil thicknesses in units of g/cm^2. From these measurements, the density of carbon foils was determined to be $1.66 g/cm^3$, which is in good agreement with the value by Gaillard *et al.*[1]

The vacuum in the collision chamber was kept to the order of $\sim 10^{-10}$ Torr during measurements. The Balmer radiation emitted 5mm downstream from the foil was focused on an entrance slit(MS1) of a scanning grating monochrometer equipped with a HAMAMATSU R649S photomultiplier by a lens system(L1,L2). To improve the signal-to-noise ratio, a chopper is inserted in the optical path, the chopper duty rate being 38.1% at 70Hz. The output pulses are accumulated in a multichannel scaler as signals per the incoming particle number preset by a charge integrator(CI). The measured photon counts were corrected for the transmission of the monochrometer and the quantum efficiency of the photomultiplier as a function of wavelength, to obtain the relative line intensities. Futher, the light intensities were corrected for the difference of the time intervals of light observation seen by the optical system due to the difference of the energies of projectiles, 0.5 and 0.8MeV/amu. The typical photon counting rate was 130 H_α counts/μC at 0.5MeV/amu H_2^+.

3. Results and discussions

Relative Balmer emission yields per proton, $Y^{H^+}(n, t_D)$, $Y^{H_2^+}(n, t_D)$, and $Y^{H_3^+}(n, t_D)$ are plotted against the principal quantum number n in Fig.2, where the energy of projectiles is 0.8MeV/amu and the dwell time t_D is 0.97fs($2\mu g/cm^2$). The yield for H^+, $Y^{H^+}(n, t_D=\infty)$, is that for the equilibrium foil thickness.

From Fig.2 , one can see that i) relative yields $Y^{H_2^+}$ and $Y^{H_3^+}$ are

much higher than Y^{H^+} for all the Balmer lines, ii) $Y^{H_3^+}$ is higher than $Y^{H_2^+}$, and iii) all the yields, Y^{H^+}, $Y^{H_2^+}$, and $Y^{H_3^+}$, are well fitted by a functional form n^{-p}, where values for the parameter p are higher for H_2^+ and H_3^+ than for H^+.

The molecular enhancement for the Balmer emission yields is given by the ratio

$$R_Y(n,t_D) = Y^{\text{molec}}(n,t_D) \;/\; Y^{H^+}(n,\infty). \tag{1}$$

The ratios $R_Y(n,t_D)$ for H_2^+ and H_3^+ are shown in Fig.3 as functions of n for t_D=0.97, 1.4, and 12.3fs. The ratios $R_Y(n,t_D)$ can be also fitted by a functional form n^{-q}, where q is a fitting parameter. The values of q decrease with the increase of t_D for both H_2^+ and H_3^+. The ratios $R_Y(n,t_D)$ for $H_\alpha(n=3)$ and $H_\beta(n=4)$ are shown as functions of t_D in Fig.4, (a) and (b), respectively, along with the corresponding ratios for the yields of total neutrals, $\Phi_0^{\text{molec}}/\Phi_0^{\text{atom}}$.1

The yield of total neutrals means that of the sum of hydrogen atoms in the ground as well as excited states. The inter-proton separations for H_2^+ and H_3^+ are for convenience shown on the upper part of Fig.4 (a). One can see in Fig.4, (a) and (b) that the molecular effects for emission of H_α and H_β are very large even in the *blue* regiem and much larger than those for the total neutral yields. However, it should be noted that the molecular effect to be compared with that for the total neutral yields is not the molecular effect for the Balmer emission yields, but that for the populations of n-excited states of neutral hydrogen atoms. Therefore, the ratio of the populations of n-excited state per proton for molecular ions, $P^{\text{molec}}(n,t_D)$, to that for H^+, $P^{H^+}(n,\infty)$, $R_P(n,t_D)$, is defined as

$$R_P(n,t_D) = P^{\text{molec}}(n,t_D) \;/\; P^{H^+}(n,\infty). \tag{2}$$

Here,

$$P(n,t_D) = \sum_{\ell=0}^{n-1} P(n,\ell,t_D), \tag{3}$$

where $P(n,\ell,t_D)$ is the relative population of the (n,ℓ) substate. Hereafter, the case of H_2^+ projectiles only will be taken into consideration.

The relative Balmer emission yields are connected to the relative

level populations by the following relation, when the contribution of the cascade process to the Balmer emission is disregarded;

$$Y(n,t_D) = \xi_n \cdot \sum_{\ell=0}^{2} \sum_{\ell'=0}^{1} A_{n\ell 2\ell'} \cdot P(n,\ell,t_D), \tag{4}$$

where $A_{n\ell 2\ell'}$ is the transition probability for the transition from state (n,ℓ) to state $(2,\ell')$ and ξ_n is the net quantum efficiency of the detection system. The contribution of the cascade process to H_α emission was estimated but it is negligibly small for both H^+ and H_2^+.[5] When the average transition probability $\langle A_n \rangle$ is defined by the following relation

$$\langle A_n \rangle = \sum_{\ell=0}^{2} \sum_{\ell'=0}^{1} A_{n\ell 2\ell'} \cdot P(n,\ell) \; / \; \sum_{\ell=0}^{n-1} P(n,\ell), \tag{5}$$

we can have the following relation from Eqs.(3) and (4),

$$P(n,t_D) = Y(n,t_D) \; / \; \xi_n \cdot \langle A_n \rangle. \tag{6}$$

From Eq.(6), one can see that, if the value of $\langle A_n \rangle$ defined by Eq.(5) is known, the relative population of n-state can be derived from the relative yield of the Balmer line $Y(n,t_D)$. In order to obtain the value of $\langle A_n \rangle$ using Eq.(5), the relative initial populations $P(n,\ell)$ of the (n,ℓ) substates have to be known for H^+ and H_2^+ and for various dwell times. Bukow *et al.*[5] experimentally derived the ratio of relative initial populations, $P(3p)/P(3s)$ and $P(3d)/P(3s)$ for H^+ and $H_2^+(H_3^+)$, for relatively large values of t_D(7-11fs). Their values of $P(3p)/P(3s)$ and $P(3d)/P(3s)$ are 0.608 and 0.422 for H^+, and 1.08 and 1.29 for H_2^+, respectively; the populations of substates with higher angular momenta are larger for H_2^+ than for H^+ and values of both ratios are smaller than those obtained from the statistical expectation. Experimental data for H^+ by Alguard and Brake[8], who obtained the ratio of excitation cross sections for substates from the measurement of the Stark beat of Lyman β, support the result of Bukow *et al.*[5] It is assumed here that: (1) The values of $P(3p)/P(3s)$ and $P(3d)/P(3s)$ by Bukow *et al.* are independent of values of t_D. (2) For $\ell \leq 2$, the ratios $P(n\ell)/P(ns)$ are equal to $P(3\ell)/P(3s)$ for all values of $n \geq 4$. (3) The values of $P(n\ell)/P(ns)$ $(n \geq 4, \ell \geq 3)$ can be estimated by extrapolation of $P(3\ell)/P(3s)$ $(\ell \leq 2)$ to higher ℓ values $(\ell \geq 3)$ by drawing a smooth curve. The values for $A_{n\ell 2\ell'}$ are taken from Wiese *et al.*[9] The resulting ratios of initial

relative populations of n-excited states in hydrogen for H_2^+ to those for H^+, $P^{H_2^+}(n,t_D)/P^{H^+}(n,t_D)$, are plotted against the principal quantum number n in Fig.5, for values of t_D(=0.97, 1.4, 12.3fs), where error bars indicate only the statistical error. Comparing Fig.3 with Fig.5, one can see that the molecular enhancement for the initial populations of n-excited states is almost independent of the values of n, in great contrast to the molecular enhancement for the yields of Balmer lines.

The ratio $P^{H_2^+}(n,t_D)/P^{H^+}(n,t_D)$ for the n=3 state is plotted as a function of t_D in Fig.6, together with the ratio by Bukow *et al.*[5] which is in good agreement with our ratio. The ratio $\Phi_0^{molec}/\Phi_0^{atom}$ by Gaillard *et al.*[1] is also shown in Fig.6.

One can see an interesting feature from Figs.5 and 6. The molecular enhancement for the relative populations of the excited states with $n\geq 3$ is much higher than that for the yields of total hydrogen atoms consisting of the ground as well as excited states. This result can be easily understood by taking account of that the mean radii of these excited states in hydrogen increase with the increase of the value of n and these radii for $n\geq 3$ are comparable or larger than the inter-proton separation in the blue regiem (t_D=2-12.3fs) considered here. Full discussions on the molecular effects in the interactions of molecular hydrogen ions with thin foils will be given elsewhere.

References

1. M.J.Gaillard, J.C.Poizat, A.Ratkowski, J.Remillieux, and M.Auzas, "Nonequilibrium effects in the proton neutral fraction emerging from solids bombarded with MeV H^0, H^+, H_2^+, and H_3^+ beams", *Phys. Rev.* A16, 2323-2335 (1977).
2. J.Remillieux, "Interaction of fast molecular ions with solids", *Nucl.Instr.Meth.* 170, 31-40 (1980).
3. N.Cue, N.V.de Castro-Faria, M.J.Gaillard, J.C.Poizat, J.Remillieux, D.S.Gemmell, and I.Plesser, "Transmission of fast H_2^+ through thin foils", *Phys.Rev.Lett.* 45, 613-617 (1980).
4. G.Gabrielse, "Measurement of the n=2 density operator for hydrogen atoms produced by passing protons through thin carbon targets",

Phys.Rev. A23, 775-784 (1981).

5. H.H.Bukow, H.v.Buttlar, D.Haas, P.H.Heckmann, M.Holl, W.Schlagheck, D.Schürmann, R.Tielert, and R.Woodruff, "Lifetimes and initial populations of foil-excited hydrogen and lithium states", *Nucl. Instr.Meth.* 110, 89-94 (1973).
6. B.Andresen, S.Hultberg, B.Jelenković, L.Liljeby, S.Mannervik, and E.Veje, "A study of molecular effects in beam-foil spectroscopy", *Phys.Scr.* 19, 335-338 (1979).
7. H.Kobayashi and N.Oda, "Molecular effects on production of excited hydrogen atoms by dissociative collisions of MeV H_2^+ and H_3^+ ions in very thin carbon foils", *XII International Conference on the Physics of Electronic and Atomic Collisions (Gatlinburg,TN,1981)*, Vol.2, 994-995 (1981).
8. M.J.Alguard and C.W.Drake, "Stark beats in Lyman-series emission", *Phys,Rev.* A8, 27-36 (1973).
9. W.L.Wiese, M.W.Smith, and B.M.Glennon, "Atomic transition probabilities, Vol.I, Hydrogen through neon", *NSRDS-NBS* 4 (1966).

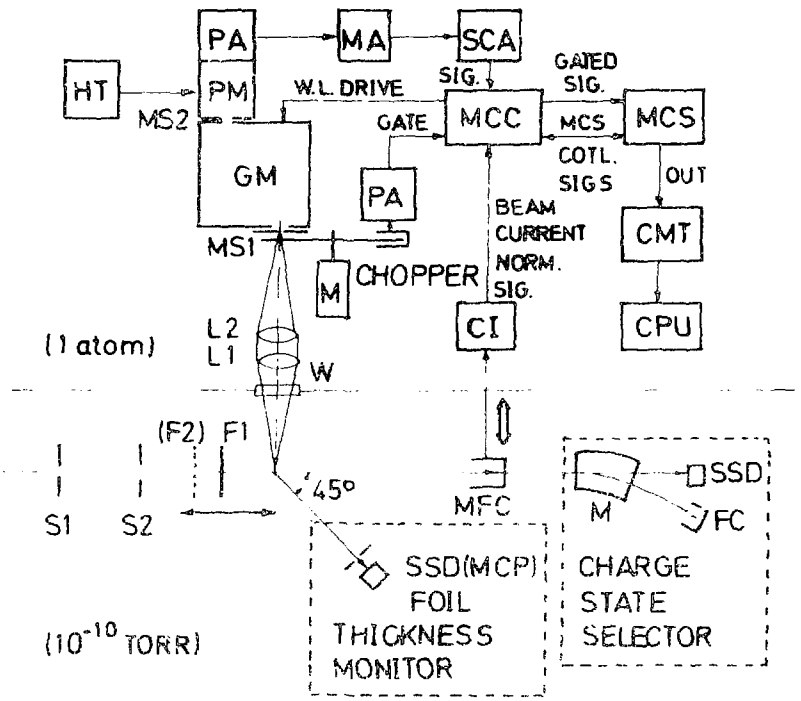

Fig. 1 Schematic diagram of the experimental set up for the beam-foil experiment and the photon counting system.

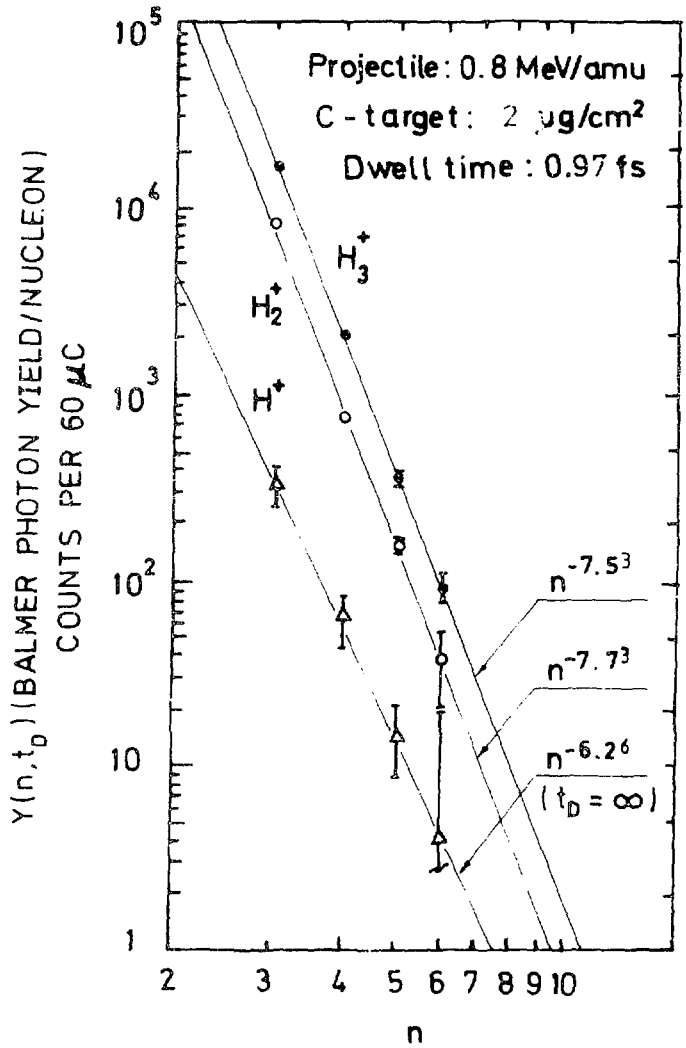

Fig.2 Balmer photon yields per nucleon (photon counts per 60μC) as functions of the principal quantum number n for 0.8 MeV/amu H^+, H_2^+, and H_3^+ at dwell time of 0.97 fs.

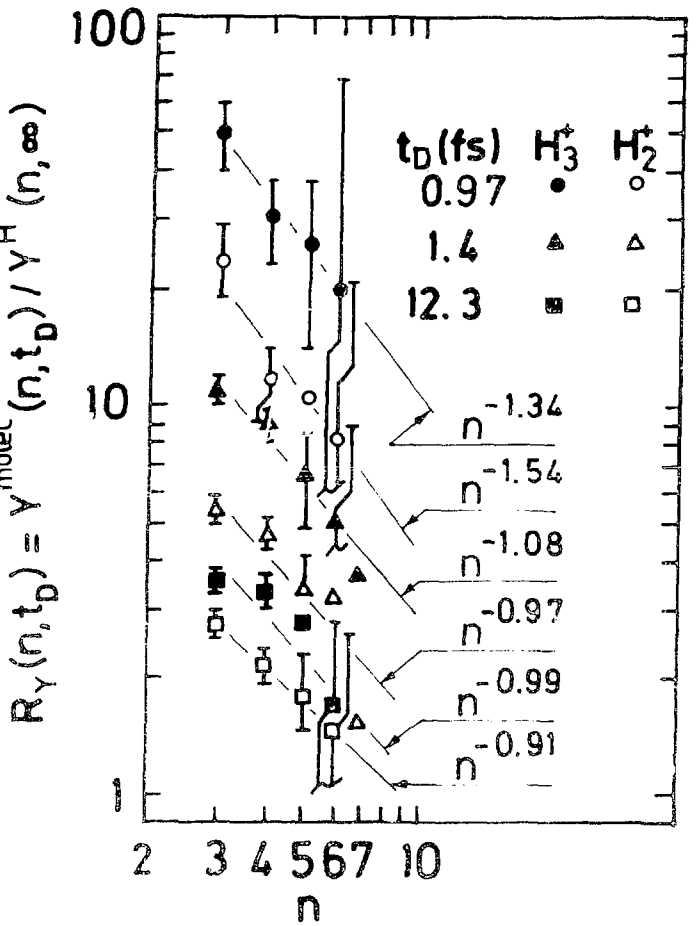

Fig.3 Ratios, $Y^{molec}(n,t_D)/Y^{H^+}(n,\infty)$, as functions of n for H_2^+ and H_3^+ ions, for t_D=0.97, 1.4, 12.3 fs. Root-mean-squares fitting lines and their slopes are also shown. Energies of projectiles are 0.8 MeV/amu for t_D=0.97 fs and 0.5 MeV/amu for t_D=1.4 and 12.3 fs.

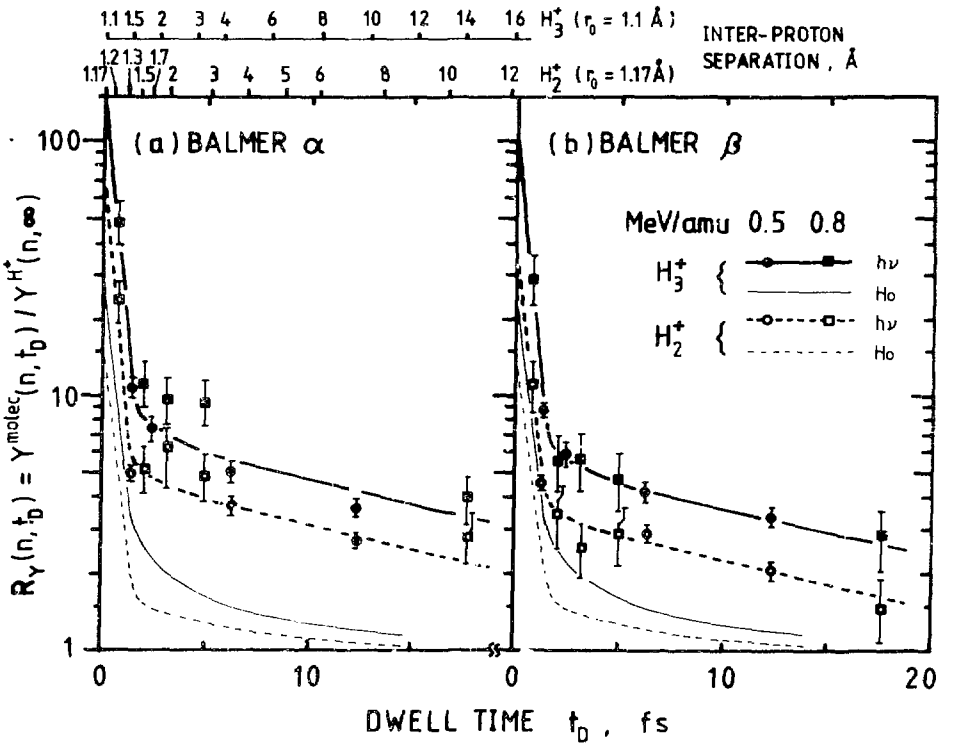

Fig.4 (a) Yield ratios, $Y^{molec}(n,t_D)/Y^{H^+}(n,\infty)$, as functions of the dwell time t_D for H_2^+ ions (○,□) and H_3^+ ions (●,■) for n=3 (Balmer α) and (b) n=4 (Balmer β) for projectile energies of 0.5 and 0.8 MeV/amu. Production ratios for total neutral hydrogens, $\Phi_0^{molec}/\Phi_0^{atom}$, are also shown for H_2^+ (thin dashed curve) and H_3^+ (thin solid curve) (Ref.1).

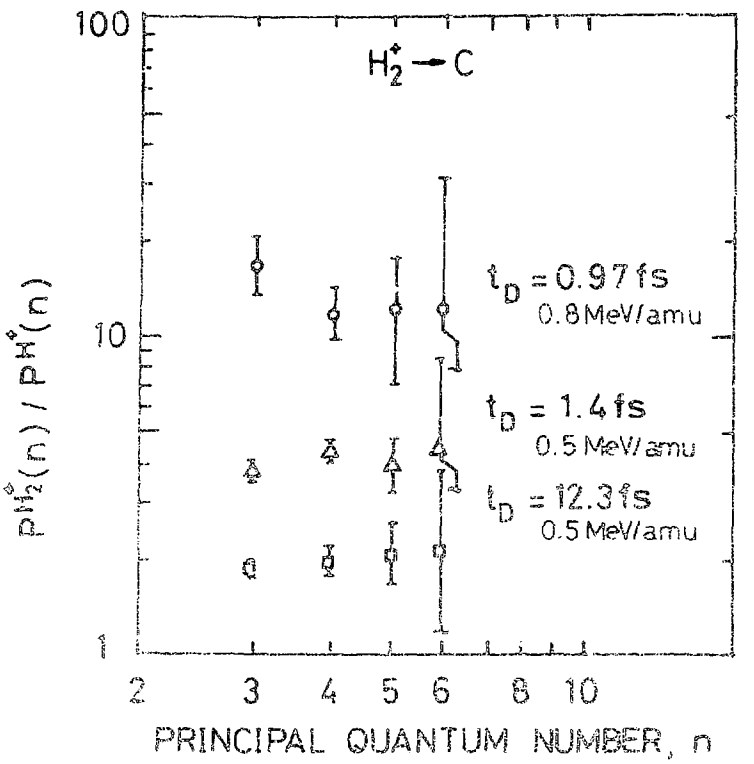

Fig.5 Population ratio, $P^{H_2^+}(n,t_D)/P^{H^+}(n,t_D)$, as a function of n for H_2^+ ions, for t_D=0.97, 1.4, 12.3 fs.

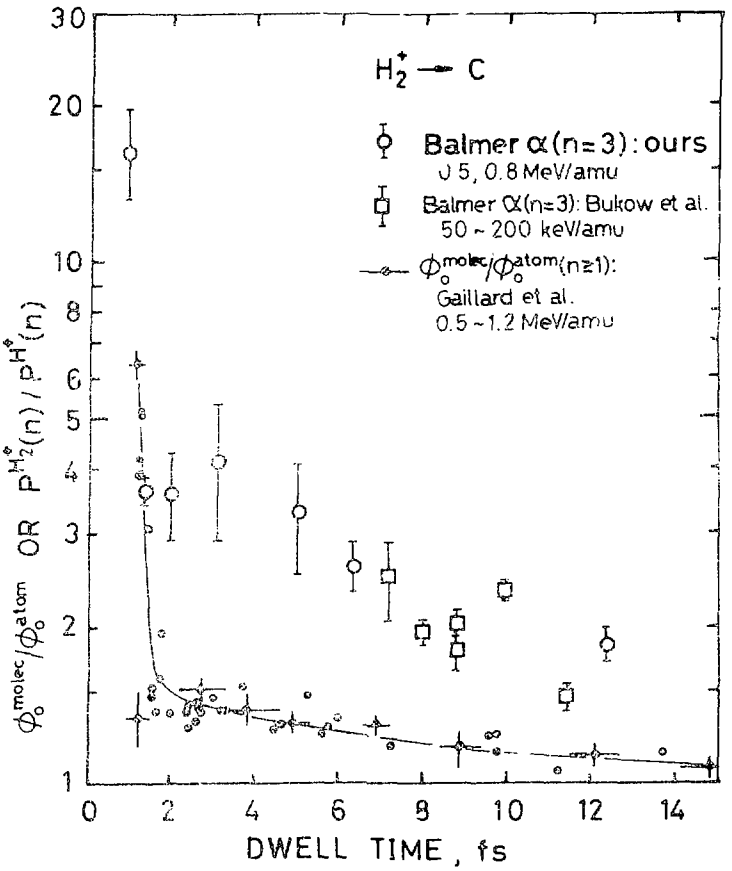

Fig.6 Population ratio, $P^{H_2^+}(3)/P^{H^+}(3)$, as a function of the dwell time t_D. Open circles, present results; open squares, estimated values from data by Bukow *et al.*(Ref.5). Production ratio for total neutral hydrogens, $\Phi_0^{molec}/\Phi_0^{atom}(n\geq 1)$, by Gaillard *et al.*(Ref.1) (closed circles and solid curve) is also shown for H_2^+.

Interaction of Hydrogen Molecular Ions with Thin Foils

III Inner-Shell Ionization

Y.Yamazaki and N.Oda

Research Laboratory for Nuclear Reactors, Tokyo Institute of Technology, Ookayama, Meguro-ku, Tokyo, 152, JAPAN

From measurements of electron spectra ejected in the backward direction from oxidized aluminum foil, it was found that H_2^+ ions(0.8-1.2MeV/amu) produce (1.4-1.6)±0.2 times as many Al-$L_{2,3}$VV Auger electrons per proton as H^+ ions do at the same velocity. This enhancement of the Auger electron yield for H_2^+ ions is mainly attributable to the vicinage effect of the constituent nuclei of molecular ions. The contribution of the projectile bound electrons to the Auger electron production is estimated to be unimportant under the present experimental conditions. Appreciable molecular enhancement of Auger electron yield was not observed on similar measurements on Auger electrons from oxide free aluminum and carbon foils.

1. Introduction

Large molecular effects have been reported in ion-foil interactions; for example, the energy loss[1], the fraction of ejected H^0 particles[2], the fraction of excited components in ejected H^0 particles[3], and convoy electron intensity for H_2^+ ions[4,5] are all larger than those for H^+ ions. A similar phenomenon is expected to occur for the inner-shell vacancy productions. Although x-ray measurements performed by Chen *et al.*[6] for thick foils and by Lurio *et al.*[7] for thin foils using H^+, H_2^+, and H_3^+ ions as projectiles did not show any increase of x-rays for molecular ions, Auger electron measurements performed by us did show an appreciable increase of Auger electrons for molecular ions (1.2MeV/amu) incident on thin aluminum foils having oxidized surfaces.[8] In the present paper, the measurements have been extended to wider species of projectiles, to wider range of projectile velocities and to aluminum foils having oxide free surfaces.

Since the adiabatic response distance, *i.e.* v/ω, where v is the projectile velocity and ω the angular frequency for the electron orbit in question, corresponds to the most effective impact parameter of the pro-

jectile that produces the electric field with angular frequency ω, it is expected that the condition $R \lesssim v/\omega$, where R is the internuclear distances of the molecular ion, makes the molecular effect due to the vicinity of the constituent nuclei appreciable. (This effect is reffered to as "vicnage effect" hereafter.) The bound electron of the molecular ion may also play some role in the inner-shell vacancy production by : 1) ionizing the inner-shell electrons when its reduced energy, $\varepsilon=(m/M)E$, where m is the electron mass, M the projectile mass, and E the projectile energy, exceeds the inner-shell binding energy and by 2) screening the nuclear charge of the projectile, the screening length being $\sim R$. These two effects of the bound electron are together called "bound electron effects" hereafter.

2. Experimental

H^+ and H_2^+ beams were supplied from the Pelletron accelerator at the Tokyo Institute of Technology. Before entering the collision chamber, the ion beams passed through double apertures and were collimated to less than about 0.75 mm in diameter at the target foil position. The angular spread of the beams was less than 1 mrad.

A H^0 beam was produced by a carbon foil neutralizer followed by a pair of deflectors to remove the charged particles and to decay the metastable excited states by the Stark effect. This system was also used as a stripper to obtain a H^+ beam from a H_2^+ beam and to obtain a He^{++} beam from a He^+ beam supplied by the accelerator. This procedure is very effective in the performance of measurements involving varying the kind of projectile, keeping the other conditions unaltered.

Clean aluminum surfaces were obtained by *in situ* evaporation under ultra high vacuum conditions ($<10^{-8}$Torr). Aluminum foils having oxide on the surface were prepared by the gradual oxidation of the *in situ* evaporated foils under the ultra high vacuum condition (>10 hr.) to eliminate the deposition of carbon and its chemical compounds.

The beam currents were 1 – 10 nA/amu for H^+, H_2^+ and He^+ beams and 100–200 pA/amu for H^0 beams. To prevent the foils from thickening and carbon deposition, beam currents were kept to less than ~10 nA/amu in this experiment.

Ejected electrons were energy analyzed by a parallel plate electro-

static analyzer, which covers angular ranges from -5° to 169° and from 175° to 180° with respect to the beam direction, and were detected by a channeltron. The output pulses of the channeltron were accumulated in a multiscaler with the standard pulse counting technique. The energy resolution of the analyzer is $\Delta E/E \sim 1.4\%$ (fwhm), and the acceptance angle is 0.75° and 4.8° for the directions parallel and perpendicular to the rotation plane of the analyzer, respectively. The collision chamber was kept at a pressure of less than 8×10^{-10} Torr during the measurements by a combination of an ion pump, a titanium getter pump, and a liquid nitrogen trap

3. Results and discussion

In Fig.1, the electron spectra measured at 150°, differential in electron energy and angle, $d^2n_e/dEd\Omega$ multiplied by the electron energy E, are plotted as a function of electron energy, for an oxidized aluminum foil perpendicularly bombarded by 1.2 MeV/amu H^+ and H_2^+ ions. Only the region around Al-$L_{2,3}$VV (V:valence) Auger spectra is shown in Fig.1. The peak observed around 52 eV correspond to Al-$L_{2,3}$VV Auger transitions of oxidized aluminum. In this figure, electron spectra are normalized to the number of protons to directly compare the Auger electron yields per proton for H^+ and H_2^+ ions. A considerable enhancement of the Al-$L_{2,3}$VV Auger electron yield is observed for H_2^+ ions. Since, although the continuum part of electron spectrum (continuum background) is also greatly enhanced for H_2^+ ions, it is not related to the inner-shell ionization, we shall not be concerned with it further here.

The enhancement factor η, the ratio of the Auger electron yield per proton for H_2^+ to that for H^+, is determined, so that, if the electron spectrum for H^+ [$I(H^+)$] multiplied by η is subtracted from that per proton for H_2^+ [$I(H_2^+)/2$], the resultant spectrum gives a smooth spectrum around the Auger electron energy region, the result being $\eta \sim 1.6\pm0.1$. The values of the enhancement factor η for various projectile velocities measured are plotted in Fig.2, as a function of the effective impact parameter v/ω. Theoretical values calculated by Basbas and Ritchie[9] using the impact parameter method which allows for only vicinage effects are also shown in this figure. Figure 2 shows that the observed molecular effect for oxide alu-

minum is i) much larger than that predicted theoretically and ii) very large even when the criterion, $R<v/\omega$, for the appreciable vicinage effect, does not hold, because R is ~2 a.u.

The $L_{2,3}VV$ Auger spectra for the oxide free aluminum foil are shown in Fig.3. Several prominent features can be seen as compared with those for the oxidized aluminum foil: i) the $L_{2,3}VV$ Auger peak appears at 67 eV as compared with the value 52 eV observed for the oxidized aluminum foil, ii) the intensities of the peak are several to ten times larger than those for the oxidized foil, and finally to be the most striking, iii) no molecular effect is observed for the $L_{2,3}VV$ Auger peaks.

In order to estimate the bound electron effect, two kinds of measurements have been performed. Firstly, the electron spectrum of H^0 projectile [$I(H^0)$] has been measured under the same conditions. The contribution of the projectile bound electron to the electron spectra is estimated by plotting two kinds of difference spectra as a function of electron energy; (1) $I(H_2^+)-2I(H^+)$ and (2) $I(H^0)-I(H^+)$, as shown in Fig.4. The difference spectrum (1) clearly gives an Auger electron peak which may originate from the vicinage effects as well as the bound electron effect. On the other hand, the difference spectrum (2) does not show any trace of the Auger electron peak which may originate only from the bound electron effect if present. Secondly, the electron spectra for He^+ and He^{++} projectiles $I(He^+)$ and $I(He^{++})$ have been measured as shown in Fig.5. Like the difference spectrum for $I(H^0)-I(H^+)$, $I(He^+)-I(He^{++})$ also shows no trace of the Auger electron peak. The intensity difference of the continuum electrons for He^+ and He^{++} changes its sign at about 45 eV. The intensity enhancement for He^+ for higher energies corresponds to the electron loss process and that for He^{++} for lower energies may correspond to the charge screening effect for glancing collisions. From these results, we can conclude that the enhancement of Auger electrons for H_2^+ ions is mainly attributable to the vicinage effect, disregarding a minor difference of the property of the bound electron between H_2^+ and H^0.

In summary, we have obtained the following results:

i) The Al-$L_{2,3}VV$ Auger transition shows large molecular effect for oxidized aluminum foils but shows little molecular effect for oxide free foils.

ii) The Al-$L_{2,3}VV$ Auger intensities are several to ten times larger for oxide free foils than for oxide foils.

iii) Under the present experimental conditions, the contribution of projectile bound electrons to the Auger electron production is estimated to be unimportant.

iv) The interpretation of the above findings may be very complicated because Auger electron intensities depend both on the excitation process of the inner-shell in question and on the Auger decay process, and the molecular effect should be taken into consideration properly for both these two processes.

REFERENCES

1. W.Brandt, A.Ratkowski and R.H.Ritchie, "Energy loss of swift proton clusters in solids", *Phys.Rev.Lett.* 33,1325-1328 (1974).
2. M.J.Gaillard, J.C.Poizat, A.Ratkowski, J.Remillieux and M.Auzas, "Nonequilibrium effects in the proton neutral fraction emerging from solids bombarded with MeV H^0,H^+, H_2^+, and H_3^+ beams", *Phys.Rev.*A16, 2323-2335 (1977).
3. W.S.Bickel, "Molecular effects in beam-foil spectroscopy", *Phys.Rev.* A12, 1801-1807 (1975), B.Andersen, S.Hultberg, B.Jelenkovic, L.Liljeby S.Mannervik and E.Veje, "A study of molecular effects in beam-foil spectroscopy", *Physica Scripta* 19,335-338 (1979), G.Gabrielse, "Measurement of the n=2 density operator for hydrogen atoms produced by passing protons through thin carbon targets", *Phys.Rev.*A23,775-784 (1981).
4. N.Oda, F.Nishimura, Y.Yamazaki and S.Tsurubuchi, "Energy and angular spectra of electrons emitted from foils by ion beams", *Nucl.Instr.and Meth.*170,571-575 (1980).
5. K.Dettmann,K.G.Harrison and M.W.Lucas, "Charge exchange to the continuum for light ions in solids", *J.Phys.*B7,269-287 (1974).
6. F.Chen, R.Laubert and W.Brandt, "Al K x-ray yields with proton clusters", *Phys.Rev.*A15,2227-2229 (1977).
7. A.Lurio, H.H.Andersen and L.C.Feldman, "Search for cluster effects in x-ray production by fast hydrogen molecules", *Phys.Rev.*A17,90-92 (1978)
8. Y.Yamazaki and N.Oda, "Inner shell ionization by molecular ion bombardment on solid foils", *Nucl.Instr.and Meth.* (to be published).
9. G.J.Basbas and R.H.Ritchie, private communication.

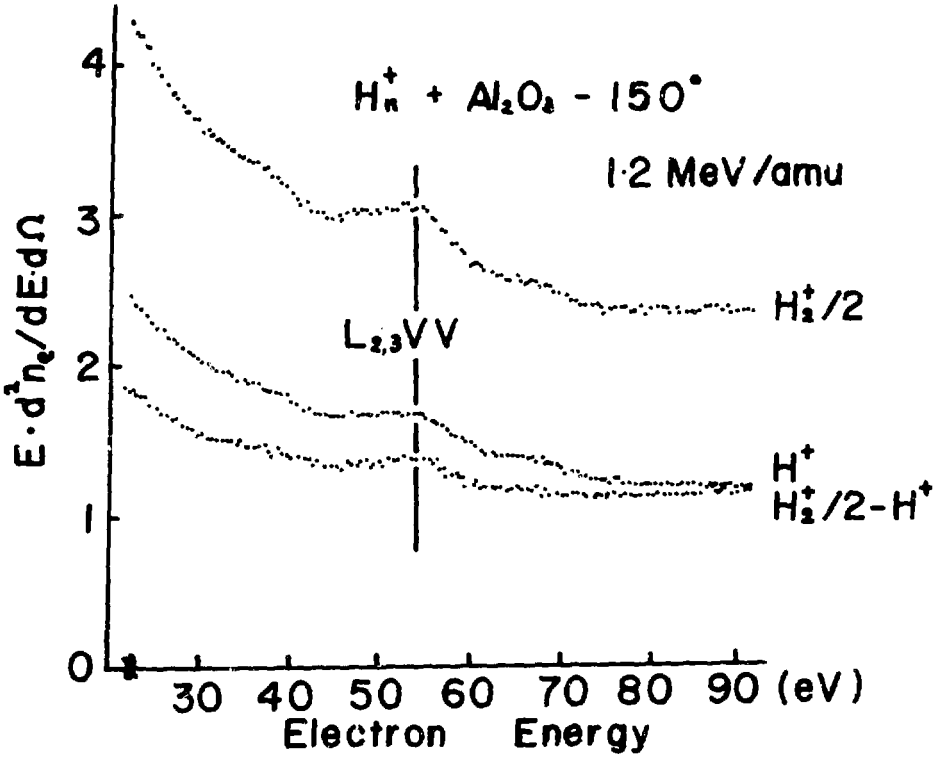

Fig.1 Differential electron spectra $d^2n_e/dEd\Omega$ multiplied by electron energy E as a function of electron energy, measured at 150° with respect to 1.2 MeV/amu H^+ and H_2^+ ion beams incident on an oxidized aluminum foil, together with a difference spectrum $I(H_2^+)/2-I(H^+)$. Spectra are normalized to the number of protons.

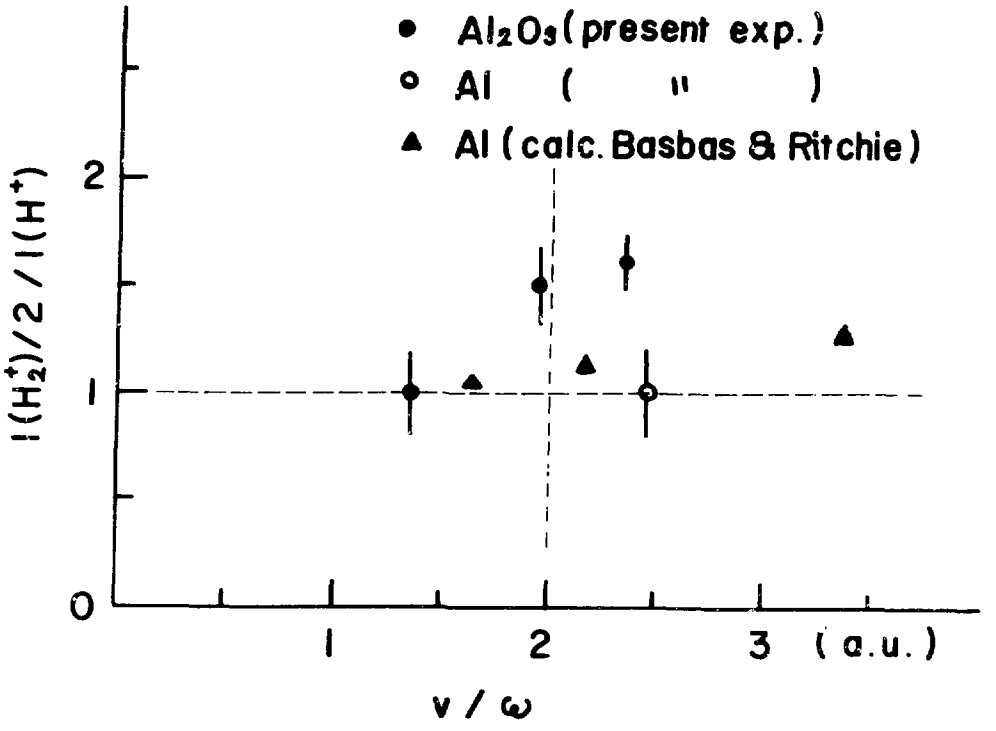

Fig.2 The enhancement factor $\eta = (I(H_2^+)/2)/I(H^+)$ for $L_{2,3}VV$ Auger electrons measured at 150° as a function of effective impact parameter v/w for both oxidized and oxide free aluminum foils. Theoretical values of η are also shown in the figure (Ref.9).

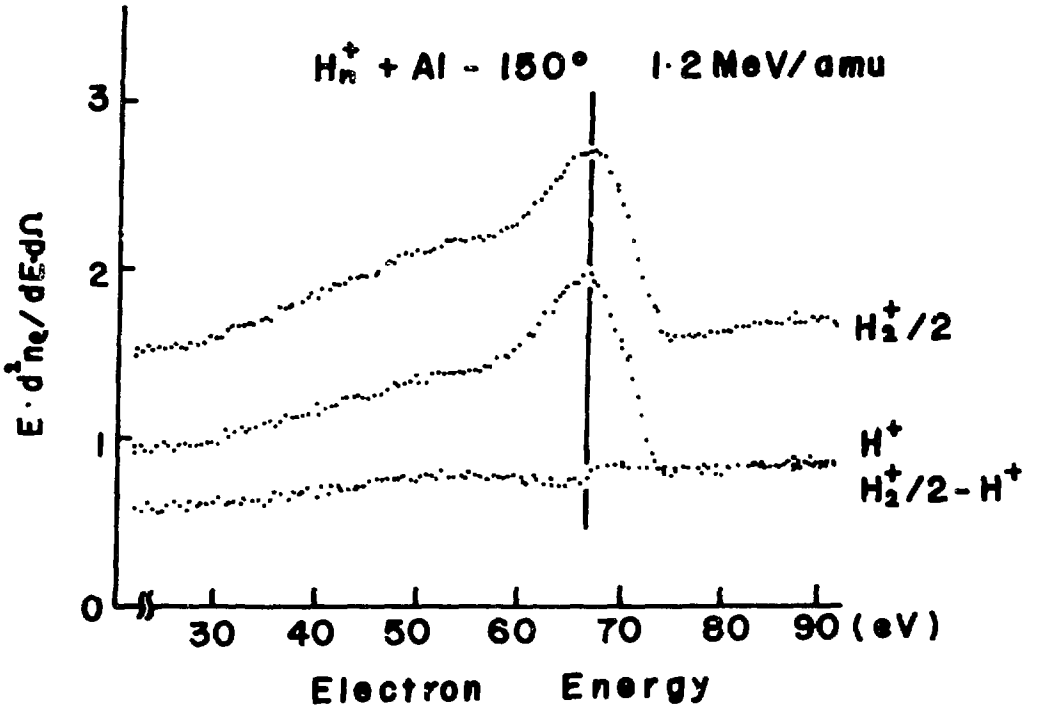

Fig.3 Differential electron spectra $E\, d^2n_e/dEd\Omega$, normalized to the number of protons measured at 150° with respect to 1.2 MeV/amu H^+ and H_2^+ ion beams incident on an oxide free aluminum foil together with a difference spectrum $I(H_2^+)/2-I(H^+)$.

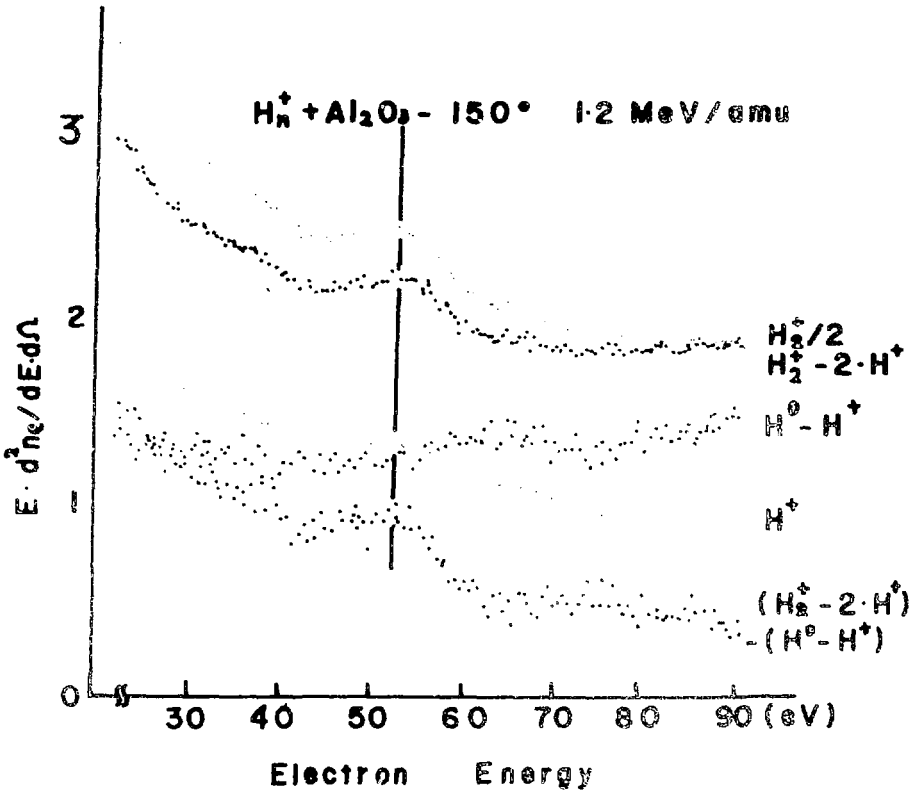

Fig.4 Difference spectra for differential electron spectra $E\, d^2n_e/dEd\Omega$, $I(H_2^+)-2I(H^+)$, $I(H^0)-I(H^+)$ and $[I(H_2^+)-2I(H^+)]-[I(H^0)-I(H^+)]$ measured at 150° with respect to 1.2 MeV/amu ion beams incident on an oxidized aluminum foil.

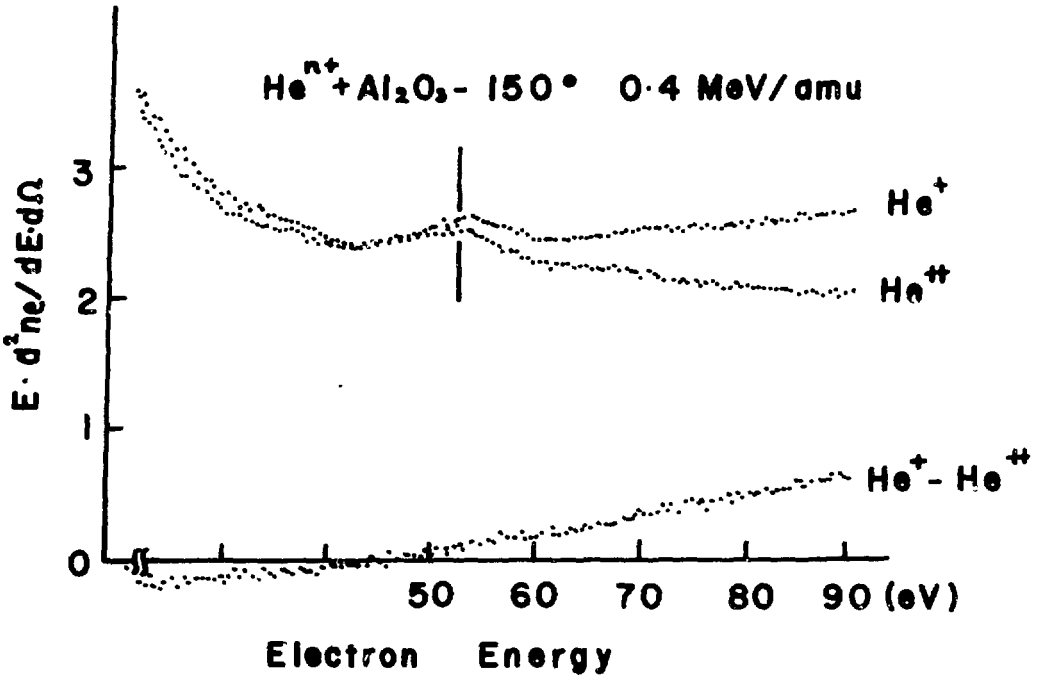

Fig.5 Differential electron spectra $E\, d^2n_e/dEd\Omega$ normalixed to the number of helium measured at 150° with respect to 0.4 MeV/amu He^+ and He^{++} ion beams incident on an oxidized aluminum foil, together with a difference spectrum $I(He^+)-I(He^{++})$.

Molecular Structure Measurements of Swift Complex Ions Traversing Thin Carbon Foils*

H.E. Wegner
Physics Department, Brookhaven National Laboratory
Upton, New York 11973 - U.S.A.

Introduction

Various preliminary results of Coulomb explosion studies have been reported at previous meetings of this group[1,2], as well as a new detector system[3] developed for these studies. This paper will report on the final data and analysis of the Coulomb explosion of two molecular systems, $C_3^{+,o,-}$ and $NCO^{+,o,-}$, each measured in the positive, neutral and negative charge state.[4] In addition, a new measurement has been made with the CH_2^+ ion and preliminary results will be reported. My collaborators in these measurements are P. Thieberger, Brookhaven National Laboratory and G. Goldring, Weizmann Institute.

All of these complex molecules are produced as negative ions by either a sputtering process with solid materials (30 kV Cs^+ ions on KCNO or C), or from a plasma by off-axis direct extraction of a duoplasmatron (operated with mixtures of H_2,NH_3 and CO_2). The extracted negative ions are then accelerated to MeV energies and studied directly or converted to neutral or positive charged molecules by charge exchange collisions with residual gas molecules in the vacuum of the beam transport system. These two completely different negative ion production systems apparently produced ions that are experimentally identical in terms of information gained from Coulomb explosion measurements, probably because they may all be at very high temperatures and close to the dissociation limit. Analysis of the three $C_3^{+,o,-}$ species showed them all to have the same internuclear separation found in normal neutral C_3; 2.5(a)Å, and similarly for the three $NCO^{+,o,-}$ species, except that the separation was rather small; 2.0(1)Å.

Preliminary analysis of the CH_2^+ data indicates that the best fit included angle, α_i, between the two hydrogen atoms is $122^o(3)$ with an average absolute deviation angle from equilibrium, $\Delta\alpha_i$, of $23^o(2)$ for a

*This work was entirely supported by the U. S. Department of Energy under contract No. DE-AC02-76CH00016.

molecular model with linear uniform oscillation, and $\alpha_i = 126^o(3)$, $\Delta\alpha_i = 19^o(2)$, for a model with simple harmonic oscillation. These preliminary values compare well with the measured value of 115^o for neutral CH_2. However, the large amplitude of oscillation may infer a high temperature similar to other molecular systems that have been previously studied.

A new cluster effect observed for all the Coulomb explosion measurements that could be due to wake effects of the highly correlated atoms of the penetrating molecular cluster, is that the multiple scattering of the centroid of the molecule is considerably larger than what would be expected in terms of direct measurements of the multiple scattering of the component single ions at the same velocities. So far, no detailed theoretical interpretation or evaluation of these presumed wake effects has been made.

Experimental Procedure

The experimental method has been described in detail elsewhere.[3] However, it will be briefly reviewed, especially for those seminar participants not familiar with such measurements. The accelerated molecular ions are collimated into a beam with a diameter of approximately 1/4 mm and an angular spread of .01 degrees. This beam of molecular ions then impinges on a 1 $\mu g/cm^2$ self-supporting foil on a 3 mm diameter holder as shown in Fig. 1. The flight path of 60 cm from the stripping foil where the Coulomb explosion takes place, to the detector, is of sufficient distance so that the Coulomb explosion separates the particles adequately for good spacial resolution in the detector.

The experimental requirement of detecting simultaneous multiple low energy heavy ions from the Coulomb explosion of accelerated molecules led to the detector in Fig. 1 which consists of a thin monolayer phosphor coating with particle size approximately 1 micron, applied uniformly on the input fiber optic plate of a commercially available image intensifier. The phosphor particles scintillate when struck by atomic ion constituents of the exploded molecule and these faint scintillations are amplified by the image intensifier whose output is viewed by a television camera. The television image is then digitized and the pixels containing useful in-

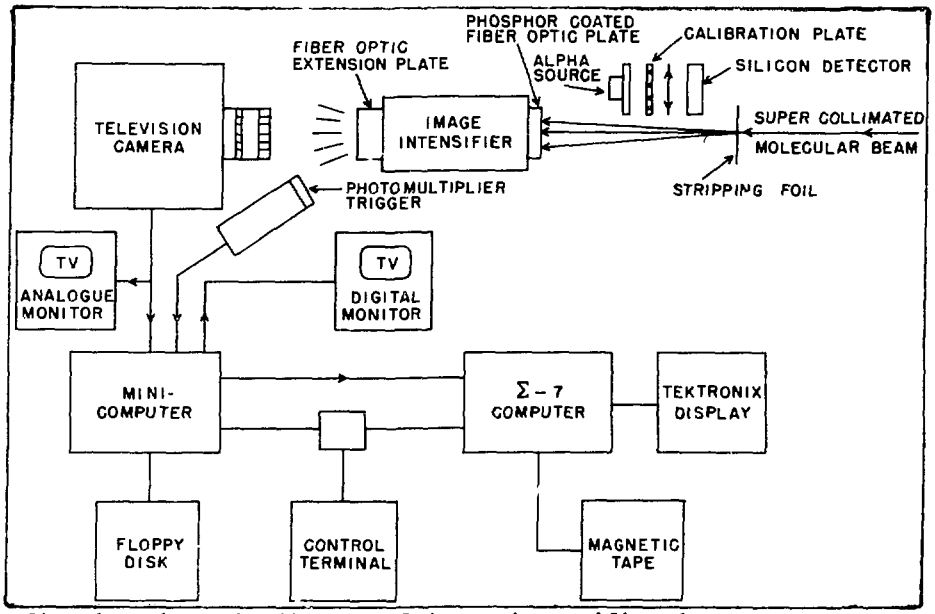

Fig. 1 Schematic diagram of image intensifier detector system and television readout and digitizing system (see text).

formation are stored for later analysis. The digitized events are stored on a floppy disk and subsequently transferred to a Sigma 7 computer where they can be analyzed and sorted into whatever parameters are desirable for comparisons to theoretical simulations of Coulomb explosions.

These digitized events can be conveniently displayed and printouts of such events from a Tektronix display terminal are shown in Fig. 2 for Coulomb exploded 4.67 MeV C_3^- ions. The different shaped points on some of the triangle events in the figure have to do with the fact that the light intensity varies

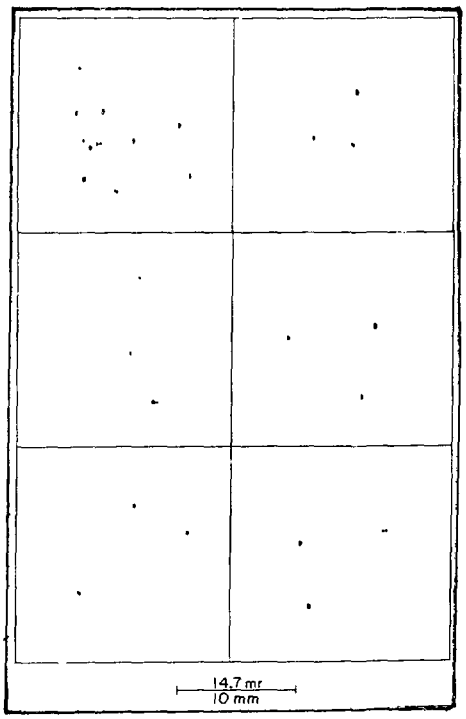

Fig. 2 Typical C_3^- Coulomb explosion data as plotted from Tektronix display.

strongly from point to point depending on just where the heavy ion strikes the phosphor grain and where it, in turn, is located in respect to the fiber optic microstructure of the entrance plate. The event in the upper lefthand part of the figure shows the situation in which multiple C_3 ions came through the system instead of one at a time which is the desirable intensity. Unfortunately, the beam intensity cannot be controlled at all times and occasionally, bursts of particles come through forming such multiple event pictures. However, the computer analysis system easily rejects such events and can be arranged to select specific three-particle events independent of any other kind that may be digitized.

Figure 3 shows the same kind of Tektronix plots corresponding to the Coulomb explosion of accelerated $C^-_{4,5,6}$ ions that were observed mostly out of curiosity and no analysis has been undertaken. In each case, approximately 100 events were recorded and of the 100, some select patterns bearing some casual resemblance from one system to another were selected for visual comparison and general interest.

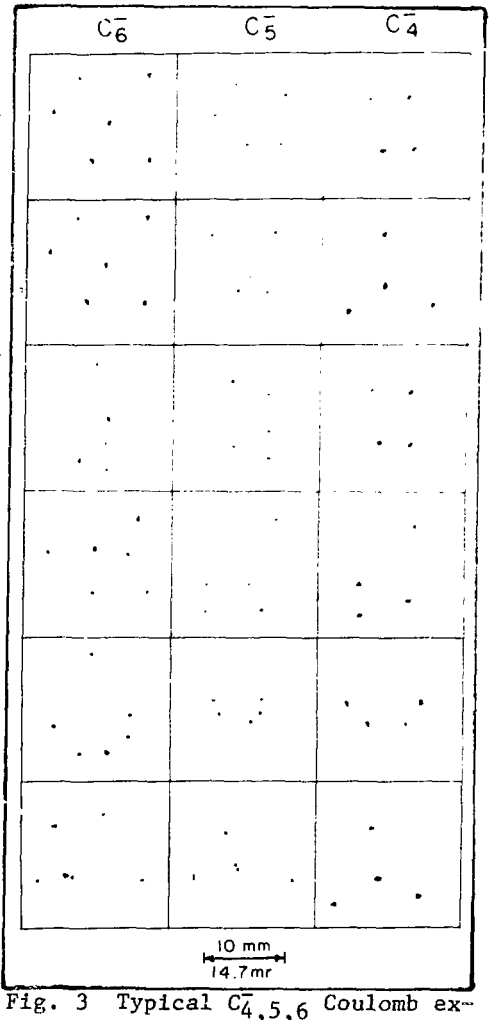

Fig. 3 Typical $C^-_{4,5,6}$ Coulomb explosion data as plotted from a Tektronix display.

Coulomb Explosion Studies of 4 MeV $NCO^{+,o,-}$ and 4.67 MeV $C_3^{+,o,-}$ Ions

The Coulomb explosion events of the triatomic molecules analyzed in these measurements require three parameters for a complete characterization, e.g. the three sides of the triangle formed by the three projections of the momenta of the three atomic ions onto the plane perpen-

dicula. to the beam. For the sake of simplicity of display and analysis, these have been reduced to two, as shown in Fig. 4: the largest side, ℓ, and the ratio R=d/ℓ, where d is the altitude to the side ℓ, integrating over the asymmetry parameter, δ/ℓ, considered to be the least significant parameter for structure characterization.

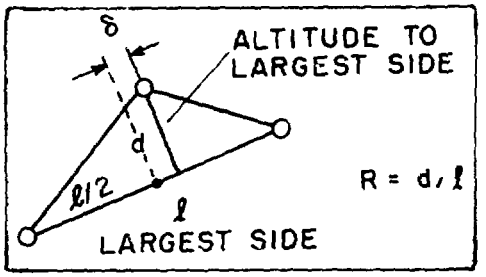

Fig. 4 Triangle parameters for a triatomic Coulomb explosion event.

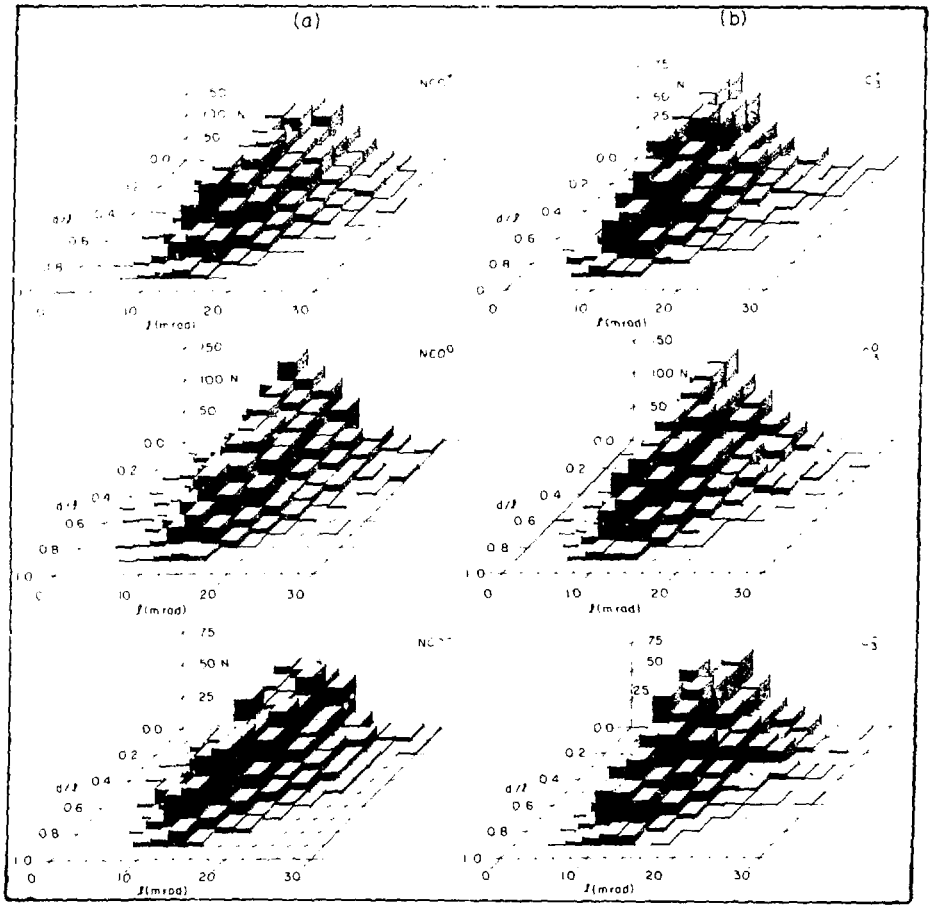

Fig. 5 Experimental distributions of Coulomb explosion events: a) ℓ vs. d/ℓ for 4.00 MeV $NCO^{+,0,-}$ ions; b) ℓ vs. d/ℓ for 4.67 MeV $C_3^{+,0,-}$ ions.

Two dimensional sorts of the ratio d/ℓ vs. ℓ, for the Coulomb explosion of (+,o,-) 4 MeV NCO molecules are shown in Fig. 5a, and similarly for 4.67 MeV C_3 molecules, in Fig. 5b. The distributions for the three different charge states for each of the molecular systems are very similar, as indicated. The shapes of the NCO distributions are also similar to the C_3 distributions; however, the NCO distributions have a mean ℓ value, approximately 2 mrad larger than that of the C_3. All of the data extend out to the d/ℓ limit of 0.866, corresponding to an equilateral triangle shape. A more detailed comparison of the two dimensional plots of the different molecules can be made by projecting all the data onto either the ℓ or the d/ℓ axis. The ℓ distributions relate most closely to the size of the molecular ion, whereas the d/ℓ distributions are more associated with the molecular shape.

Projections of the data shown in Figs. 5a and 5b onto the ℓ axis are shown in Figs. 6a and 6b, respectively. These projections, which are area normalized for comparison, show again and more clearly, that the mean of the NCO and C_3 distributions differ by about 2 mrs, and that the relative width of the NCO distribution is also somewhat larger than that of the C_3 distribution. The distributions of the $NCO^{+,o,-}$ ions are very similar; however, C_3^- appears to have a mean ℓ larger than C_3^o and C_3^+ by 0.2 or 0.3 mrs. The solid line curves are theoretical fits to the data and will be discussed later.

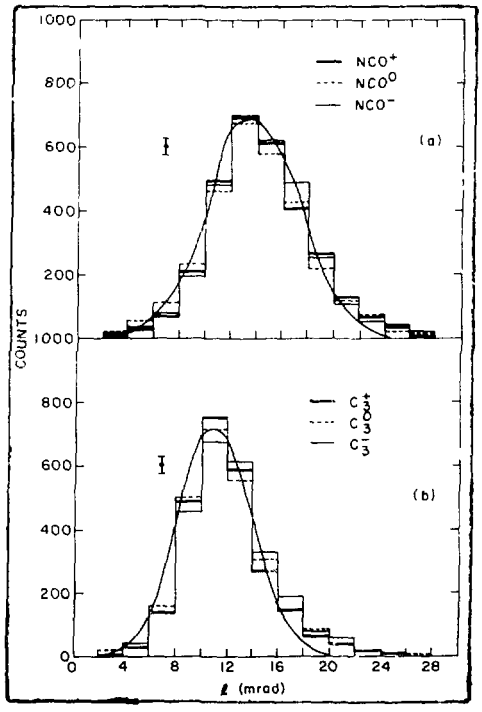

Fig. 6 Projections onto the ℓ axis of the two dimensional distributions shown in Figs. 12a and 12b. The isolated points indicate the statistical accuracy of the bars on the histogram.

Projections onto the d/ℓ axis of the two sets of data of Figs. 5a and 5b are compared in Figs. 7a and

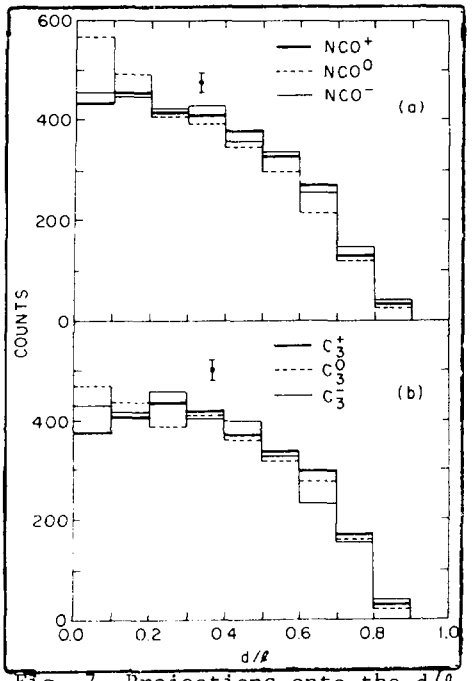

Fig. 7 Projections onto the d/ℓ axis of the two dimensional distributions shows in Figs. 12a and 12b. The isolated points indicate the statistical accuracy of the bars on the histogram. The curves through the histogram correspond to theoretical fits.

7b. These projections show that there is little difference in the d/ℓ distribution between the three charge states of either of the triatomic systems, and there is also no significant difference between the two different triatomic systems. It is interesting to note that the NCO^0 distribution shows a trend for modest peaking at small d/ℓ rat os compared to the $NCO^{+,-}$ distribution and this trend is also noticeable in the isometric display of Fig. 5a.

For the sake of comparison with model calculations, the data have been reduced in yet one more way. The shape distributions, the d/ℓ projections, have been sorted according to the magnitude of ℓ and only 40% of the data pertaining to the largest ℓ, (the largest, largest sides) have been retained. This selection has the advantage that the largest projected triangles are less sensitive to the perturbations caused by multiple scattering and such triangles also largely exclude configurations in which two fragment ions are aligned along the beam direction or perpendicular to the projection plane which considerably reduces the significance of the wake effects.

As mentioned in the Introduction, a comparison was made of NCO^+ ions produced by two completely different kinds of ion sources and a comparison of the ℓ and 40% d/ℓ projections of these two respective NCO^+ ions are shown in Figs. 8a and 8b. In terms of both the size and shape projections, the two different produced NCO^+ molecules appear to be identical even though in one case they are produced by a sputtering process and in the other, extracted directly from the hot plasma of an arc discharge.

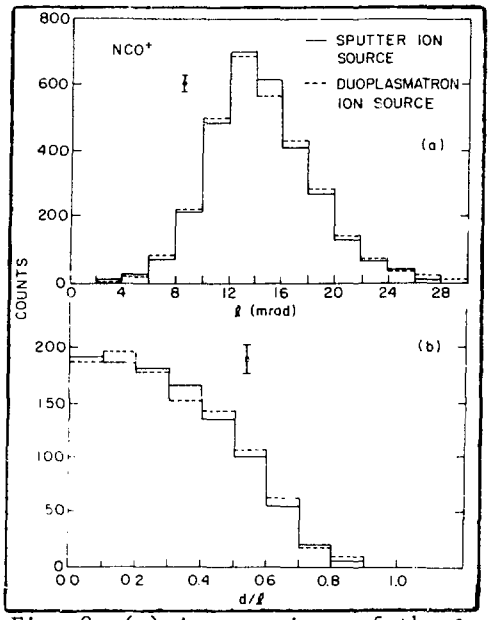

Fig. 8 (a) A comparison of the ℓ distributions corresponding to the Coulomb explosion of NCO^+ ions produced by a sputter and a duoplasmatron ion source.

(b) Comparisons of the d/ℓ distributions as in (a) but corresponding only to the 40% fraction of the largest triangles of the distribution.

The isolated points indicate the statistical accuracy of the bars on the histogram.

they are largely frozen at the time of extraction in terms of the transport time to the stripping foil where the Coulomb explosion occurs. In essence, these experiments take a snapshot of the molecule in whatever vibrational excitation state it happened to be in at the time of extraction from the source.

In order to compare these data with theoretical models, all of the various physical phenomena involved with the Coulomb explosion, as well as the excitation and oscillation of the initial molecule, and its random orientation in respect to the beam direction or the plane of the detector system have to be taken into account. All of these phenomena must be taken into account to generate a computer simulated distribution that can then be compared to the experimental data. The ion source extraction time and trarsport time through the accelerator to the stripping foil is of the order of microseconds, which means that all of the electronics states that might have been present at the time of creation of the molecule have essentially disappeared. The molecular states have time constants of milliseconds which means

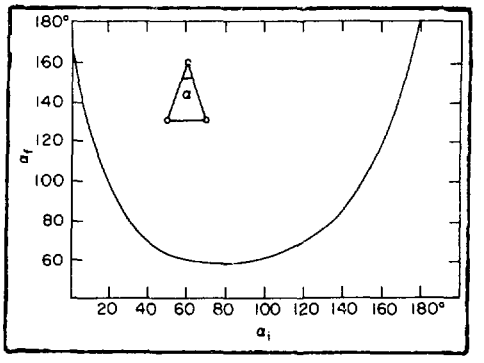

Fig. 9 Initial angle vs. final angle for a triatomic molecule bef re and after undergoing a Coulomb explosion.

The Coulomb explosion itself creates a considerable distortion in terms of the original configuration of the three atoms. Figure 9 shows this effect for an original triangular configuration with an included angle of α_i which is then transformed into a final angle, α_f, by the effects of the Coulomb explosion. Inspection of the figure shows that for any initial angles varying from approximately 40^o to 140^o, the final angle is 60^o or 70^o which means that all triangles either more acute or more obtuse than an equilateral triangle, tend to become equilateral triangles from the effects of the Coulomb explosion. This simple relationship is further confounded by the fact that each of the carbon ions may have different charge states since there is a probability distribution for the charge state varying from 1+ to 4+ at the energies encountered in these experiments. Since the charge state is not measured directly in these experiments, that variation in possible charge state has to be folded in to further confuse and mix up what might otherwise be a simple transformation.

Since the carbon ions are only of MeV energies, the 1 $\mu g/cm^2$ stripping foil introduces a modest amount of multiple Coulomb scattering which means that the trajectory of the carbon ion from the point of Coulomb explosion is perturbed in its absolute direction by a random scattering process which means that the triangle shape is somewhat smeared or blurred in some complex way by this phenomena. Wake effects also play some role in distorting the Coulomb explosion further; however, there has been no attempt to include wake effects in the model comparison. All of these phenomena can be folded together and the result compared in order to see which parameters may be most sensitive in determining the shape and structure of the original molecule in terms of the experimental data measured here.

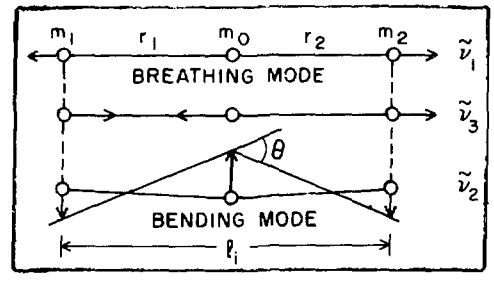

Fig. 10 Bending and breathing modes of vibration for a rod-like triatomic molecule.

The NCO molecule is considered to be a relatively rigid rod-like structure which has a principal mode of oscillation in the form of a

bending mode as illustrated in Fig. 10. Predictions of this model generate different ℓ vs. d/ℓ plots for different n values as shown in Fig. 11. For n=0, or low excitation, the distribution is strongly peaked at small d/ℓ values corresponding to the molecular structure being three atoms, close to a straight line. However, for higher excitation, like n=6, the distribution is still peaked at small d/ℓ values, but extends all the way out to the equilateral triangle limit with a relatively complex shape and distribution of events over the ℓ vs. d/ℓ map. In fact, the n=6 distribution bears a modest resemblance to the experimentally observed data.

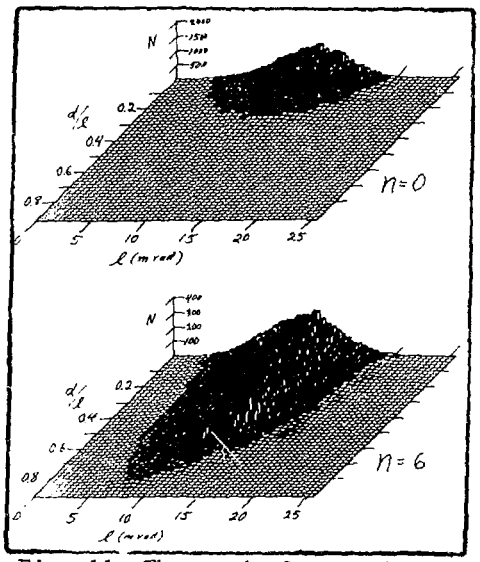

Fig. 11 Theoretical calculations corresponding to a rod-like C_3 molecule vibrating in a bending mode and undergoing a Coulomb explosion a) lowest order vibration, N=0 b) N=6.

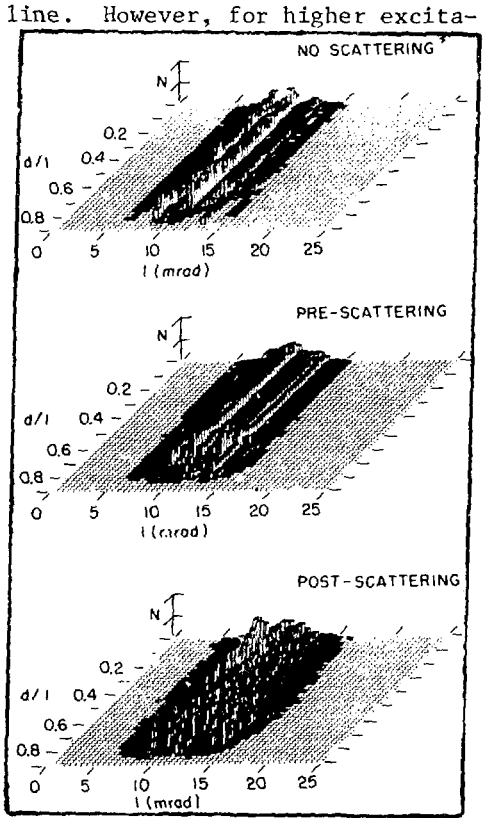

Fig. 12 Theoretical calculations corresponding to a triangular C_3 molecule undergoing a Coulomb explosion a) without multiple scattering b) with multiple scattering before the Coulomb explosion c) with multiple scattering after the Coulomb explosion.

An initial triangle-like structure can also be calculated for comparison and the results of this calculation are shown in Fig. 12. The upper figure is for the situation without any multiple scattering and shows a distribution quite different from

what was observed for the oscillating rod-like structure. Here, the distribution is quite uniform along the d/ℓ axis and a series of ridges appear which correspond to the different charge state possibilities between the three different Coulomb exploding atoms. The multiple scattering can be included in the calculation in two different ways, both of which are extreme approximations and are shown in the other two portions of Fig. 12 for the so-called pre-scattering and post-scattering cases where the multiple scattering either occurs before or after the Coulomb explosion, respectively. The real situation is somewhere between these two extremes; however, all of the theoretical calculations presented here assume post-scattering which is the most extreme in terms of mixing up and perturbing the basic trajectories produced by all the other phenomena of the Coulomb explosion. A comparison of Figs. 11 and 12 indicates that the post-scattering distribution of Fig. 12 is quite similar to the n=6 post-scattering distribution of Fig. 11 and that even with good statistics it could be very difficult to differentiate between an initial triangular-like or floppy-rod structure.

Preliminary calculations have indicated that Coulomb explosion events consisting only of atoms all of the same charge state might show a definite differentiation between an oscillating rod and triangular-like structure. A modification of the present experimental apparatus so that different charged particle groups can be completely separated with a small permanent magnet analysis system, has been tested and preliminary measurements indicate that Coulomb explosion events of different charge states can be completely separated. Consequently, in the future, data corresponding to all of the carbon ions having charge 3+ or 2+ or whatever charge desired can be selected, and these different charge state explosion events can then be compared to each other and to theoretical calculations which may hopefully better differentiate between the triangle and oscillating rod-like structure.

A comparison of the projections onto the d/ℓ axis for Figs. 5a and 5b, representing 40% of the data of the largest triangles, is shown in Fig. 13. For the $NCO^{+,o,-}$ projections, the n=7 or some combination of the n=3 to 11 distributions combine to look very much like the shape of

the d/ℓ distribution except for the small d/ℓ region where a strong peaking is observed theoretically but not experimentally. Similarly, for the $C_3^{+,o,-}$ distributions, a lower combination of n values, varying from 1 to 6, approximate the experimental data quite well, except again in the vicinity of small d/ℓ values where a st ong theoretical peaking is observed but not experimentally.

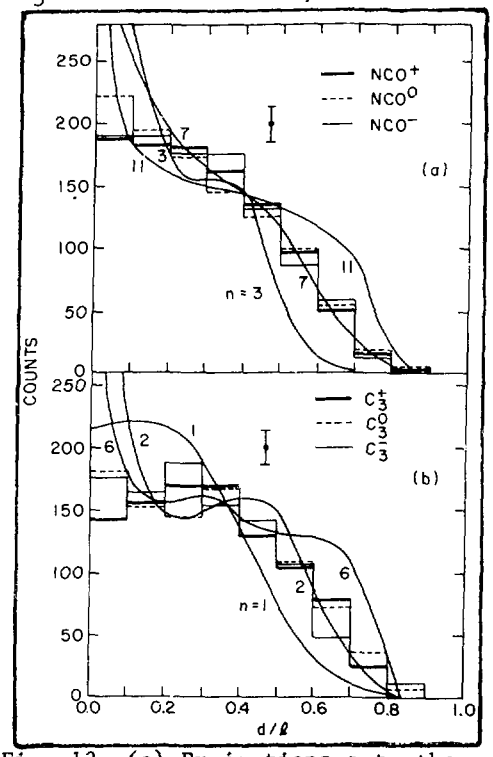

Fig. 13 (a) Projections onto the d/ℓ axis of the two dimensional distributions shown in Fig. 12a corresponding to the 40% fraction of the largest triangles of the distribution.

(b) Projections onto the d/ℓ axis of the two dimensional data of Fig. 12b corresponding to the 40% fraction of the largest triangles.

The isolated points indicate the statistical accuracy of the bars on the histogram, and the theoretical curves correspond to different calculated models of the molecular structures involved (see text). The n values refer to bending vibrational excitation.

The absence of the small d/ℓ peaking in the experimental data with the possible exception of the NCO neutral distribution which does show a small amount of peaking in small d/ℓ values, can be understood in terms of these molecules being produced at very high temperature. If the distribution of

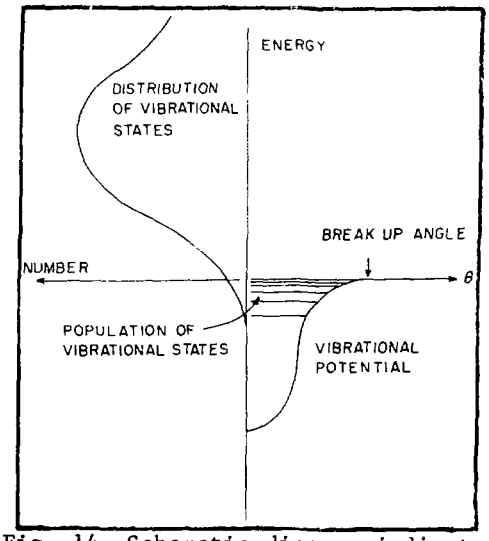

Fig. 14 Schematic diagram indicating a possible situation in which linear molecular ions would be formed in bending vibrational states close to the breakup point and assume bent configurations all the way up to the limit where they break up.

the vibrational states is as shown on Fig. 14, with all the vibrational states at extremely high amplitude, then most of the molecules break up except for a very small tail at the low energy end of the distribution. This can be compared to a vibrational potential plotted in terms of the angle of oscillation with some hypothetical breakup angle which in these measurements would correspond to approximately 40^{o}. This means then that all those molecules with higher amplitude vibration than this critical breakup angle simply disappear, while the few left at the lower energy end of the distribution have high n values, and there is an absence of low n values because of the high temperature. This model then would account for the absence of low n values and allow for an experimental distribution of only high n value. The almost complete absence of any experimental peaking corresponding to low d/ℓ values as predicted by the model could be due to the anharmonicity of the oscillation which could be extreme at high temperature.

The final conclusions of these measurements and this analysis are that the molecules are probably produced and measured in very high states of excitation and that the intranuclear separation for the C_3 species are found to have the separations found in normal neutral C_3; 2.5(1)Å and for NCO the separation was rather small; 2.0(1)Å.

Coulomb Explosion Studies with 12.656 MeV CH_2^+ Ions

Coulomb explosion studies were undertaken for 12.656 MeV CH_2^+ ions in order to see what structure information could be gained from this much more simple system. The two hydrogen atoms in CH_2 become single charged protons in the Coulomb explosion, and have only 1/12 the energy of the resulting carbon ion. This means that their scintillations are much less intense and can always be uniquely identified when compared to the ~10 MeV carbon ions. In addition, the recoil energy from the Coulomb explosion transferred to the carbon ion by the two protons is relatively small so that the carbon ion is always close to the beam position. Typical CH_2^+ explosion events are shown in Fig. 15, similar to previous events shown in Figs. 2 and 3, except in this case the computer has drawn in a line between the centroids of each of the three scintillations. In each event

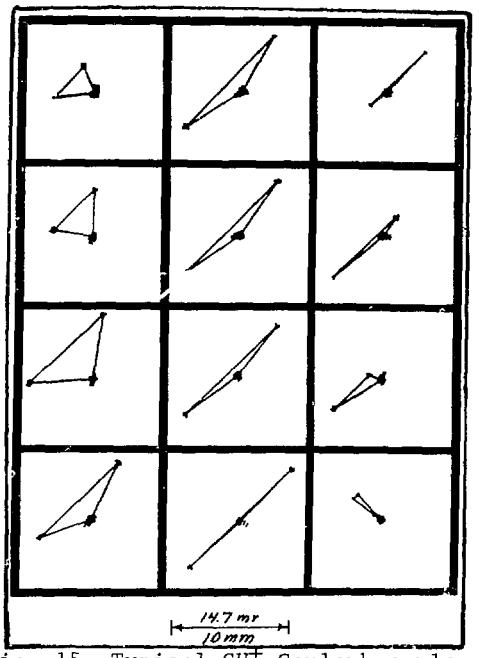

Fig. 15 Typical CH_2^+ Coulomb explosion data as plotted from a Tektronix display. The computer drawn vectors connect the centroids of the three events.

the large blobs near the center of each picture are the carbon ions and the lighter smaller blobs represent the protons. This representative sample shows the large variety of triangles that are observed in this study of the CH_2^+ system.

The bending vibrational modes of CH_2 and the angles and coordinates designating this vibration are shown in

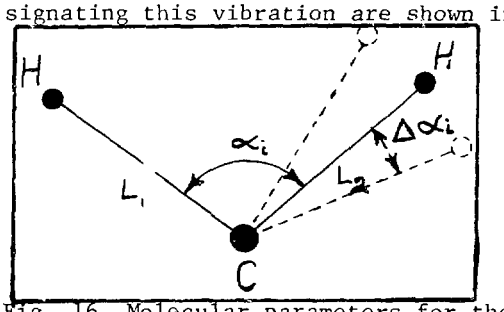

Fig. 16 Molecular parameters for the initial conditions of the CH_2^+ molecule before the Coulomb explosion.

Fig. 16. The radial distance from the carbon to the two hydrogen atoms is designated as L_1 and L_2. This included angle between these two radii before the Coulomb explosion is α_i, while the average absolute deviation angle from equilibrium is $\Delta\alpha_i$.

The triangle data were sorted in terms of different parameters from those used with the heavier triatomic molecular systems. Two sorts were carried out as a function of α_f, the angle between the two proton lines after the Coulomb explosion. The ratio L_1/L_2 vs. α_f, and the average L, or $(L_1+L_2)/2$ vs. α_f. The results of these two sorts of the experimental data are shown in Figs. 17 and 18, respectively. In order to get some feeling for what this kind of sort means in terms of an initial CH_2^+ structure, two simple models were calculated. These calculations assumed an initial molecule with no bending oscillation of any kind and two frozen extreme angles; an acute angle of 33° and an obtuse angle of 147° between the hydrogen atoms. The calculation did allow for the charge state dis-

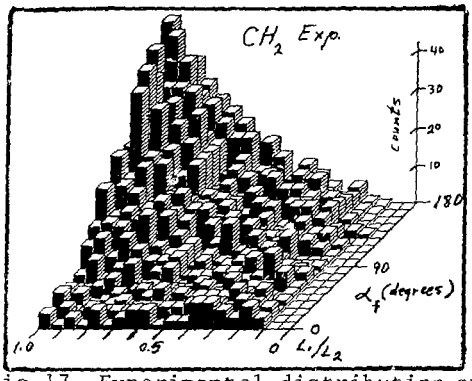

Fig.17 Experimental distribution of 12.656 MeV CH_2^+ Coulomb explosion events: α_f vs. L_1/L_2 (see Fig. 16).

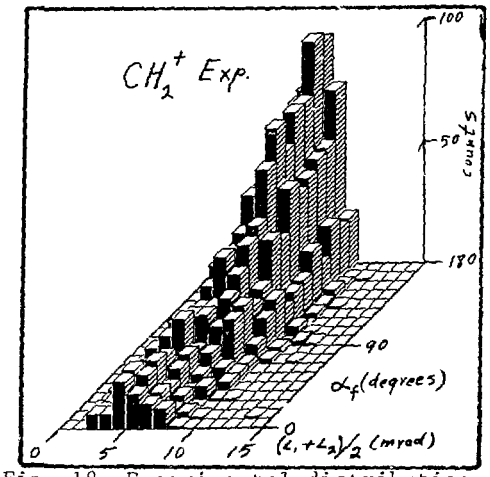

Fig. 18 Experimental distribution of 12.656 MeV CH_2^+ Coulomb explosion events: α_f vs. $(L_1+L_2)/2$ (see Fig. 16).

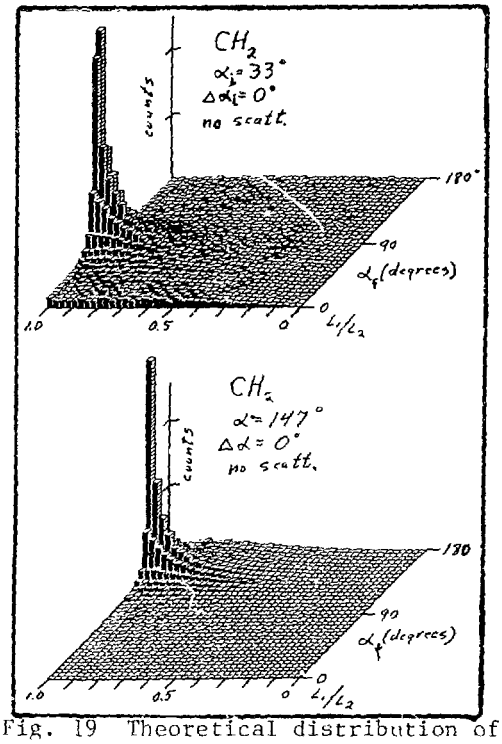

Fig. 19 Theoretical distribution of α_f vs. L_1/L_2 for Coulomb exploded 12.656 MeV CH_2 molecules with rigid acute and obtuse included angles between the two hydrogen atoms; no multiple scattering.

tribution of the carbon ion; however, it did not include any multiple scattering. The results of these two calculations are shown in Figs. 19 and 20. The effect of these two extreme angles for the initial conditions of the molecule, and subsequently going through Coulomb explosion, indicates what might be expected in terms of a real molecule that is oscillating with some amplitude around some average angle. From these extreme conditions it can be seen that the real molecule should generate a superposition of these peak-like structures, smeared out to some degree by multiple Coulomb scattering effects.

The final model included the measured charge state distribution of the carbon ions along with multiple scattering. A search was then made

for the best fit to the $(L_1+L_2)/2$ vs. α_f distribution using a least squares criteria of fit for an optimum α_i and $\Delta\alpha_i$. The best fit for two different CH_2 models compared to experiment is shown in Fig. 21 for the $(L_1+L_2)/2$ vs. α_f distribution. Inspection of the figure indicates

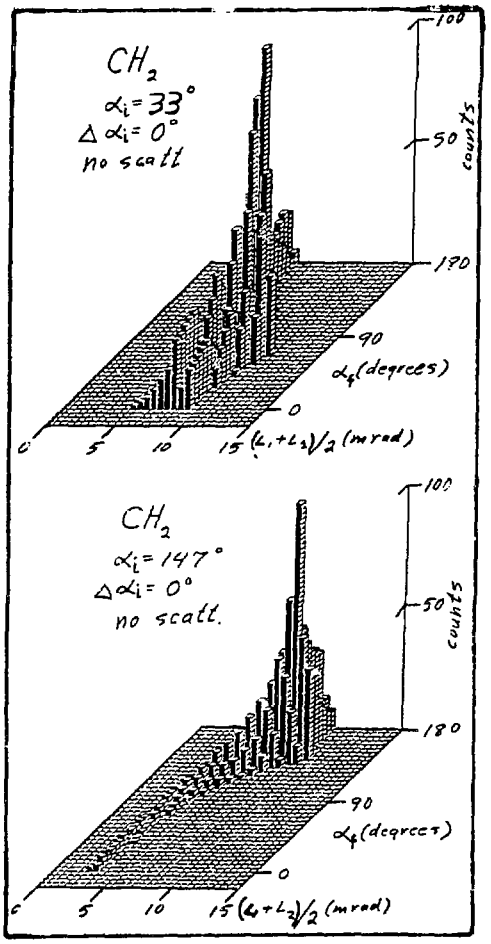

Fig. 20 Theoretical distributions of α_f vs. $(L_1+L_2)/2$ for Coulomb exploded 12.656 MeV CH_2 molecules with rigid acute and obtuse included angles between the two hydrogen atoms; no multiple scattering.

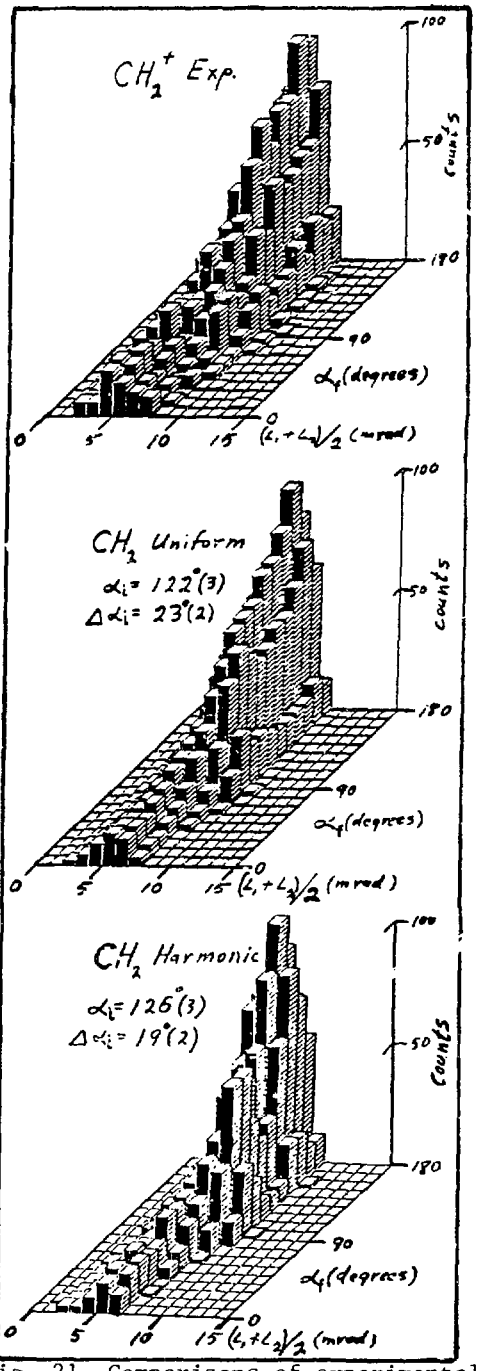

Fig. 21 Comparisons of experimental and best fit theoretical distributions of α_f vs. $(L_1+L_2)/2$.

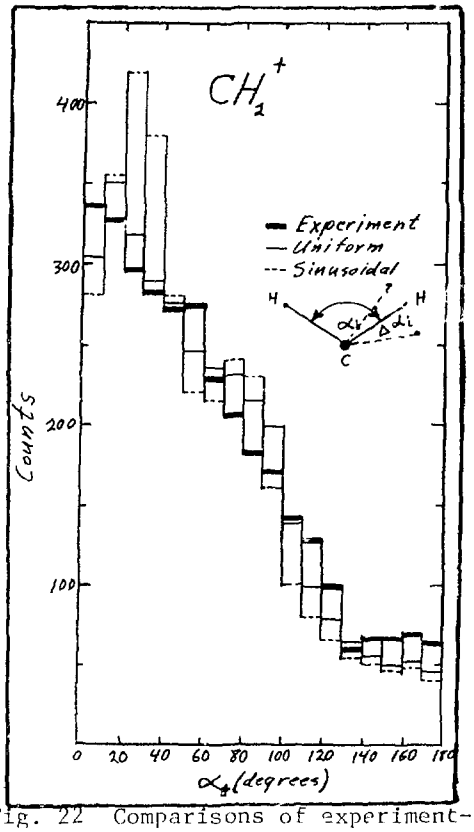

Fig. 22 Comparisons of experimental and best fit theoretical projections onto the α_f axis.

that the best fits for two different models bear a remarkable resemblance to the experimentally observed distribution. In one case, for a uniform or linear oscillation of hydrogen, the best fit corresponded to $\alpha_i = 122^o(3)$ and $\Delta\alpha_i = 23^o(2)$. For a simple harmonic oscillation the best fit corresponded to $\alpha_i = 126^o(3)$ and $\Delta\alpha_i = 19^o(2)$ which compares favorably with the experimentally, spectroscopically measured value of neutral CH_2 of $\alpha_i = 122^o$. Projections of these two dimensional distributions onto the α_f axis are shown in Fig. 22 which illustrates the systematic differences between the theoretical fits and the experimental data. In this case, the uniform linear oscillation appears to fit the data better than the sinusoidal model. However, both linear and sinusoidal seem to show a peaking characteritic not observed in the experimental data which is relatively smooth.

Some of the differences between the model predictions and data can be made more obvious in terms of the L_1/L_2 vs. α_f distributions and such comparisons are shown in Fig. 23. This comparison shows that the L_1/L_2 distributions are considerably different from the experimental in the sense that the experimental data maintains amplitude well out onto the plane of the figure and shows none of the peaking characteristics observed in the uniform and harmonic models. It must be emphasized that all of these data and analyses are preliminary and the CH_2^+ system is still under intensive study and consideration. Other models of the system may also be tried as well as different parameter sorts of the data than those presented here.

Since the energy of the CH_2^+ ion is considerably higher than any of the complex molecules previously studied, there was some question as to what the charge state distribution of the carbon ions would be, considering the fact that the 1 $\mu g/cm^2$ Coulomb explosion foil is considerably thinner than the equilibrium charge thickness for carbon ions of this energy which is about 6 $\mu g/cm^2$. Relatively minor modifications of the equipment allowed the charge separation of the outgoing carbon ions magnetically. A small permanent magnet analyzing system was arranged so that all of the charge states could be displayed simultaneously on the image intensifier face plate. With this arrangement, the CH_2^+ ions could be passed through the foil, Coulomb exploded, and the carbon ions collected in relative intensities corresponding to the charge state distributions. The accelerator could then be readjusted to provide C^+ ions of the same velocity, or 10.848 MeV energy, and passed through the same foil to provide a distribution of carbon ions without the associated hydrogen atoms of the CH_2^+ molecule and their possible wake effects. A comparison of these two

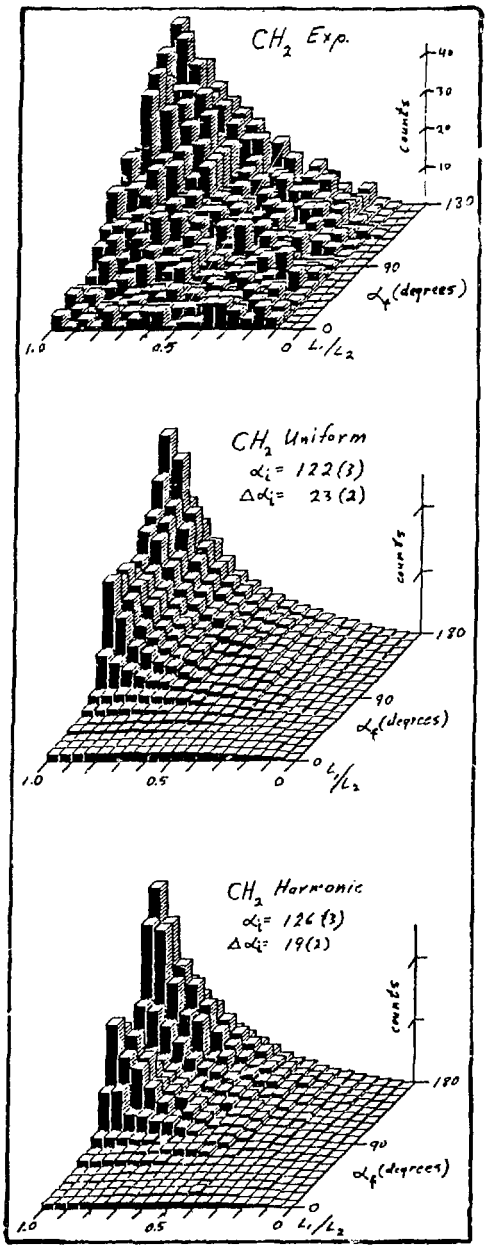

Fig. 23 Comparison of experimental and best fit theoretical distributions of α_f vs. L_1/L_2.

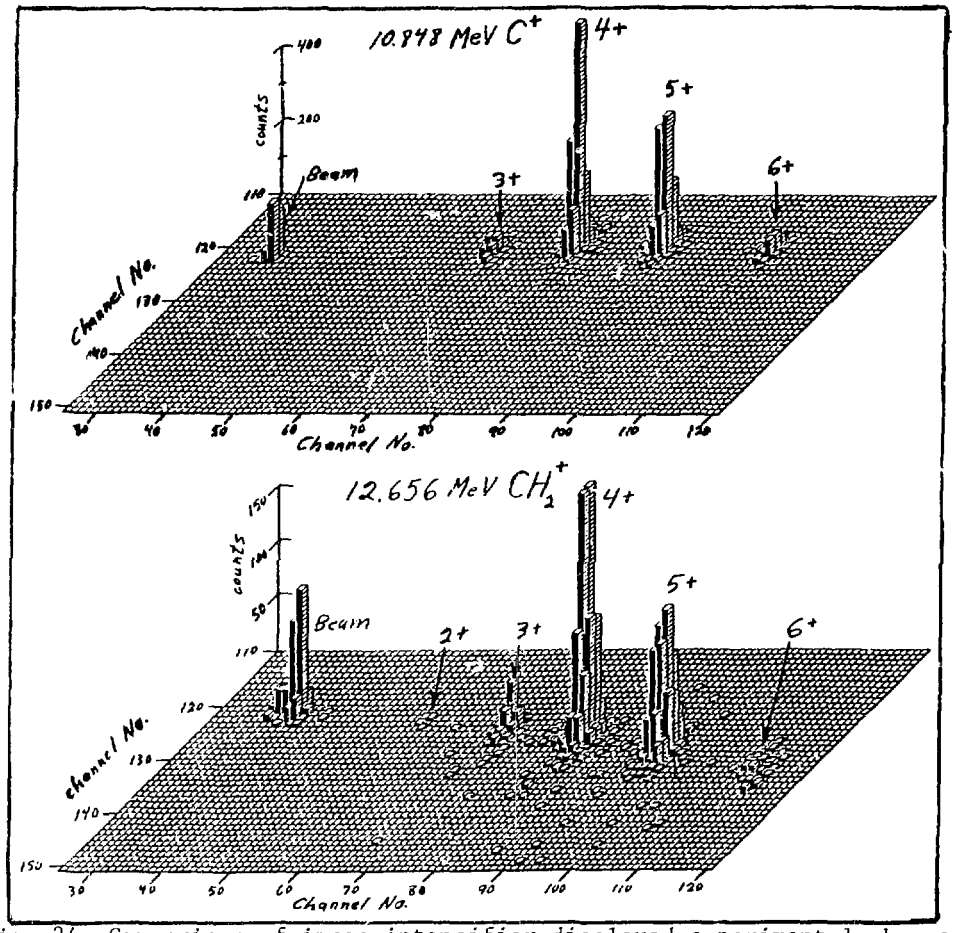

Fig. 24 Comparison of image intensifier displayed experimental charge distributions for carbon ions from 10.898 MeV C^+ ions and 12.656 MeV CH_2^+ ions after penetrating a 1 $\mu g/cm^2$ carbon foil.

distributions as observed with the image intensifier system is shown in Fig. 24. Somewhat to our surprise, the charge distribution was essentially at equilibrium for this energy even though the stripping foil is much thinner than one would expect to be necessary to attain an equilibrium charge state. It was also found that the charge state distributions are almost identical whether the fast moving carbon ion is or is not associated with two hydrogen atoms.

The two dimensional data of Fig. 24 can be summed, normalized and compared as shown in Fig. 25. If there is any difference at all, it is

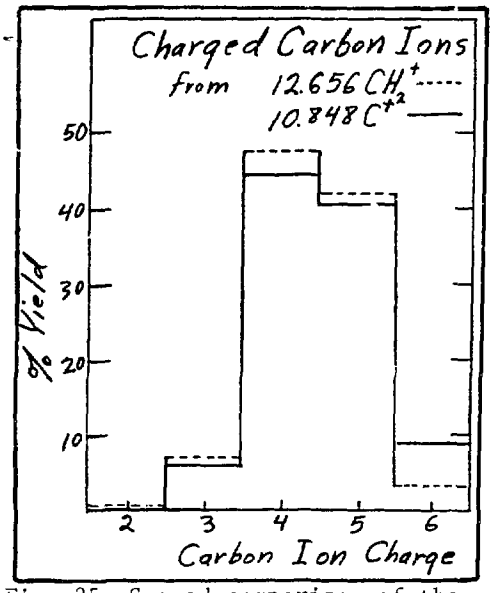

Fig. 25 Summed comparison of the data of Fig. 24.

possible that the bare carbon ions produce a slightly larger amount of 6+, compared to the other charge states. However, the shift in the charge state distribution is probably considerably less than half a charge state, which means that cluster effects of the associated hydrogen atoms in the CH_2 are considerably less than what was observed for similar measurements with the $C_{2,3,4}$ molecular systems.

In summary, we have found that this new detector system allows many kinds of molecular systems to be studied with Coulomb explosion techniques, and future refinements of the technique may make these measurements much more quantitative than is now possible.

References

1. Wegner, H.E. $C^-_{3,4,5}$ and $NCO^{+,-}$ Molecular Ion Structure Determination by Coulomb Explosion. Proceedings of the Informal Workshop on the Penetration of Charged Particles in Matter Under Extreme Conditions. New York University, New York, Jan. 3-5, 1980. Editor Stanley Stern.

2. Wegner, H.E. and Thieberger, P. Molecular Explosion of Large Penetrating Clusters. Proceedings of the Informal Workshop on the Penetration of Exotic Particles in Matter, New York University, New York, Jan. 8-11, 1981 (in press).

3. Thieberger, P. and Wegner, H.E. 2D Multiple Event Image Intensifier Scintillation Ion Detector. Bull. Am. Phys. Soc. 25, 46 (1981).

4. Goldring, G., Eisen, Y., Thieberger, P., Wegner, H.E. and Filevich, A. C_3 and NCO (+,o,-) Molecular Ion Structure Studies by Coulomb Explosion. Phys. Rev. A (in press).

CHARGED PARTICLE TRACK STRUCTURE IN INSULATORS*

R. H. Ritchie
Oak Ridge National Laboratory
Oak Ridge, Tennessee 37830
and
Carsten Claussen
Odense University
Odense, Denmark

The structure of charged particle tracks has been of great interest in radiation physics, radiochemistry, and radiobiology for many decades. There is, however, no generally accepted mechanism to explain atomic displacement in and sputtering of solids by swift charged particles. An ion with velocity $v \gtrsim v_0 = e^2/\hbar = 2.19 \times 10^8$ cm/s loses most of its energy to electrons in the stopping medium, but atomic displacement is necessary for track registration. The complex sequence of events following excitation and ionization of atoms near a track that leads finally to displacement or sputtering of atoms is so poorly understood that only phenomenological analysis has been made.

A complete theory must explain how material in which tracks form becomes strained following the passage of swift ions and how atoms acquire enough energy to become sputtered.

The ion explosion model has been much discussed. It assumes that electrons ejected from the track core are trapped far from the track and that the potential energy of the residual ions becomes converted to kinetic energy. The final stages involving sputtering and atomic displacement must occur despite competitive processes.

---

* Research sponsored in part by the Office of Health and Environmental Research, U.S. Department of Energy, under contract W-7405-eng-26 with Union Carbide Corporation.

We have been led to a new model of track formation by the difficulty, remarked by several authors, of justifying the trapping of the ejected electrons away from the track. We hypothesize that these electrons return quickly to form a core electron-ion plasma fed by energy from excited states that should exist in high concentration near the core region.[1] These aspects of track structure have not been emphasized before in this connection.

Numerical calculations based on this model have been carried out. We have assumed that positive ions formed close to the track are described by hydrodynamical theory and that the transport of ejected delta-ray electrons is represented in a nonlinear age-type theory. Preliminary results indicate that our mechanism may be very important in some insulators. More accurate numerical work is under way.

---

[1] R.H. Ritchie and Carsten Claussen, *Nucl. Instrum. Methods* (1982) in press.

SUMMARY DISCUSSIONS

Remarks intended to highlight topics of importance for future research were made by three of the participants at the conclusion of the Seminar. The following gives a brief listing of topics discussed by each of these rapporteurs:

Prof. F. Fujimoto

I. Stopping Cross Sections

A. Experimental values of I, b, C(z), Z*, etc.

1. These values do not always agree well with corresponding theoretical values. Such differences should be studied in detail.

2. Experiments should be done at high energies where exchange effects need not be considered.

3. Experiments should be done with μ^+ and μ^- to obtain accurate values of the Z_1^3 correction.

B. The stopping power for channeled ions

1. Theory shows good agreement with observation.

2. Values of random stopping power should be inferred from measurements or theory of the corresponding stopping power for channeled particles so that comparison with well-studied values may be made.

C. Effective charge Z_1^* theory shows good agreement with experiment.

D. Experimental charge exchange cross sections were explored semi-quantitatively by atomic collision theory.

E. Empirical formulas for stopping power for any projectile and any material over a wide range of projectile energies were proposed.

1. Agreement with observed values was found to be within ± 20%.

F. The effect of target thickness on stopping power

1. Geometrical effects, multiple scattering may be important under some circumstances.

2. Surface plasmon generation may be quite important at very small incident angles.

G. The formation of tracks in insulators

1. Closely correlated with the stopping power problem

2. The intricate sequence of physical and chemical effects is not yet clear.

H. Stopping power of compounds

1. Physical and chemical effects need further experimental and theoretical study.

II. Molecular Ions in Solids

A. Convoy electrons

1. There may be appreciable contributions from field-ionized Rydberg electrons.

B. Target excitation by molecular ions

1. Why is a vicinage effect observed in Al_2O_3 but not in Al?

C. Energy loss by molecular ions

1. Clearly correlated with dissociation, Coulomb explosions, etc.

2. Contrast in STIM - H_2^+ ion STIM

D. Structure of molecular ions shows up

1. In ring patterns

2. In track patterns

E. Surface scattering of ions

1. Dissociation probability has close relation with foil transmission of ions, dwell times.

2. Image potential theory predicts "stand-up" of molecular ions.

F. Scanning ion microscopy - Ga ion beam size ∿100 Å

1. Striking contrast due to channeling

2. SIM may be more useful than SEM for surface studies.

Dr. O. H. Crawford

I. Measurements of I

A. Hard to find unique I from data, although excellent theoretical guides for interpolating dE/dx are available. Continuing effort necessary.

B. Determination of dE/dx to high projectile energies from optical data should be encouraged (synchrotron radiation data would be very valuable).

II. Other Formulations of -dE/dx theory

A. May be useful alternative to using I with corrections.

B. May be computed from optical data parameterized to yield $\epsilon^{-1}(k,\omega)$ or from the local density approximation with the electron gas model.

C. Sum rules may be invoked in the parameterization, structure factors may be used.

D. Applicable in a more general context, e.g., energy straggling.

III. Perturbation Theory of dE/dx at Low Velocities

A. Perturbation α v as $v \to 0$

B. Perturbation series $S(v) = \sum_n S^{(n)} v^n$

C. By symmetry $S(-v) = S(v)$; hence, $S(v) = S^{(1)}v + S^{(3)}v^3 + \ldots$

IV. Other Effects of Current Interest

A. Molecular projectiles - screening and wakes

B. Charge state effects

C. Scattering angle dependence of -dE/dx

D. Directional effects on -dE/dx

E. Thickness effects on -dE/dx

F. Surface effects on -dE/dx

G. Secondary electrons from solids - convoy, Rydberg states

H. Connection with collisions in the gas phase

Prof. R. H. Ritchie

A brief listing of some recommendations for future work of importance to this field follows.

- Z_1^3 Theory. More work needs to be done toward understanding the Z_1^3 effect for atomic systems. In particular there should be a comparison of contributions from close and from distant collisions on the basis of atomic models.
- Relativistic Shell Corrections. The electron gas statistical model of Bonderup seems to be quite useful for describing shell corrections for nonrelativistic electrons in the stopping medium. It should be

extended to the relativistic region. This will require an expression for the complete RPA dielectric function for a Dirac electron gas. Bonderup has derived such an expression but has never published it. He should be encouraged to do so.

- Density Effect. Modern calculations of the Sternheimer density effect correction to the stopping power of condensed matter have been carried out recently for Al metal and for H_2O. This work was based on oscillator strength measurement and theory. Extension to other materials would be useful.
- Stopping Power in the Region $0 \lesssim v \lesssim v_o$. Recent theoretical work by Brandt and Kitigawa seems to give surprisingly good agreement with experiment in this range. This semi-empirical approach should be extended and should be studied for $v << v_o$ where their use of linear response theory may be tested against phase shift results.
- Effective Charge. It may be useful to compare Z^* for energy loss with Z^* for Coulombic interactions responsible for convoy electron formation, etc.
- Inner-Shell Excitation. Further developments of perturbed stationary state theory that were discussed would be desirable in this active research area.
- Impact Parameter Dependence of Energy Loss. This theory has been discussed and gives good agreement with experiment, but more work should be done, perhaps with alternative approaches.
- Convoy Electron Theory. Although the theory for ion-atom collisions seems to be in good quantitative agreement with experiment, the same is not true for electrons ejected from solids. A thorough theoretical

treatment of the CTC process and the contribution of wake-riding electrons to the convoy spectrum is needed.

- Vicinage Effect Theory in Nonmetallic Solids. Experimental data from the University of Chicago group seems to indicate that existing theory of the vicinage effect does not apply when $v \lesssim v_o$ and when the cluster penetrates a carbon medium. This should be studied.
- Availability of Argonne Dynamitron Beam. The Dynamitron beam line with its high angular and energy resolution and ability to separate charge states may be used for accurate measurements of stopping powers. It should be excellent for finding stopping power as a function of projectile charge state. D. S. Gemmell welcomes workers interested in using this Argonne facility.
- Bloch Corrections. During the conference it was suggested by J. A. Golovchenko that Bloch corrections to -dE/dx theory for partially screened ions should be made using the full ionic charge rather than the Z^* value. This is due to the fact that for velocities >> v_o, the relevant impact parameters are so small that the full ionic charge is seen by the struck atom.
- Directional Dependence of I. The theory of energy loss in crystals has been shown to lead to the prediction that the mean excitation energy for energy loss by an ion proceeding in a given crystal direction should depend, in general, on that direction. In addition, it shows that in optically anisotropic materials, a "wiggly wake" should develop in certain directions.
- Dielectric Data. More work should be done to infer I from optical response measurements on solids.

- Inertial Confinement Conditions. Theoretical work toward understanding energy losses by ions under extreme conditions of temperature and pressure is very challenging. The presentation and synthesis of theoretical methods from different areas of physics point toward substantial progress.
- Charge State Theory. The systematic approach toward evaluating capture and loss cross sections based on atomic models for the ion-solid interaction should be encouraged. Solid state effects are thus highlighted and may be understood by comparison with theory based on atomic models.
- Rydberg States Contribution to Convoy Electrons. The work reported on the contribution to convoy electrons of field-ionized electrons in Rydberg states on ions emerging from solids casts new light on the phenomenon of convoy electron measurement.
- Determination of the Structure of Molecular Ions. Analysis of Coulomb explosion patterns to determine molecular ion structures yields much useful information. This method promises to be a very useful tool in the future.

SEMINAR PARTICIPANTS

J. C. Ashley
Health and Safety Research Division
Oak Ridge National Laboratory
Oak Ridge, Tennessee 37830

G. J. Basbas
Physical Review Letters
P.O. Box 1000
Ridge, New York 11961

M. J. Berger
Center for Radiation Research
National Bureau of Standards
Washington, D.C. 20234

J. P. Biersack
Hahn-Meitner-Institute
Glienicker Str. 100
1000 Berlin 39
West Germany

O. H. Crawford
Chemistry Division
Oak Ridge National Laboratory
Oak Ridge, Tennessee 37830

T. Doke
Science and Engineering Research
Laboratory
Waseda University
Kikui-cho Shinjuku-Ku Tokyo 162
Japan

Fujimoto
College of General Education
The University of Tokyo
Komaba Meguro-Ku Tokyo 153
Japan

F. Fukuzawa
Department of Nuclear Engineering
Kyoto University
Sakyo-Ku Kyoto 606
Japan

D. S. Gemmell
Physics, Bldg. 203
Argonne National Laboratory
9700 S. Cass Avenue
Argonne, Illinois 60439

J. Golovchenko
Bell Laboratories
600 Mountain Avenue
Murray Hill, New Jersey 07974

R. Ishiwari
Department of Physics
Nara Women's University
Nara 630
Japan

M. Kitagawa
Department of Electronics
North Shore College
Atsugi-Shi 243
Japan

K. Komaki
College of General Education
The University of Tokyo
Komaba Meguro-Ku Tokyo 153
Japan

W. N. Lennard
Atomic Energy of Canada Limited
Research Company
Chalk River Nuclear Laboratories
Chalk River, Ontario
Canada K0J 1J0

R. Levi-Setti
The Enrico Fermi Institute
and Department of Physics
University of Chicago
Chicago, Illinois 60637

M. Mannami
Faculty of Engineering
Kyoto University
Sakyo-Ku Kyoto 606
Japan

R. M. More
Lawrence Livermore Laboratory
University of California
P. O. Box 808
Livermore, California 94550

N. Oda
Research Laboratory of Nuclear
Reactors
Tokyo Institute of Technology
Ookayama Meguro-Ku Tokyo 152
Japan

Y. Ohtsuki
School of Science and Engineering
Waseda University
Okubo Shinjuku-Ku Tokyo 160
Japan

L. E. Porter
Department of Physics and Astronomy
University of Montana
Missoula, Montana 59812

R. H. Ritchie
Health and Safety Research Division
Oak Ridge National Laboratory
Oak Ridge, Tennessee 37830

N. Sakamoto
Department of Physics
Nara Women's University
Nara 630
Japan

F. Schulz
Gesellschaft fur Strahlen-und
Umweltforschung
Physikalisch-Technische Abteilung
D-8042 Neuherberg
West Germany

N. Shiomi
Department of Physics
Nara Women's University
Nara 630
Japan

H. E. Wegner
Department of Physics
Brookhaven National Laboratory
Upton, New York 11973

J. F. Ziegler
IBM Research
Yorktown Heights, New York 10598